The new PWO Crystal Generation and Concepts for the Performance Optimisation of the PANDA EMC

vorgelegt von

Dipl.-Phys. Tobias Eißner
aus Ortenberg
Gießen, 2013

Contents

Contents

Abstract

The finally achievable performance of the PANDA EMC, which was aiming for an extremely compact and radiation hard calorimeter, covering for the first time an energy regime from $15\,\mathrm{GeV}$ down to a few MeV, strongly relies on the quality parameters of the $PbWO_4$ crystals. Therefore a very complex test procedure was elaborated, which basically consists of three stages of quality control at the locations BTCP, CERN and Gießen. The obtained data of $9,336$ crystals was analysed with respect to the specification limits. Furthermore, correlations and discrepancies between the different facilities, mainly caused due to the different treatment of crystal geometries, are discussed in detail. Finally, an outlook of the still mission fraction of crystals for the PANDA EMC is given. The SICCAS company at China is a promising manufacturer of $PbWO_4$ experienced by the production of a significant fraction of crystals for the CMS experiment. Here, the quality of 50 test samples were tested and compared, in particular with respect to the different growing technology. The obtained results are promising, but all parameters scatter over too wide distribution and a more homogeneous quality is expected from a pre-production run.

A sufficient time resolution for the EMC is necessary to provide an accurate time stamp for the detected physics events synchronously with the time distribution system SODA of PANDA and for the rejection of background events. The time-walk corrected resolution under different conditions and digitisation procedures was determined at three separate beamtimes and compared to results from the CMS experiment. The achievements presented in this work represent an upper limit for the final time resolution, since the foreseen APFEL ASIC with two dynamically adjustable and independent gain branches will further improve the timing performance.

As additional aspect of this thesis, a possible energy sum correction algorithm is introduced. Due to the presence of passive material between the crystals, the energy reconstruction is significantly reduced, if the point of impact is located close to the edge of a crystal. The so called $\ln(E_2/E_1)$-method considers the shape of the lateral shower distribution and was successfully exploited for showers initiated by positrons and photons, as well. Especially for hits in between two crystals a significant improvement has been achieved.

Zusammenfassung

Das Designziel des EMC des zukünftigen PANDA Detektors ist, einen möglichst kompakten und strahlungsresistenten Detektor zu entwickeln, der es erstmalig ermöglicht, einen Energiebereich von $15\,\mathrm{GeV}$ bis einigen MeV abzudecken. Dessen endgültige Effizienz und Präzision hängt stark von den Qualitätsparametern der verwendeten $PbWO_4$ Szintillationskristalle ab. Dies wird durch eine dreistufige Prozedur bei BTCP, CERN und Gießen realisiert. Die gesammelten Daten von 9.336 Kristallen wurden mit Hinblick auf die gestellten Anforderungen analysiert. Desweiteren werden in dieser Arbeit Korrelationen und Diskrepanzen der einzelnen Teststationen, die hauptsächlich auf die unterschiedliche Handhabung der Kristallgeometrien zurückzuführen sind, diskutiert. Letztendlich wird ein Überblick über den noch nicht produzierten Anteil der benötigten Kristalle gegeben. Das Unternehmen SICCAS in China ist ein vielversprechender Hersteller von $PbWO_4$ und produzierte bereits einen signifikanten Anteil der Kristalle für das CMS Experiment. 50 Testkristalle von SICCAS wurden getestet und ausgewertet gemäß ihrer Brauchbarkeit und unter Anbetracht des unterschiedlichen Wachstumsprozesses im Vergleich zu BTCP. Die erhaltenen Resultate sprechen für eine Verwendung im PANDA Detektor, aber nichtsdestotrotz gilt es die Homogenität des Herstellungsprozesses weiter zu optimieren.

Eine ausreichende Zeitauflösung für das EMC ist notwendig, um eine genaue Zeitmessung zu liefern und um die physikalischen Ereignisse mit Hilfe des Zeitverteilungssystems SODA zuzuordnen. Die time-walk korrigierte Auflösung unter verschiedenen Bedingungen und Digitalisierungsverfahren wurde bei drei seperaten Strahlzeiten bestimmt und mit den Resultaten des CMS Experiments verglichen. Die in dieser Arbeit aufgeführten Resultate, bezüglich der Zeitauflösung, sind als eine obere Grenze anzusehen. Mit der Einführung des APFEL ASIC mit zwei regelbaren Verstärkungskanälen, ist eine weitere Verbesserung der Zeitbestimmung zu erwarten.

Ein zusätzlicher Aspekt dieser Arbeit ist die Anwendung eines Algorithmus zur Korrektur der gemessenen Gesamtenergie. Durch das Vorhandensein des passiven Materials zwischen den Kristallen, wird die Energierekonstruktion signifikant verschlechtert, falls der Auftreffpunkt des einfallenden Teilchens nahe der Kristallkante liegt. Die sogenannte $\ln(E_2/E_1)$-Methode berücksichtigt die transversale Ausbreitung des elektromagnetischen Schauers und wurde erfolgreich für Positronen und Photonen angewendet. Speziell im Falle eines Strahls, der zwischen zwei Kristalle gerichtet ist, lässt sich eine erhebliche Verbesserung der Energieauflösung erzielen.

Chapter 1

Introduction and Motivation

The planned FAIR[1] facility in Darmstadt is a new and unique international accelerator facility for the research with ions and antiprotons. The concept of FAIR has been developed in cooperation with an international community of 45 countries and about 2,500 scientists and engineers. The accelerator and storage ring structure is capable of simultaneously providing high-intensity and -energy beams for various experiments.
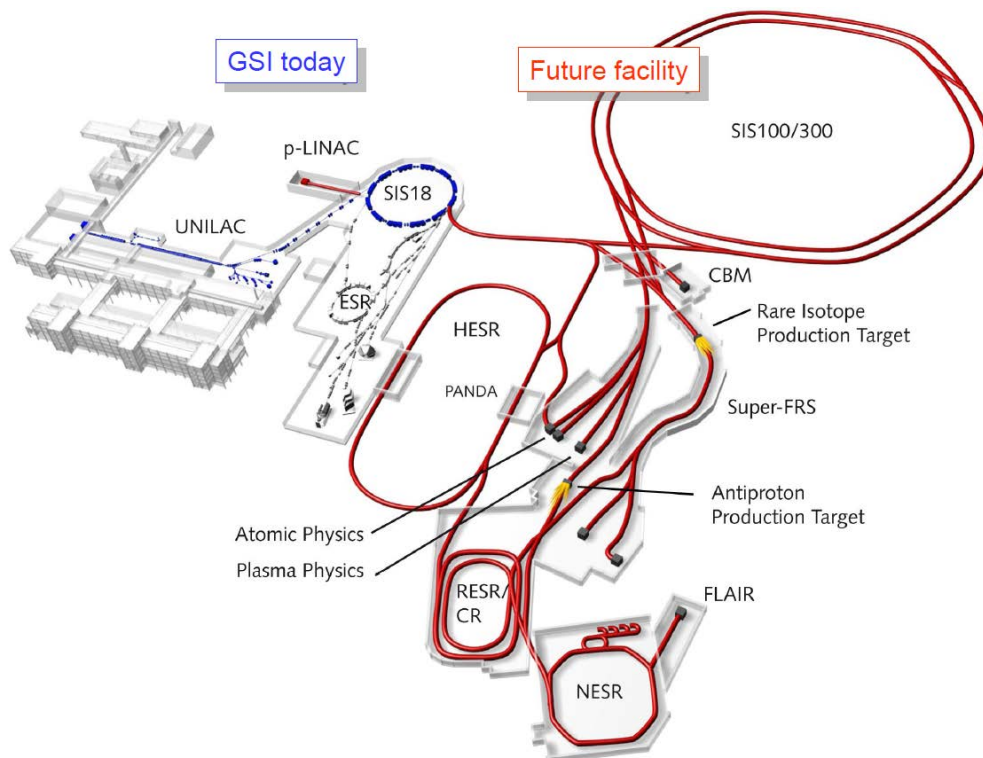
Figure 1.1: Existing GSI (blue) with planned FAIR facility (red) [1].

---

[1]Facility for Antiproton and Ion Research

The existing accelerator facility of GSI[2] (compare Fig. 1.1) consists of a multi-purpose linear accelerator UNILAC[3], a heavy-ion synchrotron SIS[4] and a storage ring ESR[5]. All these constituents were built from 1975 to 1990 and are able to accelerate and store nuclei of all elements in the periodic system up to 90% of the speed of light. For the FAIR accelerator framework, the SIS18 will act as an injector. The central component of the new accelerator system are two superconducting synchrotron rings with maximum magnetic rigidities of $100\,\mathrm{Tm}$ and $300\,\mathrm{Tm}$ called SIS100 and SIS300, respectively. Both rings have an identical circumference of almost $1,100\,\mathrm{m}$. For the production of antiprotons, the SIS100 provides pulsed proton beams in the order of 10^{13} protons per bunch with an energy up to $30\,\mathrm{GeV}$ which will impinge on a metal target. Antiprotons are subsequently accumulated and cooled down to $3.8\,\mathrm{GeV}/c$ and injected either in the HESR[6] or the NESR[7].

The experiments of the FAIR facility will help to understand a large amount of unsolved physical issues, which basically can be subdivided in three aspects:

- structure and properties of matter

- evolution of the universe

- technology and applied research

Tab. 1.1 summarises the four main experiments focussing on various topics.

Experiment	Topic
APPA	**A**tomic, **P**lasma **P**hysics and **A**pplications
CBM	**C**ompressed, **B**aryonic **M**atter
NUSTAR	**NU**clear **ST**ructure, **A**strophysics and **R**eactions
PANDA	Anti**P**roton **A**nnihilation at **DA**rmstadt

Table 1.1: FAIR experiments [2]

This thesis invariably focus on the PANDA experiment, in particular the technical performance of one designated subdetector: the EMC[8].

---

[2]**G**esellschaft für **S**chwerionenforschung GmbH
[3]**U**niversal **L**inear **A**ccelerator
[4]**S**chwer **I**onen **S**ynchrotron
[5]**E**xperimental **S**torage **R**ing
[6]**H**igh **E**nergy **S**torage **R**ing
[7]**N**ew **E**xperimental **S**torage **R**ing
[8]**E**lectro**m**agnetic **C**alorimeter

1.1 The PANDA Experiment

PANDA[9] is a state-of-the-art experiment to study various aspects of the strong interaction in the momentum range up to $15\,\mathrm{GeV}/c$ and is located as an internal detector at the HESR (shown in Fig. 1.2). The HESR is designed as a racetrack shaped ring and exploits different cooling methods to ensure unprecedented beam quality and precision. Two different operation modes are available (Tab. 1.2).

High resolution mode	luminosity momentum spread $\Delta p/p$ $\bar{p}$ momentum range	$2 \cdot 10^{31}\,\mathrm{cm}^{-1}\mathrm{s}^{-1}$ 10^{-5} 1.5 - 9 GeV/c
High luminosity mode	luminosity momentum spread $\Delta p/p$ $\bar{p}$ momentum range	$2 \cdot 10^{32}\,\mathrm{cm}^{-1}\mathrm{s}^{-1}$ 10^{-4} 1.5 - 15 GeV/c

Table 1.2: Parameters for the two operation modes of the HESR.

This section is intended to describe a selected fraction of the physics program, the PANDA detector and the EMC, focussing on its main components and readout chain.
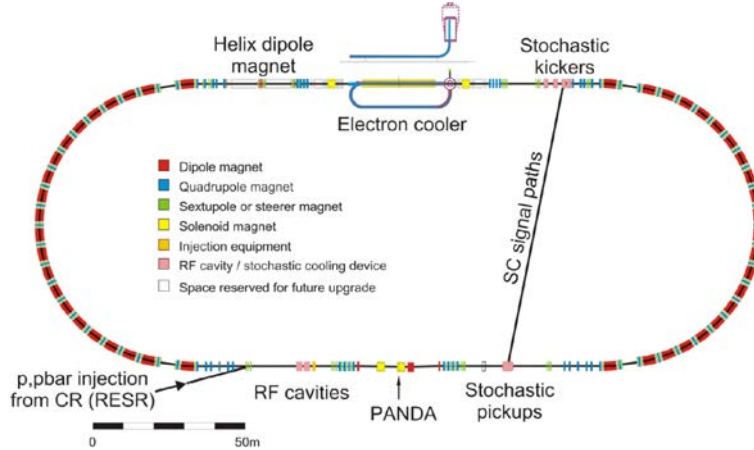
Figure 1.2: Schematic view of the HESR [3]. The electron cooler is placed in the centre of one of the straight sections. For the stochastic cooling, pick-up and kicker devices are also located in the straight sections opposite to each other. The maximum beam rigidity of 50 Tm will be achieved by dipole magnets, indicated in red. Lateral beam focussing elements are quadrupole and sextuple magnets coloured in blue and green, respectively.

---

[9]Anti-Proton Annihilation at Darmstadt

1.1.1 Physics Program

PANDA aims to study fundamental questions of the strong force using the interaction of high energetic antiprotons with nucleons and nuclei. In this momentum range of 1.5 to $15\,\mathrm{GeV}/c$ strange and charmed quarks, as well as hybrids and glueballs will be accessible. An overview of the potentially produced particles for PANDA is shown in Fig. 1.3.
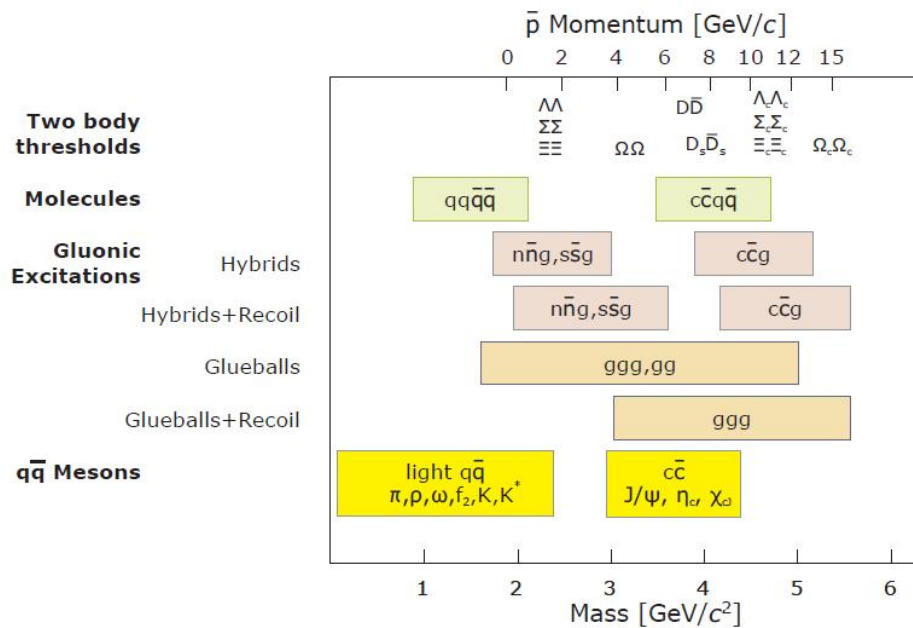
Figure 1.3: The accessible mass range in correlation with the required momentum of the antiproton beam for hybrids, glueballs, light and heavy mesons [1].

The established theory of the strong interaction is QCD[10], which is well understood at high energies, where the coupling constant becomes small and perturbation calculations can be applied. But the experimental knowledge in the non-perturbative regime is rather limited. Therefore, studies of bound states are of particular importance for the understanding of QCD. Fig. 1.4 gives an overview of expected states for various particle configurations with respect to simulations and previous experiments. In that context, the spectroscopy of the so called charmonium ($c\bar{c}$), which describes a bound state of a charm quark and its antiparticle, is one of the major topics of PANDA. The first excited state (called J/Ψ) was independently discovered in 1974 by two different groups. For the first approximation, the relatively high mass of a c quark ($\mathrm{m}_c \approx 1.5\,\mathrm{GeV}/c^2$) allows a non-relativistic description. The charmonium is also known as the "molecule of strong interaction" and its characteristics, especially

---

[10]<u>Q</u>uantum <u>C</u>hromo <u>D</u>ynamics
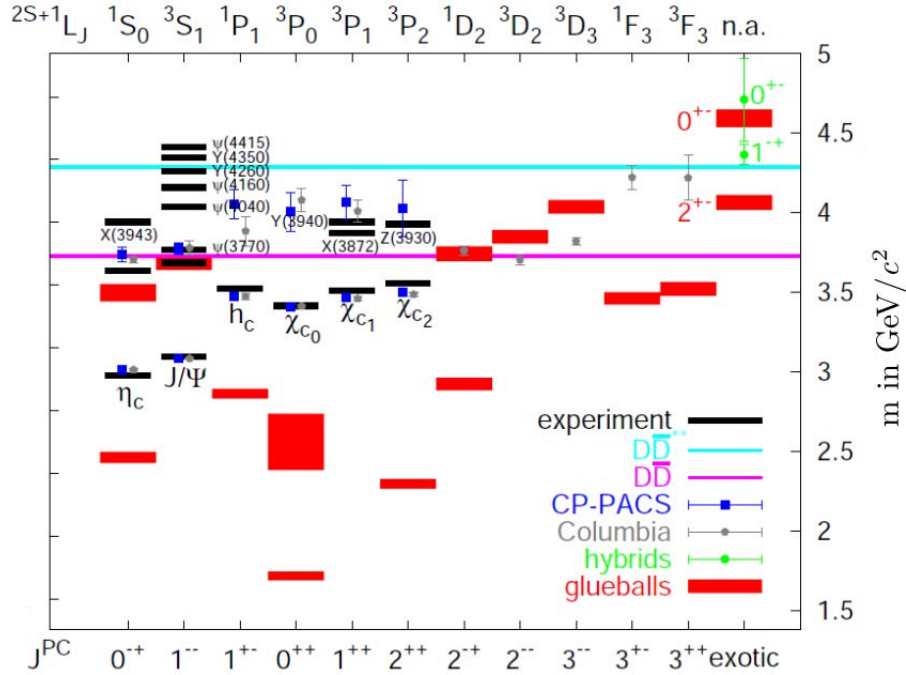
Figure 1.4: Various charmonium energy levels including states of glueballs (red
bars) and hybrids (green data) for different quantum number configurations in
the mass range of $1.5 - 5.0\,\text{GeV}/c^2$ [4]. The CP-PACS and Columbia data are
states obtained by lattice QCD calculations. The light blue and purple coloured
lines correspond to the $D^*\bar{D}^*$- and $D\bar{D}$-threshold, respectively.

the structure of the first set of energy states, very similar to the positronium (bound
state of a positron and an electron) in the electroweak interaction. This fact implies
a Coulomb-like $1/r$-term in addition to the linearly rising confinement potential. For
the formation of charmonium states, PANDA has the advantage that all charmonium
states can be populated directly via $\bar{p}p$-annihilation, because of the substructure of the
proton and the antiproton. This is not true for e^+e^--annihilation, since only states
with $J^{PC} = 1^{--}$ can be formed directly due to quantum number restrictions of the
virtual photon. Another interesting feature of $p\bar{p}p$-annihilation is the exploitation of
a scanning technique, which was used for the first time by the E385 experiment at
Fermilab. The energy of the antiprotons is successively increased, while for each step
the production rate of a certain reaction is measured. The great advantage of this
method is that the width of a certain resonance only depends on the beam spread.
Concerning charmonium spectroscopy PANDA has the task to search for the up to
now undiscovered $\eta'_c(2^1S_0)$-state, confirm the $h_c(1^1P_1)$-state, measure transition rates
more accurately and identify states above the open charm threshold ($D\bar{D}$-threshold),
which is indicated in Fig. 1.4 as purple coloured line. In addition, an accurate mea-

surement of the h_C and the χ_{C_1} energy levels will give important information on the spin contribution, since both states have the same quantum numbers, except the spin. The search for glueballs and hybrids are further important topics for PANDA. Glueballs are colour neutral objects which only consist of gluons. Former experiments (e.g. Crystal Barrel experiment at LEAR[11]) brought up various glueball candidates. For instance, the mass of the found $f_0(1500)$-resonance is close to the theoretical prediction of the ground state mass, but on the other hand there are also discrepancies due to the non-flavour blind decay mode. The expected glueball spectrum for the mass range of $1.5 - 5.0\,\mathrm{GeV}/c^2$ shows up relatively narrow and almost non-overlapping states, which is advantageous for their spectroscopy with PANDA. In the case of hybrids, one has to distinguish between light quark and charmed hybrids. Basically, hybrids are composed objects of two quarks and an excited gluon ($q\bar{q}g_{\mathrm{excited}}$). The following shows a possible decay chain of the $X(1^{-+})$-hybrid.

$$\bar{p}p \to X + \underbrace{\eta}_{\gamma\gamma} \to \underbrace{\chi_{c1}}_{J/\Psi+\gamma} + \underbrace{\pi_0}_{\gamma\gamma} + \underbrace{\pi_0}_{\gamma\gamma} + \gamma\gamma \to \underbrace{J/\Psi}_{e^+e^-} + 7\gamma \to e^+e^- + 7\gamma$$

Another interesting aspect of the PANDA physics program is the in-medium modification of hadrons in $\bar{p}A$ reactions. An expected lowering of the D-meson mass in the nuclear medium would have the consequence, that the Ψ' is kinematically able to decay in $D\bar{D}$ and other branching ratios would change as well. Also a suppression of the J/Ψ in antiproton heavy ion collisions is considered to be a signal for the formation of a quark-gluon plasma. Therefore, the $e^+e^-/\pi^+\pi^-$ discrimination capability of the PANDA detector has to be on a sufficient level to discriminate against the most dominant $\bar{p}p \to \pi^+\pi^-$ background channel. Hyperon - antihyperon pairs can also be formed in $\bar{p}A$ collisions, which allows a direct comparison of baryon and antibaryon potentials. The production and detection of double hypernuclei becomes possible, but requires a further modification of the PANDA detector in a later stage. The backward calorimeter and the innermost tracking detector (MVD[12]) have to be replaced by Germanium semiconductor detectors (Fig. 1.5b), to provide keV energy resolution for the spectroscopy of γ-decays of excited nuclei down in the MeV range. The production and detection strategy for double hypernuclei is illustrated in Fig. 1.5a.

All the mentioned physics topics of the PANDA experiment strongly rely on the performance of the electromagnetic calorimeter (EMC). Especially the accurate reconstruction of multiple neutral mesons by the obtained energy signal and momentum of the decay photons, like it was exemplary shown for the $X(1^{-+})$-hybrid, underlines the important role of the EMC over a large dynamic range.

---

[11]<u>L</u>ow <u>E</u>nergy <u>A</u>ntiproton <u>R</u>ing
[12]<u>M</u>icro <u>V</u>ertex <u>D</u>etector
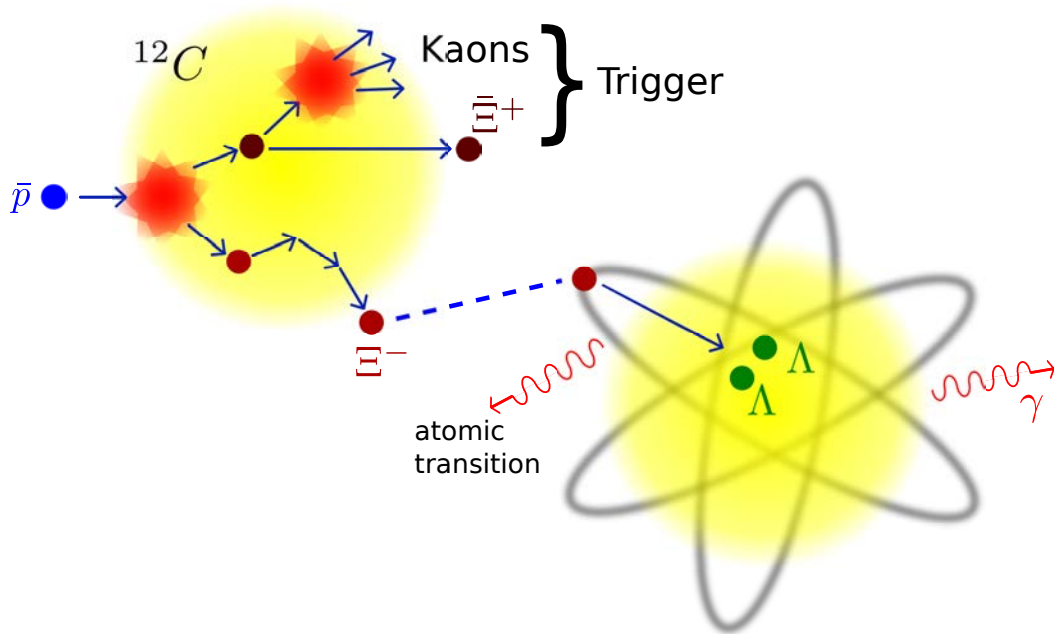
(a) The Ξ^- which is produced via $\bar{p}p \to \Xi^-\bar{\Xi}^+$, rescatters in the primary ^{12}C target nucleus and is stopped in a secondary target. After an atomic transition two Λ's are produced by the following reaction: $\Xi^-p \to \Lambda\Lambda$. γ-spectroscopy gives information about the structure of the double hypernucleus. The produced $\bar{\Xi}^+$ and kaons serve as an external trigger.
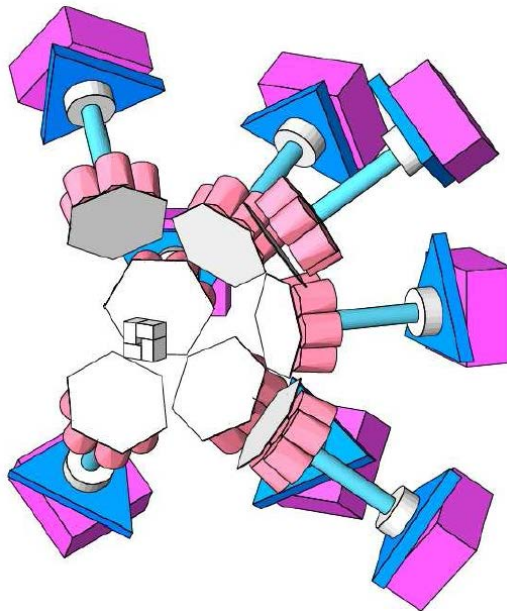
(b) Germanium detectors for the implementation in backward direction.

Figure 1.5: Hypernuclei spectroscopy.

1.2 The PANDA Detector

PANDA is a fixed target experiment with Lorentz-boosted decay products downstream the $\bar{p}$-beam. The final interplay of the shell-like arranged subdetectors is the key to guarantee the realisation of the mentioned physics program. The detector, which is operating in a triggerless mode, has the ability to detect and distinguish a large variety of charged and neutral particles (γ-rays, leptons, muons, kaons, etc.). In principle, the PANDA detector is build out of two almost azimuthally symmetric units (shown in Fig. 1.6) with nearly 4π solid angle coverage. A target spectrometer (TS) surrounds the interaction point and is designed for the detection of particles which are emitted from the target point with a larger polar angle than $10°$ and $5°$ for the horizontal and vertical direction, respectively. The operational area of the TS is superimposed by a $2\,\mathrm{T}$ magnetic field produced by a superconducting solenoid. Extremely forward boosted particles will be detected by the forward spectrometer (FS) after passing a dipole magnet with a field integral of $2\,\mathrm{Tm}$. The FS is able to cope with the highest count rates to be expected in the order of $\gtrsim 0.5\,\mathrm{MHz}$ for the innermost region. In the TS region, the count rate will remain below $100\,\mathrm{kHz}$. Furthermore, the detector has to sustain a large radiation dose, which becomes more crucial for the forward region. In the following, the submodules of the PANDA detector will be discussed focussing on their purpose and physical functionality.
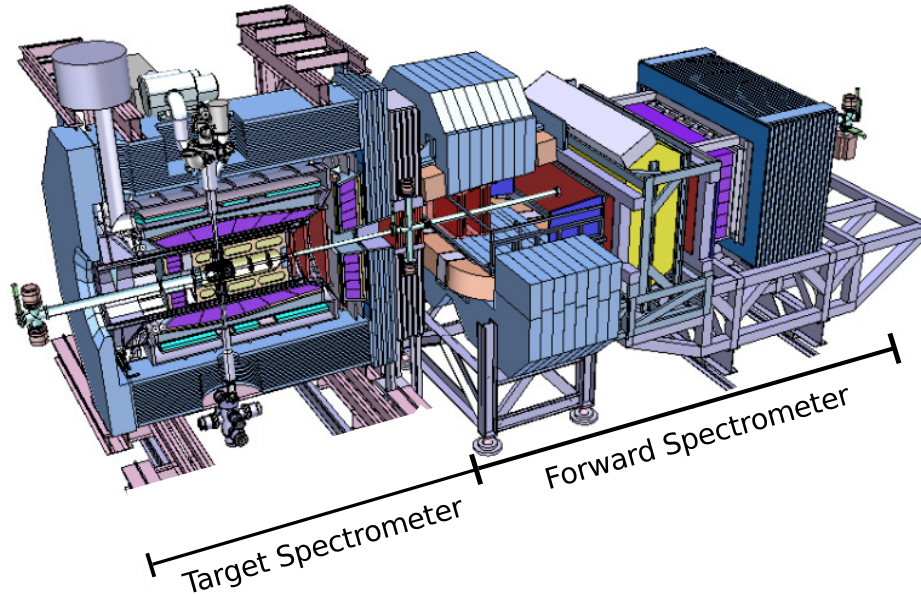
Figure 1.6: TS and FS of the PANDA detector.

1.2.1 Target Spectrometer

A variety of target materials will be available for PANDA depending on the experiment. The major part of the physics program requires a high density hydrogen target, which is realised by frozen pellets with an areal density in the order of a few 10^{15} atoms/cm^2. At the interaction point, the falling speed of $\sim 60\,\frac{\mathrm{m}}{\mathrm{s}}$ of sized pellets with $\sim 25\,\mu$m diameter results in about 100 interactions during a single pellet passing the $\bar{p}$-beam. After the production and collimation on top of the PANDA detector, the hydrogen pellets are pumped through a magnetically shielded injection pipe cooled down to 14 K, which is occupies a minimal space. The target beam dump is installed at the end of this straight section below the PANDA detector. In addition a cluster-jet target and heavier solid targets for hypernuclear studies will become available.
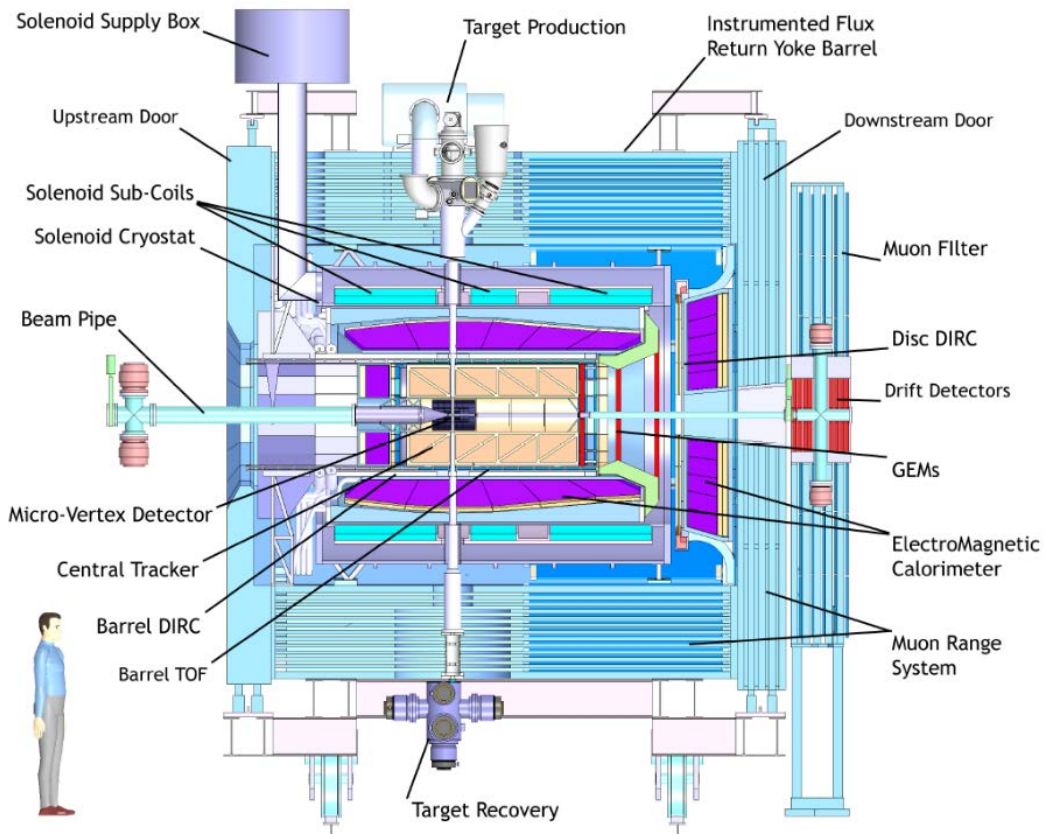
Figure 1.7: The TS is outlined in a shell-like structure detector [5]. The antiprotons enter from the left and interact with the target. Each subdetector has a different task according to the final reconstruction of the events, which will be discussed in the following. The asymmetric position of the interaction point accomplishes the fixed target kinematics.

The MVD is the innermost tracking detector surrounding the target region in a cylindrical shape. Its extension along the beam axis is roughly $\pm 23\,\text{cm}$ with respect to the nominal interaction point with a radius of 15 cm. It is composed of silicon pixel and strip sensors (shown in Fig.1.8) with a thickness of $100\,\mu\text{m}$ and $280\,\mu\text{m}$, respectively [6].
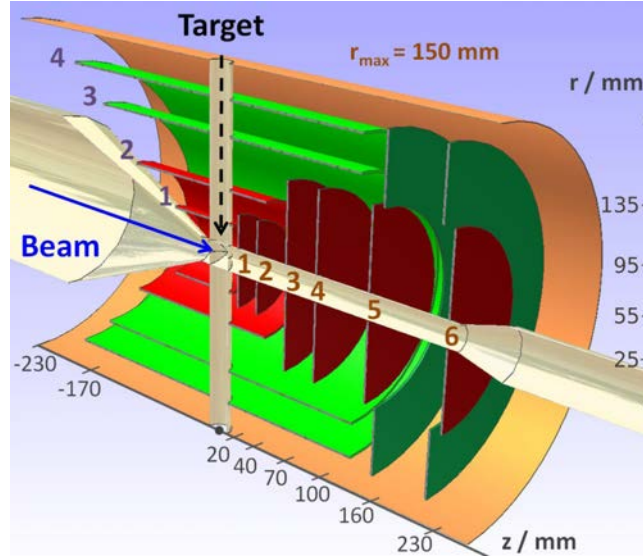
Figure 1.8: Schematic layout of the MVD. The barrel shaped innermost modules (red, 1-2) and the first set of discs in forward direction (dark-red, 1-4) are equipped with silicon hybrid pixel sensors ($100 \times 100\,\mu\text{m}^2$) with a channel granularity of 11M channels per $0.13\,\text{m}^2$. The outer two modules (green) solely consist of double sided silicon strip sensors with 200k channels per $0.5\,\text{m}^2$. Discs 5 and 6 are composed of both, pixels and strips.

An important requirement to the MVD besides the spatial resolution ($\leq 100\,\mu\text{m}$), is the minimum material budget. The total amount of material in units of radiation length should be kept below $X/X_0 = 4\%$ to minimize pair production due to photon conversion. A charged particle propagating through the active material of the MVD loses energy due to ionisation and produces electron-hole pairs along its trajectory. This effect can be described by the Bethe-Bloch equation (Eq. 1.3). For thin absorbers, the mean energy loss is fluctuating and follows a Landau-distribution. The produced charge is collected applying an external voltage. MIPs[13] ($\beta\gamma \approx 3$) have an average energy loss in $300\,\mu\text{m}$ silicon of 90 keV which corresponds to $\sim 25,000$ electron-hole pairs [7]. The position and energy loss information is subsequently used for the track reconstruction and particle identification. A necessary feature of the MVD is the reconstruction of secondary decay vertices. The detection efficiency of

---

[13]<u>M</u>inimum <u>I</u>onising <u>P</u>articles

weak-interacting decay modes e.g. of charmed hadrons with a decay length in the order of $100\,\mu$m, can additionally be improved by adding two so called "Lambda-discs" made of Si-pixels further downstream at $40\,$cm and $60\,$cm from the target point. This scenario is currently under discussion.

Another tracking detector, which encloses the MVD, is the STT[14] with an overall length of $1.5\,$m and a radial extension of $15.0\,\text{cm} \leq r \leq 41.8\,\text{cm}$ with respect to the beam line [5]. The main task of the STT is the precise spatial reconstruction of the bent trajectories of charged particles in a magnetic field. The principle of the more than 4600 cylindrical straw tubes of the STT is very similar to a conventional wire chamber. A charged particle passing one of the gas-filled tubes produces electron ion pairs along its path. The produced charge is subsequently collected and amplified by the applied voltage of a few kV between the coaxial wire (anode) and the conductive inner layer (cathode) of the straw tube. Due to secondary gas ionisations one can achieve an amplification of about $10^4 - 10^5$ of the primary signal. Furthermore, the STT is able to determine the particle specific energy loss dE/dx. The position information along the tube can be obtained by the runtime of the signal. The STT has a low material budget of $X/X_0 \approx 0.05\%$ and a high rate capability, because of improved drift properties of the gas. A further tracking detector for covering the polar angle from $3°$ to $20°$ are the GEM[15]-discs. In the present version of the disc layouts, three GEM-discs are placed at $117\,$cm, $153\,$cm and $189\,$cm from the target (Fig 1.7, coloured in red). Fig. 1.9 shows a microscopic photograph of a perforated GEM foil and the structure of the electric field for one hole. The applied voltage between the pair of Cu layers is in the order of $\sim 400\,$V. Under these conditions the primarily produced electrons undergo an avalanche multiplication due to the strong electric field within the holes. With three GEM stacks one can achieve an overall gain of $\sim 10^4$.

The effect of emitted Cherenkov light, while a charged particle propagates through a medium with a certain index of refraction n, is used by two different detector modules in the TS. The Barrel DIRC[16] covers the polar angle between $22°$ and $140°$ and the Disc DIRC the forward direction (Fig. 1.10). If a charged particle has a velocity larger than c/n, Cherenkov radiation is emitted at an emission angle with respect to the particle direction of

$$\Theta_C = \arccos\left(\frac{1}{n\beta}\right) \tag{1.1}$$

While the Cherenkov photons propagating through the active material of the DIRC the initial emission angle Θ_C is conserved due to total reflections at the media transitions. Therefore, the velocity of the particle is determinable according to Eq. 1.1.

---

[14]Straw Tube Tracker
[15]Gaseous Electron Multipliers
[16]Detection of Internally Reflected Cherenkov light
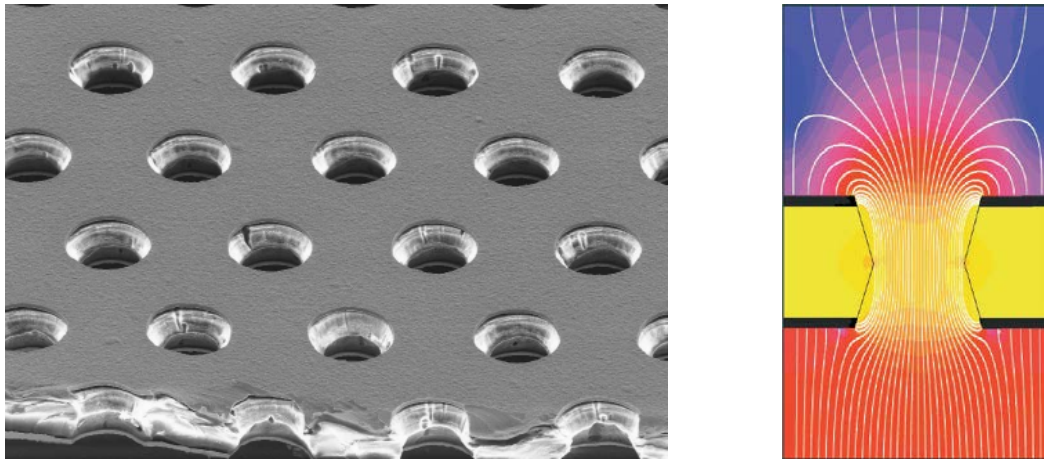
(a) Microscopic photograph of a perforated GEM foil which consists of a $50\,\mu$m Kapton enclosed by two $5\,\mu$m Copper layers.

(b) Electric field of one hole of the GEM detector with an inner diameter of $50\,\mu$m.

Figure 1.9: GEM detector with a typical level of perforation of 10^4 holes per cm^2 [8].
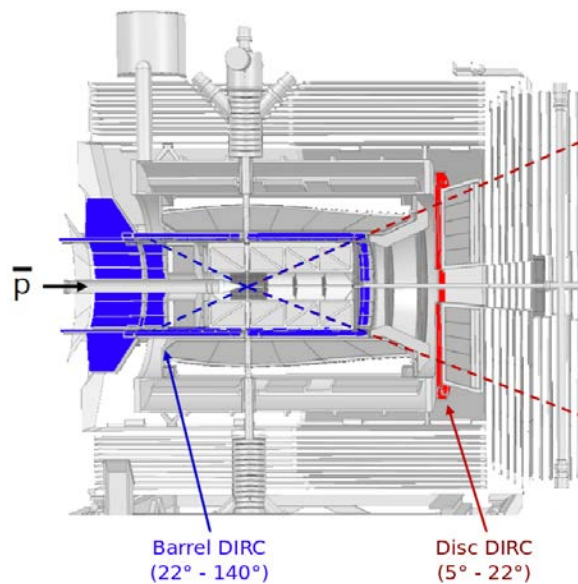
Figure 1.10: Positions of the two DIRC detector in the PANDA detector. [9]

Thus, the mass of a particle can be calculated from the momentum obtained by the tracking system and the velocity information given by the detection of the Θ_C angle. This is essential for PID[17] and the discrimination of pions and kaons on a 3σ-level. The components of both DIRC concepts consist of highly polished fused silica pieces with an index of refraction of $n \approx 1.47$. In case of the barrel DIRC, the active material is shaped in long rectangular bars arranged parallel to each other. The vertical disc plate in forward direction is subdivided into quarters for the simplification of manufacturing. The detection of the visible and near UV range Cherenkov light has to be done by fast and compact multi-pixel photo detectors with a good time resolution in the order of $\sim 100\,\text{ps}$ and a rate tolerance up to $1\,\text{MHz/cm}^2$.

Section 1.3 is intended to give a detailed overview of the next outer detector system: the EMC. Particles which are able to traverse the EMC and the solenoid in the energy range of PANDA are mainly high-energy muons and pions. For several physics branches a good muon identification is required. Each subsystem of the MUD[18] system consist of a sandwich of MDT[19] detectors and iron slabs. The slices of the MDT are oriented perpendicular to each other to obtain a two dimensional position information, which is on the level of $1 \times 1\,\text{cm}^2$ for a single MDT, but sufficient to match with the inner tracking detectors (STT and MVD). For the TS and FS, MUD devices are located at different areas (Fig. 1.11). The muon filter system (Fig. 1.11 and Fig. 1.12) has in addition the purpose of separating the magnetic fields generated by the solenoid and the dipole magnet, respectively.
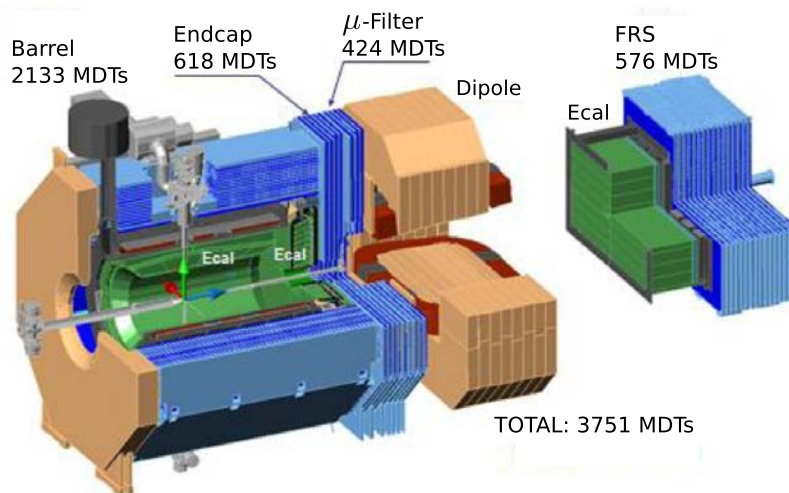
Figure 1.11: Position of the muon detectors [8].

---

[17]Particle Identification
[18]Muon Detection
[19]Mini-Drift Tube

1.2.2 Forward Spectrometer

PANDA is a fixed target experiment, therefore a large fraction of the decay fragments is boosted in forward direction due to the kinematics in the laboratory system. The physics program of PANDA requires an excellent momentum resolution for particles with a smaller polar angle than 10° and 5° for the horizontal and vertical direction, respectively. A 220 t dipole magnet provides a field rigidity of 2 Tm to achieve a momentum resolution for charged particles below 1%. Another important issue is the ramp capability, since this device has to operate fully synchronous with the HESR. Fig. 1.12 shows a schematic overview of the FS.
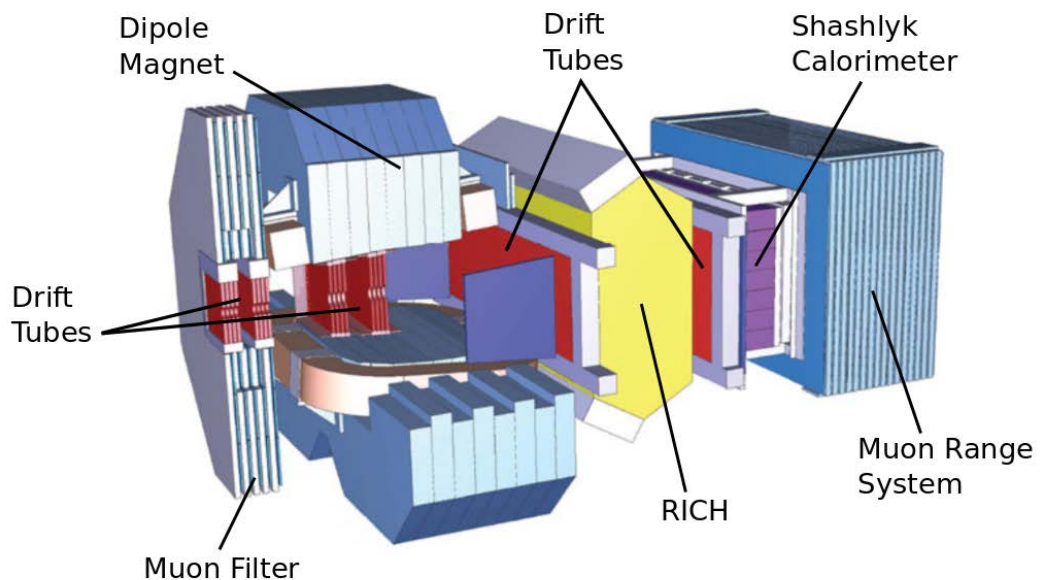
Figure 1.12: Layout of the FS [10].

The task of tracking in the very first stage of the FS is done by MDCs[20]. Three pairs of planar tracking stations are distributed within the FS: in front, inside and behind the dipole magnet (drawn in red in Fig. 1.12). This arrangement allows to track also particles with very low momenta, which will curl up and hit the magnet yoke. One single tracking station has a material budget of $\sim 0.3\% X_0$ and with an

---

[20]Multi-wire Drift Chamberss

expected position resolution in the sub-mm level, a momentum resolution of better than 1% is achievable. Another important requirement is the rate capability of up to $10^4 \, \text{cm}^{-2}\text{s}^{-1}$ close to the beam pipe. The concept of the MDC is very similar to the one in the central tracker of the TS. Electric charge produced by ionizing particles in the gas volume of the straws is collected by $20 \, \mu\text{m}$ gold plated tungsten wires for the determination of x- and y-position.

For PID in the FS it is foreseen to have a RICH[21] detector based on high quality aerogel with a refractive index of about $n = 1.02$. The detector concept is well suited for π/K separation and shows a good transmission stability and radiation hardness.

The second to last detector with respect to the beam direction is the so called Shashlyk calorimeter. The name already gives a hint to the design of this device, namely the alternating arrangement of passive lead and active plastic scintillator sheets with a thickness of 1.5 mm and 0.275 mm, respectively. One unit of a Shashlyk module has a cross section of $11 \times 11 \, \text{cm}^2$ and can be divided in four submodules (Fig. 1.13). Due to the high interaction probability in the lead, a lot of energy of the secondary decay products is deposited in the scintillating material. The de-excitation in terms of scintillation light is subsequently picked up by WLS[22] fibres, which are embedded into holes in the absorber/plastic sandwich. A pair of holes is read via a single fibre, which is bent by $180\,^\circ$ at the front of the module. The fibre ends are attached to PMTs[23] for fast light conversion and signal generation.

The estimated performance requirements for the Shashlyk detector are:

Energy resolution	$4.0\%/\sqrt{E[\text{GeV}]}$
Time resolution	$100 \, \text{ps}/\sqrt{E[\text{GeV}]}$

Table 1.3: Most important requirements of the Shashlyk detector [11].

Another part of the muon detection system is the rectangular shaped FRS[24]. It has the same structure like all other submodules of the MUD system and is mainly responsible for the separation of muons and charged pions due to their different penetration depth.

---

[21]Ring Imaging Cherenkov Counter
[22]Wavelength Shifting
[23]Photomultiplier Tubes
[24]Forward Range System
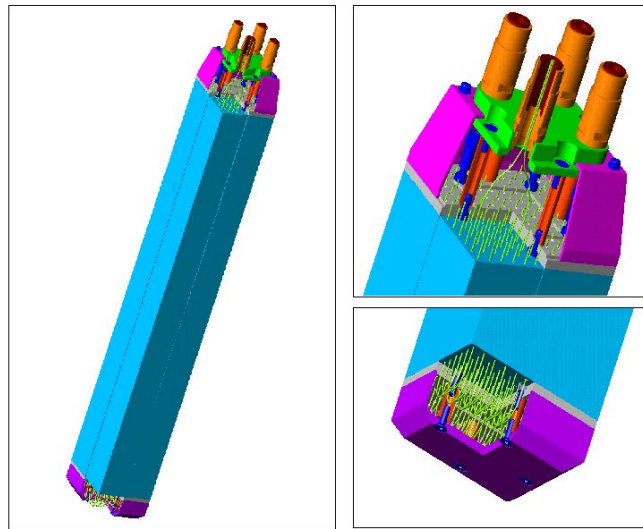
(a) Technical drawing of a Shashlyk module.

(b) Photograph of a prototype without photo sensors.

Figure 1.13: Shashlyk module [11].

1.3 Electromagnetic Calorimeter

As it was pointed out in Sec. 1.1.1, the EMC is the most important subdevice of the PANDA detector for the detection of electromagnetic probes in various benchmark channels of the physics program. The EMC can be subdivided in three parts for the coverage of different polar angles (Fig. 1.14). For clarity, the nomenclature introduced in Tab. 1.4 is used for the remainder of this thesis.

EMC part	Nomenclature	Polar angle range
Forward End Cap EMC	FEC	$\geq 5°$
Barrel EMC	Barrel	$\geq 22°$
Backward End Cap EMC	BEC	$\geq 140°$

Table 1.4: Nomenclature and angular coverage of the EMC components.

This section explains the physics of such a kind of calorimeter, summarise the requirements and highlights different components of the EMC readout chain.
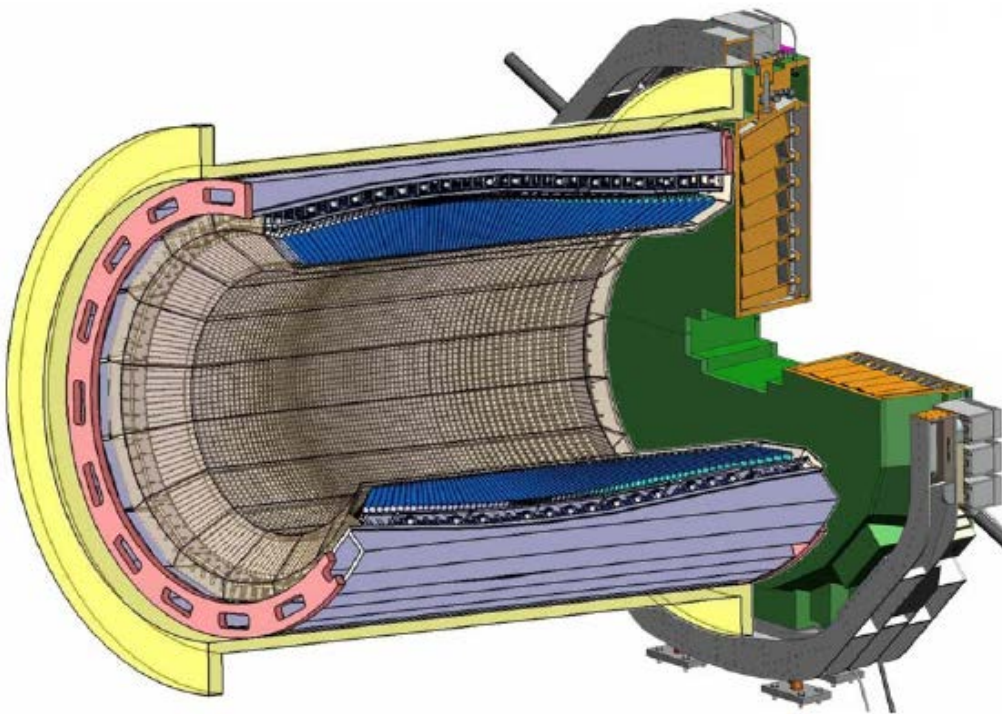
Figure 1.14: Layout of the PANDA EMC including Barrel and FEC [12].

1.3.1 Physics of the EMC

The active material of the PANDA EMC consists of an inorganic scintillator: Lead tungstate ($PbWO_4$). Basically, a scintillator converts deposited energy into visible scintillation light, which is subsequently readout by appropriate photo sensors. Ideally, the final energy information scales with the incident energy, but there can also be inhomogeneities depending on the kind of detected particle, energy region and used scintillator material. In the following the different interaction modes of electromagnetic radiation and charged particles with matter will be discussed.

1.3.1.1 Interaction of charged Particles with Matter

Several effects contribute to the overall energy loss of a charged particle propagating through a certain medium (listed in Eq. 1.2; [1, 13]). The relative fraction depends on type of particle, type of medium and energy of the impinging particle. Moreover, one has to distinguish between two groups of particles: heavy particles starting from muons, pions up to nuclei, and electrons and positrons.

$$\left(\frac{dE}{d(\varrho x)}\right) = \underbrace{\left(\frac{dE}{d(\varrho x)}\right)}_{\substack{\text{inelastic}\\\text{scattering}}} + \underbrace{\left(\frac{dE}{d(\varrho x)}\right)}_{\substack{\text{elastic}\\\text{scattering}}} + \underbrace{\left(\frac{dE}{d(\varrho x)}\right)}_{\substack{\text{Cherenkov}\\\text{radiation}}} + \underbrace{\left(\frac{dE}{d(\varrho x)}\right)}_{\substack{\text{nuclear}\\\text{reactions}}} + \underbrace{\left(\frac{dE}{d(\varrho x)}\right)}_{\substack{\text{brems-}\\\text{strahlung}}} \quad (1.2)$$

The heavier the particle, the more important is the energy loss due to **inelastic scattering**. In a collision of the impinging particle with a lattice atom, a certain fraction of the kinetic energy is transferred, causing an ionization or excitation of the system, called hard or soft collision, respectively. If a hard collision produces free electrons, which are able to ionise further atoms, these electrons are called δ-electrons. The energy loss per pathlength can be calculated by the Bethe-Bloch equation.

$$-\frac{dE}{dx} \sim \varrho \frac{Z}{A}\frac{z^2}{\beta^2}\left[\ln\left(\frac{2m_e\gamma^2 c^2 W_{\max}}{I}\beta^2\gamma^2\right) - 2\beta^2 - \delta - 2\frac{C}{Z}\right] \quad (1.3)$$

with

m_e: electron mass $\qquad\qquad\qquad\qquad$ ϱ: density of absorbing material
I: mean excitation potential $\qquad\qquad$ z: charge of incident particle in units of e
Z: atomic number of absorber $\qquad\quad$ $\beta = v/c$ of the incident particle
A: atomic weight of absorbing material $\quad$ $\gamma = 1/\sqrt{1 - \beta^2}$
δ: density correction $\qquad\qquad\qquad\quad$ C: shell correction
$W_{\max}$: maximum energy transfer in a single collision

The parameter I is correlated with the atomic number Z and is in the order of hundreds of eV. δ and C are, in principle, extensions to the original Bethe-Bloch equation and become more important for very low and relativistic energies. Further improvements of Eq. 1.3, like e.g. taking into account the substructure of the incoming particle or higher order effects, are negligible up to 1%. At lower energies the energy loss by ionisation is dominated by the β^{-2}-term. As a direct result, a charged particle looses more energy at the end of its path. This can be visualised by the so called Bragg-Peak. For momenta of $\beta\gamma = \frac{p}{Mc} \approx 3$, which corresponds to a velocity of $\sim 0.96c$, Eq. 1.3 reaches a minimum (compare Fig. 1.15).

In this region particles are called MIPs and lose the same amount of energy per path length, namely $\sim 2 \frac{\text{MeV}}{\text{g/cm}^2}$, if they have a charge of $\pm e$. At very high energies the ionising probability rises again due to the flattening of the electric field of the incoming particle. The characteristic energy loss dE/dx as a function of energy is usually exploited for PID. One assumption in the derivation of Eq. 1.3 is that the incoming particle remains undeflected while ionising and penetrating through matter. This does not hold for electrons and positrons and certain modifications of Eq. 1.3 have to be considered for the applicability to this kind of particle.

The contribution of **elastic scattering** off the nuclei gets significant at very low velocities of $\beta < 10^{-3}$ and plays a major role for the detection of neutrons.

The Cherenkov effect itself was already discussed in Sec. 1.2.1 and causes an energy loss via emission of light. For PWO, a small fraction of the final detected energy information originates from **Cherenkov radiation**. Eq. 1.5 leads with a typical spectral sensitivity of a PMT from $350\,\text{nm}$ to $550\,\text{nm}$, an incoming particle with $z = 1$ and $\beta \approx 1$, and an averaged index of refraction of PWO to 385 photons per cm. This corresponds to $\sim 21\%$ of the overall light output at $+18\,\text{C}$ for a MIP in $1\,\text{cm}$ PWO.

$$\frac{d^2N}{d\lambda dx} = \frac{2\pi z^2}{137\lambda^2} \left(1 - \frac{1}{\beta^2 n^2(\lambda)} \right) \tag{1.4}$$

$$\frac{dN}{dx} = 2\pi z^2 \alpha \sin^2(\Theta_C) \int_{350\,\text{nm}}^{550\,\text{nm}} \frac{d\lambda}{\lambda^2} = 475 z^2 \sin^2(\Theta_C) \text{photons/cm} \tag{1.5}$$

A **nuclear reaction** occurs if a particle is able to overcome the Coulomb barrier and subsequently strikes a target nucleus. In general, the cross section for a nuclear interaction is small compared to electromagnetic processes. Therefore the free mean path of the nuclear reaction Λ_{NR} is larger than the radiation length X_0, introduced in Eq. 1.8.

Energy loss via **bremsstrahlung** plays a major role in the development of an electromagnetic shower. In a typical energy range up to $100\,\text{GeV}$ for high-energy experiments, this effect basically only becomes relevant for electrons and positrons, since the cross section of bremsstrahlung scales with m^{-2}. Bremsstrahlung occurs mainly in the Coulomb field of the nucleus and therefore, strongly depends on the screening caused by atomic electrons. Eq. 1.6 describes the energy loss of a particle with initial energy E_0 and mass m, number of atoms per cm^3 N and the atomic number of the
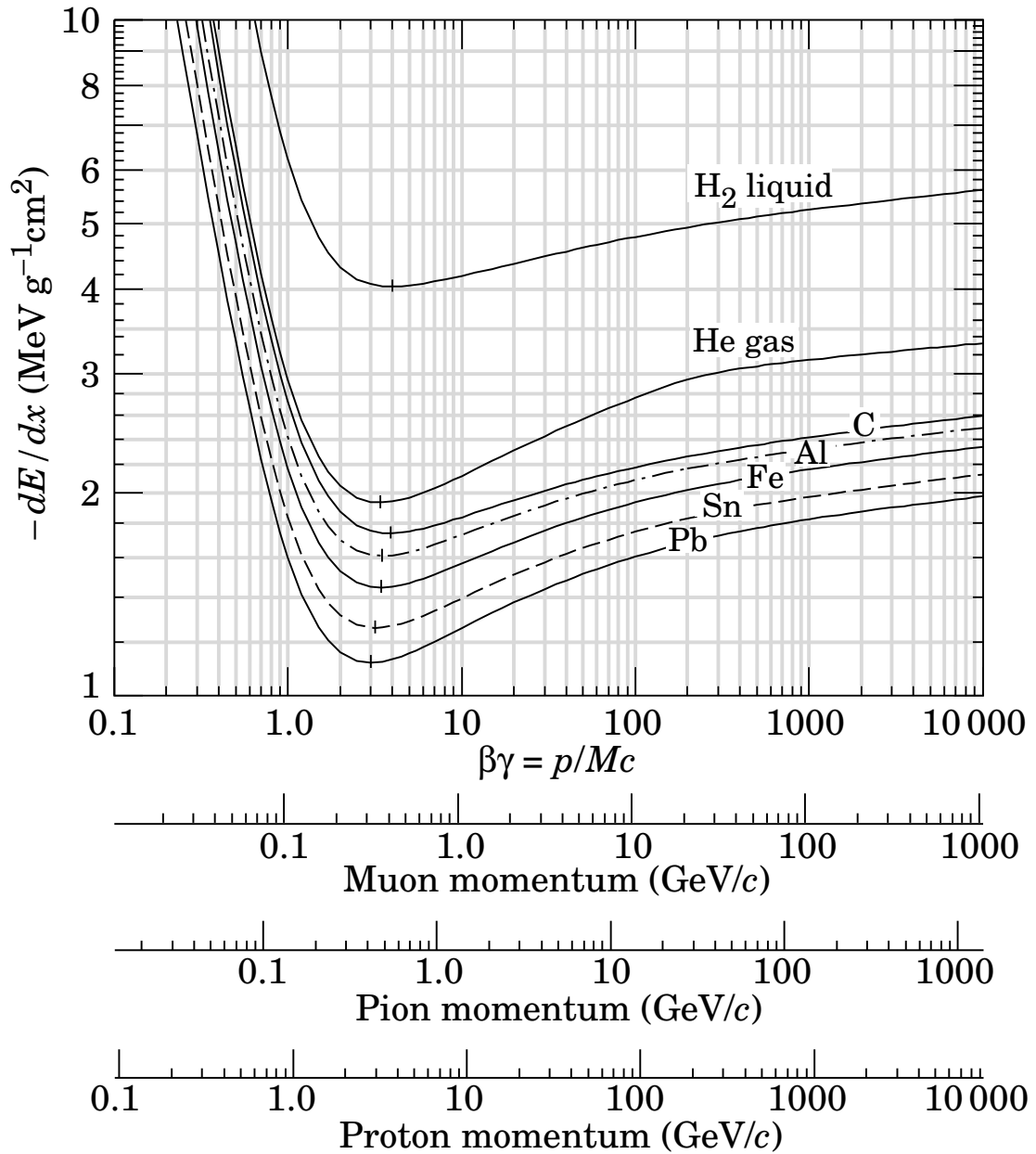
Figure 1.15: Visualisation of the Bethe Bloch equation for different particles and various materials. The differences between the curves originate from the ratios of Z/A for the plotted material.

material Z.

$$\frac{dE}{dx} = \frac{4NE_0Z^2r_e^2}{137} \begin{cases} \ln\left(\frac{2E_0}{m_ec^2}\right) - \frac{1}{3} - f(Z), & \text{for } m_ec^2 \ll E_0 \ll 137m_ec^2Z^{-1/3} \\ \ln\left(183Z^{-1/3}\right) + \frac{1}{18} - f(Z), & \text{for } E_0 \gg 137m_ec^2Z^{-1/3} \end{cases} \quad (1.6)$$

$f(Z)$ represents a Coulomb correction for the emitting electron in the field of the nucleus. The distinction of both cases in Eq. 1.6 is due to screening of the atomic electrons. The initial particle with a higher energy E_0 (lower case) "sees" a more effective field configuration of the whole atom, whereas for smaller energies (upper case) the sensitivity to the electric field of the nucleus is more pronounced. In addition, bremsstrahlung also occurs in the field of the atomic electrons, but here one has to replace Z^2 with $Z(Z+1)$ in Eq. 1.6.

1.3.1.2 Interaction of Photons with Matter

A photon has several possibilities for the interaction with matter: Photoeffect, Rayleigh-Scattering, Compton-Scattering, and pair production in the electric field of the nucleus or of the electrons. Fig. 1.16 shows the energy dependence for the mentioned effects for lead tungstate. In the energy range of PANDA only Photoeffect, Compton-Scattering and pair production in the field of the nucleus are important. These effects also show a significant dependence on the atomic number Z (compare Tab. 1.5).

Photon Interaction	Dependence
Photo Effect	$\sim Z^{4-5}E^{-3.5}$
Compton Effect	$\sim ZE^{-1}$
Pair Production	$\sim Z^2\ln E$

Table 1.5: Dependence on the photon Energy E and the atomic number Z for different interactions of photons with matter. At higher energies screening of the nucleus field results in a suppression of the pair production cross-section which goes with $\sim Z^2\ln Z$ [15].

1.3.1.3 Electromagnetic Shower

The listed effects lead to a development of an electromagnetic shower (Fig. 1.17). Such a shower can be subdivided into generations in which each generation produces a factor of around 2 more particles, whereupon the initial energy is fragmented and
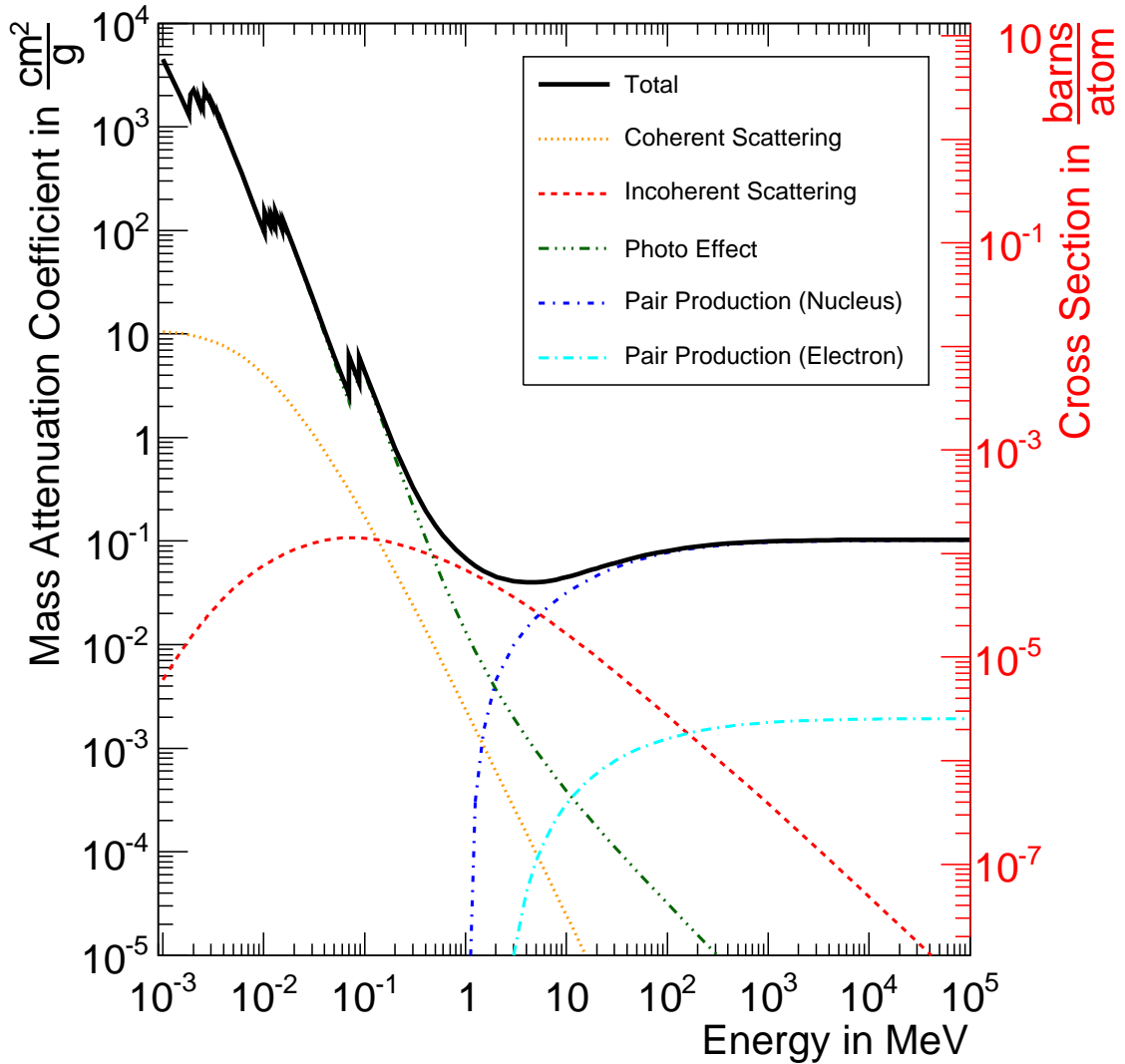
Figure 1.16: Mass attenuation coefficient and cross-section in terms of cm^2/g and barns/atom, respectively, for the different interaction options with $PbWO_4$ (data obtained by [14]). Coherent scattering and pair production in the electron shell play only a minor role in the energy regime of PANDA. At lower energies the photo effect is dominant, but decreases with energy according to the dependencies in Tab. 1.5. At higher energies the pair production in the electric field of nucleus is the main contribution to the total interaction cross section.

follows statistical fluctuations. An average energy of the produced particles in each generation can thereby be calculated by:

$$< E > = \frac{E_0}{2^n} \text{ with } E_0: \text{ Initial energy; } n: \text{ Shower generation} \tag{1.7}$$

An important parameter for the scale length of such kind of shower is the radiation length X_0. This parameter has two meanings and can be calculated with Eq. 1.8

- X_0 is the mean distance over which a high energetic electron losses up to $1/e$ of its energy via bremsstrahlung

- $\frac{7}{9} X_0$ is the free path for pair production by a high-energy photon

A useful approximation of the radiation length X_0 for a given material can be calculated by Eq. 1.8 [13].

$$X_0 = \frac{716.4 \frac{\text{g}}{\text{cm}^2} \cdot A}{Z(Z+1) \ln\left(287/\sqrt{Z}\right)} \tag{1.8}$$

with
A: atomic weight of absorber $\quad$ Z: atomic number of absorber

The continuation of the electromagnetic shower process stops if the cross section of the electron/positron for ionisation processes overcomes the one for bremsstrahlung characterised by the critical energy E_C. In first order this threshold energy can be parametrised in solids and liquids as follows [16]:

$$E_C = \frac{610\,\text{MeV}}{Z_\text{eff} + 1.24} \tag{1.9}$$

For $PbWO_4$ with $Z_\text{eff} = 75.6$ the critical energy is of approximately $7.94\,\text{MeV}$.

The geometrical expansion of an electromagnetic shower can be characterised by two parameters: $y = \frac{E}{E_C}$ and $t = \frac{x}{X_0}$. Tab. 1.6 summarises the longitudinal expansion for an electron and a photon.

	Incident electron	Incident photon
Peak of shower, t_max/X_0	$1.0 \cdot (\ln y - 1)$	$1.0 \cdot (\ln y - 0.5)$
Centre of gravity, t_med/X_0	$t_\text{max} + 1.4$	$t_\text{max} + 1.7$

Table 1.6: Parameters for a longitudinal development of an electromagnetic shower.

The transverse dimensions caused primarily by multiple scattering of the electrons
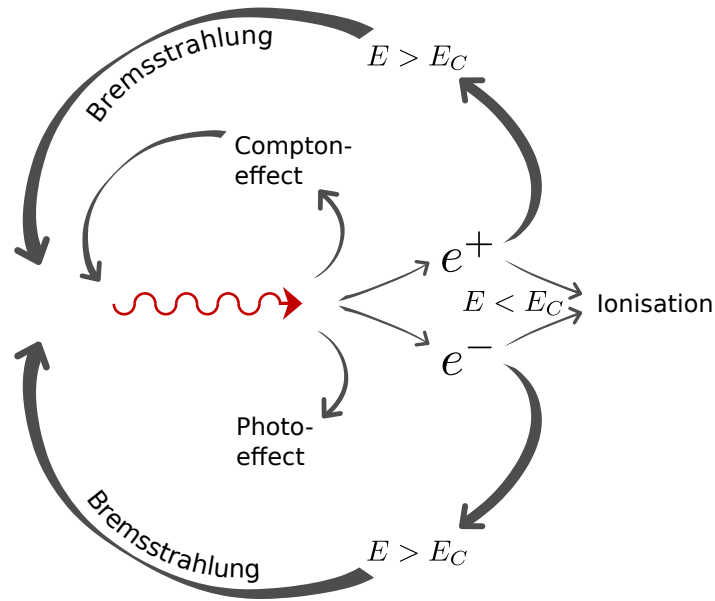
(a) Schematic development of an electromagnetic shower. A photon deposits energy via the effects mentioned in Sec. 1.3.1.2. The photon disappears in case of photoeffect and pair production, whereas in the latter an electron and positron pair is produced. If the energy of the produced leptons is above the critical energy E_C, there is a high probability for emission of bremsstrahlung and the drawn cycle starts from the beginning with smaller initial energy.
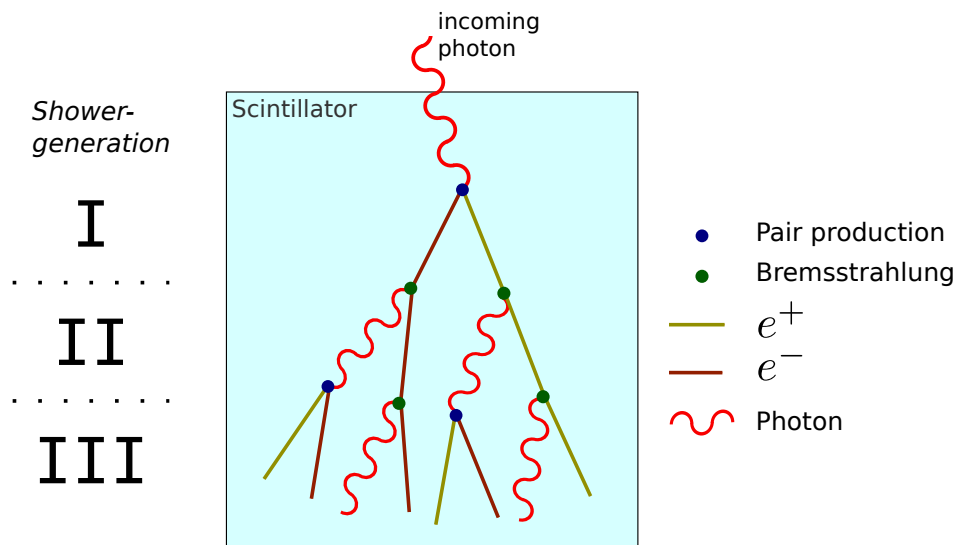
(b) The figure shows a simplified electromagnetic shower for the first three shower generations. A shower stops if the mean energy of a generation is below the threshold of E_C.

Figure 1.17: Involved effects and schematic process of an electromagnetic shower.

are given by the Molière radius R_M, which is defined as the radius of a cylinder containing 90% of the energy deposition. R_M scales proportional to X_0 is essential for the geometrical design of calorimeter modules. Fig. 1.18 a) and b) show the typical expansion of an electromagnetic shower in a Caesium iodide crystal (CsI) caused by photons.

(a) Transversal shower profile. (b) Longitudinal shower profile.
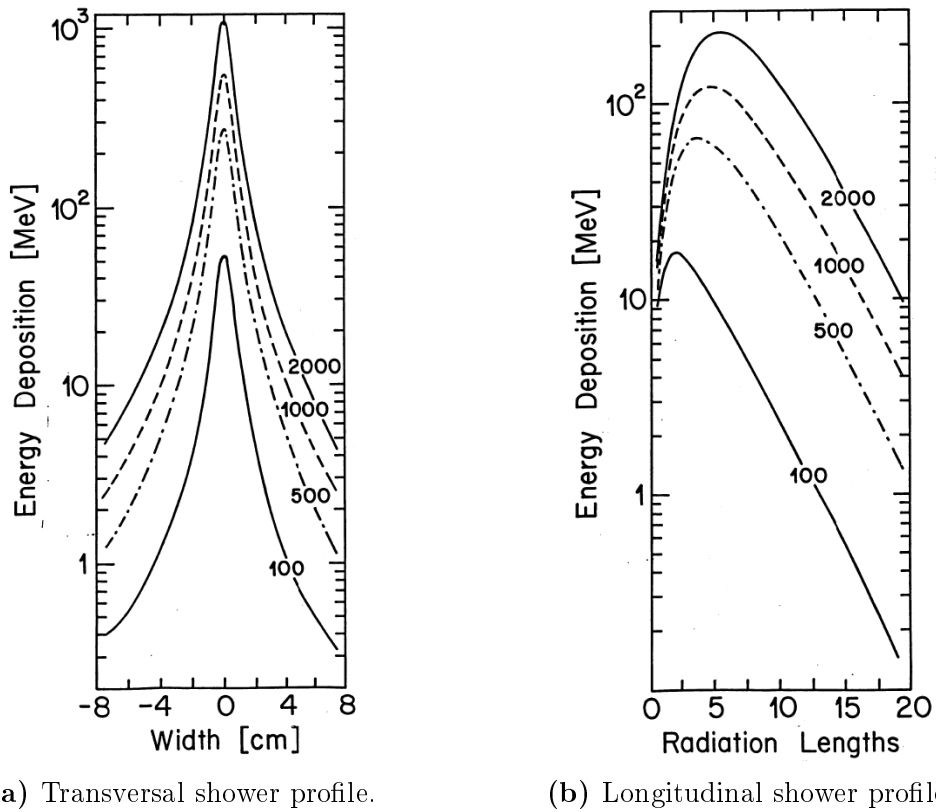
Figure 1.18: Expansion of an electromagnetic shower in CsI caused by photons with various energies [17].

1.3.2 Requirements

The layout of the EMC is driven by the requirements of the physics program and the available budget. In the case of PANDA, the EMC is divided in three parts which are labelled in the following according to Tab. 1.4. The main task of an EMC is the efficient detection of electromagnetic probes, like photons, electrons and positrons. The coverage of the solid angle and the chosen energy threshold should be appropriate to reject background, mostly originating from π^0 and η rich states. The acceptance for $e^\pm$ and γ can be approximated by $(\Omega/4\pi)^n$, in which Ω is the covered solid angle and n is the number of electromagnetic particles in the final state.

The relevant observables for the EMC are energy, point of impact (position) and time. An accurate measurement of the latter one is mandatory and serves as a time stamp for the triggerless PANDA readout and to discriminate background not related to the detected event. Sec. 4 will describe the achievable time resolution of the whole detection chain, ranging from the generation of scintillation light up to the final digitisation, which has to cope with the final annihilation rate of 10^7 Hz. Another crucial requirement of the EMC regarding the financial point of view is the compactness. The price for the scintillators and the surrounding magnet scales with the cube of their dimensions. Finally, Tab. 1.7 summarises the most important requirements based on a luminosity of $2 \cdot 10^{32}\,\mathrm{cm}^{-1}\mathrm{s}^{-1}$ [18].

General property	Required performance value		
energy resolution	$\leq 1\% \oplus \frac{\leq 2\%}{\sqrt{E/\mathrm{GeV}}}$		
energy threshold (cluster)	10 MeV		
energy threshold (single crystal)	3 MeV		
energy equivalent of noise	1 MeV		
angular coverage	99% of 4π		
subdetector specifications	BEC ≥ 140	Barrel ≥ 22	FEC ≥ 5
energy range with respect to energy threshold	0.7 GeV	7.3 GeV	14.6 GeV
spatial resolution	0.5	0.3	0.1
maximum rate capability	100 kHz		500 kHz
shaping time	400 ns		100 ns
dose per year	10 Gy		125 Gy

Table 1.7: Requirements of the EMC.

1.3.3 Scintillator Material

Lead tungstate, $PbWO_4$ (PWO) was chosen as scintillator material for the PANDA EMC after becoming the dominant material in high-energy application. PWO has a negative birefringent nature and due to its high Z-materials the radiation length X_0 is in the order of $0.89\,cm$, which is short compared to other potential candidates such as BGO with $1.12\,cm$. This is mandatory for a compact design of the calorimeter. Fig. 1.19 shows the tetragonal symmetric crystal structure of PWO. The optimisation and large scale production was initiated by the stringent requirement, on fast response, compactness and radiation hardness to design the electromagnetic calorimeter of the CMS detector at the LHC[25].
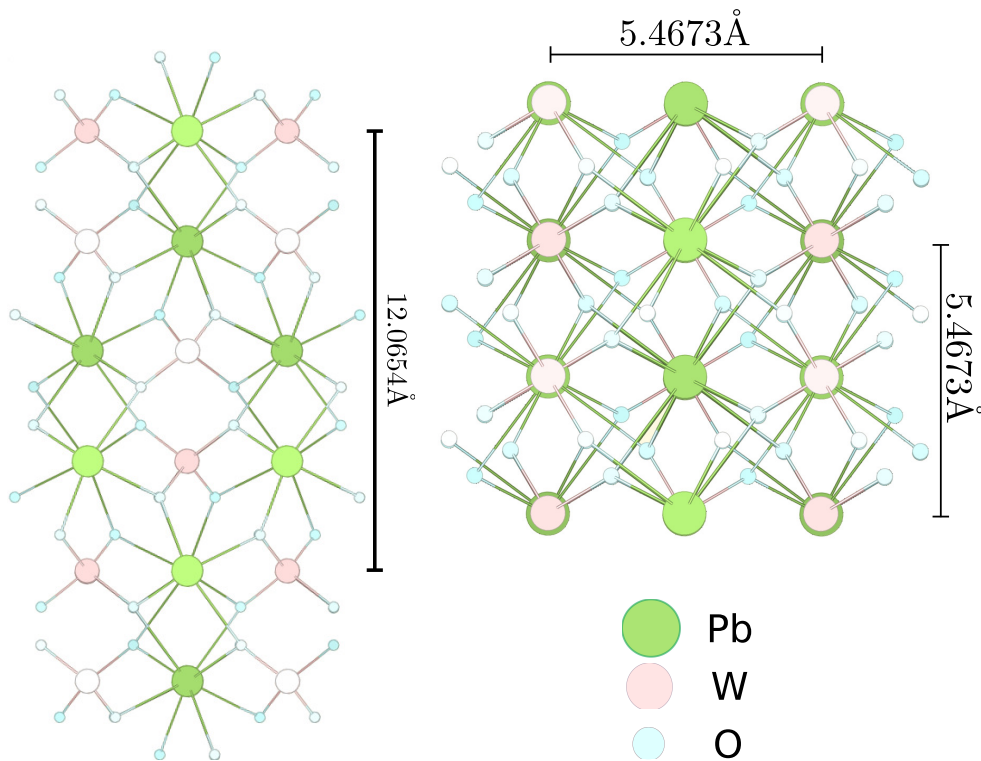
(a) Crystal Structure of PWO along the long crystal axis. (b) Cross section of PWO crystal structure perpendicular to the long crystal axis.

Figure 1.19: The pictures show the microscopic crystal structure of PWO for two orientations. The hue of the atoms gives an impression of the spatial depth. The three optical axes are perpendicular to each other, whereas two axes are identical due to the birefringent nature. The dimensions for the unit cell are given and result in a volume of approximately $360,92\,Å^3$ [19].

---

[25]Large Hadron Collider

The short decay time of 6.5 ns due to thermal quenching, which makes this material capable for high count rates, since more than 80 % of the scintillation light can be collected within 20 ns at room temperature. In addition, Lead tungstate shows only a negligible slow component with $\sim \mu$s on a few percent level. Concerning the temperature dependence of the scintillation kinetics, only a small change becomes visible within the first 50 ns (compare Fig. 1.20) when the crystal is slightly cooled down.
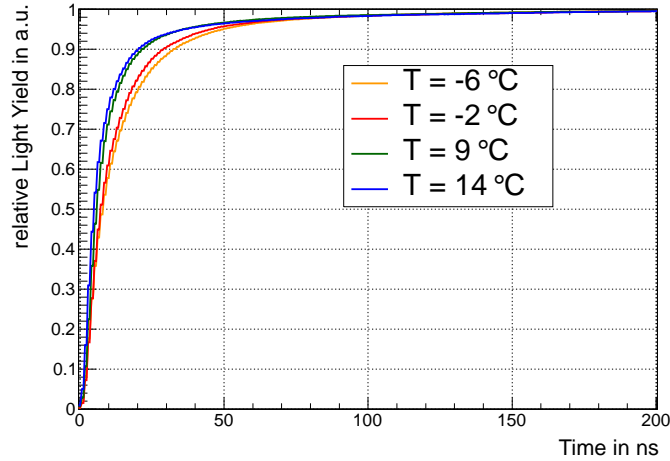
Figure 1.20: Scintillation kinetics of PWO as a function of integration time for different temperatures [20].

On the other hand, the main disadvantage of PWO is the relatively low LY compared to other standard scintillator materials, which did not play a role for LHC applicant. In order to test and prepare the application in a much lower photon energy regime, a R&D[26] program hat been started to improve the scintillation efficiency by doping, reducing defect concentration or change operation temperature. Section 2.1 is intended to describe the most important changes to this new generation of quality, called PWO-II, necessary for the PANDA EMC. In addition, the calorimeter will be operating at -25 C to achieve a further enhancement of the LY (factor ~ 4 compared to 25 C). Table 1.8 summarises the general properties of PWO in comparison to BGO and LYSO. Sec. 2 shows in detail the procedure of quality control and the up to now achieved quality of the crystals for the EMC.

---

[26]Research and Developement

Parameter	Unit	LYSO	BGO	PWO	PWO-II
ρ	g/cm^3	7.4	7.13	8.28	
X_0	cm	1.14	1.12	0.89	
R_M	cm	2.30	2.30	2.00	
τ_{decay}	ns	40	300	6.5	
λ_{max}	nm	420	480	420	
n at λ_{max}		1.82	2.15	2.24/2.17	
relative LY to NaI	%	75	9	0.3† 0.8*	0.6† 2.5*
dLY/dT	%/C	0	−1.6	−2.7†	−3.0†
dE/dx (MIP)	MeV/cm	9.6	9.0	10.2	

Table 1.8: Properties of PWO in comparison to BGO and LYSO [18]. Especially the small decay constant of PWO and the light yield enhancement between the two quality versions are conspicuous [18]. (†: at room temperature; *: at −25 C)

1.3.4 Photo Detectors

For the PANDA EMC it is not possible to read out the crystals with conventional PMTs due to the strong magnetic field of $\sim 2\,$T. Therefore the used sensors should be insensitive to a magnetic field. Due to the relatively low LY[27] of PWO (compare Tab. 1.8) the photo sensor should also have an internal gain for the amplification of the primary signal. Furthermore, the sensors have to be radiation hard down to the operation temperature of −25 C. In the following the envisaged types of photo sensors are discussed in more detail: LAAPD[28], VPT[29] and VPTT[30].

1.3.4.1 LAAPD

APDs[31] with a large effective area are intended to readout the barrel part of the EMC mainly due to the insensitivity to the magnetic field. In a common effort of the CMS collaboration and *Hamamatsu Photonics*, a special kind of APD was optimised for the detection of scintillation light of PWO. In addition, these sensors have some other advantages:

- thickness of 200 μm

---

[27]<u>L</u>ight <u>Y</u>ield
[28]<u>L</u>arge <u>A</u>rea <u>A</u>valanche <u>P</u>hoto <u>D</u>iode
[29]<u>V</u>accum <u>P</u>hoto <u>T</u>riode
[30]<u>V</u>accum <u>P</u>hoto <u>T</u>etrode
[31]<u>A</u>valanche <u>P</u>hoto <u>D</u>iodes

- thin conversion layer

- high QE[32] in the wavelength range of PWO ($\sim 80\%$)

- insensitive to magnetic field

- low cost for mass production

Fig. 1.21 shows the general structure of an APD which is operating in reversed voltage.
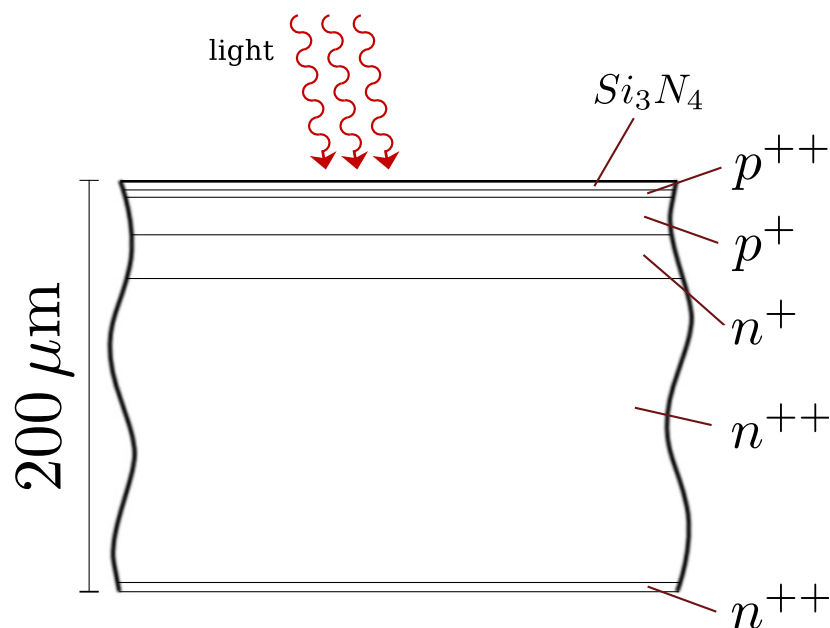
Figure 1.21: The APD structure consists of various layers of doped silicon. p and n corresponds to the kind and the number of + to the level of doping. The chosen doping profile leads to a strong electric field close to the junction. This results into an avalanche of the primarily produced charge carriers and finally to an internal amplification. After drifting, the final charge collection takes place in the n^{++} electrode. The additional layer of silicon nitride (Si_3N_4) on the entrance face reduces loss of the light due to reflections.

The gain of an APD strongly depends on applied voltage and temperature. Therefore, to ensure the performance of the photo sensors, temperature and applied bias voltage have to be kept stable within an accuracy of $\Delta T = \pm 0.1\,$C and $\Delta U = \pm 0.1\,$V. Therefore the characteristics of an individual APD has to be known. For determining the gain M, dark current I_d and photo current I_{ill} are recorded while illuminating

---

[32]Q̲uantum E̲fficiency

the sensitive area of a fixed wavelength ($T_{\mathrm{max/PbWO4}} = 420\,\mathrm{nm}$). The obtained signal amplification is derived from the relation to the $M = 1$ equivalent, according to Eq. 1.10. Fig. 1.22 shows the dependencies of gain, dark current and applied voltage of a randomly chosen APD for different temperatures.

$$M = \frac{I_{ill}(U) - I_d(U)}{I_{ill}(M = 1) - I_d(M = 1)} \tag{1.10}$$
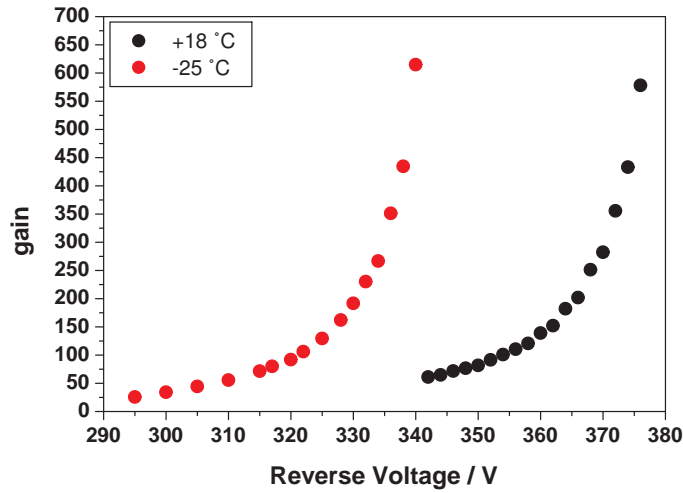
Figure 1.22: Correlation of gain and applied voltage of an APD for two different temperatures. The shape corresponds to the characteristic curve of a diode.

The obtained gain M is a result of the avalanche process within the APD. Such a statistical process also brings up uncertainties caused by fluctuations which enter in the final performance. This can be expressed by the Excess Noise Factor F and is basically connected to the broadening of produced photoelectrons N_{pe} and contributes to the energy resolution by:

$$\frac{\sigma_E}{E} = \frac{1}{\sqrt{E}} \cdot \sqrt{\frac{F}{N_{\mathrm{pe}}}} \tag{1.11}$$

With respect to the PANDA EMC, a further R&D step was necessary. The relatively low envisaged energy threshold of $10\,\mathrm{MeV}$ requires to collect as much scintillation light as possible. This can be achieved by increasing the area of the APD, which leads to another generation called LAAPD. The effective area was enhanced from $0.25\,\mathrm{cm}^2$ to $1\,\mathrm{cm}^2$. The rectangular shape allows to equip two APDs on one crystal and therefore

to improve the energy resolution by another factor of $\sqrt{2}$. Two sensors per crystal bring another advantage, namely the rejection of fake events caused by neutrons, for the first time realized by the CMS experiment. There is a non-zero probability that a neutron crossing the volume of an APD creates a physically unusual high energy signal due to spallation. Those events can be identified by comparing the signal of both sensors for one event. Another effects, which leads to a worsening of the energy resolution, occurs if a charged particle reaches the silicon layers of the APD and produces electron hole pairs (~ 100 e/h pairs per μm) in addition to the signal caused by the PWO scintillation light (NCE[33]). This effect is more crucial for PANDA, since the relative signal contribution is higher due the lower energy regime, compared to CMS. Therefore it is advantageous to have a thin conversion layer.

1.3.4.2 VPT/VPTT

The functionality of a VPT or a VPTT is very similar to the principle of a conventional PMT except the number of dynodes. A schematic layout of both kind of sensors is displayed in Fig. 1.23. The photo cathode serves as a converter from photons to electrons which will then be accelerated to the mesh anode and afterwards to the dynode where the amplification takes place. The produced secondary electrons will subsequently be accelerated backwards and collected by the anode. In case of a VPTT, an additional mesh dynode is placed between cathode and anode. On the one hand this results in an additional gain, but on the other hand the tube gets more sensitive to the magnetic field. Both types of sensors have a typical quantum efficiency of bialkali photo cathodes in the order of $\sim 20\,\%$.
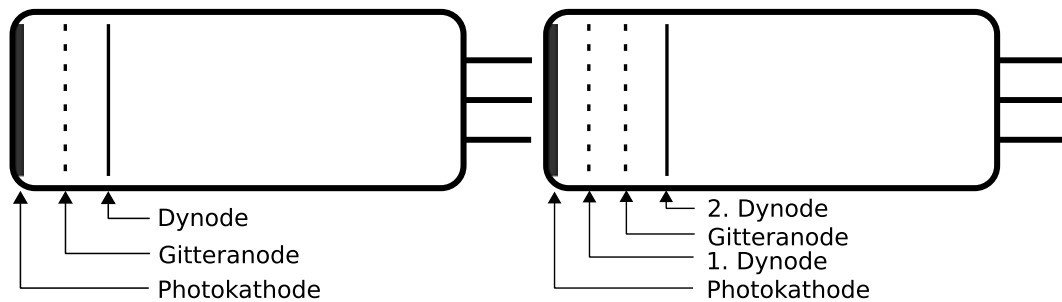
(a) High voltage setting for the VPT: Cathode at $-1000\,$V, anode on ground and dynode at $-200\,$V.

(b) High voltage setting for the VPTT: Cathode on ground, first dynode on $500\,$V, anode at $1200\,$V, second dynode at $1000\,$V.

Figure 1.23: Schematic layout and high voltage settings for VPT and VPTT [21].

---

[33]<u>N</u>uclear <u>C</u>ounter <u>E</u>ffect

This kind of photo detector will read out the crystals of the FEC, since they are more capable for higher rates (up to 500 kHz in the FEC) and show a better radiation hardness. In the outermost region of the FEC, the angle between sensor axis and magnetic field is ~ 18, which reduces the gain due to the Lorentz force on the electrons. Current studies [22] show a degradation of a VPTT gain up to 45 % for a magnetic field of 1.2 T.

1.3.5 Electronics

Several requirements are dictated to the readout electronics to achieve the designated performance of the PANDA EMC. A dynamic range of 12,000 is necessary to cover the energy range from the low energy threshold of 1 MeV and the maximum expected energy deposition in a single crystal of 12 GeV. Furthermore, the limited available space should be occupied as efficiently as possible. Therefore, the geometry of the preamplifiers should fit into the EMC cooling compartment to be as close as possible to the crystal sensors (compare Fig. 1.24). This will have a positive impact on the analogue circuits and decrease the probability of pick-up noise. A low power consumption of the electronics is mandatory as well, to guarantee the homogeneity of cooling along the 20 cm long crystals. Two different concepts were developed and will
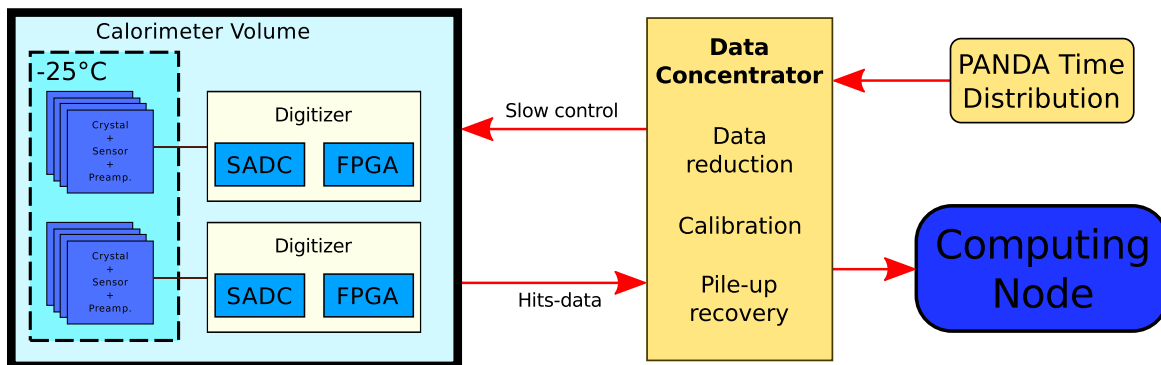
Figure 1.24: Schematic readout chain of the PANDA EMC [23]. The amplified signals are forwarded to digitiser modules which consist of SADC-chips and digital logics for the evaluation of the necessary informations (explained in Sec. 3.1.4). The digitiser modules are at a distance of $20 - 30$ cm and $90 - 100$ cm for the barrel and FEC, respectively, away from the cold EMC volume. Via an optical link (drawn in red) the data stream reaches the stage of the data concentrator, where diverse algorithms are applied to the data. A general time distribution of the PANDA detectors provides a clock. Finally, the obtained values are collected by the computing node.

be presented in the following subsections. On the one hand an ASIC[34] for the signal processing in the barrel part and on the other hand a Low Noise/Low Power Charge Preamplifier (LNP-P) in the FEC.

1.3.5.1 ASIC

Each crystal of the barrel EMC is equipped with two LAAPD which are read out simultaneously by one ASIC, called APFEL[35]. This chip will split up the input of a single LAAPD and provide two channels with different gains. In the current version (1.4.) the ratio between these two gain branches is programmable between 16 and 32. Further prototype tests will show which factor gives the best compromise. Due to the increased capacity of the LAAPDs and therefore higher contribution to the dark current, the preamplifier should have, among the already mentioned requirements, a low noise level. The maximum input charge is in the order of $8\,pC$ and results with an ENC[36] of $0.74\,fC$ ($4625\ e^-$) to a dynamic range of more then $10,000$. Concerning rate capability, this ASIC is able to handle event rates up to $500\,kHz$ (barrel max. rate $100\,kHz$), which is a design trade-off between noise issues and pile-up. The power consumption per APFEL is approximately $55\,mW$. All the provided data of the APFEL 1.4. was determined at room temperature [24]. Fig. 1.25 shows a block diagram and a photograph of the APFEL.

1.3.5.2 Low Noise and Low Power Charge Preamplifier

A LNP-P[37] has been developed for the adaptation of the VPTs for the FEC based on J-FET[38] technology. In a former stage of the development this preamplifier is implemented in a barrel EMC prototype detector (compare Sec. 3.1). The input charge of the preamplifier is linearly converted to a positive output voltage. The overall power consumption of the preamplifier depends on the event rate and registered photon energy and ranges for PANDA from $45\,mW$ to $90\,mW$. Concerning noise issues, the anode capacitance of a VPT is one order of magnitude less compared to a LAAPD which results in a significantly lower dark current ($\sim 1\,nA$). The maximum positive output voltage of $2\,V$ is caused by the charge sensitivity of $0.5\,V/pC$ and the maximum single pulse input charge of $4\,pC$ at $50\,\Omega$. Fig. 1.26 shows a photograph of the top and bottom side of single-channel LNP-P prototype.

---

[34]Application Specific Integrated Circuit
[35]ASIC for PANDA Front-end Electronics
[36]Equivalent Noise Charge
[37]Low Noise and Low Power Charge Preamplifier
[38]Junction Field Effect Transistor
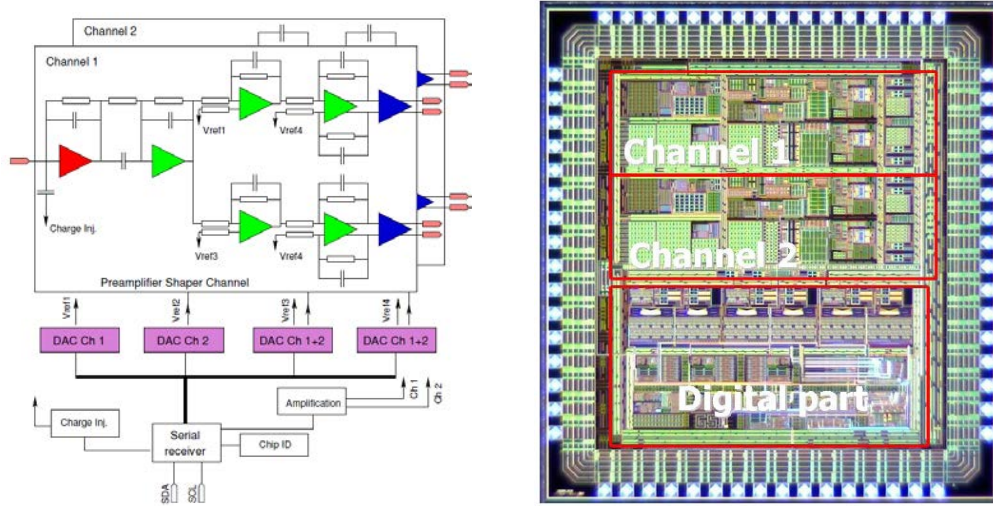
(a) Schematic layout of the APFEL ASIC.

(b) Photograph of the APFEL ASIC.

Figure 1.25: The pictures give an impression of the layout of the APFEL ASIC for the readout of two LAAPD and the two different gains [24].
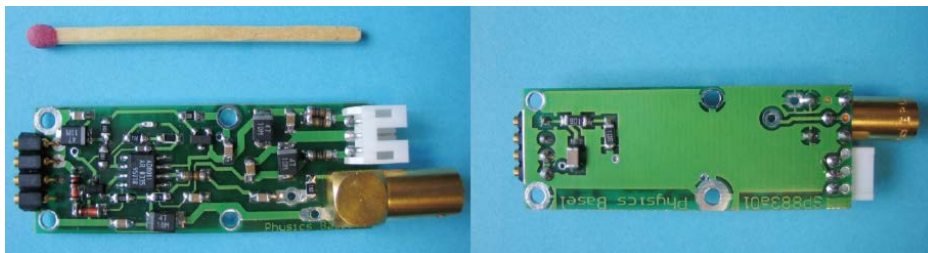
Figure 1.26: Photograph from both sides of a LNP-P [18].

Chapter 2

Quality Control of PbWO$_4$ Crystals for PANDA

For securing the defined quality requirements of the crystals for PANDA, an appropriate test procedure has to be defined. The relevant properties of each individual crystal are measured and tested by three independent facilities: BTCP, CERN and the university of Gießen. Therefore, different ways of measuring, which can give rise to inconsistencies, should be taken into account. Up to now, all crystals were produced by BTCP, where also the first stage of quality control takes place. At BTCP, the crystals were grown using the so called Czochralski method (Fig. 2.1a). A small seed crystal is pulled out of melted raw material with a purity level close to 6N[1]. The purification was achieved by several steps before such as the appropriate mixture of raw material to reach the final stochiometric ratio considering losses due to evaporation. In addition a pre-crystallisation was used to separate impurities with a different segregation coefficient. This procedure results in 25 cm long ingots with elliptical cross-section shown in Fig. 2.1b, which will be subsequently cut into the PANDA geometries adjusting the final surfaces parallel to the main crystal axis. This chapter has the intention to explain the relevant parameters and the procedure of the performed quality control. Finally, the obtained results will be summarised and discussed, also with regard to the status of the remaining crystals.

2.1 Improvement of Lead Tungstate Crystals

Lead tungstate was mainly chosen by the PANDA collaboration due to its high rate capability and radiation hardness. But the relatively low light yield (compare Tab. 1.8) required further steps, especially for the efficient detection of low energetic probes down to 10 MeV. At first, the overall light yield of PWO was enhanced by a collaborative R&D development by the PANDA collaboration and BTCP [25] funded by

---

[1] purity level of $\geq 99.9999\%$

(a) Czochralski method.

(b) Uncutted PbWO$_4$ ingots.
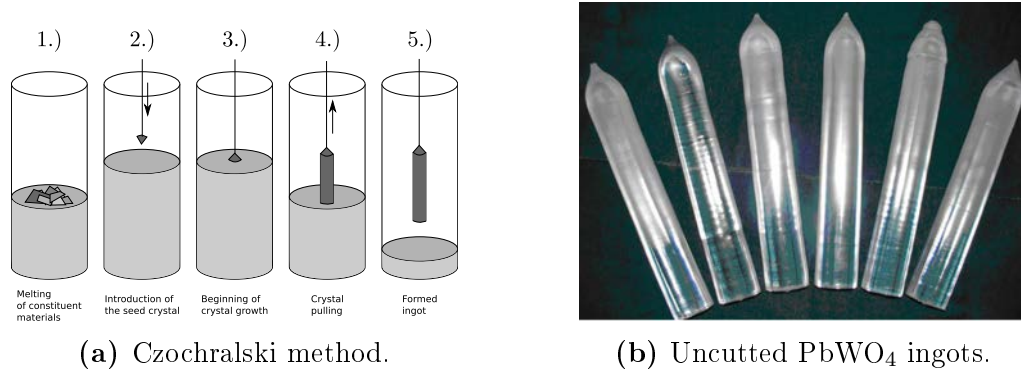
Figure 2.1: Manufacturing of PWO crystals.

the EU[2] project "Hadron Physics". In a first iteration of research, different doping compositions consisting of molybdenum (Mo) and another series of pure terbium (Tb) were tested. The performed measurements for low energetic photons from a ^{137}Cs source showed a significant improvement of the light output (Fig. 2.2a). A certain doping combination of Mo (500 ppm) and lanthanum (La) (100 ppm) even resulted in a light yield a few times higher as compared to CMS[3] type crystals. But there are a couple of drawbacks, since a higher level of Mo-doping causes an increase of the decay time which limits the application at higher rates (compare Fig. 2.2b). In addition, the crystal structure is less radiation hard and the maximum of the scintillation light is shifted towards the green region (~ 500 nm) [26]. The situation is rather similar for Tb doped crystal. Here the light yield increases by lowering the Tb-concentration, but unfortunately the radiation hardness is degrading as well.

An additional enhancement of the light yield of $30\% - 50\%$ can be achieved by a reduction of the La- and Y-concentration down to a level of ~ 40 ppm, which leads to a degradation of deep traps in the crystal structure. This is possible due to an improved control of the stoichiometric composition of the melt. La and Y have different distribution coefficients, which lead to different concentration gradients within the crystal while pulling out of the melt. To avoid this imbalance, the doping elements can be introduced in different stages during the crystal growing process. The mentioned innovations result in a significant lower number of vacancies in the crystal structure. Altogether, this new type of PWO, called PWO-II, shows an increased light yield in the order of 80% compared to CMS-type quality. Concerning timing issues, this next generation of PWO shows a clear dominance of the fast decay component of 97% and a decay time in the single-digit ns-region, measured at room temperature.

On top of the already increased light yield, the whole calorimeter is cooled down to a temperature of $-25\,°$C, which results in an additional enhancement of the light yield by a factor ~ 4 compared to room temperature due to the thermal quenching effect.

---

[2]<u>E</u>uropean <u>U</u>nion
[3]<u>C</u>ompact <u>M</u>uon <u>S</u>olenoid
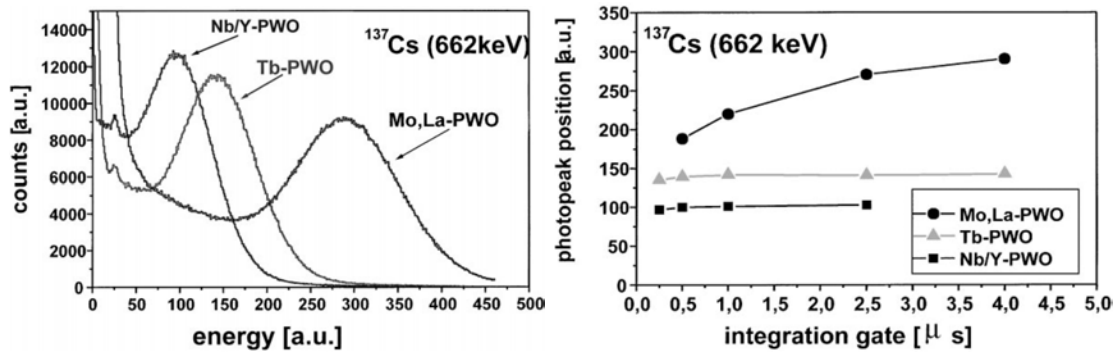
(a) Energy response of 662 keV photons for PWO for various kinds of doping. The measurements were performed with a conventional PMT with an integration time 2.5 μs.

(b) Photopeak position as a function of integration gate. The Mo, La co-doped crystal shows significant slower decay components.

Figure 2.2: Performance measurements of PWO with various kinds of doping with a ^{137}Cs source [25]. The co-doped sample with niobium (Nb) and yttrium (Y) corresponds to a sample of CMS quality.

In this region, the temperature gradient is almost constant and is shown in Fig. 2.3. A non-negligible drawback of the cooling is the reduced spontaneous recovery of radiation damage.
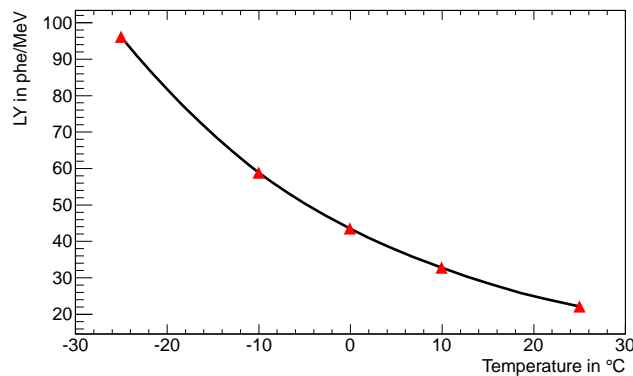
Figure 2.3: General temperature dependence of the light yield for lead tungstate. In the shown range, the temperature gradient varies from -3% to -2.5% per °C (values obtained by [20]).

2.2 Crystal Requirements

To guarantee the final performance and the long term stability of the EMC, the PWO crystals have to have sufficient quality. Based on the physical goals and also for the mechanical integration, the crystals should reach minimum requirements. This can be characterised by different properties, which will be described in the following subsections in more detail. The limit for each parameter was chosen with respect to previous experiences and detailed studies. Another aspect are the Gaussian-like distributed parameters due to the manufacturing of large quantities. Therefore a certain fraction of crystals can belong to a tail with insufficient quality, but on the other hand those statistical variations can also bring up crystals with excellent quality. All fixed requirements concerning quality control are summarised in Tab. 2.1.

Property	Unit	Limit
longitudinal transmission at 360 nm	%	≥ 35
longitudinal transmission at 420 nm	%	≥ 60
longitudinal transmission at 620 nm	%	≥ 70
non-uniformity of transversal transmission at T= 50%	nm	≤ 3
LY at T= 18 °C	phe/MeV	≥ 16.0
LY(100 ns)/LY(1 μs)		≥ 0.9
induced absorption coefficient Δk at room temperature, integral dose 30 Gy	m^{-1}	≤ 1.1
mean value of Δk distribution for each lot of delivery	m^{-1}	≤ 0.75

Table 2.1: Relevant specifications of the crystals for the PANDA EMC.

2.2.1 Longitudinal Transmission

A reasonable transmission of a crystal is important for the propagation of the produced luminescence light of the scintillation process. The almost Gaussian distributed scintillation light of PWO is peaking at around 420 nm with a FWHM[4] of ~ 40 nm. Fig. 2.4 shows the luminescence light and the natural transmission of an unharmed and an irradiated PWO crystal.

In order to judge whether a crystal has sufficient longitudinal transmission, one has to compare the measured values with the specification limits at three selected and very

---

[4]<u>F</u>ull <u>W</u>idth at <u>H</u>alf <u>M</u>aximum
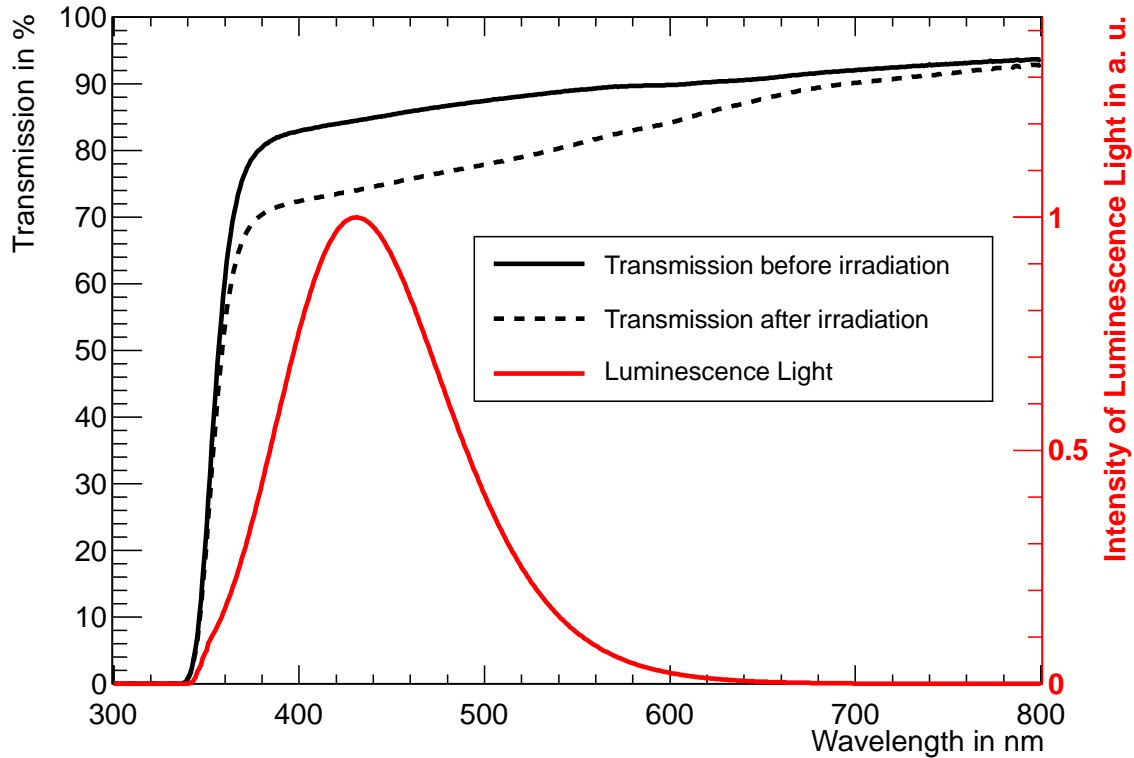
Figure 2.4: Luminescence and transmission characteristics of PWO as a function of
wavelength. The shift in transmission is caused by γ-irradiation with an integral
dose of 30 Gy. Both transmission spectra are smoothed curves originating from
averaged values from 10 randomly chosen crystals, which were measured with the
spectrometer introduced in Sec. 2.3.2.1 with a step size of 1 nm. The distribution
of the luminescence light has a Gaussian shape with slightly bigger tail on the
right hand side (data obtained by [18, 20]).

sensitive wavelengths: $360, 420$ and $620\,\text{nm}$. With the discovery of PWO as scintillator, it was desired to shift the fundamental absorption edge to lower wavelengths via doping, as well as reduction of defects. The required transmission at $360\,\text{nm}$ was chosen to avoid a cutting into the emission spectrum and to provide an optimum coverage. In addition, the transmission at $360\,\text{nm}$ shows a useful correlation with the light yield, which could be exploited later on for a first order relative energy calibration of the crystals among each other. A requirement at the peaking wavelength of $420\,\text{nm}$ is self-evident. $620\,\text{nm}$ is chosen as longest relevant wavelength in order to avoid absorption bands caused by any kind of complexes in the crystal matrix. In each stage of the quality control the longitudinal transmission is measured via a light beam which enters the crystal in one end face perpendicularly, proceeds along the long crystal axis and leaves the sample at the other end face. This way of measurement already causes losses due to reflections at media transitions. The reflected and transmitted fraction r and t of a certain light intensity for one surface transition with different indices of reflection n_1 and n_2 can be calculated by:

$$r = \left(\frac{n_1 - n_2}{n_1 + n_2} \right)^2 \qquad (2.1)$$

$$t = 1 - r \qquad (2.2)$$

Fig. 2.5 illustrates the individual contributions to the overall transmitted light intensity.
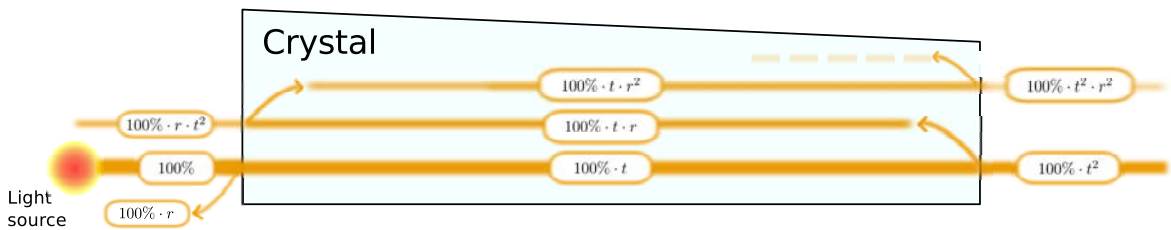
Figure 2.5: The picture shows the propagation for multiple reflected photons in an optical system. The relative intensities are marked for the individual light beams according to Eq. 2.1 and 2.2.

By summing up all fractions, one can determine the theoretical limit for the longitudinal transmission which is achievable for this method.

$$T_{\max} = 100\% \cdot t^2 \cdot (1 + r^2 + r^4 + \ldots) \qquad (2.3)$$

$$= 100\% \cdot \frac{1 - r}{1 + r}$$

These considerations, with the mentioned importance at the relevant wavelengths, lead to the requirements for the longitudinal transmission.

2.2.2 Transversal Transmission

The homogeneity of a crystal is a crucial aspect for the final performance of the EMC and is mainly determined by the quality of the crystal growing process. Therefore, a nearly constant transversal transmission along the crystal is mandatory. For PANDA, the spectrum in the relevant wavelength range is measured perpendicular to the 20 cm long crystal axis at equidistant positions. For each position, the wavelength, where the 50 % threshold is passed, is recorded. From the largest and smallest obtained wavelength, one can characterise the homogeneity of the crystal by the so called $\Delta\lambda$-parameter:

$$\Delta\lambda = \lambda_{\mathrm{max}/50\%} - \lambda_{\mathrm{min}/50\%}. \tag{2.4}$$

This parameter should not exceed 3 nm.

2.2.3 Geometry

In general, a crystal has the geometry of a truncated pyramid with a length of 20 cm. In order to achieve a hermetically closed barrel part of the EMC, 11 differently tapered crystal shapes are used. In addition, each of these shapes is produced in two versions symmetric to one of the side faces. All the crystals in the barrel region are symmetrically aligned to a plane, which contains the target point and is perpendicular to the beam. This mirror symmetry allows the reduction of necessary shapes from originally 18 to 11. Moreover, two additional shapes are foreseen for the mounting in FEC and BEC. A schematic drawing of the crystal model for the explanation of the geometry parameters and the values for each shape is given in Fig. 2.6 and Tab. 2.2.

For the mounting of the calorimeter, the crystals are not pointing directly to the final vertex point in order to prevent energy deposition in dead material. The crystals including wrapping have to fit into carbon alveoles. Therefore each geometry parameter should not exceed the desired limits of Tab. 2.2. On the other hand, the deviation should be less than 0.1 mm. The roughness is a parameter which is not explicitly measured for the quality control. This parameter should be below or equal $0.02\,\mu$m and $0.5\,\mu$m for the polished crystal surfaces and the edges, respectively. Furthermore, in a case of doubt, no crystal with cracks deeper than 0.5 mm is allowed.
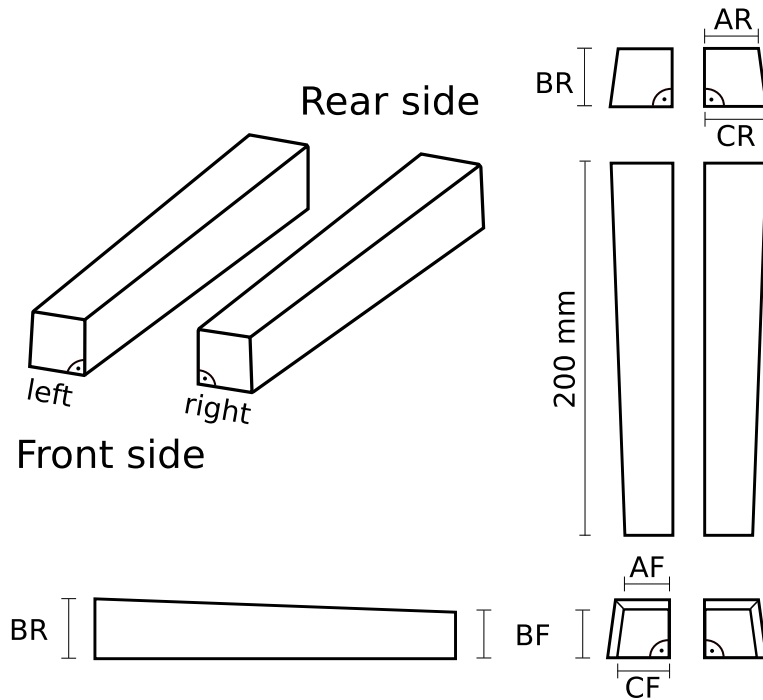
Figure 2.6: Schematic drawing of a PANDA crystal including the definition of the geometry parameters. All crystals have a right angle corner in order to simplify manufacturing.

Type	Volume cm^3	AF	BF	CF	AR	BR	CR
		mm					
1	126.86	21.21	21.28	21.27	29.04	28.75	29.12
2	126.56	21.18	21.28	21.39	28.78	28.75	29.07
3	125.79	21.17	21.28	21.51	28.36	28.75	28.81
4	120.85	21.17	21.28	21.60	27.90	27.22	28.45
5	119.69	21.17	21.28	21.69	27.35	27.22	28.01
6	118.35	21.19	21.28	21.78	26.72	27.22	27.47
7	112.90	21.22	21.28	21.86	26.23	25.47	26.99
8	111.75	21.23	21.28	21.91	25.70	25.47	26.51
9	110.52	21.23	21.28	21.95	25.14	25.47	26.00
10	107.01	21.25	21.28	22.00	24.70	24.42	25.56
11	106.25	21.25	21.28	22.02	24.35	24.42	25.23
EC	126.88	24.38	24.38	24.38	26.00	26.00	26.00
EC-R	118.58	24.35	24.35	24.35	24.35	24.35	24.35

Table 2.2: Definition of the geometrical parameters of the lead tungstate crystals. The EC and EC-R geometry corresponds to crystals for the FEC and the BEC, respectively.

2.2.4 Light Yield

The LY is an important quality parameter, since it describes the ability of a crystal to convert deposited energy into scintillation light and has a significant contribution to the stochastic term of the energy resolution. For the quality control of PANDA, the LY is determined by conventional bialkali PMTs and therefore, the LY is characterised in terms of photoelectrons per MeV (phe/MeV) and can be calculated by:

$$\mathrm{LY[phe/MeV]} = \frac{\mathrm{pp_{Source}} - \mathrm{pp_{Pedestal}}}{\mathrm{pp_{SEP}} - \mathrm{pp_{Pedestal}}} \cdot \frac{1}{E_\gamma}. \qquad (2.5)$$

$$\mathrm{pp : peak\ position}$$
$$\mathrm{SEP : Single\ Electron\ Peak}$$
$$\mathrm{E_\gamma : Energy\ of\ photon\ in\ MeV}$$

The position of the pedestal $\mathrm{pp_{Pedestal}}$ corresponds to the zero level of the signal. A SEP occurs if only one electron is emitted from the photocathode due to thermal excitation and getting amplified by the dynod structure of the PMT. For quality control it would not be economical to cool each crystal down to the final operating temperature of $-25\,^\circ$C. Fortunately, there is a well established linear correlation between the LY at different temperatures [27]. Therefore, the measurements of the LY-parameter are performed at $+18\,^\circ$C. The minimum LY-requirement is $16\,\mathrm{phe/MeV}$, which is only crucial for the less tapered crystals of both end caps. This will be explained and further discussed in Sec. 2.4.3.

2.2.5 Scintillation Kinetics

The kinetics of the scintillation mechanism describes the necessary time for the collection of a certain amount of scintillation light and can be expressed as decay times of the scintillation components. For mass quality inspection, the ratio of the collected LY within $100\,\mathrm{ns}$ and $1\,\mu\mathrm{s}$ gives a feedback about the kinetics of a scintillator. This ratio should be above or equal $90\,\%$ and is measured at $+18\,^\circ$C. This property is by far not expected to become problematic, since for the majority of crystals this requirement is even fulfilled at $-25\,^\circ$C. For a small set of randomly chosen crystals, this parameter was remeasured $+18\,^\circ$C and $-25\,^\circ$C to confirm the uncrucial situation with respect to rejection (Fig. 2.7). Therefore this parameter is not further discussed in the analysis of the quality control.
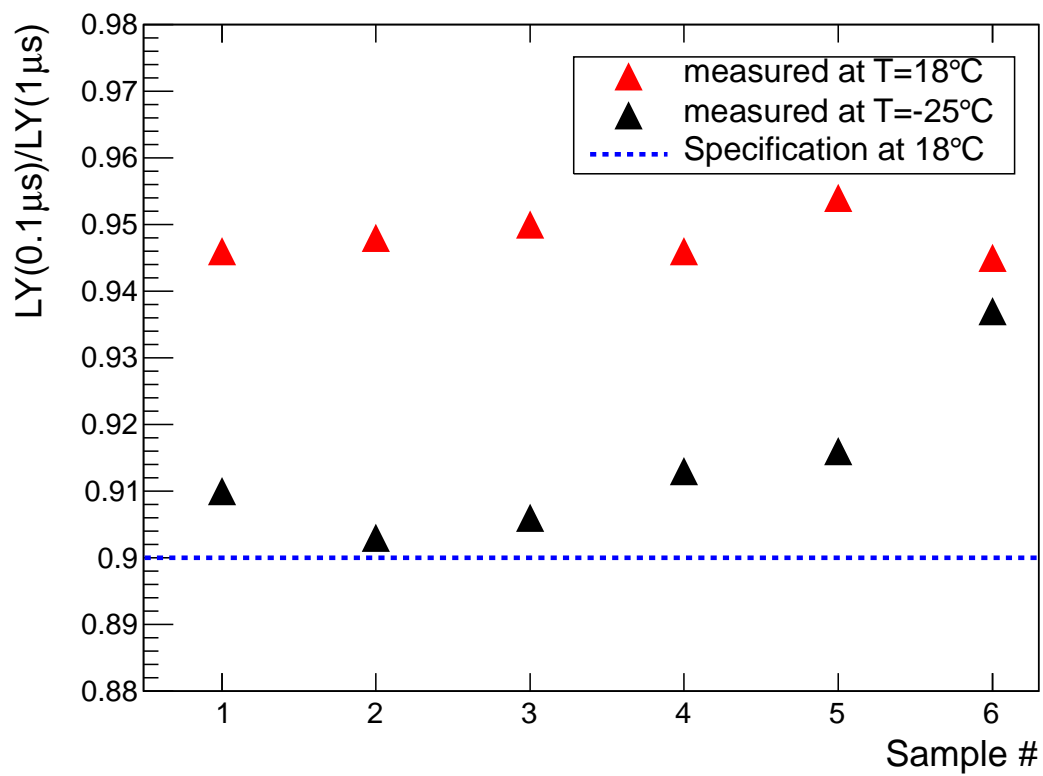
Figure 2.7: Scintillation kinetics of a small group of crystals at $+18\,°\mathrm{C}$ and $-25\,°\mathrm{C}$ with integration times of $100\,\mathrm{ns}$ and $1\,\mu\mathrm{s}$.

2.2.6 Radiation Hardness

To guarantee a proper operation over a long runtime period in a radiative environment, the crystals have to cope with ionizing and non-ionizing radiation. This can cause absorption bands originating from colour centres, which is directly connected to the loss of transmission in the relevant spectral region. The scintillation mechanism itself is not affected. To prove the transmission stability after a certain amount of irradiation, the change of the absorption coefficient, based on the Lambert law, was chosen as a criteria:

$$\Delta k = k_{\text{after irradiation}} - k_{\text{before irradiation}}$$
$$= \frac{1}{d} \ln \left(\frac{T_{\text{before irradiation}}}{T_{\text{after irradiation}}} \right) \tag{2.6}$$
$$\text{with d} = 20 \, \text{cm}.$$

The fixed accumulated dose for the determination of the radiation hardness is $30 \, \text{Gy}$ caused by γ-irradiation of a set of ^{60}Co, which corresponds to a runtime of PANDA of half a year for the innermost region of the FEC. The selected requirement of the radiation hardness, expressed by the Δk-value at $420 \, \text{nm}$ is $1.1 \, \text{m}^{-1}$. This modified specification limit with respect to the contract, includes all possible error contributions, e.g. from multiple reflected photons, errors of the transmission measurements or the presence of a fast recovery component at room temperature. In contrast to the CMS calorimeter, the requirement of the radiation hardness is more strict, in spite of the lower expected dose. This originates from the significantly suppressed spontaneous recovery at $-25 \, ^{\circ}\text{C}$. Fig. 2.8 shows typical spectra of Δk for three categories of quality in radiation hardness.
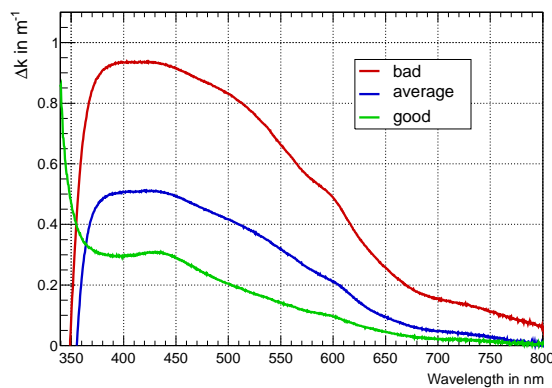
Figure 2.8: Typical Δk-spectra for PWO for a good, average and bad crystal according to the quality in radiation hardness.

2.3 Procedure of Quality Control

The securing of the necessary quality of the crystals is a common task of three test stations. The first quality check of the crystals is performed by the manufacturer BTCP, in order to avoid the delivery of crystals with insufficient quality. Afterwards, each lot is shipped to CERN to pass the next iteration of quality control. Finally, the last and deciding quality check is done at Gießen, where also the storage until the final mounting of PANDA takes place. Fig. 2.9 shows the path of the crystals from their production to different test stages. This subsection describes the test procedures and setups for the individual stages.

Figure 2.9: The defined procedure for securing the minimum quality of the crystals.

Not all parameters are measured by each facility, therefore Tab. 2.3 gives an overview between test facility and corresponding quality parameter.

Property	BTCP	CERN	Gießen
geometries	✓	✓	✗
longitudinal transmission	✓	✓	✓
transversal transmission	✓	✓	✗
light yield	✓	✓	(✓)
scintillation kinetics	✓	✓	✗
radiation hardness	✓	✗	✓

Table 2.3: Overview of the quality control of the crystals and where they are tested. Only for a few random crystals of each lot and geometry the LY was measured in Gießen to determine the calibration coefficients (Sec. 2.3.2.2).

2.3.1 Quality Control at BTCP and CERN

The test procedure of BTCP and CERN are very similar, both using a special device for handling a larger number (up to 30) of crystals simultaneously. This device is the so called ACCOS[5] machine (Fig. 2.10) and was in both cases already used for testing crystals of the CMS calorimeter, ECAL[6].

Figure 2.10: The moveable server of the ACCOS machine has a diameter of $1.1\,\text{m}$ and is able to carry several crystals, including reference crystals, at the same time.

The ACCOS machine is a composed system of devices for the single quality measurements [28]. A 3D-laser system[7] measures the geometry with a precision of $5\,\mu\text{m}$. For the determination of the crystal edges, each crystal face is reconstructed by measuring a certain number of points (15 for lateral faces; 9 for one end face). The transmission along and perpendicular to the long crystal axis is in each case measured by a compact spectrometer using a $20\,\text{W}$ halogen lamp. But here only a set of discrete wavelengths, chosen from $330 - 700\,\text{nm}$ for the best recognition of the absorption edge and possible absorption bands, is measured and realized by narrow band pass filters. The detection of the transmitted light is done by a large area UV-extended pin photodiode. The obtained data are subsequently fitted with a four parametric function to minimise the time for one transmission measurement:

$$T(\lambda) = e^{-e^{-(\lambda - P_0)P_1} \cdot P_2 \cdot (1 - P_3 e^{-\lambda/92\,\text{nm}})}. \tag{2.7}$$

---

[5]<u>A</u>utomatic <u>C</u>rystal quality <u>Co</u>ntrol <u>S</u>ystem
[6]<u>E</u>lectromagnetic <u>Ca</u>lorimeter
[7]Johansson Topaz 7

In case of the transversal transmission, the measurement is performed as explained in Fig. 2.11, for equidistant points.
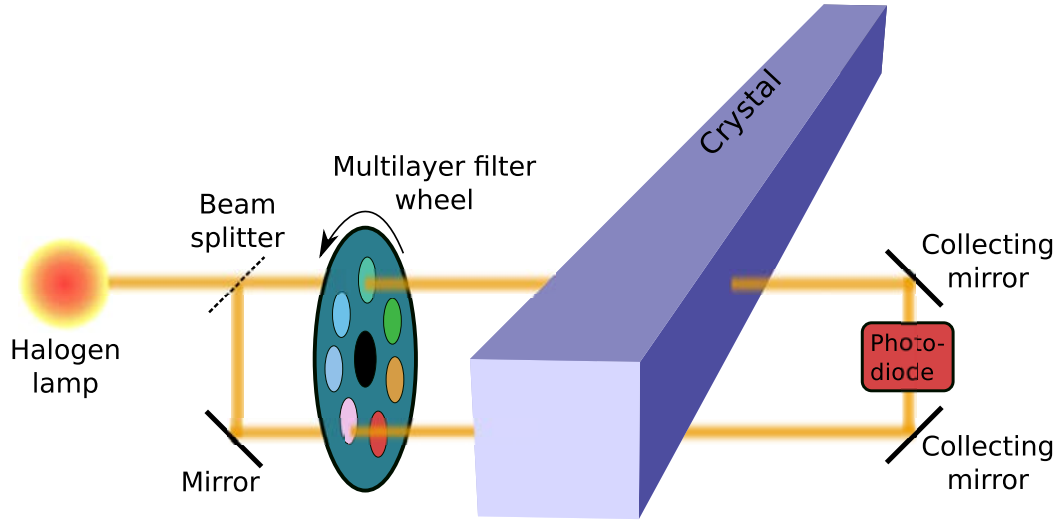
Figure 2.11: Schematic process of the transversal transmission measurement performed by the ACCOS machine. The sample and reference beam pass the filter wheel circulating with 50 Hz in sequence. Finally, both beams are guided by collecting mirrors to the photo diode, which is operating fully synchronous with the filter wheel.

The setup for the simultaneous measurement of the light yield, light yield kinetics and the dependence on the point of impact along the crystal axis is shown in Fig. 2.12. The exploited method is called delayed coincidence and is performed at 18 °C. A ^{22}Na ($< 10^5$ Bq) source is being moved along the crystal and emits positrons which directly annihilate with surrounding electrons. The two emerging photons are emitted back-to-back and are separately registered by a BaF$_2$ and the tested PWO crystal, respectively. The former one has a fixed connection to its PMT and provides a start signal, whereas the PWO crystal has a certain distance from the readout sensor to attenuate the scintillation light to single photon level. In addition, the PWO crystal delivers the stop signal for this method. A time stamp is only stored in the time spectrum of the TDC[8] if there is a matching of start and stop signal. The entries of this time spectrum, which represents for the matching efficiency, directly scales with the light yield of the scintillator. The coincidence measurement allows a clear identification of the scintillation light caused by the 511 keV photons via timing. Radioactive source and BaF$_2$ crystal are moved along the crystal in equidistant steps. This method is practical for a scintillator with low light yield, measured by a fully automatic device and has no necessity of wrapping or an optical coupling, which would lead to a further error contribution due to the lack of reproducibility. The final calibration of these

---

[8] <u>T</u>ime-to-<u>D</u>igital-<u>C</u>onverter

values is done at Gießen and will be explained in Sec. 2.3.2.2. To get data of the kinetics of a crystal, the mentioned routine is evaluated for time gates of $0.1\,\mu s$ and $1\,\mu s$ out of the TDC-information. With this, the ratio of the light yield for both integration times can be derived. For each cycle of measurements, reference crystals serve as comparison and subsequent correction due to variations caused by e.g. thermal effects.
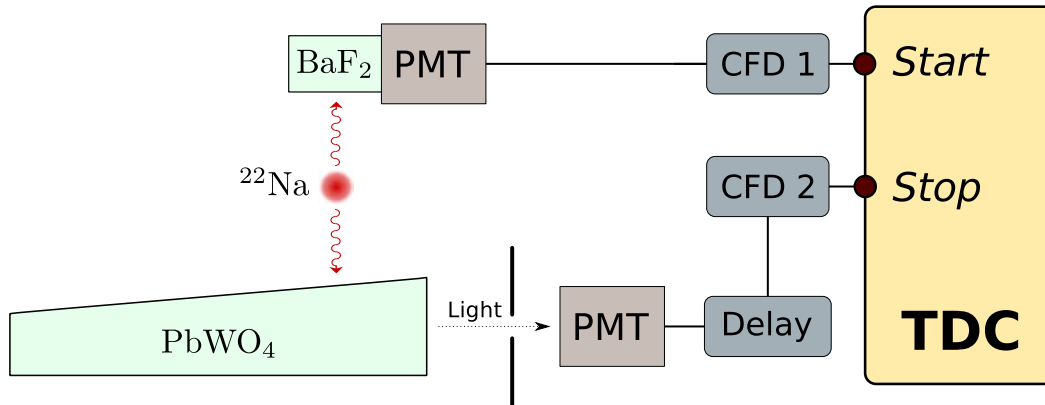
Figure 2.12: Principle of the light yield measurement of the ACCOS machine. A start signal is provided by the BaF$_2$ crystal. The first arriving signal above threshold of the PWO crystal initialises the stop signal.

The radiation hardness is measured by BTCP by checking the transmission before and after an exposure to a cobalt source with an overall dose of $30\,\mathrm{Gy}$. This irradiation facility was installed for the mass production for the CMS detector with technical assistance of RINP[9], which is described in more detail in [8, 27]. The time between irradiation and the second transmission measurement is not documented and was not fixed in the contract with BTCP. This duration is a source of inconsistencies between the measurements of the radiation hardness at Gießen and BTCP due to the spontaneous recovery of PWO at room temperature (compare Fig. 2.15).

2.3.2 Quality Control at Gießen

The longitudinal transmission and the radiation hardness are remeasured at Gießen. Concerning the light yield, only a small set of crystals is remeasured to determine the calibration coefficients. Both experimental setups, including arising error contributions, will be discussed in detail in the following.

---

[9]Research Institute for Nuclear Problems of Belarussian State University

2.3.2.1 Transmission and Radiation Hardness Measurements

The measurement of the longitudinal transmission is done by a conventional double beam spectrometer[10] (Fig. 2.13a). According to the measured range from $325-900\,\mathrm{nm}$ with a sampling rate of $0.5\,\mathrm{nm}$, only a halogen bulb is used. But for the quality control of the PANDA crystals, the light path of the sample beam has to be modified. A special optics setup (Fig. 2.13b) consisting of mirrors and lenses has to be adapted to the spectrometer, so that the light can be guided almost perfectly parallel across the full length of the crystal. A drawback of this modification is the significant intensity loss of the sample beam, but this can be compensated by a baseline correction (measurement without sample). With a scan rate of $300\,\mathrm{nm/min}$, one measurement over the relevant wavelength range takes almost $3\,\mathrm{min}$.

There are several uncertainties of the measurement, which have to be estimated. The

(a) Photo spectrometer.   (b) Additional optics by [29].
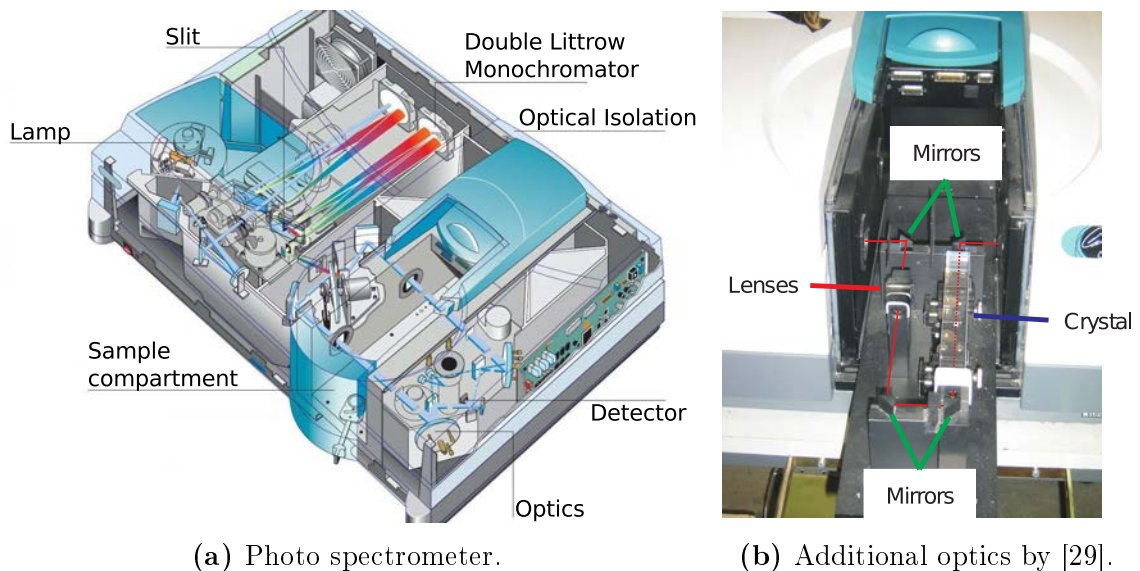
Figure 2.13: *VARIAN* spectrometer.

probably most obvious error contribution is due to the non-perfectly reproduceable crystal position in the spectrometer. Moreover, the transmission can shift caused by thermal effects. For the quality control, the transmission is remeasured from time to time without sample to check the stability. It was decided to recalibrate the spectrometer after a deviation of 0.1% from 100%. By measuring the same crystal several times in a row, one can get an upper limit for both error contributions at the relevant wavelengths: $\Delta T(620\,\mathrm{nm}) = \Delta T(420\,\mathrm{nm}) = 0.4\%$ and $\Delta T(360\,\mathrm{nm}) = 0.8\%$. The measurements for the radiation hardness are performed with the same spectrometer, which is placed at the irradiation facility at the Gießen Strahlenzentrum. Between the measurements, a crystal is put into the moveable compartment (shown in Fig. 2.14)

---

[10]Cary 4000, supplied by *VARIAN*

for irradiation with photons from a ^{60}Co source.

Figure 2.14: A compartment, which is installed in a circular moveable for irradiating different kind of samples. After a rotation of 180 the samples are exposed to a ^{60}Co source.

The duration of irradiation is in the order of 8 min and is frequently adapted according to the life time and loss of activity. Concerning the homogeneous illumination, 5 flat dosimeters were put into the corners and the centre of this compartment [27]. After an exposure to the cobalt source of 140 min, the dosimeters were analysed by KHG[11]. With an averaged integral dose of 500 Gy, the homogeneity was confirmed to be on a level of 3.6 Gy/min. Several error contributions for Δk have to be taken into account. One error already originates from the error of the transmission measurements and can be evaluated at 420 nm by:

$$\Delta(\Delta k) = \sqrt{\left(\frac{\partial(\Delta k)}{\partial \mathrm{T_B}}\Delta \mathrm{T_B}\right)^2 + \left(\frac{\partial(\Delta k)}{\partial \mathrm{T_A}}\Delta \mathrm{T_A}\right)^2} = \frac{1}{0.2\,\mathrm{m}}\sqrt{\left(\frac{\Delta \mathrm{T_B}}{\mathrm{T_B}}\right)^2 + \left(\frac{\Delta \mathrm{T_A}}{\mathrm{T_A}}\right)^2}. \quad (2.8)$$

With ordinary values of the transmission before irradiation ($\mathrm{T_B}$) and after irradiation ($\mathrm{T_A}$), and transmission errors of 0.4% at 420 nm one gets a relative error of $\sim 4\%$. Another error contribution could be caused by different points in time for the remeasurement after irradiation. Fig. 2.15 shows the recovery of the harmed crystal as a function of time. Due to this strong dependence on time, especially in the first minutes, the duration between irradiation and second transmission measurement was fixed to 30 min for all crystals.

Furthermore, in each measurement there arises an error, because of multiple reflected photons. The determination of Δk is based on the pure exponential behaviour of the transmission, described by Eq. 2.6. In principle, the presence of these multiple reflected photons worsens the Δk, since photons which pass the damaged crystal a couple of times, have an even higher probability to get absorbed. For estimating the

---

[11]Kerntechnische Hilfedienst GmbH
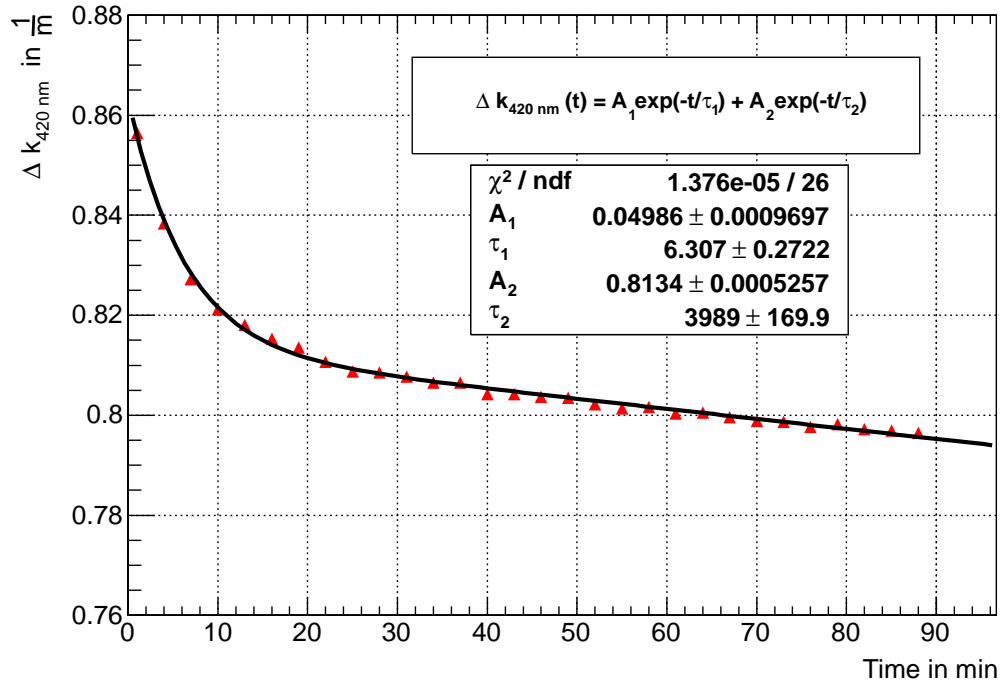
Figure 2.15: Spontaneous recovery for PWO at room temperature. A very fast recovery component gets visible with a constant of 6.3 min.

final contribution to the $\Delta(\Delta k)$, LITRANI[12] simulations were performed. As an input parameter, the absorption length of crystals with different quality was deduced by experimentally determined transmission according to Eq. 2.9 (from [30]).

$$l_{abs} = \left[\frac{-1}{d} \cdot \ln \left(\frac{-t^2 + \sqrt{t^4 + 4T_{\mathrm{Exp}}^2 r^2}}{2T_{\mathrm{Exp}} r^2} \right) \right]^{-1} \tag{2.9}$$

This procedure is explained in detail in [27] and results in a maximum relative error of 3.7%. To take into account all the mentioned errors of the measurement, the original specification limit of $1\,\mathrm{m}^{-1}$ was increased by 10% to $1.1\,\mathrm{m}^{-1}$.

---

[12]<u>Light</u> <u>Tr</u>ansmission in <u>Ani</u>sotropic media / http://gentitfx.fr/litrani/

2.3.2.2 Light Yield Measurements

For each crystal type 10 randomly chosen crystals per lot are remeasured at Gießen to obtain the calibration factor C for the CERN data according to Eq. 2.10.

$$\mathrm{LY[phe/MeV]} = C \cdot \mathrm{LY_{CERN}[a.u.]} \tag{2.10}$$

The used setup is shown in Fig. 2.16. Each test crystal is wrapped in eight layers of teflon and an aluminum-foil to optimize the light collection for photons, which are not totally reflected and escape the crystal. After wrapping, the crystal is attached with optical grease to a conventional PMT[13] with fused silica window and bialkali photocathode with a typical quantum efficiency of 20% at 420 nm. The excitation of the crystal is done by 662 keV photons from a ^{137}Cs from the top.
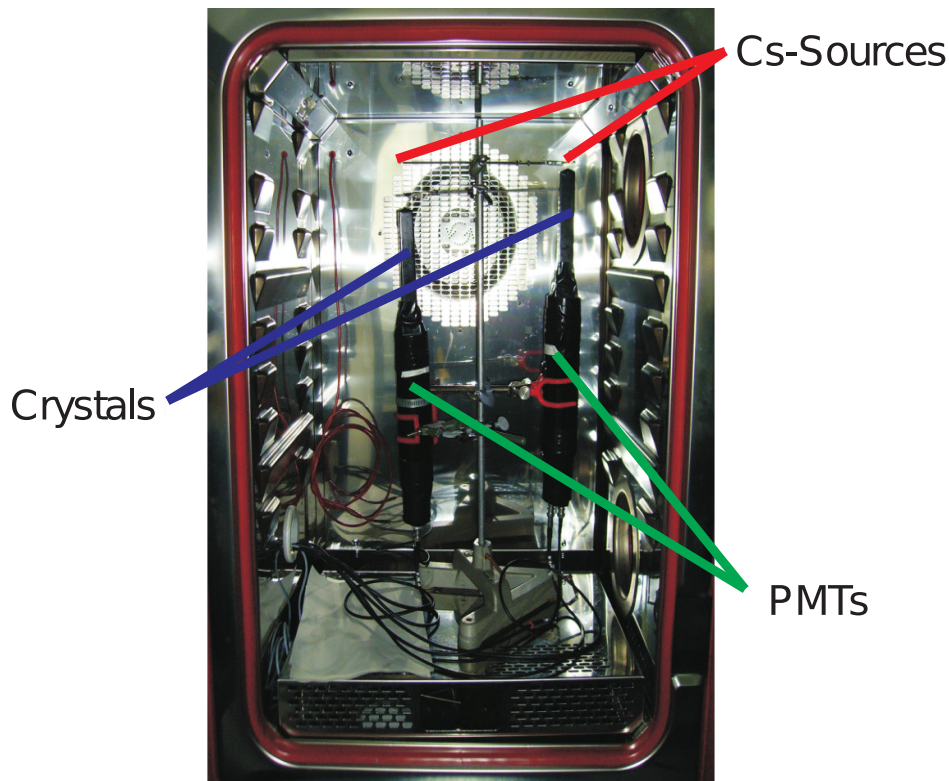
Figure 2.16: Setup for LY calibration at Gießen in a climate chamber for a stable temperature of 18 °C. The whole setup comprises two identical readout chains, where two crystals can be measured simultaneously.

This energy is well suited for the light yield determination of PWO, since it does

---

[13]*Hamamatsu* R2059-01

not overlap with the intrinsic activity of α-emitters which create signal amplitude corresponding to $1.2 - 1.4\,\text{MeV}$ photon energy due to quenching of the scintillation light. The PMT signal above an appropriate threshold is integrated in time gates of $100\,\text{ns}$ and $1,000\,\text{ns}$, respectively, and digitised by a QDC[14]. The positions of the photopeak, SEP[15] and pedestal are determined by Gaussian functions, whereas the light yield is evaluated with Eq. 2.5.

---

[14] Charge-to-Digital-Converter, CAMAC, Le Croy 2249W
[15] Single Electron Peak

2.4 Results Quality Control

Up to now, $9,336$ crystals were produced by BTCP[16], subdivided in 10 lots, comprising all crystals for FEC and BEC and 6 geometries for the barrel EMC. In an earlier stage, an 800 crystal preproduction lot, consisting of all 11 PANDA shapes for the barrel part, proved the ability for mass production with constant quality. In the following subsections, the obtained results with respect to the specifications will sequentially be presented and discussed. Moreover, Sec. 2.4.6 is intended to expose several discrepancies between the different test facilities and a summary of the quality control will be provided. At the end of this section, SICCAS[17], a potential manufacturer for the remaining crystals, will be introduced by testing a small amount of test samples.

2.4.1 Transmission

The transmission is an uncrucial parameter with respect to rejection. There is no dependence on the crystal geometry, since the used spectrometers have a negligible beam deviation and pass through the two parallel end faces of the crystals. Therefore, no dependencies caused by different crystal types in Fig. 2.18 becomes visible. Furthermore, no significant shift in absolute transmission with production date can be found by plotting the mean of the obtained values at Gießen versus the lot number (Fig. 2.17). Altogether, only **15 crystals** show an insufficient transmission.
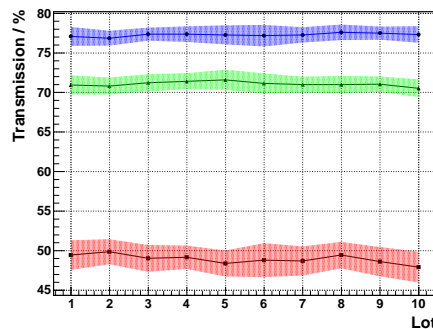
Figure 2.17: Transmission as a function of delivered lot for the three relevant wavelengths: $620\,\text{nm}$ (blue), $420\,\text{nm}$ (green) and $360\,\text{nm}$ (red).

---

[16]Bogoroditsk Techno Chemical Plant
[17]Shanghai Institute of Ceramics, Chinese Academy of Sciences
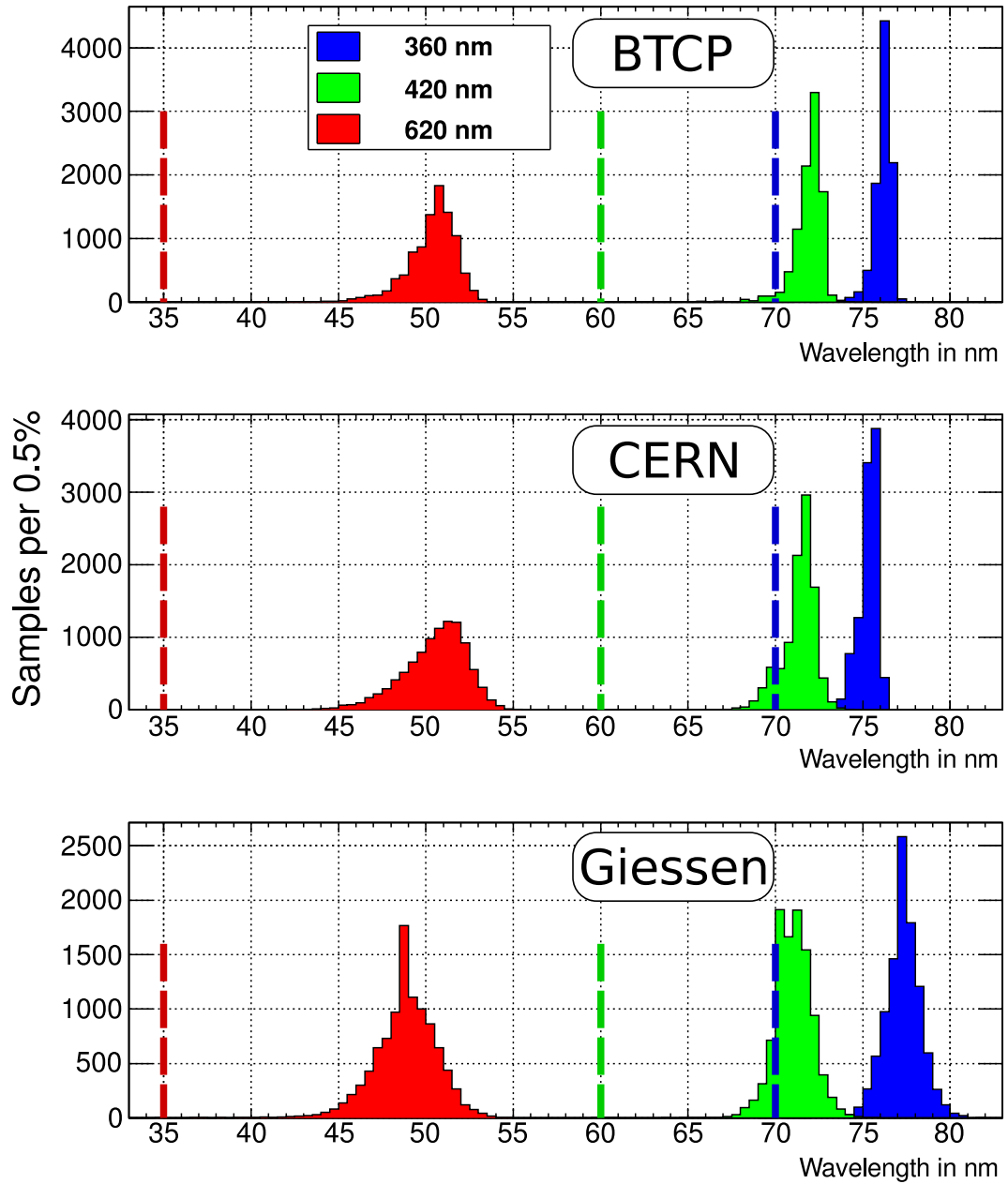
Figure 2.18: Distribution of transmission values for the three test stations. The specification requirements are marked as dashed lines with corresponding colour. Only a handful of crystals show an insufficient transmission, mostly at 360 nm.

2.4.2 Geometry

All crystals including wrapping have to fit into carbon alveoles. Fig. 2.19 shows the distributions for the different edges of all crystal types according to Tab. 2.6. The edge B3 corresponds to the in Tab. 2.6 labelled B-edge, while the specification of B4 in the rear and front face is given by:

$$B4 = \sqrt{(B3)^2 + (C - A)^2}. \tag{2.11}$$

The x-axis of each histogram represents the difference of desired and measured value for the individual types (compare Tab. 2.2). The geometrical requirements dictate a maximum deviation range from 0 to $100\,\mu$m. The majority of all crystals show a perfect geometry with a quite narrow spread within the limits. A second structure gets visible for the edges A and C for both faces, which is, without exception, visible for crystals of the last delivery. Measured dimensions smaller than the specified value are not crucial. Also slightly larger values on the μm-level can be tolerated. Altogether, there was no necessity to reject any crystal based on the measured geometry data.
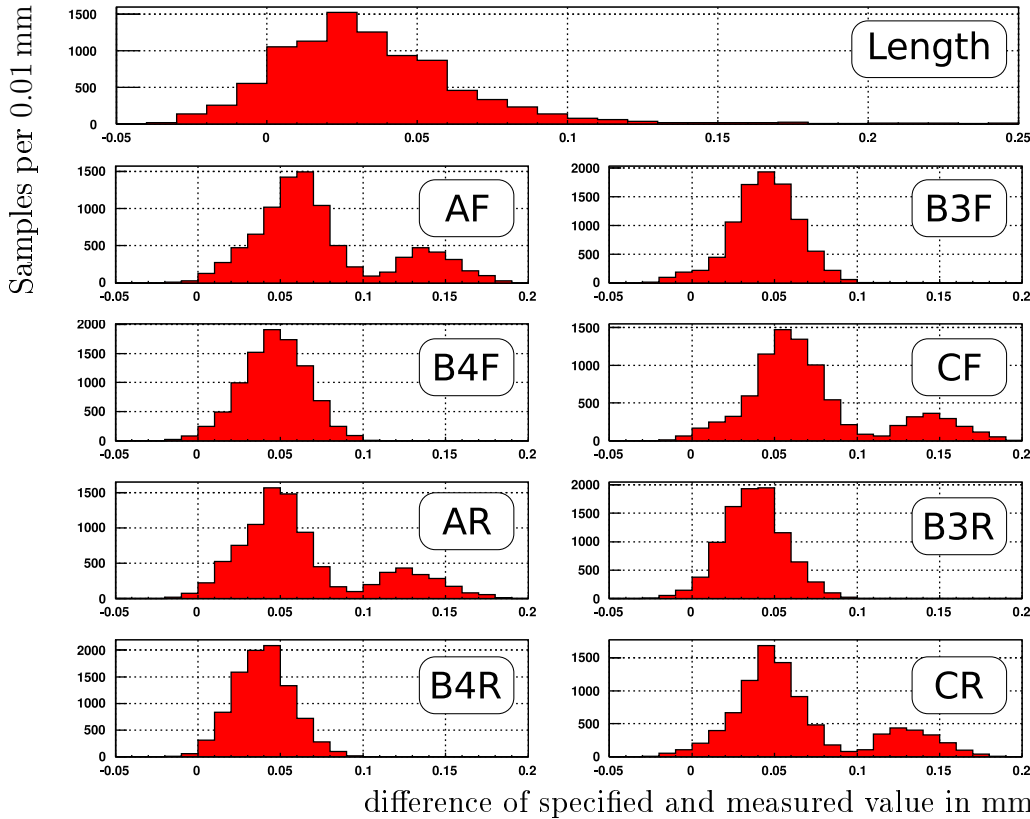
Figure 2.19: Distribution of geometry yield measured at CERN. F and R stand for the front (small face) and rear side (big face) of the crystal.

2.4.3 Light Yield

Fig. 2.21 shows the measured light yield data measured at CERN[18] and calibrated at Gießen. The shown data is distinguished by the level of tapering and starts in the top row with the least tapered shape: the crystals for the BEC. The spectra show a clear correlation of the obtained values with the crystal geometry. The larger the level of tapering, the higher the light yield output. This fact can be explained by the so called NUF[19]-effect in light collection. For the performed method of calibration, explained in Sec. 2.3.2, the energy deposition occurs in the front part of the crystal, far away from the photo sensor. This non-uniformity is caused by an interplay of light focussing and absorption, illustrated in Fig. 2.20. Possible corrections of this NUF-effect and impact on the energy resolution of the EMC are discussed in [31] in detail. The specification concerning light yield is only crucial for crystals for both end caps, which are almost completely cuboid-shaped. The light yield is the second most crucial rejection parameter and **78 crystals** show an insufficient light output below $16\,\frac{\text{phe}}{\text{MeV}}$.
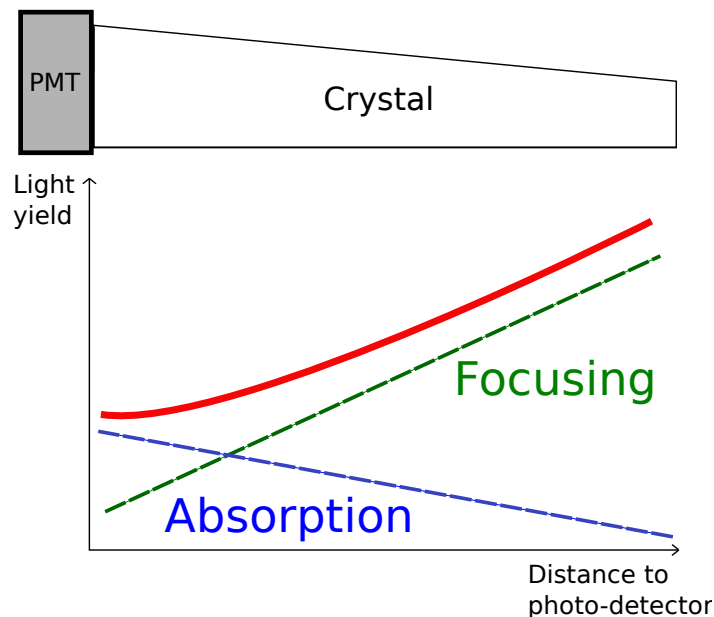
Figure 2.20: Schematic explanation of the NUF-effect. The further away from the photo sensor the scintillation light is produced, the higher the final light output. This originates from focussing, which guides the light towards the sensor. The final shape of the NUF-effect is a result of focussing and self absorption of the crystal. CMS-type crystals with worse quality, have a more U-shaped curve, due to the higher contribution of absorption.

---

[18]European laboratory for particle physics
[19]Non-Uniformity in light collection
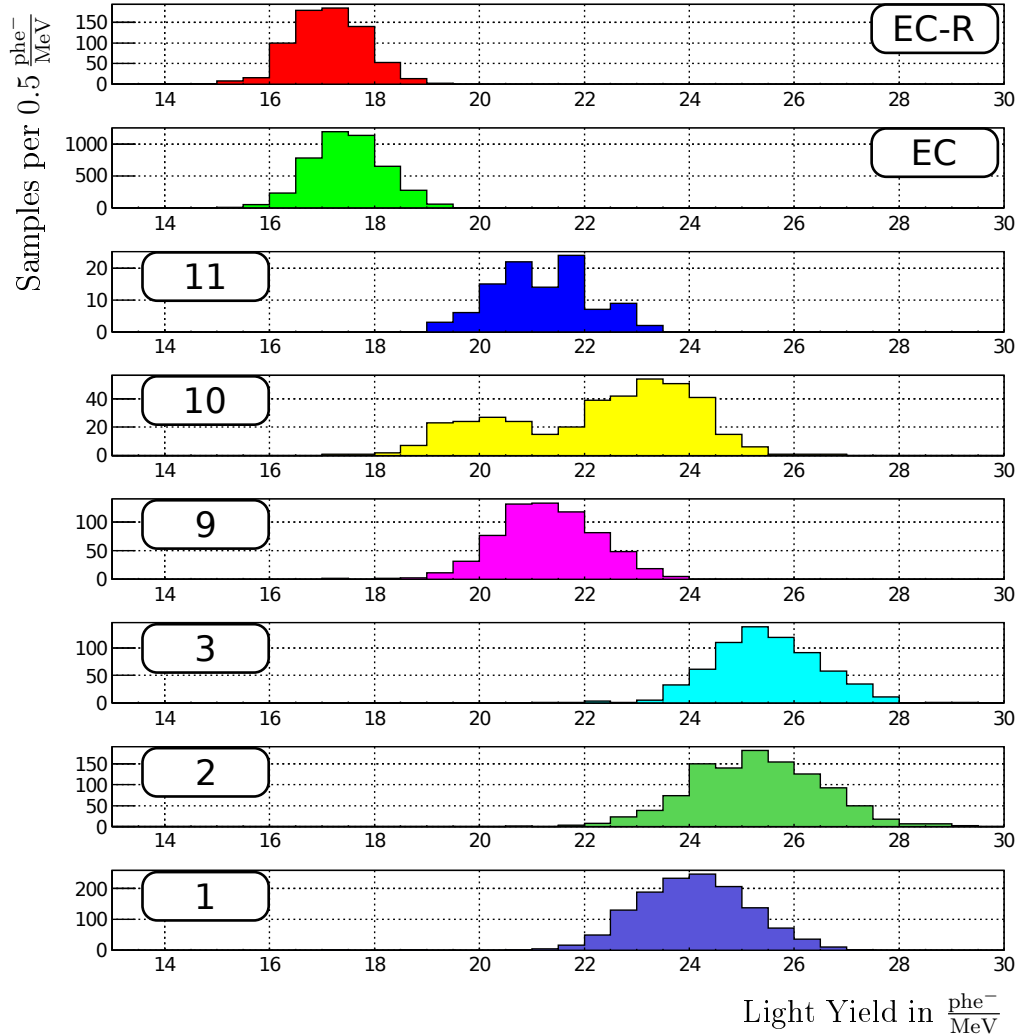
Figure 2.21: Distribution of light yield values sorted by the degree of tapering for the different denoted crystal geometries. Only for crystals of both end caps the specification limit of 16 phe/MeV becomes crucial.

2.4.4 Transversal Transmission

The transversal transmission of a crystal gives an important information about the homogeneity of a crystal along its axis and is presented in Fig. 2.22 in terms of the $\Delta\lambda$-value (compare Eq. 2.4). The discrepancy between the distributions of CERN and BTCP will be analysed in Sec. 2.4.6. The majority of the shown data are far below the requirement of 3 nm, which is strongly related to the improved process of manufacturing. **19 crystals** do not fulfil the specification.
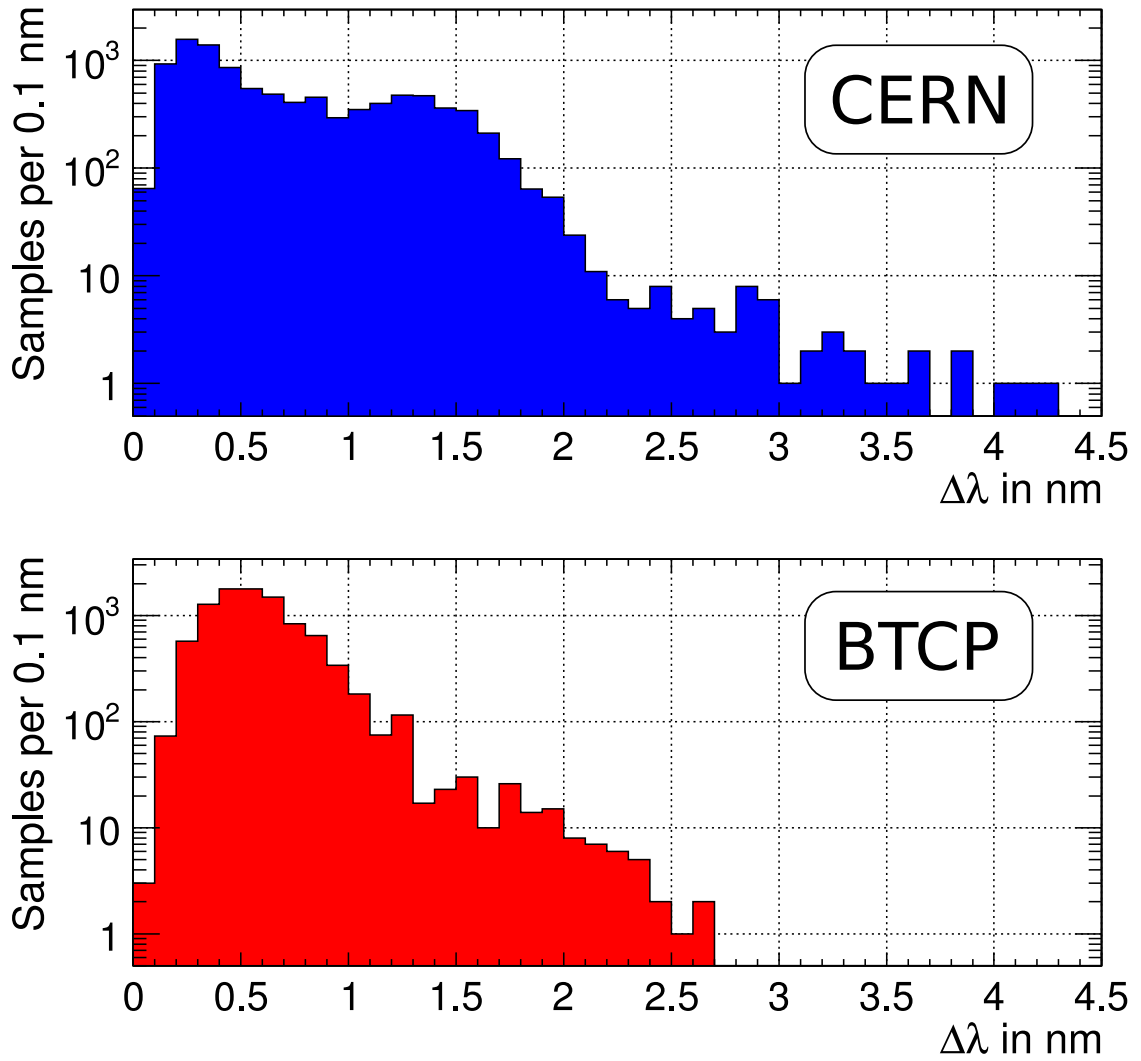
Figure 2.22: Distributions of the $\Delta\lambda$-parameter for BTCP and CERN. The crystals show a satisfying longitudinal homogeneity.

2.4.5 Radiation Hardness

Fig. 2.23 shows the values for radiation hardness from BTCP and Gießen. No notice-able substructure becomes visible due to different geometries. For the final judgement of the quality, the measurements of Gießen are deciding. A significant tail on the right comprises **553 crystals**, which have a Δk above $1.1\,\mathrm{m}^{-1}$. With this value, the radiation hardness is the most crucial parameter with respect to rejection. But on the other side, also very radiation resistive crystals show up. The overall quality in terms of Δk has been improved by $\sim 30\%$ with respect to CMS-type PWO crystals, which set the an rejection limit to $1.5\,\mathrm{m}^{-1}$.
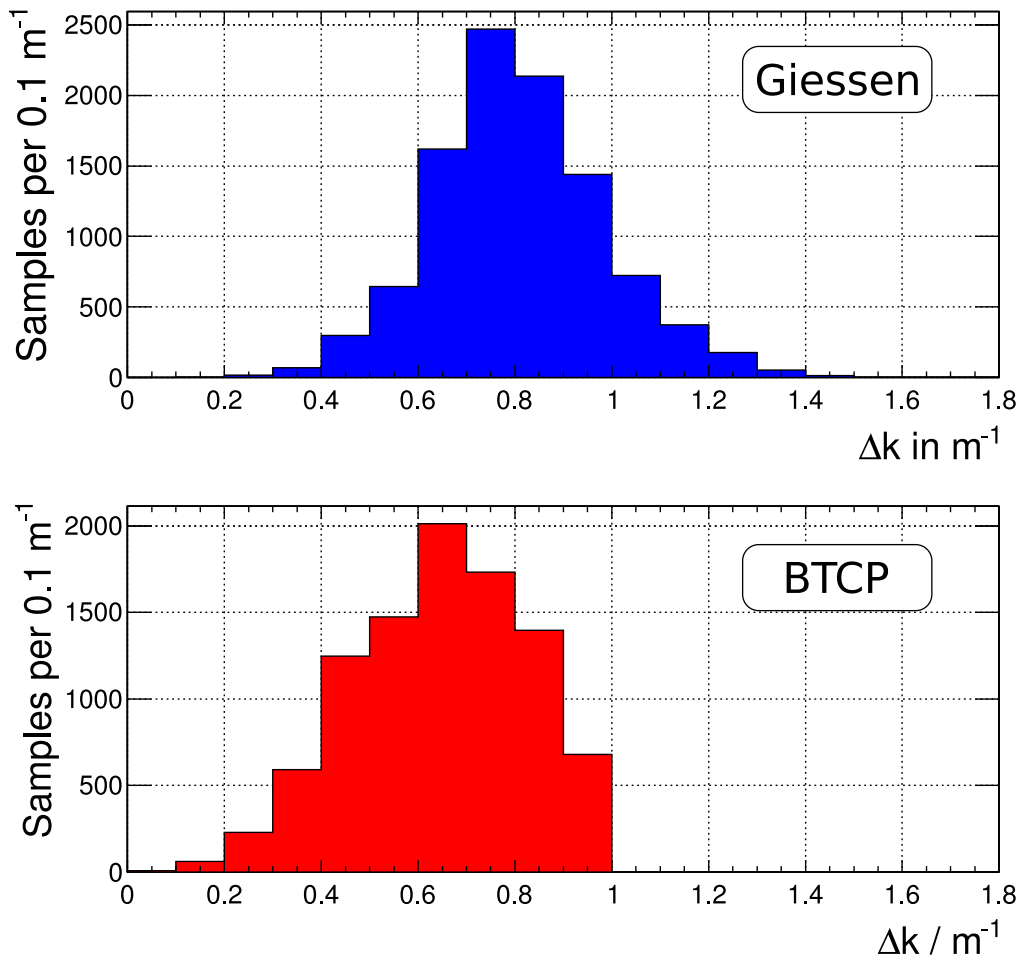
Figure 2.23: Distribution of radiation hardness for BTCP and Gießen. In average, the data from Gießen is slightly shifted compared to the BTCP data (Sec. 2.4.6) .

2.4.6 Correlations between the Test Facilities

A couple of histograms show a inconsistency between the individual test facilities. E.g. both $\Delta\lambda$-distributions in Fig. 2.22 have a good matching for values up to 1 nm, except a small shift to higher values in case of the BTCP data. This structure originates mainly from EC and EC-R crystals. For the CERN data, a second enhancement (around 1.5 nm) becomes visible, which is broader and can be subdivided into types (compare Fig. 2.24). Such type-specific contributions can not be spotted in case of BTCP. A possible explanation would be the different treatment of the measured data, e.g. by a path correction.
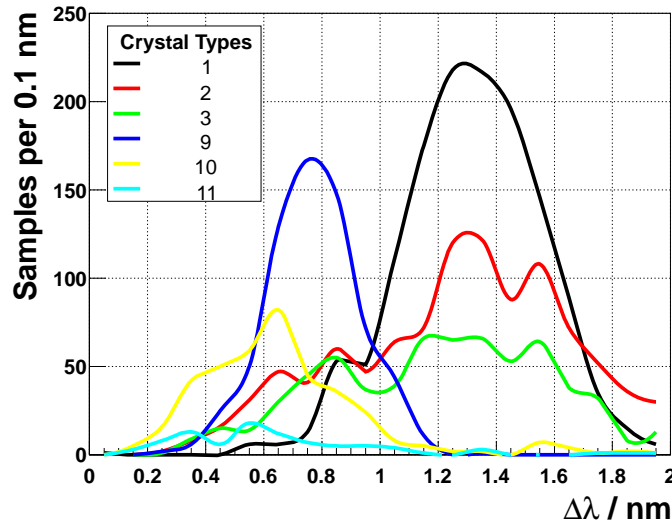
Figure 2.24: The figure shows $\Delta\lambda$-values separated by types from CERN. The data points are represented by smooth curves. One can see a clear correlation with the type, and therefore with the level of crystal tapering.

Also, the determination of the light yield at CERN is strongly influenced by the geometry, which was already shown in Fig. 2.21. In contrast to that, the BTCP-data does not show any type dependence (Fig. 2.25). As it was mentioned, the final light output is strongly connected to the point of origin of the energy deposition, due to the NUF-effect. Therefore, it is possible that BTCP illuminated relatively close to the rear face, where the photon sensor is mounted. In case of CERN, the energy deposition occurs further away from the sensor, as explained in Sec. 2.3.2.

Another conspicuous correlation can be found between BTCP and Gießen concerning the radiation hardness. The Gießen-data seems to be systematically about $0.1 - 0.2\,\text{m}^{-1}$ higher. With a correlation coefficient[20] of 0.7 the data is nicely correlated.

---

[20]correlation coefficient for two sets of data X and Y: CC $= \frac{<(X-<X>)\cdot(Y-<Y>)>}{\sigma_X\cdot\sigma_Y} \in [-1;+1]$
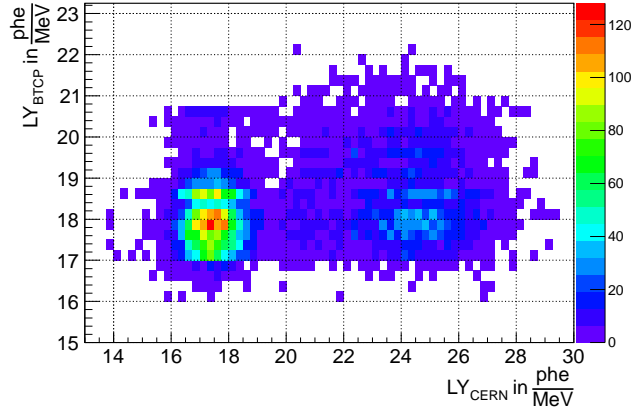
Figure 2.25: Light Yield correlation between BTCP and CERN. Only the CERN
data shows a strong type dependence.

Such a constant shift is caused by the not fully identical test procedure. Possible
variation could occur by the dose rate or the time between irradiation and the second
transmission measurement. This duration was not fixed in the contract with BTCP.
The latter one has a big impact on the measured Δk due to the existence of a fast
recovery component at room temperature (Fig. 2.15). This parameter was initially
not fixed in the contract for the crystal delivery.
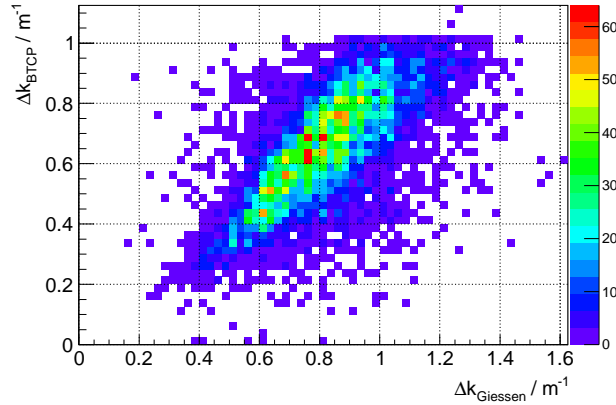
Figure 2.26: Δk correlation at 420 nm between BTCP and Gießen.

A further point is the longitudinal transmission for all facilities of the relevant wave-
lengths (Fig. 2.27). The data from Gießen and CERN are in relatively good agreement,
whereas the correlation to BTCP is much smaller. Moreover, the particular distribu-
tions from Gießen are broader (compare Fig. 2.18). This is probably connected to the
non-perfect reproducibility of the crystal position in the photospectrometer.
It can be concluded, that the main contribution to the discrepancies, is mainly caused
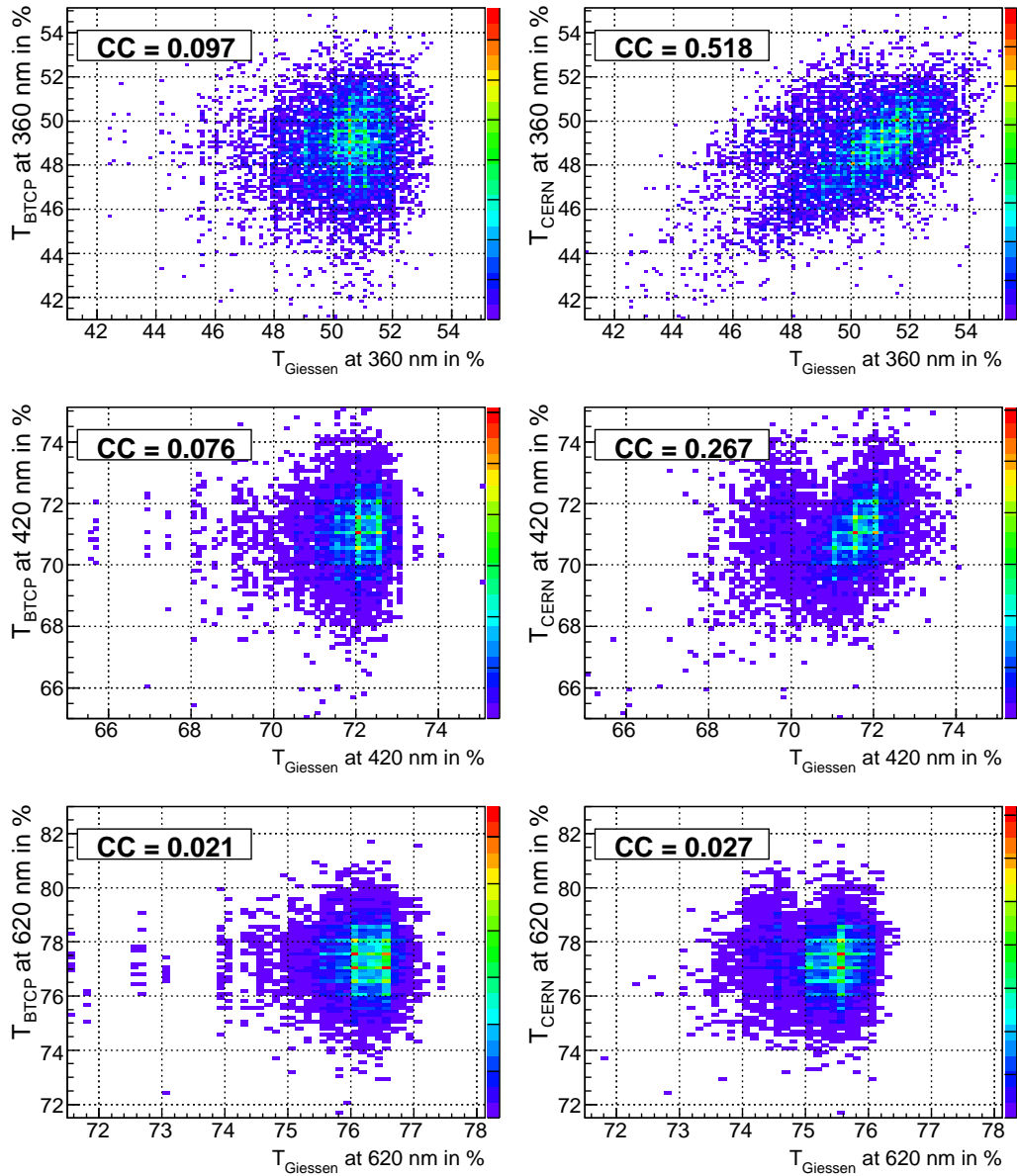
Figure 2.27: The left column shows the correlation between BTCP and Gießen data for the three relevant wavelengths. In the right column, the measured values from CERN and Gießen are compared. The latter ones are more correlated than the data sets in the left column. The general correlation gets worse at 620 nm, since here the values are distributed much narrower.

by variations in the test procedure of the single facilities. Furthermore, certain treatments for the different versions of the crystal shape are obvious, especially for the Light Yield and $\Delta\lambda$ parameters.

2.5 Status and Outlook of Crystal Delivery

Sec. 2.4.1 to 2.4.5 discussed the individual parameters of $9,336$ crystals with respect to rejection. This is again summarised in Fig. 2.29, distinguished by two groups of crystal:

1. Crystals for one of the end caps

   - Crystals for the FEC with small tapering

   - Crystals for the BEC with no tapering

2. Crystals for the barrel with significantly stronger tapering

This distinction in Fig. 2.29 underlines again the shape dependence of some certain parameters, which was already explained in Sec. 2.4.6. A small number of crystals has more than one insufficient parameter. This was not considered in the rejection numbers mentioned up to now. Under the assumption that the whole PANDA EMC finally needs $\sim 18,000$ crystals including spares, Fig. 2.28 gives the current status of the crystal delivery with the final rejection number. The large fraction of the missing crystals is still an open question. For this purpose, a set of test samples of an alternative crystal producer was ordered and tested. The results are presented in the next subsection.
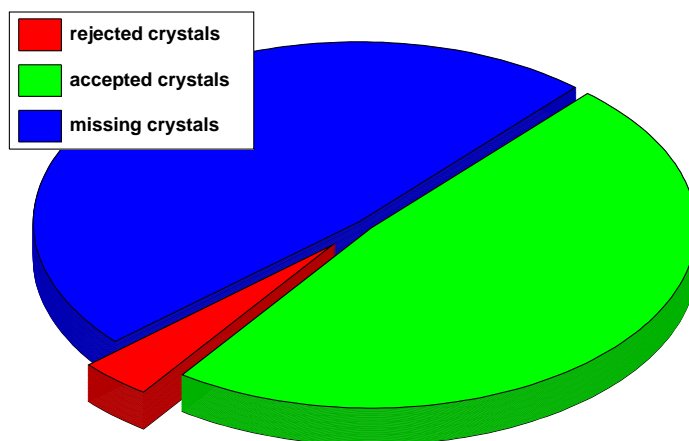
Figure 2.28: Status of crystal delivery.
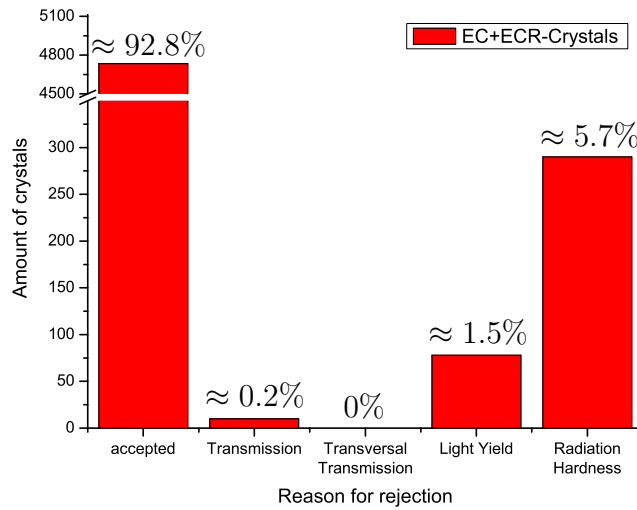
(a) A summary of all crystals of both end caps of the EMC, which comprise $5,100$ crystals. These crystals have specific problems for the LY, since the focussing effect is less pronounced (compare Sec. 2.4.3).
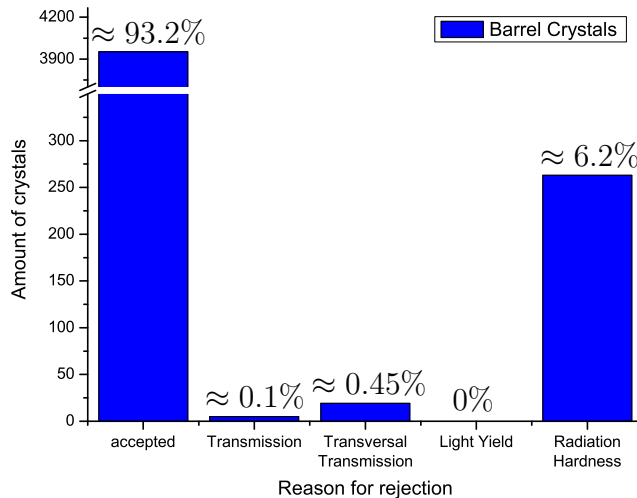
(b) A summary of all crystals of the barrel part of the EMC, which comprise $4,236$ crystals. As it was shown in Sec. 2.4.6, there is a type dependence for the measurements of the $\Delta\lambda$ and this parameter gets worse for more tapered crystals.

Figure 2.29: Summary of the reason of rejection for altogether $9,336$ crystals, distinguished by less tapered (EC and EC-R) and strong tapered crystals for the barrel. The marked information in percent does not consider any overlapping between the reasons of rejection. One can see, that the transmission and the radiation hardness are rejected to the same fraction and no geometrical dependence becomes visible.

2.5.1 SICCAS - A potential Crystal Manufacturer

The PANDA EMC still requires $\sim 8,500$ crystals for the final completion, which corresponds to 47.2% of the total amount for this detector. The previous producer BTCP filed bankruptcy and is not able to produce additional crystals at all. Various possibilities were discussed, e.g. to equip the remaining solid angle with a different kind of material. But this would lead to dramatic drawbacks, like significant inhomogeneities and an inappropriate cooling concept. Fortunately, there is a second major supplier of PWO crystals, which is located in China: SICCAS [32]. This company has a long research history since 1928 (renamed to SICCAS in 1984) and has many experiences in developing and manufacturing different kinds of ceramics and other inorganic materials. For the mass production of the remaining PANDA crystals, a set of 50 test crystals was ordered and tested according to the most crucial parameters. All those crystal are of type 11R, which is the third least tapered geometry in the PANDA EMC. The manufacturing process of SICCAS differs from the one exploited by BTCP, since all crystals are grown via the so called Bridgeman method (Fig. 2.30).
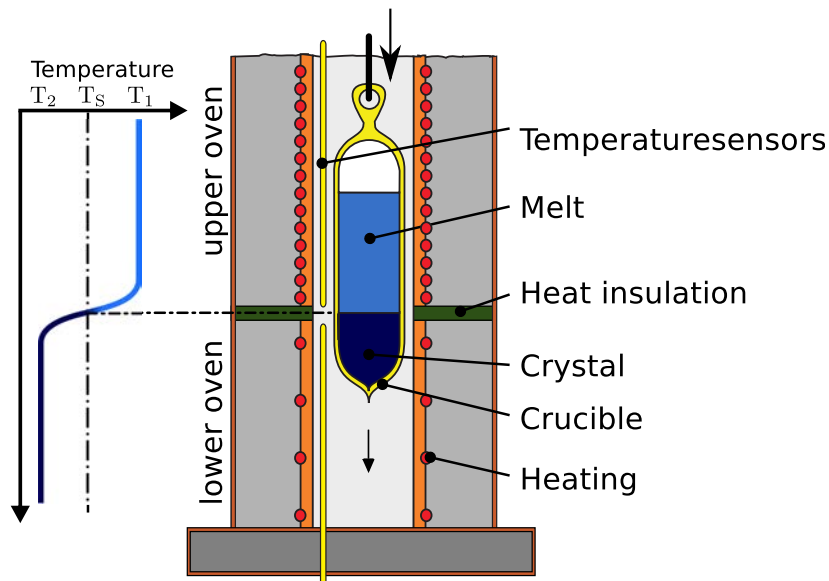
Figure 2.30: Bridgeman method for the crystal production by SICCAS. A crucible containing the crystal melt is lowered into the oven for the crystallisation. The oven itself is horizontally subdivided into two temperature regions. The upper half is above and the lower one below the specific melting temperature. While the crucible is slowly rotating, the melt starts to crystallise in the transition area [33].

Moreover, an essential difference between both processes (shown in Fig. 2.1a and Fig. 2.30) is the growing direction. The Czochralski method by BTCP grows crystals along the long axis of the elementary cell. In contrast to that, the SICCAS crystals

are grown along the small crystal axis, which has a different index of refraction. The different indices of refraction and the connected maximum transmission according to Eq. 2.3 for ordinary and extraordinary direction are displayed in Fig. 2.31.
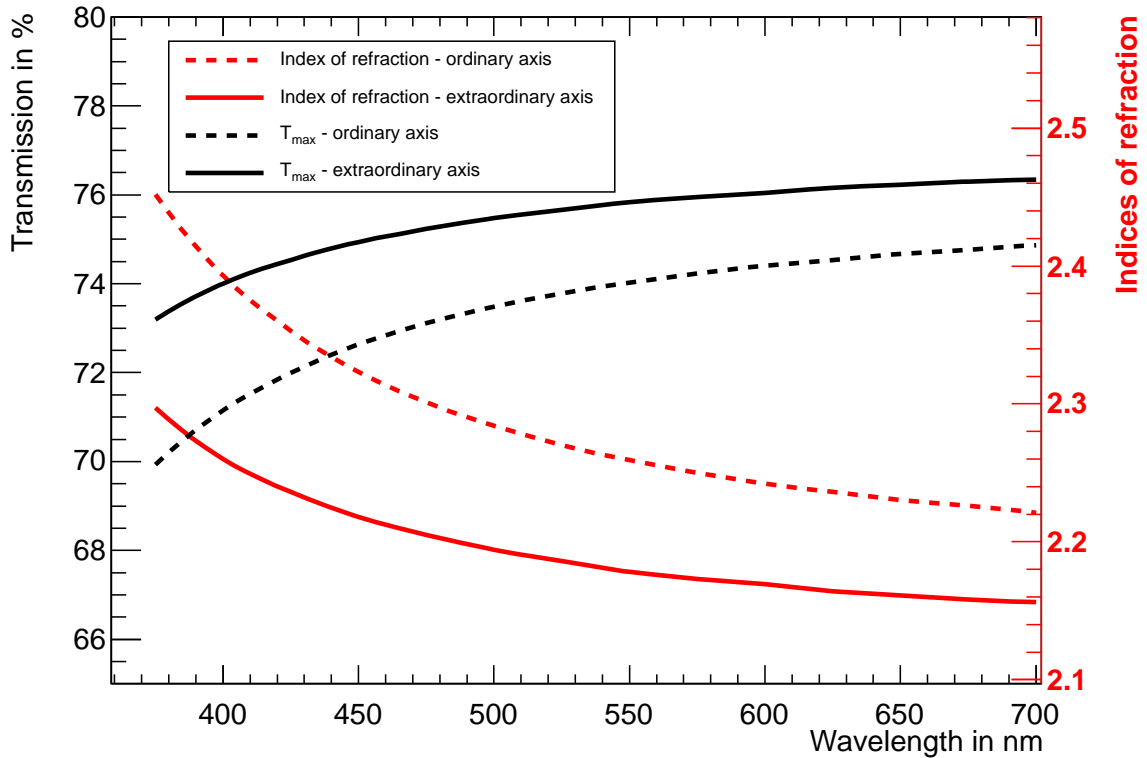
Figure 2.31: Indices of refraction for PWO for ordinary and extraordinary direction. The large difference between the indices already causes a significant change in the maximum transmission without absorption. The values for the indices were obtained by [30].

In the following, the results for the 50 test samples are presented and discussed for the longitudinal transmission, LY, homogeneity of the transversal transmission and the radiation hardness.

2.5.1.1 Results of the tested Parameters

The longitudinal transmission for the crystals from SICCAS was independently measured by CERN and Gießen (Fig. 2.32).
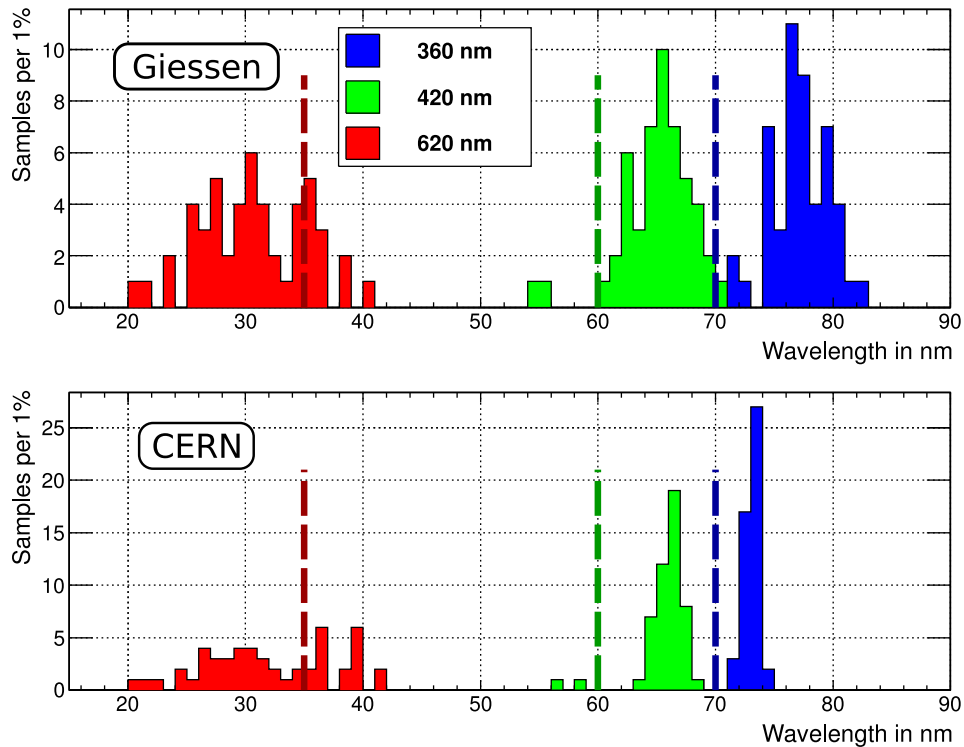
Figure 2.32: Longitudinal transmission for the 50 test samples from SICCAS measured at CERN and Gießen. The specification limits are drawn in corresponding colour.

The data from both facilities is nicely correlated, whereas the measurements from Gießen show the typical wider spread. One can directly see that the transmission values are significantly lower compared to crystals from BTCP (compare Fig. 2.18). This does not need to be an indication for reduced quality. As it was explained before, SICCAS grows crystals along the extraordinary direction, which has a higher index of refraction. This circumstance directly leads to a reduction of the longitudinal transmission.

The homogeneity of the transversal transmission in terms of $\Delta\lambda$ was only measured at CERN. The values are distributed much broader, compared to the presented data in Fig. 2.22, but here one has to take into account the tapered shape of the type 11 crystals and the type-dependence on the $\Delta\lambda$-values measured by CERN. Nevertheless, 16% of the crystals are above the specification limit of 3 nm, which is a significant

fraction compared to the crystals based on BTCP quality.
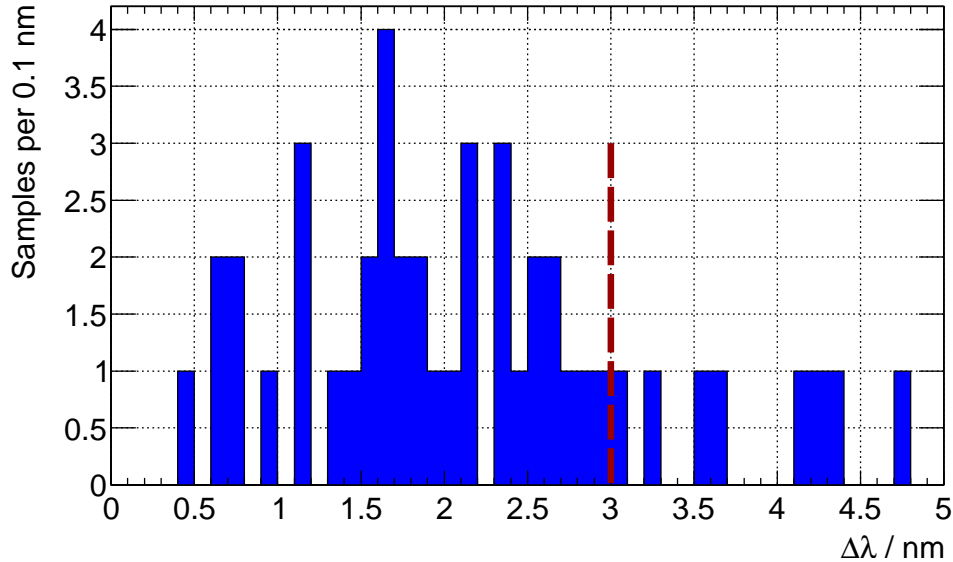
Figure 2.33: $\Delta\lambda$ distribution of SICCAS crystals measured at CERN.

The fact of the quality being distributed broader holds for the LY values as well, which were measured in Gießen. From the statistical point of view, the histogram in Fig. 2.34 has a RMS[21] of 3.6 phe/MeV, whereas the value of the same crystal geometry in case of BTCP is significantly lower at 0.9 phe/MeV (compare Fig. 2.21). The mean value seems to be comparable, but here one has to wait for better statistics.

Also the radiation hardness was tested in Gießen according to the procedure introduced in Sec. 2.3.2.1 and the result is shown in Fig. 2.35. In spite of the low statistics, the obtained radiation hardness looks similar to the distribution observed for BTCP, and also here a small tail reaching above the specification limit is visible. One crystal has a change in the absorption coefficient of almost $5\,\mathrm{m}^{-1}$, which is not shown in Fig. 2.35, but this crystal even shows macroscopic defects visible to the naked eye. Altogether, one can conclude that SICCAS is able to deliver crystals, which fit to the quality requirements of PANDA. A conspicuous and negative aspect is the wide spread of the obtained values for building up a homogeneous calorimeter. Nevertheless, a larger number of crystals in form of a preproduction lot would be helpful to obtain more reliable information about the crystals provided by SICCAS.

---

[21]<u>R</u>oot <u>M</u>ean <u>S</u>quare
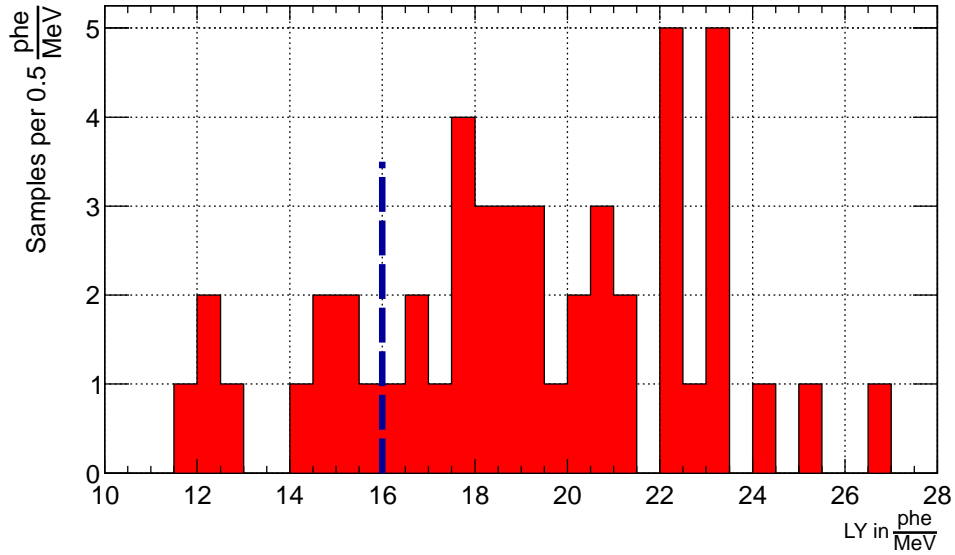
Figure 2.34: LY distribution of SICCAS crystals measured in Gießen.
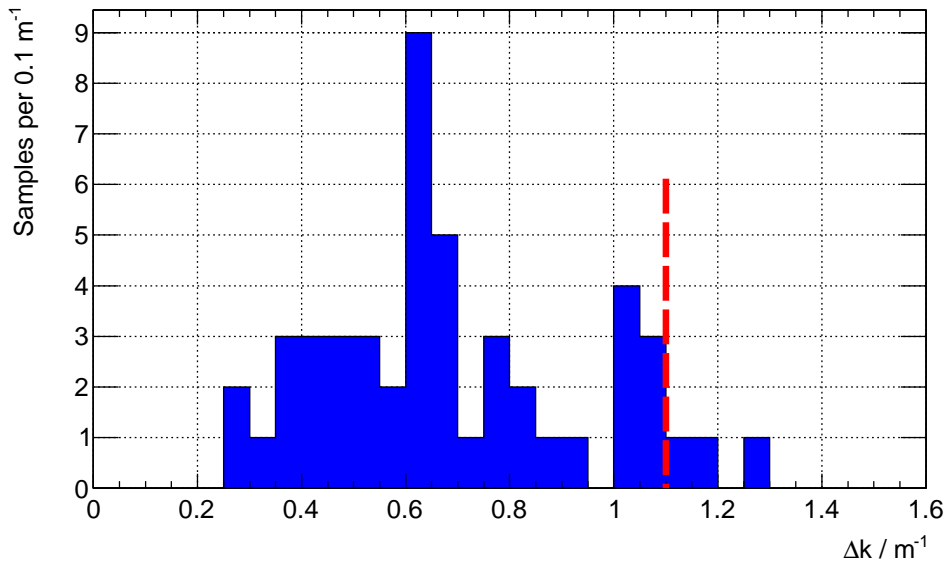
Figure 2.35: Δk distribution of SICCAS crystals measured in Gießen.

Chapter 3

Beamtimes with PROTO60

To verify the envisaged performance, mechanical stability and the thermal robustness of the EMC (listed in Tab. 1.7), a first real-size prototype was build up, called PROTO60, which comes very close to the final conception. Several response measurements were carried out at MAMI[1] and CERN with photons, leptons and muons focussing on different aspects. This chapter serves as an introduction to the achieved results, presented in Sec. 4 and 5. At first, the setup of PROTO60 is presented, including geometrical arrangement and used materials for the single parts, as well as the used readout chain and the signal extraction. Furthermore, the individual test stations at MAMI and CERN will be shown with a detailed outlook on the aims for these particular runs.

3.1 PROTO60

The first real-size prototype of the future PANDA EMC is the PROTO60 and consists of 60 PWO crystals, arranged in 10 columns and 6 rows. All implemented crystals have type 6 geometry (compare Tab. 2.2), which corresponds to a polar angle of roughly $45°$ ($135°$) in the barrel region. The barrel part represented by the PROTO60 is marked in red in Fig. 3.1, with the small difference, that the PROTO60 has 6 rows with the same geometry. This is not true for the final EMC, since maximum 4 rows with the same shape are grouped together. In the following subsections different aspects of the construction of this prototype are discussed in more detail, ranging from the mechanical structure up to the realised data acquisition (based on [34]).

---

[1]Mainzer Mikrotron
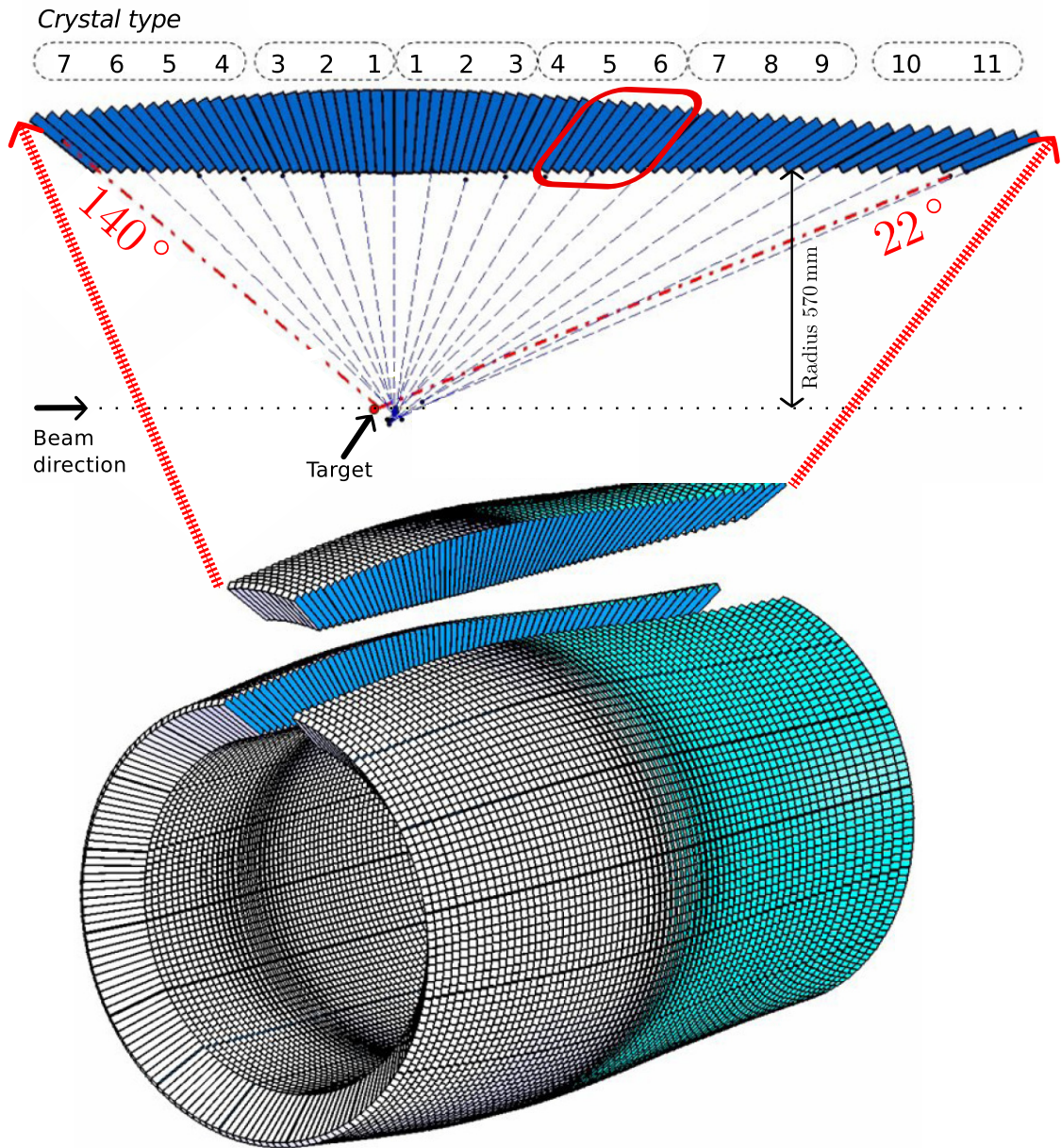
Figure 3.1: The barrel part covers the polar angle region from $22°$ to $140°$ and consists of 16 slices. Each slice is composed of 710 crystals, arranged in a 10×71 matrix. The long axis of one slice is divided in 6 subgroups, indicated with dashed rounded rectangles, containing crystal types with appropriate tapering. In order to minimise energy deposition in dead material, all crystals are pointing off the vertex point by about $4°$, which is also true for the azimuthal direction. The part of the slice framed in red in the upper part of the picture is represented by the PROTO60.

3.1.1 Mechanical Structure

At first, a single crystal has to be wrapped properly with a foil in order to optimise the light collection in it and to avoid optical cross talk. In case of PANDA, VM2000 (also known as ESR[2]-film) was chosen, which is quite mirror-like with a reflection coefficient at 440 nm of 0.944 and a thickness of 65 μm [35]. Moreover, VM2000 is non-metallic and basically a multilayer polymer. Altogether, the crystals including geometrical uncertainties and wrapping have to fit into carbon alveoles. Fig. 3.2 illustrates the expected occupied space between two crystals.

Figure 3.2: Each crystal has a geometrical tolerance of $+0/-100\,\mu$m. The gap of 150 μm considers mechanical tolerances (50 μm) and deformation of the alveoles (100 μm). Altogether the distance between the borders of two neighbouring crystals is in the order of 680 μm [34].

After wrapping, the back side of a crystal is outfitted with an LAAPD. The coupling between crystal and sensor is realised by optical grease with an index of refraction close to 1.5 at 420 nm. This has the purpose to avoid an air gap, which would cause an additional reduction of the collected scintillation light. In contrast to the final envisaged rectangular shape of the LAAPD, the crystals of PROTO60 are equipped with quadratic LAAPDs with an effective area of 1 cm². Furthermore, the LAAPDs are fixed in central position by black capsules made of plastic. For the connection to the preamplifiers, shielded twisted pair wires are fed through an opening of the capsules. Two pairs of left and right crystals are grouped to a subunit of four crystals (Fig. 3.3a), which is subsequently placed into the carbon alveoles including aluminium inserts Fig. 3.3b.

The aluminium inserts are mandatory for the mechanical stability of the prototype. They are glued to the alveoles and have to carry the weight of the 6×10 matrix of crystals with ~ 1 kg each. Moreover, the aluminium structure integrates the cooling system, the electronics and the possibility of a monitoring system to control the properties of the PWO crystals by constant light pulses fed in via optical fibres. All the

---

[2]<u>E</u>nhanced <u>S</u>pecular <u>R</u>eflector
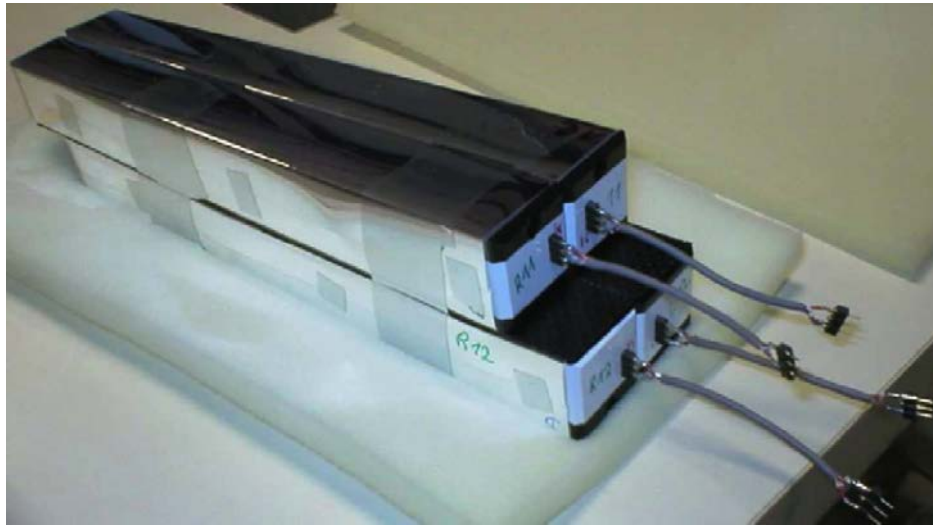
(a)
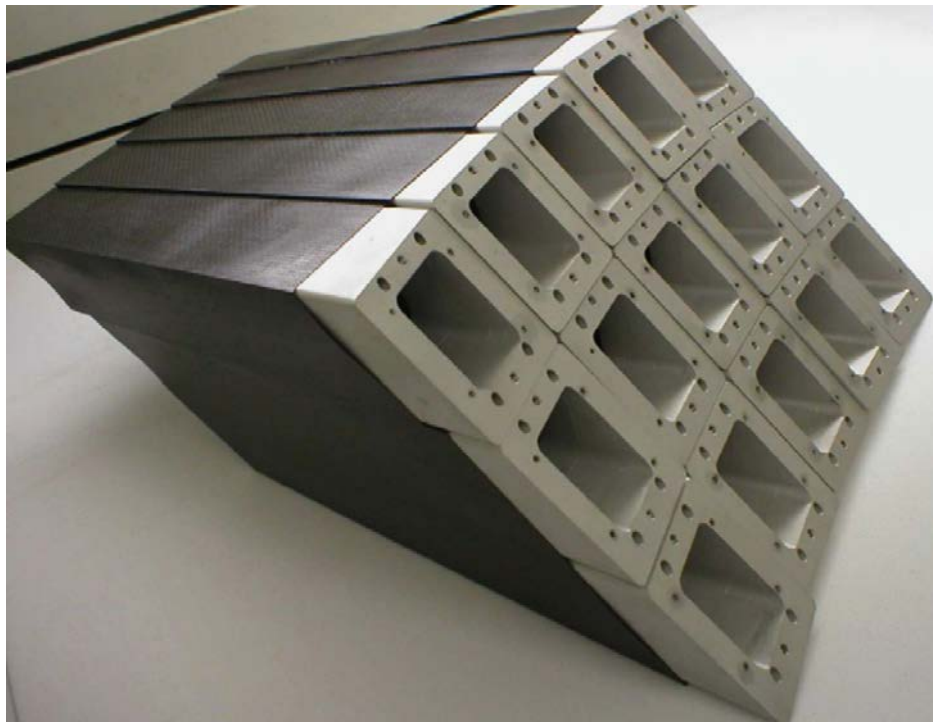
(b)

Figure 3.3: (a) A packed subgroup of four crystals including wrapping, photo sensor plus capsule and connection to the outside. (b) Carbon alveole assembly with aluminium inserts for mounting and holding the packs of crystals in Fig. 3.3a.

mentioned elements are mounted on a support frame, which simplifies the transportation to various test experiments. In addition, the whole prototype including support structure can be placed on a so called $x - y$-table for a two-dimensional alignment relative to the impinging beam.

3.1.2 Cooling and Electronics

As it was mentioned in Sec. 1.3, the whole calorimeter will be cooled down to a temperature of $-25\,°\text{C}$. Therefore, also the prototype has to be cooled to come as close as possible to the final condition in order to gain experiences with cooling stability and the actual performance. The cooling itself is realised by a chiller[3] for achieving the required thermal power of $80\,\text{W}$. The chiller recirculates the cooling fluid, which flows in copper serpentine through the prototype. The whole prototype, except the front part, is thermally insulated with a $4\,\text{cm}$ thick styrene foam layer and in addition surrounded with a gas-tight plastic skin to avoid ice formation (compare Fig. 3.4). The front part of the prototype is enclosed vacuum tight by a prototype insulation panel, composed of a sandwich-like structure of two skins of aluminium and one carbon-fibre layer. The applied vacuum of $\sim 2 \cdot 10^{-2}\,\text{mbar}$ within this structure has a conduction coefficient of lower than $2 \cdot 10^{-2}\,\frac{\text{mW}}{\text{mK}}$ and allows a reduction of the insulation from $4\,\text{cm}$ to $2\,\text{cm}$. A set of 13 thermocouple elements controls and records the temperature at different selected positions within the prototype. It is verified that the temperature variation of the crystals stays within $\pm 0.05\,°\text{C}$.

Each crystal of the PROTO60 is equipped with one quadratic LAAPD of type S8664-1010SPL. The technical data for this type of photo sensor is given in Tab. 3.1.

Parameter	
effective area	$100\,\text{mm}^2$
spectral response range	$320 - 1000\,\text{nm}$
QE at $420\,\text{nm}$	$70\,\%$
capacitance	$270\,\text{pF}$
maximum gain	~ 500
operating voltage	$\sim 350\,\text{V}$

Table 3.1: LAAPD properties in PROTO60 [36].

The signals from the LAAPDs are forwarded to the LNP-P type preamplifiers (compare Sec. 1.3.5.2), where four items are grouped together on one PCB[4] and screwed

---

[3]supplied by *Julabo*
[4]Printed Circuit Board

on the inserts. Supply voltage for photo sensors and preamplifiers, as well as signal lines, are provided by additional back-PCBs, which traverse the transition of cold and warm volume via narrow slights.
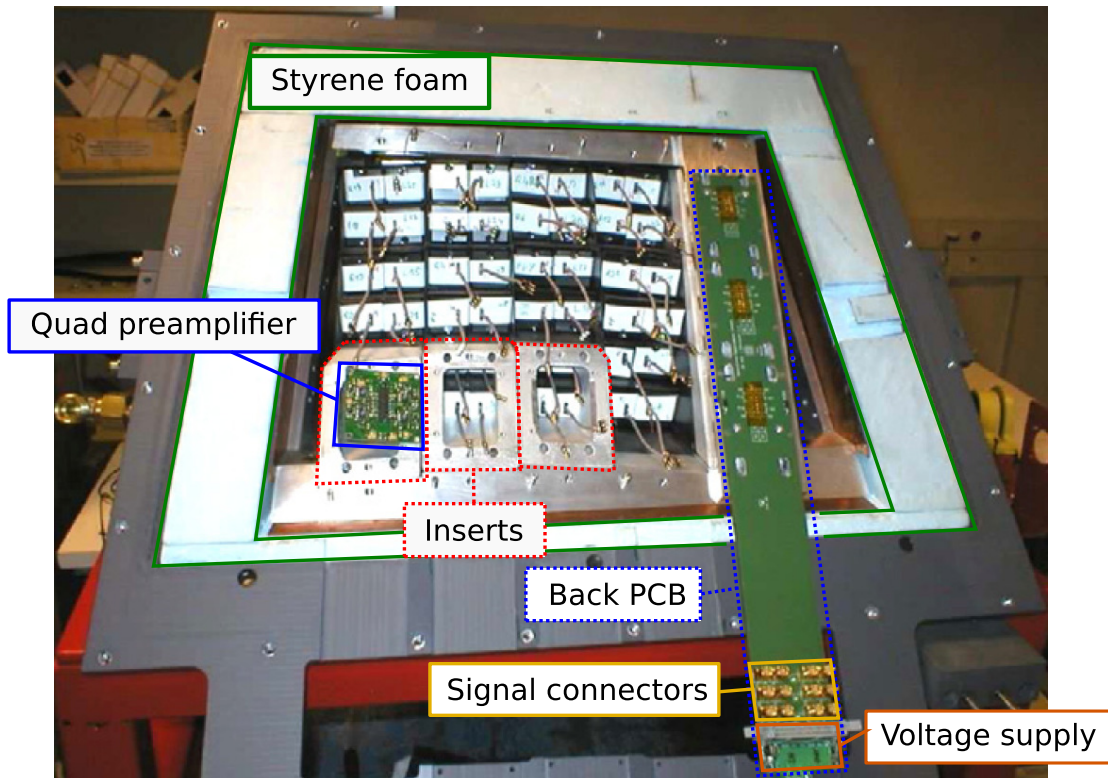
Figure 3.4: Back view of PROTO60 with all mounted crystals and some partially mounted components marked and labelled with corresponding colours. Two columns of the PROTO60 comprising 12 crystals are covered by one back-PCB.

3.1.3 Readout and Data Acquisition

The intention of this subsection is to illustrate the path of the obtained primary signal of the photo sensor to the digitisation. In all beamtimes, performed at MAMI and CERN, the readout chain was slightly modified due to trigger aspects and the digitisation procedure and will be discussed in more detail. At first, the scintillation light of the PWO is converted by the LAAPD to a charge pulse and subsequently amplified by one of the LNP-P preamplifier. For the beamtime at MAMI, the subsequent processing of the signals is displayed in Fig. 3.5 and the used components are listed

in Tab. 3.2.
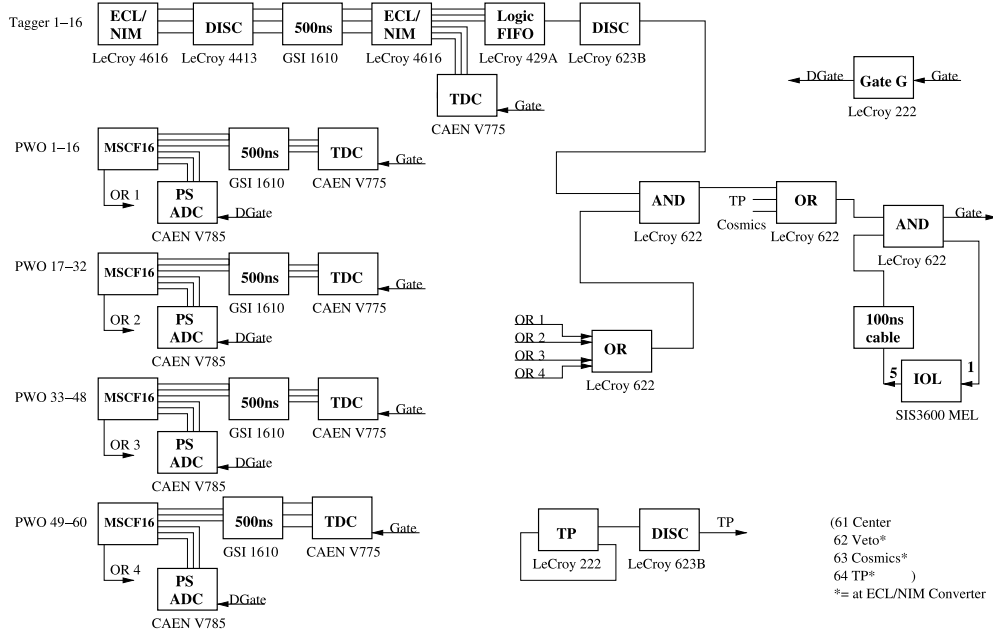
Figure 3.5: Readout chain PROTO60 at Mainz in 2010.

Each crystal of the PROTO60 is equipped with one quadratic LAAPD of type S8664-1010SPL. The technical data for this type of photo sensor is given in Tab. 3.1. The individual signals of crystal and LAAPD are amplified, shaped and discriminated by an spectroscopy amplifier (MSCF16). The shaped and amplified trace output is processed by PS-ADCs[5], where the amplitude is determined and digitised for the energy information. The time stamp is obtained by an internal CFD[6] of the spectroscopy amplifier and is digitised by TDCs. Furthermore, a binary trigger signal is provided, which is in principle created by an OR of all crystals and contributes to the final coincidence condition (beamtime Mainz 2010). An overview of the trigger conditions for all beamtimes, obtained by the detectors, is provided in Tab. 3.3. The second branch for the coincidence originates from the tagger, which delivers a logical OR of the responding tagger channels. Moreover, a time stamp is digitised and recorded by means of a TDC. Functionality and setup of the tagger is described in Sec. 3.2.1. After the AND of the coincidence requirement, an additional OR module allows the plug in of a pulser for test purposes or further detectors for calibration purposes, e.g. via cosmic radiation. If the combined logical signal is true, a fixed time gate for the

---

[5]Peak Sensing - Analogue to Digital Converters
[6]Constant-Fraction Discriminator

Component	Quantity	Type
ECL/NIM	4	LeCroy 4616
FAN IN / FAN OUT	2	LeCroy 429A
Dual Gate Generator	1	LeCroy 222
Octal Discriminator	1	LeCroy 623B
Quad Coincidence Unit	1	LeCroy 622
Spectroscopy Amplifier	4	Mesytec MSCF-16
Discriminator	1	LeCroy 4413
Delay	6	GSI 1610
PS-ADC	4	CAEN V785
TDC	3	CAEN V775

Table 3.2: Components of the PROTO60 readout.

readout of the PS-ADCs and TDCs is initiated. A special IOL[7]-module blocks the readout for a certain time window and waits for the next trigger afterwards.

For the CERN beamtime in 2011, the existing readout chain was significantly modified. The trigger was provided by an external detector, which is shown in Sec. 3.2.2. TDCs and PS-ADCs were exchanged with a 16-bit SADCs (SIS3302) supplied by *Struck*. In contrast to the PS-ADCs, a SADCs records the response for a predefined time window. The converting of the stored SADC signals (or the so called traces) for obtaining time and energy information is explained in 3.1.4. In the mode used for this SADC, the input range is in the order of $5\,\mathrm{V}$, for signals arriving from the preamplifier. The sampling rate was chosen to $50\,\mathrm{MHz}$, which corresponds to a time fragmentation of $20\,\mathrm{ns}$ and is proven to be sufficient for achieving the required time resolution.

3.1.4 Signal Treatment of SADC data

In the final stage of the readout chain for the PANDA EMC, the digitised signals from the ADCs[8] will be processed by FPGAs[9], for the extraction of time and energy information. This has to be realised by a fast and robust algorithm, the so called feature-extraction algorithm. Fig. 3.6 explains schematically the path from the raw data, obtained by the LNP-P preamplifier, to the relevant observables energy and time.

For test purposes, the data from the SADC was stored and analysed offline with an implementation of the mentioned algorithm via software. The following shows the

---

[7]Input Output Logic

[8]Analogue to Digital Converters

[9]Field Programmable Gate Arrayss
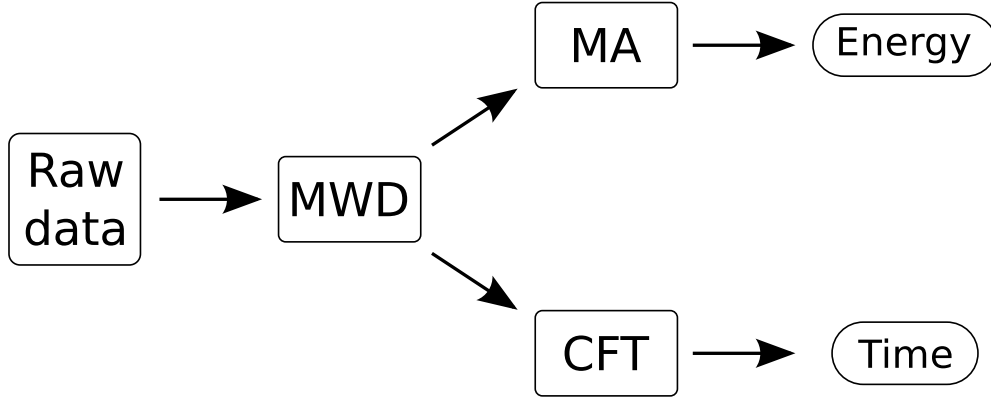
Figure 3.6: Schematic explanation of feature extraction. After the MWD-step the obtained trace is modified for extracting the energy and time separately.

single steps and how the relevant information is extracted. The chosen values for the input parameters of M, τ, L, D and R for this algorithm are based on [37] and will be explained in the relevant sections of the algorithm.

The signal of a crystal for one event is displayed exemplary in Fig. 3.7 and consists of 250 time bins with a single width of 20 ns. Due to the relatively long decay time of the LNP-P preamplifier signal in the order of $\sim 25\,\mu$s, it has to be shaped to reduce the pile-up probability of signals occurring in a short time sequence. This is done by the first step of the feature extraction algorithm, which is called MWD[10] and can be determined by Eq. 3.1, in which $x(n)$ is the bin content of channel n and $x_{\mathrm{MWD}}(n)$ the output of the MWD-step for channel n. M defines the final length of the output pulse and should be larger than the rising part of the raw signal. This was chosen to 20 corresponding to 400 ns. τ is the decay constant of the LNP-P preamplifier signal and has a value of $1,250$ channels ($25\,\mu$s).

$$x_{\mathrm{MWD}}(n) = x(n) - x(n - M) + \frac{\ln(2)}{\tau} \sum_{i=n-M}^{n-1} x(i) \tag{3.1}$$

Fig. 3.8 shows a comparison of the same data like in 3.7, before and after applying the MWD-step.

The obtained trace, shown in Fig. 3.8b, is the initial point for the next iterations of the feature extraction. The next step, called MA[11], is responsible for reducing the noise level with the smoothing length L. For each channel with the index n, the new content is calculated by summing up the channels ranging from $n - L$ to n:

$$x_{\mathrm{MA}}(n) = \sum_{i=n-L}^{n} x_{\mathrm{MWD}}(i). \tag{3.2}$$

---

[10]Moving Window Deconvolution
[11]Moving Average
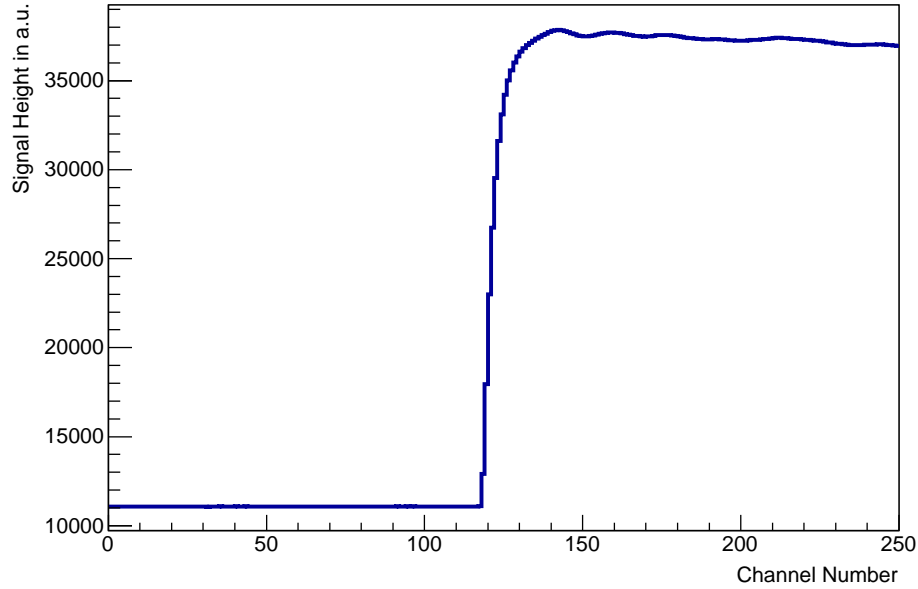
Figure 3.7: Raw data of an SADC for a randomly chosen crystal with a high
energy deposition of 10 GeV via positrons. The shown data corresponds to the
direct output of the LNP-P preamplifier. The supply voltage of the LAAPD was
adjusted in such a way that the highest signals to be expected signals fit into the
dynamic range of the SADC of 40,000. Each channel on the horizontal axis has
a size of 20 ns, which results in an overall time window of 5 μs.

(a)   (b)
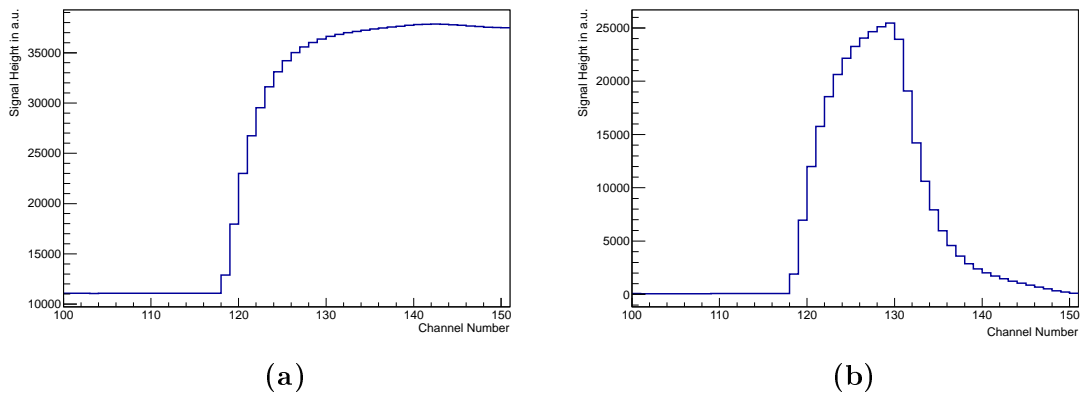
Figure 3.8: Visualisation of the MWD-step for a zoomed region of the SADC. (a)
Unshaped output signal of the LNP-P preamplifier. (b) Shaped output signal of
the LNP-P preamplifier according to Eq. 3.1.

Only for low energetic signals, with a small signal to noise ratio, the MA-step becomes mandatory. For a high-energetic signal the actual shape stays almost identical (compare 3.8b and fig:masignal), except the amplitude.

The maximum amplitude of Fig. 3.9, which linearly scales with the detected energy,
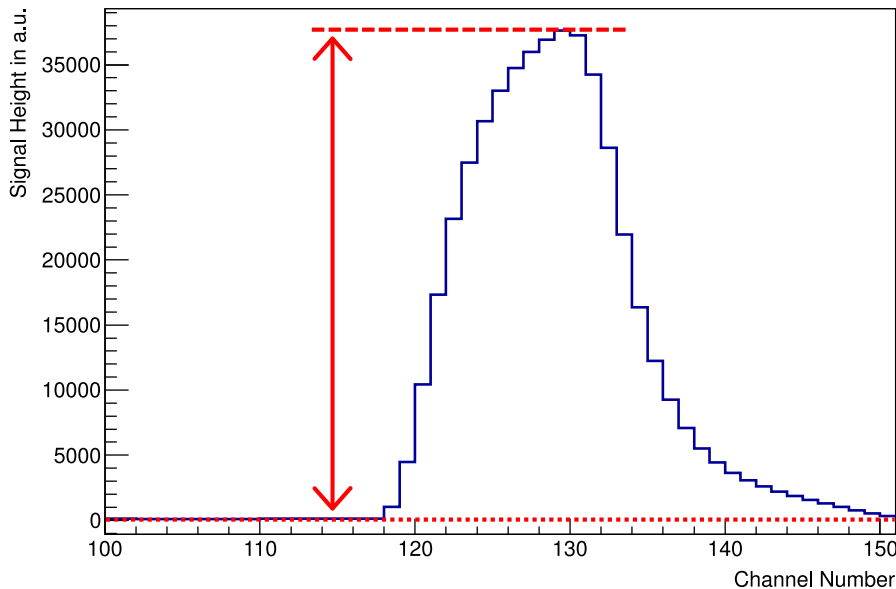
Figure 3.9: Shaped and smoothed signal of the LNP-P preamplifier. The baseline, which is represented by the dotted red line in the bottom part of the figure, is determined by averaging the channels in the range from 40 to 100. The solid line stands for the determined maximum amplitude of the signal and is subsequently used as energy information.

is finally determined with a simple software algorithm. For Fig. 3.9, the obtained amplitude with respect to the baseline is in the order of $\sim 38,000$ a.u.. For getting a statement of the corresponding energy in terms of eV, the amplitude has to be calibrated (compare Sec. 4.1).

For getting a time information of the single event, the data of Fig. 3.8b has to be treated in a different way, independently from the MA-step. Therefore, the basic functionality of a conventional CFD-module is simulated by the CFT[12]-step (Eq. 3.3). The signal out of the MWD-step is delayed by $D = 5$ channels $= 100$ ns, scaled by a certain factor R and subtracted from the original signal. It turned out, that $R = 0.45$ is an optimal value [34].

$$x_{\mathrm{CFT}}(n) = x_{\mathrm{MWD}}(n - D) - R \cdot x_{\mathrm{MWD}}(n) \tag{3.3}$$

---

[12]Constant-Fraction Timing

After the CFT-step, a small number of points are extrapolated with a linear function to determine the zero-crossing. This method allows a timing information in sub-channel region. The final data for the determination of time, including the mentioned linear fit, is shown in Fig. 3.10.
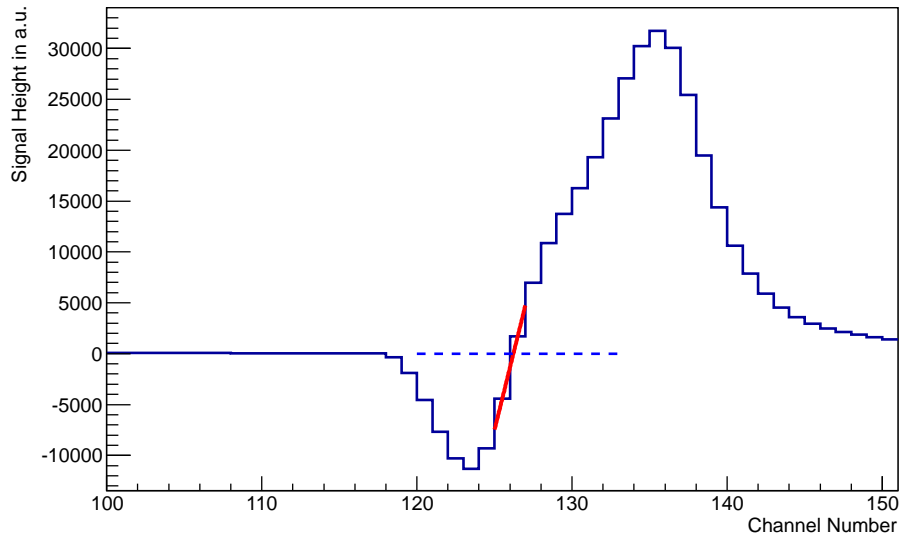
Figure 3.10: Determination of the time information out of the obtained data after CFT-step. At first the baseline level, which is represented by the dashed blue line, is determined by averaging the channels from 40 to 100. The solid red line is an extrapolation of one bin below and one above the baseline. The horizontal coordinate of the intercept point is finally used as time information.

3.2 Experimental Setups

Altogether, three beamtimes were performed, for testing different aspects of the PROTO60 at the lowest and highest envisaged energies of PANDA. The main intention was to test the performances of the prototype under the different aspects listed in Tab. 1.7. The obtained results still slow options for future improvements. A replacement, like e.g. of the present preamplifier modules with the designed ASIC, which will cover two different dynamic ranges simultaneously, promises better results. Moreover, an additional LAAPD per crystal will collect twice as much scintillation light, compared to a single photo sensor. This will result in an improvement of up to $\sqrt{2}$ of the energy resolution. Another essential modification will be the replacement of the digitisation modules with SADCs, which was done for the beamtime at the CERN-SPS[13] (compare Sec. 3.2.2). Here a significant change of the obtained time resolution is expected and will be discussed in Sec. 4.

Tab. 3.3 summarises the benchmark parameters for all beamtime tests. Moreover, a detailed description of the used setups at MAMI and CERN-SPS, comprising detector arrangement and additional necessary modules, is given in the following of this subsection..

Beamtime	Beam type	Energy range	Trigger condition	Digitisation module
MAMI 2009	γ	$150 - 1,500\,\mathrm{MeV}$	Tagger AND Central crystal	PS-ADC (CAEN V785)
MAMI 2010	γ	$50 - 690\,\mathrm{MeV}$	Tagger AND OR of all crystals	PS-ADC (CAEN V785)
CERN-SPS 2011	e^+	$15\,\mathrm{GeV}$	Plastic detector	SADC (SIS3302)

Table 3.3: PROTO60 beamtimes with beamtype and energy range. A PS-ADC is responsible for obtaining the energy information for both MAMI beamtimes, whereas out of the digitised SADC-data energy and time can be determined.

---

[13]$\underline{S}$uper $\underline{P}$roton $\underline{S}$ynchrotron

3.2.1 MAMI

In 2009 and 2010, the first two beamtime tests were carried out at the A2 experimental hall in the Institut für Kernphysik of the Johannes Gutenberg University in Mainz, Germany. An energy tagged bremsstrahlung photon beam is produced by the MAMI electron accelerator, in combination with the Glasgow Tagged Photon Spectrometer (Tagger). Both constituents will be discussed in the following and can be found on the floor plan of the facility (Fig. 3.11). Basically, the MAMI facility consists of an
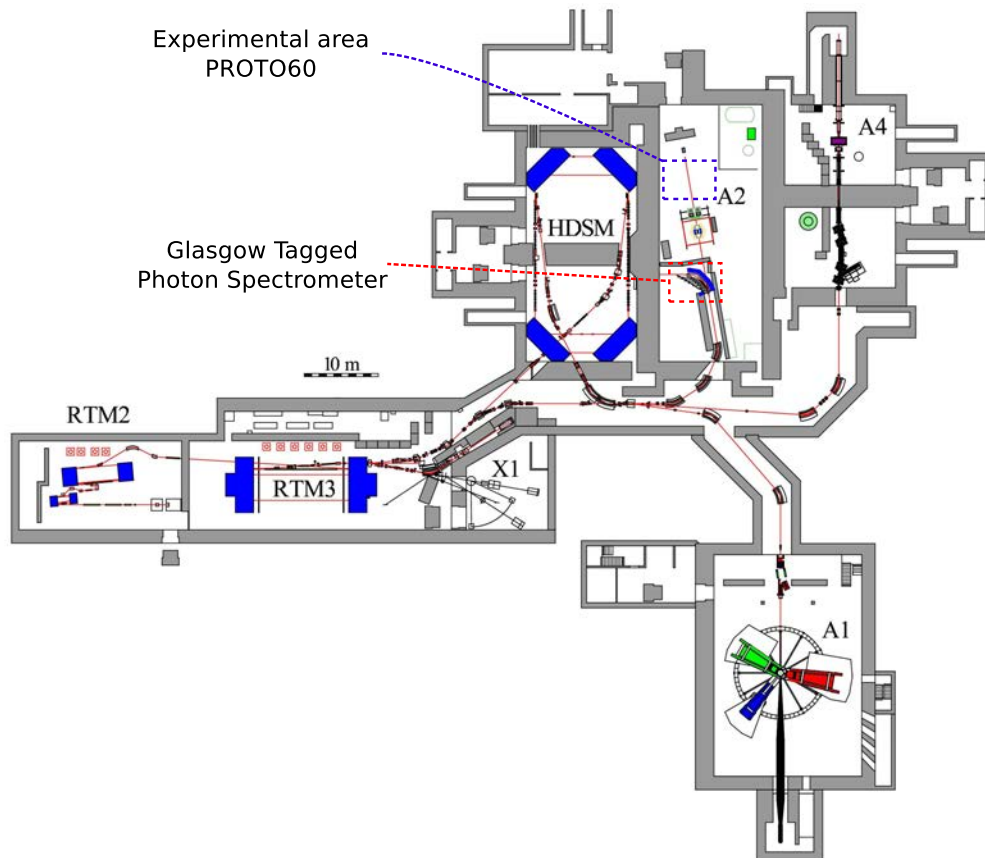
Figure 3.11: Floor plan of the MAMI accelerator facility at Mainz comprising the experimental halls A1, A2, A3 and X1. The position of the PROTO60 for both beamtimes and the Tagger system are marked.

injector LINAC[14] and three RTMs[15], providing electron beams of $100\,\mu A$ up to an energy of $1.5\,GeV$ since 1991. At first, the LINAC supplies electrons with an energy of $3.97\,MeV$ which are accelerated stepwise by the single RTMs, according to Tab.

---

[14]Linear Accelerator
[15]Race Track Microtrons

3.4. In 2006, an upgrade of the existing facility was realised by a fourth stage of the accelerator structure, the HDSM[16]. Thus, energies up to 1.5 GeV became available. MAMI supplies continuous electron beams of the experimental halls (A1, A2, A4, X1), situated at the research facility in Fig. 3.11.

3.2.1.1 RTMs and HDSM

The MAMI acceleration facility comprises three RTMs with a similar functionality. Fig. 3.12 shows the basic setup of a RTM. An electron beam with a certain energy is injected and recirculates several times through the RTM. In each cycle, the beam passes RF[17]-cavities, in which the energy is increased stepwise by ΔE. Here the difference in time between each recirculation loop has to be an exact integer multiple of the period of the RF supply. In Fig. 3.12 the grey coloured areas correspond to a constant magnetic field ($\Delta B/B \leq 10^{-4}$) for bending the beam back to the RTM. Due
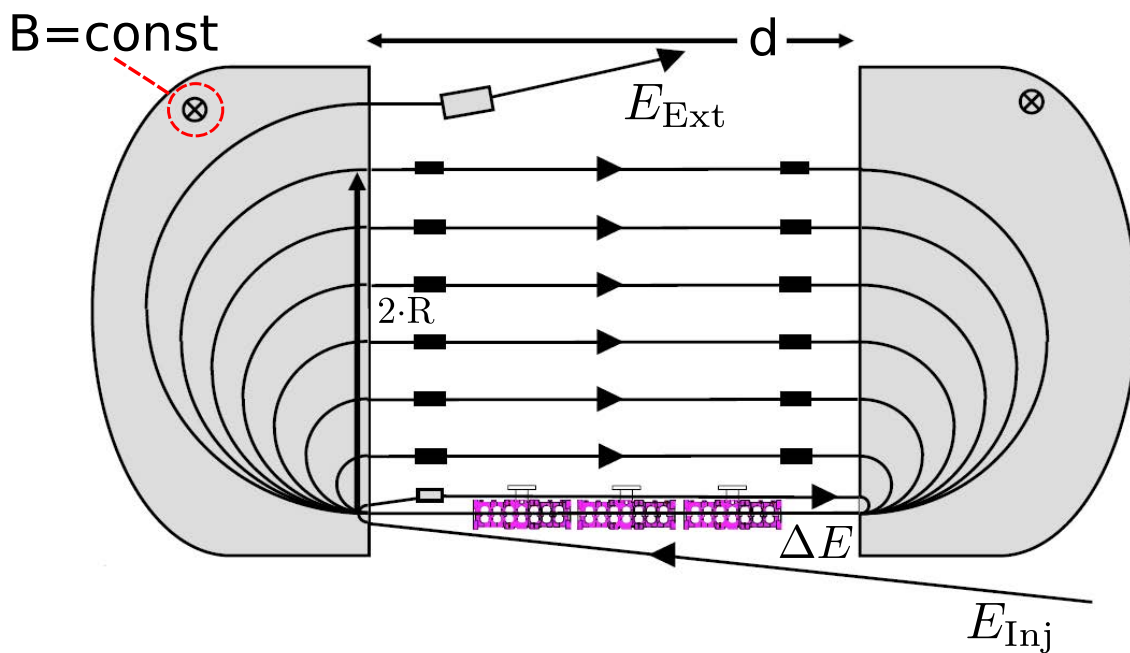
Figure 3.12: General layout of a RTM. The electron beam enters the RTM with an energy E_{Inj} and leaves it after N cycles with E_{Ext}. In each cycle, the energy gain is ΔE, while passing the cavities.

to the unchanged magnetic field B the bending radius R of the beam with velocity

---

[16]<u>H</u>armonic <u>D</u>ouble-<u>S</u>ided <u>M</u>icrotron
[17]<u>R</u>adio <u>F</u>requency

$\beta = v/c \approx 1$ increases linearly with the energy E, according:.

$$R = \frac{\beta \cdot E}{e \cdot c \cdot B}.$$ (3.4)

The provided beam shows a very small spread in energy, due to an automatic phase correction. If an electron in a certain cycle has a larger energy than desired, the path in the bending sections will be larger and the electron arrives later in the acceleration section. Therefore the particle is under-accelerated in the next cycle or, in case of an earlier arrival, over-accelerated. This technique achieves an energy spread after the third RTM of FWHM $\approx 30\,\text{keV}$.

After a fixed amount of N cycles within an RTM, the beam is extracted by a 'kicker' magnet with an energy of

$$E_{\text{Ext}} = E_{\text{Inj}} + N \cdot \Delta E.$$ (3.5)

Tab. 3.4 summarises the main parameters of the injector LINAC, the RTMs and the HDSM.

Parameter	Unit	Injector LINAC	RTM 1	RTM 2	RTM 3	HDSM
E_{Inj}	MeV	-	3.97	14.86	180	855
E_{Ext}	MeV	3.97	14.86	180	855	1.500
magnetic field	T	-	0.103	0.555	1.284	$1.53 - 0.95$
number of turns	-	-	18	51	90	43
energy gain per turn	MeV	-	0.60	3.24	7.50	$16.58 - 13.66$
LINAC length	m	4.93	0.80	3.55	8.87	8.6 and 10.1
total power consumption	kW	92	92	220	650	1400

Table 3.4: General parameters of the injector LINAC, RTM and HDSM.

The HDSM is the last section of the acceleration structure at MAMI, which was finalised in 2006. The schematic setup, including acceleration-, focussing- and bending sections, is shown in Fig. 3.13. This upgrade allows an increase of the electron energy up to 1.5 GeV. Two straight LINAC sections accelerate the beam stepwise to the final energy, whereas four 250 t dipole magnets bend the beam by $\sim 90\,°$. After 43 turns within the HDSM, the beam is extracted to the experimental areas.
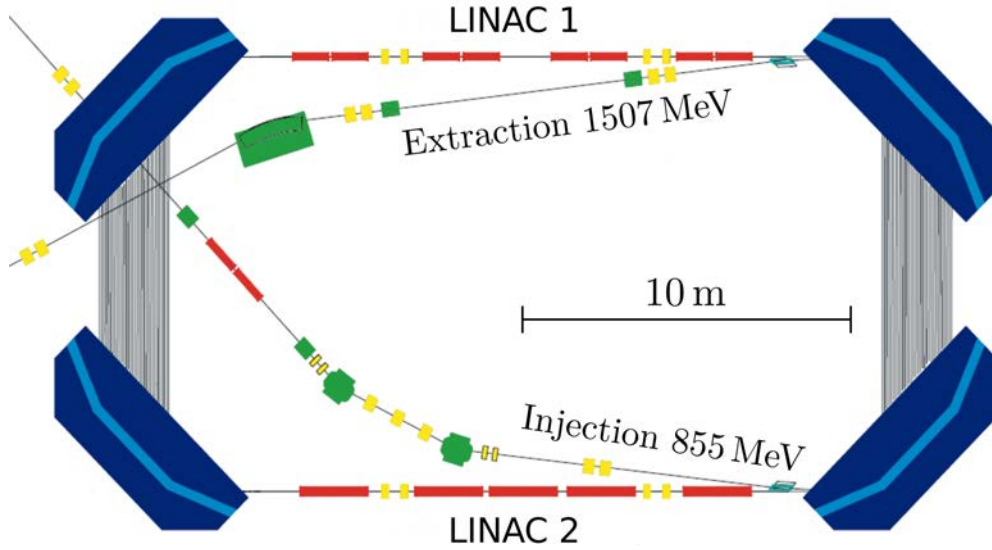
Figure 3.13: Schematic layout of the HDSM. Four dipole magnets bend the beam about 90°, whereas two LINACs are responsible for the stepwise acceleration.

3.2.1.2 The Glasgow Photon Tagging Spectrometer

The tagging system of the MAMI acceleration facility (Fig. 3.14) converts the electron beam into a continuous and collimated photon beam [38]. The electrons with energies of up to 1.5 GeV impinge on an exchangeable radiator made out of copper or diamond for the production of bremsstrahlung photons, according to the process explained in Sec. 1.3.1.1. The electrons are subsequently bent by a magnetic field of a dipole magnet with a flux of $B = 1.8\,\mathrm{T}$ and detected in the focal plane, which basically consists of 353 overlapping plastic detectors. The higher the bending radius of the electrons, the lower is the energy of the created photon. With the knowledge of the initial energy E_0 and the bending radius r of the electrons in the dipole magnet, the energy of the resulting photon beam is determined due to energy conservation:

$$E_\gamma = E_0 - E_{e^-} \tag{3.6}$$
$$\text{with } E_{e^-} = \sqrt{(qBcr)^2 + (m_0 c^2)^2} \sim r,$$

where q and m_0 is the charge and the mass at rest of an electron, respectively, and c the speed of light. The energy range of the tagging system depends on the maximum operating energy of the accelerator. If the HDSM is included, energy marked photons up to 1.5 GeV are available with an accuracy of 4 MeV. In the low energy region up to 820 MeV, the error bars of the tagger are reduce to 2 MeV depending on the momentum range of the individual plastic scintillator covering the focal plane. The readout of the focal plane detectors is done by conventional *Hamamatsu* PMTs, within the stray field ($\sim 0.01\,\mathrm{T}$) of the dipole magnet. The obtained signal is discriminated

and serves as trigger input (compare Tab. 3.3) and is digitised by TDCs.
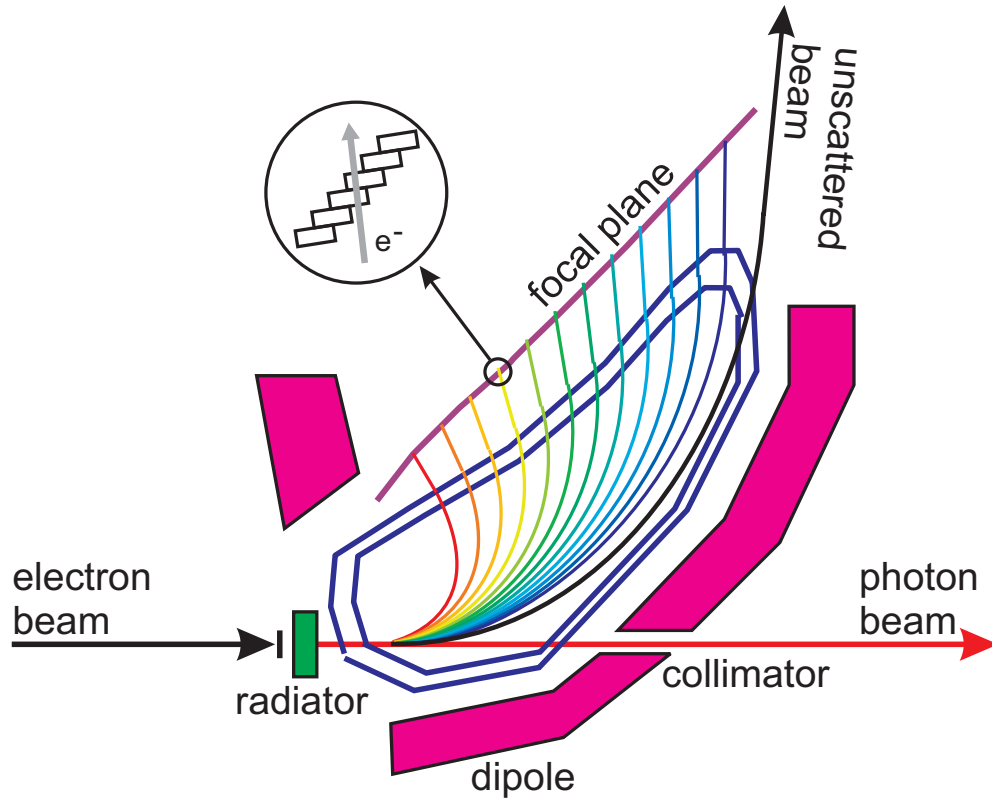
Figure 3.14: Photon tagging spectrometer at Mainz [39].

Furthermore, the covered solid angle of the photon beam was determined by a lead collimator with a diameter of 1.5 mm located 2.5 m apart from the radiator (compare Fig. 3.15a). Under geometrical considerations, this leads to an opening angle of 0.0172° for the photon beam and therefore to an upper limit of the diameter for the impinging beam on the PROTO60 of 9.3 mm.

3.2.1.3 Beamtimes in 2009 and 2010

The schematic setup of the PROTO60, relative to the beam, is shown in Fig. 3.15a, whereas the prototype was placed on the so called $x - y$-table for a movement perpendicular to the beam line. Moreover, a photograph of the setup with all necessary devices is shown in 3.15b. The marked plastic detector in front of the PROTO60 was used for identifying leptons, caused by pair production in the air or solid material in between. The plastic detectors above and below the prototype were used for calibration purposes, which is further discussed in Sec. 4.1.

In both beamtimes at the MAMI accelerator facility, 16 photon energy channels of the tagging system were selected via software, summarised in Tab. 3.5). For the

TDC Channel	Beamtimes at MAMI Photon Energy in MeV	
	2009	2010
1	1441.06	685.58
2	1356.89	650.81
3	1257.31	601.77
4	1156.56	579.10
5	1057.70	509.88
6	956.16	443.77
7	857.98	387.38
8	756.58	339.67
9	657.34	269.95
10	556.97	200.35
11	456.26	152.72
12	355.88	107.98
13	256.41	93.97
14	158.31	84.67
15	-	61.54
16	187.99	52.34

Table 3.5: Selected tagger channels at both MAMI beamtimes. In 2009, one channel was broken and two channels were exchanged from the hardware point of view.

beamtime in 2009, the output of the individual detector modules was adjusted with an appropriate high voltage setting to a dynamic range of 200 MeV, except the central crystal, where the beam was impinging. Here, the direct output of the preamplifier was reduced by a passive attenuator of 15 dB, to cover the envisaged dynamic range. The assumption of the dynamic range is based on the expected energy deposition in the central crystal of $\sim 70\,\%$ of the initial energy. In 2010, with a maximum photon energy of 685 MeV, an attenuator with 6 dB was chosen. All LAAPDs were operated with estimated gain of 150. All details, concerning adjustments of the dynamic range and noise levels of the three beamtimes, are listed in Tab. 4.1 in Sec. 4.
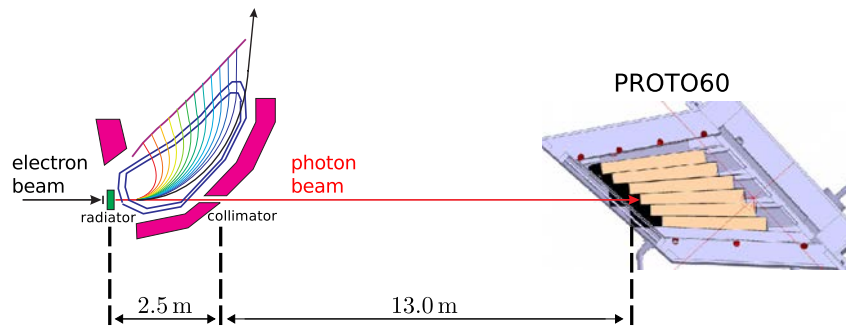
(a) Schematic setup of the PROTO60 at the MAMI beamtimes.
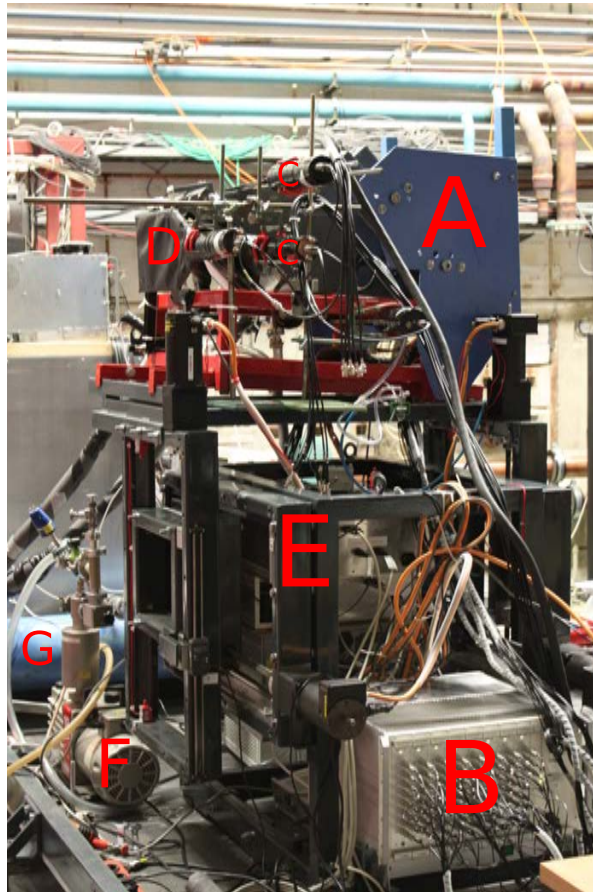
(b) Photograph of the PROTO60 setup at Mainz. A: PROTO60, B: HV-supply, C: Plastic, D: Plastic detector for identifying converted photons, E: $x - y$-table, F: Vacuum pump, G: Nitrogen supply.

Figure 3.15: PROTO60 setup at MAMI beamtimes.

3.2.2 CERN-SPS

The latest test beamtime of the PROTO60 was performed at the SPS of the CERN accelerator complex (compare Fig. 3.16). This accelerator is able to handle many different kinds of particles, like e.g. positrons, electrons, protons and antiprotons with energies up to $450\,\mathrm{GeV}$ partly as secondary beams. It has a circumference of $7\,\mathrm{km}$ and serves as an input stage for the LHC. Furthermore, the stored beam at the SPS can be provided to a separated experimental area (called North Area), which is designated for different experimental purposes of external users. In case of the PROTO60, the test beamtime was carried out with a $15\,\mathrm{GeV}/c$ positron and a $150\,\mathrm{GeV}/c$ muon beam. For the production of the beam, different scenarios can be chosen, depending on the type of necessary particles. For the bunched positron beam, the output of the SPS was used and additionally collimated to an estimated momentum spread of $\Delta p/p \approx 0.7\,\%$. In case of the muon beam for calibration purposes, a high energetic proton beam strikes a beryllium target and produces a hotchpotch of particles. The originated charged pions decay to almost $100\,\%$ via $\pi^+ \to \mu^+\nu_\mu$ or $\pi^- \to \mu^-\bar{\nu}_\mu$, respectively. The remaining pions are absorbed by an additional beryllium absorber, whereas the μ^+ are subsequently momentum selected and accumulated.
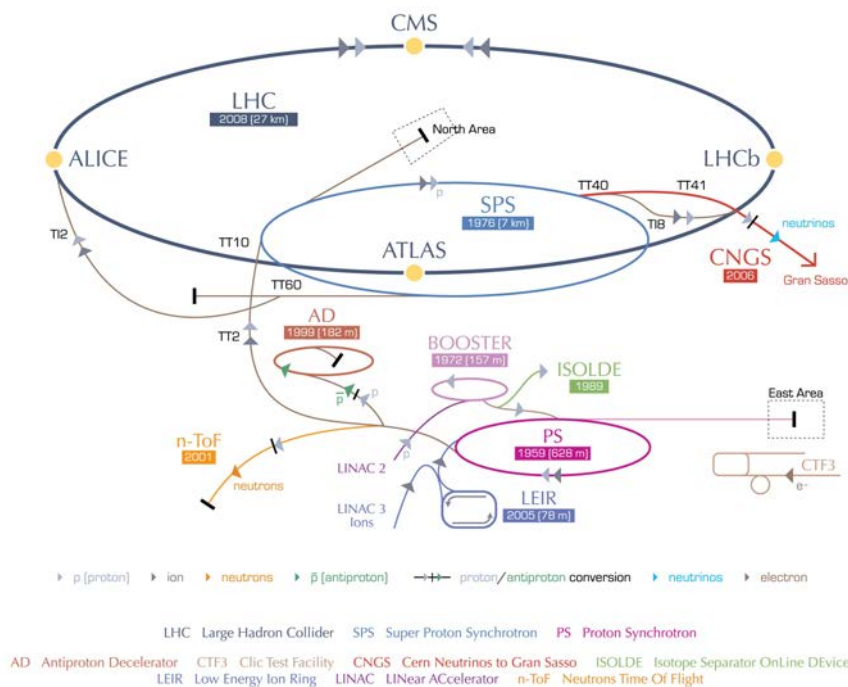
Figure 3.16: Schematic layout of the CERN accelerator complex [40]. The PROTO60 was located at the experimental area of the SPS, which is labelled here as North Area. The picture is not to scale.

3.2.2.1 Setup for Beamtime 2011

The setup of the beamtime at the SPS is illustrated in Fig. 3.17. A special feature of this setup is the ability to track charged particles, due to a prototype of the MVD detector, which is placed directly in front of the PROTO60. The purpose and basic functionality of the MVD is explained in Sec. 1.2.1. Two of these silicon based detectors provides two dimensional information for each registered particle. Both tracking detectors have a granularity of 384 stripes in x- and y-direction, with a width of $50\,\mu$m, which results in a sensitive area of $\sim 2 \times 2\,\text{cm}^2$. Thus the direct impact on the crystal matrix could be extrapolated for determining the pure position resolution of the PROTO60.
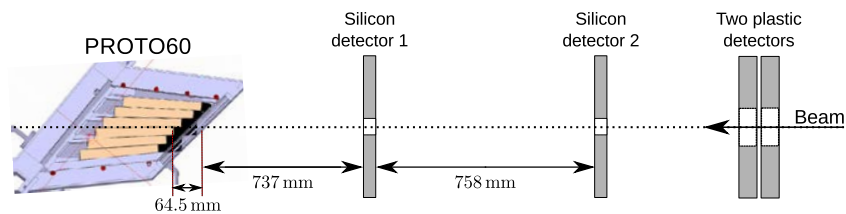
(a) Schematic setup of the PROTO60 at the CERN beamtime.
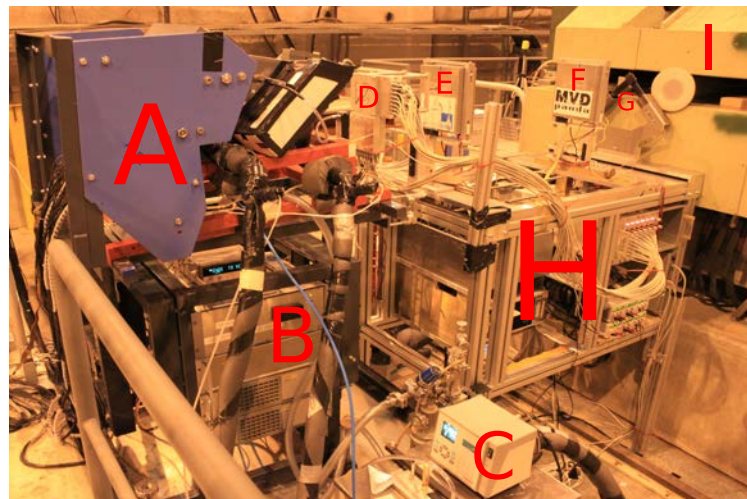
(b) Photograph of the PROTO60 beamtime at the CERN. A: PROTO60, B: $x-y$-table, C: Cooling chiller, D: Fibre cross (not used in the analysis), E: First tracking detector, F: Second tracking detector, G: Plastic cross (trigger), H: Mechanical support and readout for modules D-G, I: Goliath magnet.

Figure 3.17: PROTO60 setup at the CERN beamtime.

3.2.3 Beamtime Procedures

This subsection gives an overview of the performed program, with respect to the alignment of beam and prototype, for the three beamtimes. In the 2009 beamtime at MAMI, altogether four runs were performed with different points of impact. The main intention of this beamtime was to study the detector resolution, in which one detector is hit centrally, as well as the loss of energy information, when the beam is pointed in between two crystals and a significant energy fraction is deposited in non-sensitive material. Fig. 3.18 shows the four points of impact on a schematic crystal map of the PROTO60.
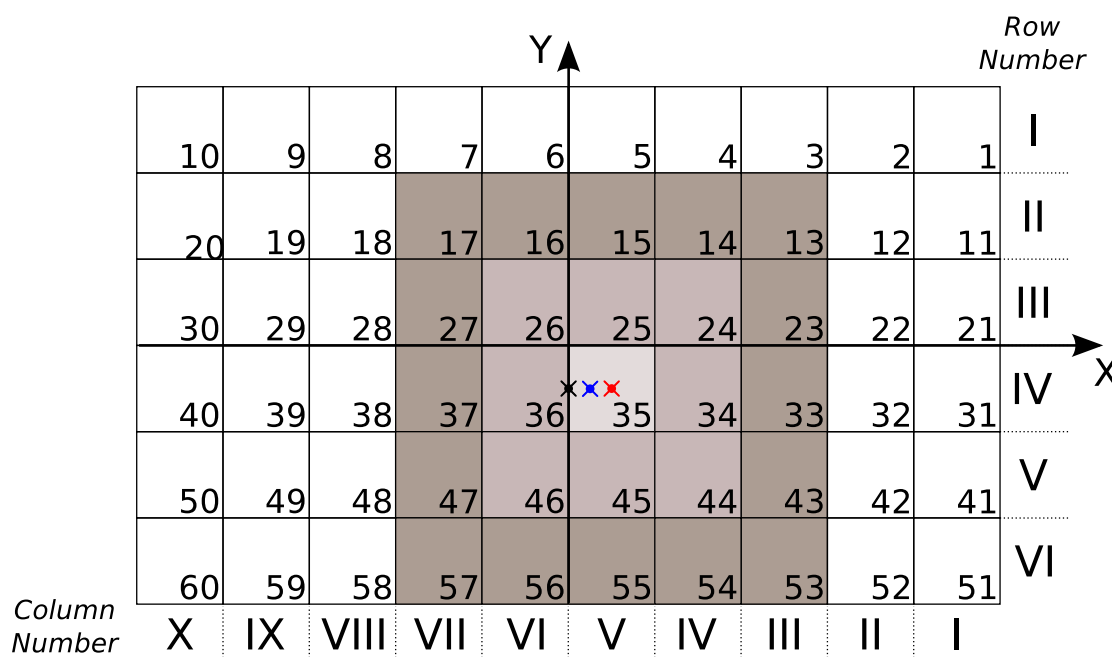
Figure 3.18: Schematic crystal map of the PROTO60 at MAMI. The figure corresponds to the point of view from the direction of the photon beam. The red cross corresponds to the point of impact of the first and fourth run in this beamtime, whereas the black one belongs to the run in which the beam hits in between two crystals. One run had the intention to fill the area in between the other ones and is marked with a blue cross. The internal PROTO60 coordinate system is indicated with a y- and x-axis and has its origin in the centre of this graphic.

In the MAMI beamtime of 2010, only the outcome of a particular run will be presented in this thesis. Here the photon beam hits centrally one crystal, which is labelled with

number 35 in Fig. 3.18.

For the CERN 2011, only 48 crystals were read out due to the limitation of SADC channels, so that both outer columns were ignored. Therefore, Fig. 3.19 shows the labelling of the used modules. Two test runs were performed shooting again into the centre of the 'old central crystal' and in between two crystals.

Figure 3.19: Schematic crystal map of the PROTO60 at CERN. Due to the different amount of read out crystals the matrix was relabelled. In the first run the positron beam was aimed to the centre of crystal 28 and in the second one between crystals 28 and 29.

Chapter 4

Time Resolution

An accurate determination of the time information of a signal is mandatory to allocate a time stamp to the registered energy signal. For the barrel part of the EMC the readout chain has to cope with interaction rates up to $100\,\mathrm{kHz}$. This chapter presents the achieved time resolutions, obtained by the PROTO60, with respect to the desired limits specified in [18]. Furthermore, the difference between the two digitisation procedures, explained in Sec. 3.1, and inhomogeneities caused by electronics will be discussed. The analysis in the following chapters was carried out with the software package ROOT[1] and is based on the programming language C++.

4.1 Energy Calibration

There are different possibilities to calibrate a detector, so that an obtained pulse height signal in terms of voltage is converted into energy. Therefore, an appropriate method has to be established in order to get a linear scaling for the envisaged energy range. An energy calibration is composed of different iterative steps, like relative and absolute calibration.

$$E_{\mathrm{cal}} = C_{\mathrm{abs}} \cdot \sum_i S_i(t) \cdot c_i \cdot E_{i/\mathrm{uncal}} \tag{4.1}$$

In a relative calibration, the signal from each crystal, which corresponds to the same energy deposition, is normalized to a reference, e.g. the signal of the central crystal via a factor c_i. Finally, the energy sum of the detector has to be calibrated to the real deposited energy with C_{abs} in order to convert the signal in terms of MeV. A time dependent factor $S_i(t)$ is introduced to take signal loss due to radiation damage into account. For beamtimes with a duration of a few days and an irradiation on a reasonably low dose level $S_i(t)$ can be assumed as constant. In this thesis, the

---

[1]http://root.cern.ch

calibration scenarios for the mentioned beamtimes are listed in the following without further discussion. Differences and inconsistencies of the listed methods and possible alternatives are discussed in detail in [41].

MAMI 2009 In the first beamtime with photon energies up to $1.5\,\text{GeV}$, the prototype was calibrated via cosmic radiation (see Fig. 4.1a). Here the muons, which are produced in the atmosphere, are assumed to be MIPs and deposit on average $10.2\,\text{MeV}$ per cm in PbWO_4. Due to the trigger condition, one can assume that the muons cross the full width of the crystals in one column and the energy deposition is almost constant. For a relative calibration, the signal of each crystal caused by cosmic radiation is divided by the response of the central crystal. An absolute calibration is achieved by setting the new peak position to the corresponding energy according to Eq. 4.2. Here an average path through a single crystal of $2.4\,\text{cm}$ was assumed. A major uncertainty for this method is the impact of the non-uniformity in light collection (explained in Sec. 2.4.3).

$$E_{\text{Channel}} = \frac{24.5\,\text{MeV}}{\text{pp}_\mu - \text{pp}_{\text{Pedestal}}} \tag{4.2}$$

$$\text{pp : peak position}$$

MAMI 2010 In 2010 an alternative calibration method was tested in addition. The prototype was turned about $90°$, so that the muons can propagate through the complete length of each crystal. This can be ensured by requiring only one responding crystal. On the one hand this method delivers a larger lever arm with a reference point of $\sim 204\,\text{MeV}$, but on the other hand this method gives an integral of the light collection efficiency. It turned out that both methods differ about $\sim 7\,\%$ due to different reasons [42]. In the frame of this thesis, the energy was calibrated like in 2009, where the PROTO60 is in horizontal position and the cosmic muons traverse perpendicular to the longitudinal crystal axis.

CERN 2011 A muon beam with a momentum of $150\,\text{GeV}/c$ was exploited to calibrate the detectors relatively to each other. For the absolute calibration several options were tested. Finally it turned out that the best reconstruction of the energy could be achieved based on a GEANT4[2] simulation. There, a $15\,\text{GeV}/c$ positron beam was simulated, which impinges on the implemented PROTO60 matrix. The obtained energy response was subsequently assigned to the energy sum of the experimental data (compare Fig. 4.1b).

---

[2]Toolkit for the simulation of the passage of particles through matter / http://geant4.cern.ch/
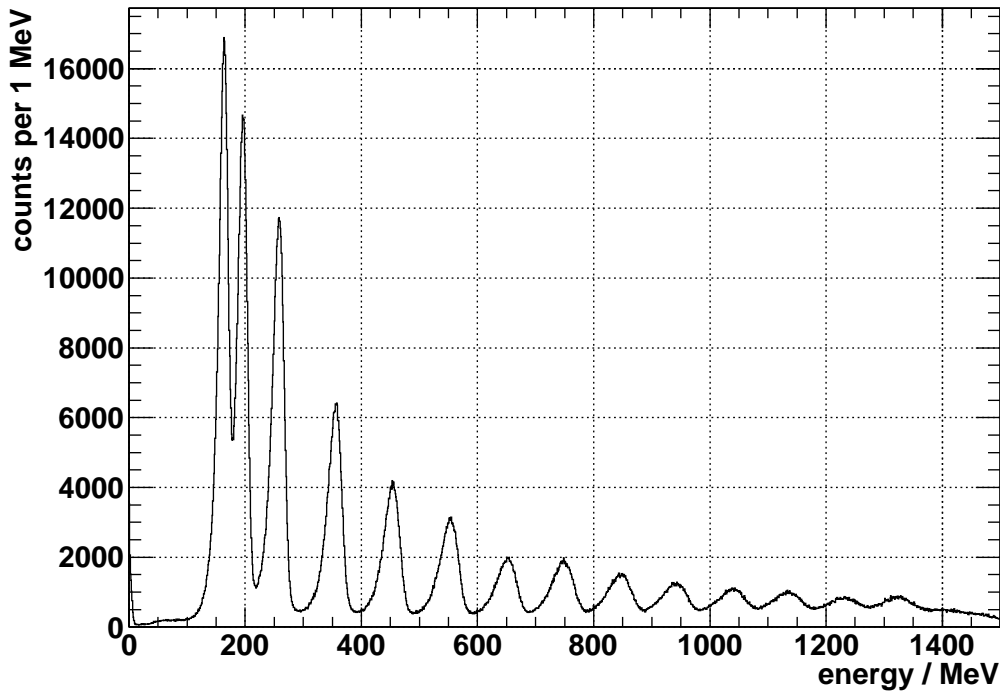
(a) Calibrated energy sum of the 15 selected photon energies in 2009 according to Tab. 3.5. The spectrum shows the typical energy dependence.
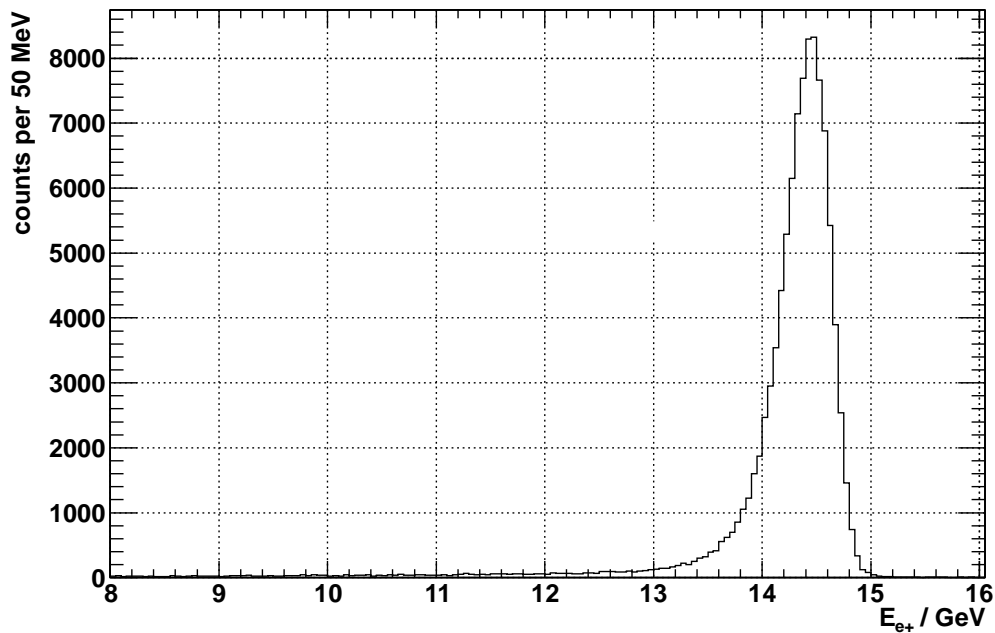
(b) Calibrated energy sum of $15\,\mathrm{GeV}/c$ positrons during the CERN beamtime.

Figure 4.1: Calibrated energy sum of the read out modules. In both spectra the energy threshold of a single crystal was set to $1\,\mathrm{MeV}$.

4.1.1 Noise Determination and Dynamic Range Adjustments

Since the final time resolution does depend strongly on noise and the available dynamic range of the particular readout chain, Tab. 4.1 serves as an summary of the relevant values for all beamtimes. As mentioned before, on a case to case basis, the crystals with the highest expected energy deposition were set to a lower gain by lowering the APD operating voltage or plugging adequate passive attenuators in series. This directly results in an enhancement of the dynamic range. This approach is advisable and comes close to the final readout strategy, since the envisaged ASIC will have two independent gain channels per APD, in order to have an optimum covering of signals in two overlapping energy ranges. The listed noise values in Tab. 4.1 were derived from the width of the pedestal and the corresponding calibration factor c_i (compare Eq. 4.3). The dynamic range of the used 12-bit PS-ADC was estimated according to Eq. 4.4. The calculated energy loss $E_{\mu \text{ in MeV}}$ for a muon with an average path length of 2.4 cm is determined to be 24.5 MeV and serves as a reference for the $4,096$ available channels of the PS-ADC. The values given in the "Other"-column are average values, determined for a couple of modules.

$$\sigma_{\text{Noise}} = \sigma_{\text{Pedestal}} \cdot c_i \tag{4.3}$$

$$E_{\max} = \frac{\text{ADC-Range}_{\text{in channels}} - \text{Pedestal}_{\text{in channels}}}{\mu\text{-peak}_{\text{in channels}} - \text{Pedestal}_{\text{in channels}}} \cdot E_{\mu \text{ in MeV}} \tag{4.4}$$

Beamtime	Noise in MeV		Dynamic range in MeV	
	Center	Other	Center	Other
MAMI 2009	0.510[1]	0.225[1]	1576	200
MAMI 2010	0.303[1]	0.276[1]	936	400
CERN-SPS 2011	2.568[2]	0.970[1]	12500	4500

Table 4.1: Noise and dynamic range adjustments of the PROTO60. [1] APD gain ≈ 150. [2] APD gain ≈ 50. For the CERN beamtime, the given values for the dynamic range represent a rough extrapolation.

4.2 Triggerless Readout of PANDA

The developed readout concept for the EMC was already shown in Fig. 1.24 and contains digitiser modules, DCON[3] and a DAQ[4]. The PANDA experiment will be operated without a general hardware trigger and will collect constantly about 100 GBytes of data per second from more than a thousand front-end modules [43]. At first, the individual detectors of PANDA get self-triggered by the attached FEE[5]. For this purpose, these subdetectors have to have a general time distribution system (SODA[6]), which shares the time information via optical connections. The developed time distribution system SODA aims to provide a common reference time with a RMS better than 20 ps [43].

The motivation of a triggerless readout is the flexibility to select different criteria for the event selection, adjusted to a specific physics case by an individual software trigger. A major drawback is the significantly higher data rate. For interaction rates up to 30 MHz the stored data for a single event can reach 20 kB. Fig. 4.2 shows schematically treatment of the obtained data by any subdetector of PANDA.
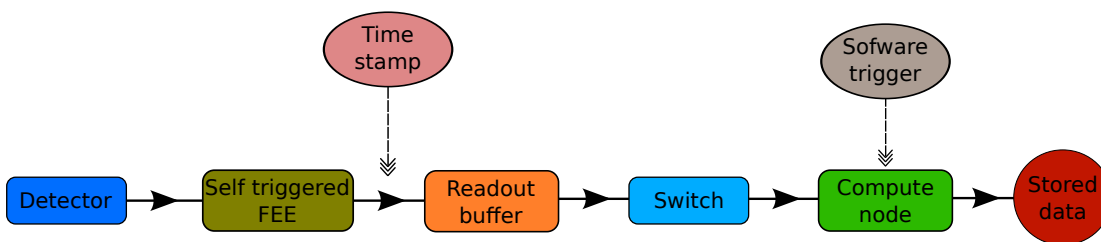
Figure 4.2: General signal treatment of PANDA. The obtained signals of the individual detectors get triggered by FEE, obtain a time stamp and are forwarded to the readout buffer. A switching network serves as an interface between the buffered data to the computing node. Depending on the physics case, a modifiable software trigger can be applied to select the relevant data set.

---

[3]<u>D</u>ata <u>C</u>oncentrator
[4]<u>D</u>ata-<u>A</u>cquisition
[5]<u>F</u>ront-<u>E</u>nd <u>El</u>ectronics
[6]<u>S</u>ynchronisation <u>of</u> <u>D</u>ata <u>A</u>cquisition

4.3 Time Resolution Requirement and Limit

Concerning timing, the EMC of PANDA has to cope with $p\bar{p}$-annihilation rates of $\mathcal{O}(10^7)$ per second. Therefore, a minimum time resolution in the order of $1\,\mathrm{ns}$ is desirable to reject background hits or random noise [18]. A good basis to build up a detector with a fast response is to choose a fast scintillator material. The relaxation of excitations in a scintillator includes complex mechanisms, which occur in different time sections after excitation. Fig. 4.3 gives an impression of the time development of scintillation light from excitation to emission and is subdivided in 5 steps, which will be discussed in the following. For simplification, a core band comprises the lower energy levels and the upper edge of the valence band is set to energy 0 and has a width ΔE_{v}.

1. In a first step after the primary excitation, a large amount of fast electrons and deep holes are generated. Within the first $10^{-16}\,\mathrm{s}$ to $10^{-14}\,\mathrm{s}$, the energy of the fast electrons is more equally distributed via inelastic electron-electron scattering. This process holds on until each electron has an energy smaller than $2 \cdot E_{\mathrm{g}}$. In case of the deep holes, a sequence of Auger processes occurs and all holes travel energetically upwards to the valence band.

2. Afterwards, the energy is further distributed to the crystal grid by phonons (up to $10^{-12}\,\mathrm{s}$). Here the kinetic energy of the electrons is decreased to a minimum level, which leads to an occupation of the lower edge of the conduction band and upper edge of valence band by electrons and holes, respectively.

3. Until $10^{-10}\,\mathrm{s}$, electrons and holes can be trapped by impurities and defects in the solid structure. As a consequence, excitons[7] can be generated.

4. Around $1\,\mathrm{ns}$ the excitations themselves, like e.g. radiative and non-radiative excitations, can interact with each other and the energy is redistributed within the band gap structure.

5. In the order of $10^{-8}\,\mathrm{s}$ the de-excitation of occupied centres takes place and the actual scintillation light is emitted.

In case of PANDA, the chosen material for the EMC, $PbWO_4$, has a relatively fast decay constant of $6.5\,\mathrm{ns}$ (compare Tab. 1.8) and provides an excellent base for timing purposes. A scenario of for instance sub pico-second timing would not work via the detection of scintillation light. This only can be realised with the direct registration of electron-hole pairs.
The dominant contributions for determining an accurate time information originate from the photo sensors and the propagation time inside the crystal. Basically, the

---

[7]Bound state of an electron and electron hole
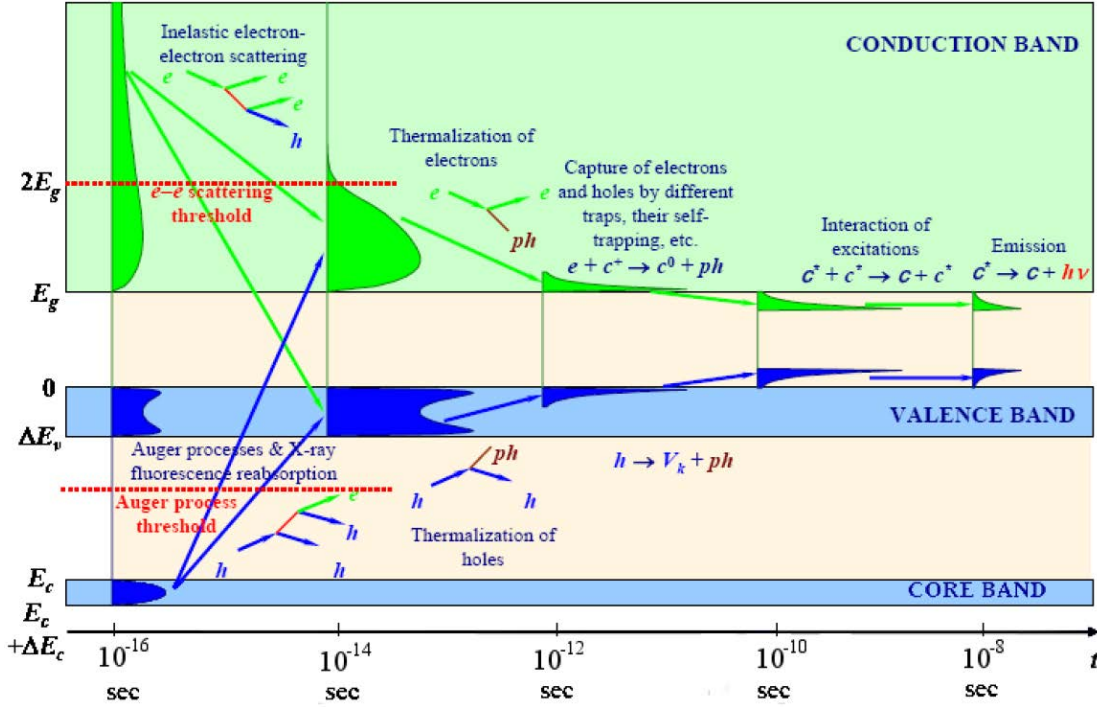
Figure 4.3: Time development of scintillation light [44].

overall time resolution σ_t depends on the width of signal noise σ_N, signal slope dV/dt and the jitter σ_{jit} and can be parametrised in first order approximation by:

$$\sigma^2_{t/total} = \left(\frac{\sigma_N}{dV/dt}\right)^2 + \sigma^2_{jit}. \tag{4.5}$$

The equation expresses that an accurate determination of a certain time marker, like it is done with the CFT-step explained in Sec. 3.1.4, gets worse with higher noise level. Noise is always present and can shift the time stamp of a signal randomly to the positive or negative direction in time. This effect will get significantly smaller, if the SNR[8] is high, like in the case of PMT readout. Moreover, the slope and accordingly the rise time of a signal matters. The steeper the slope, the more negligible is the impact of the noise level to the resulting time resolution. This is again illustrated in Fig. 4.4. Here, the slope of the signal $\Delta V/\Delta t$ at t_0 can be derived by

$$\frac{\sigma_N}{\sigma_t} = \left(\frac{\Delta V}{\Delta t}\right)_{t_0} \tag{4.6}$$

$$\Rightarrow \sigma_t = \frac{\sigma_N}{dV/dt}, \tag{4.7}$$

---

[8]Signal-to-Noise Ratio
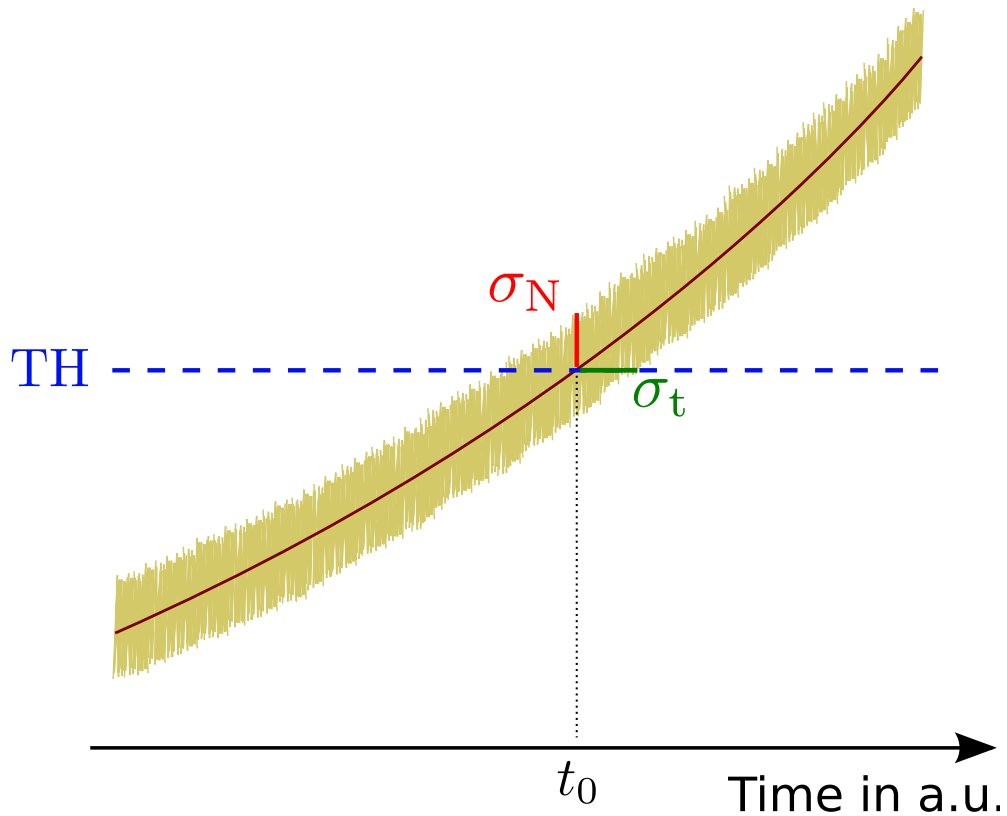
Figure 4.4: Dependencies of the time resolution on the noise level and rise time of the rising part of a recorded signal.

which directly leads to the mentioned dependencies described in Eq. 4.7. This part of the contribution gets worse for LAAPD readout, since here the noise level is higher and the SNR is significantly smaller, due to the relatively low gain. In the following sections of this thesis, the obtained time resolution measured with LAAPDs will be presented. Worse results compared to PMT readout are to be expected because of the mentioned reasons. Furthermore, the stability of the arrival time of the signal, called jitter, contributes to the time resolution via σ_{jit} and is connected to the intrinsic resolution of the digitiser module. Due to the independence of both mentioned error contributions, they are added quadratically in Eq. 4.5.

4.3.1 Time-Walk Effect

The time-walk effect occurs due to the dependence of the rise time on the height of the signal, which is illustrated in Fig. 4.5a. For a fixed trigger threshold, the time-walk is more pronounced. This can be corrected by several methods. One relatively intuitive method is called *High-Low-Coincidence* (compare Fig. 4.5b). Here two thresholds are set: one very close to the noise and the second one on an appropriate higher level. If the coincidence between both levels becomes true, the time marker of the low threshold will be used as time information. This allows to discriminate real signals from noise and therefore keep the time-walk on a reasonably low level.

The more convenient and conventional way to correct the time-walk effect is the *Constant-Fraction-Discrimination*, which was basically used in all beamtimes analysed in this thesis. In contrast to the method mentioned before, the trigger threshold is not on a fixed level, but dynamically generated, according to the height of the incoming pulse. A time stamp is recorded, when the pulse passes a certain fraction R of its maximum amplitude (compare Fig. 4.5c). In practice, the pulse gets rescaled by a factor $R < 1$ and subsequently subtracted from the original pulse. For the final time information, the zero-crossing has to be determined. The value of R has to be adapted to specific applications and is realised differently for the performed beamtimes. For the MAMI beamtimes, the signals were discriminated by conventional CFDs, originally used in the TAPS[9] experiment at Mainz. With a delay of 3 ns and $R = 0.3$ as CFD input parameters, which corresponds to the standard values of the TAPS experiment, no further adaption was done for the prototype test. The very short delay of 3 ns is tuned to the fast PMT readout of the TAPS experiment.

In case of the CERN beamtime, the discrimination is simulated offline by the CFT-step explained in Sec. 3.1.4. For this signal treatment, a delay of 100 ns and $R = 0.45$ were chosen.

In general, this method does not guarantee a completely walk-free performance, but suppresses it significantly down to an acceptable level. Another iteration to minimize this time-walk effect can be done offline via software and will be introduced in Sec. 4.4 and 4.5, since none of the collected data shows a completely walk-free behaviour.

---

[9]<u>T</u>wo <u>A</u>rm <u>P</u>hoton <u>S</u>pectrometer
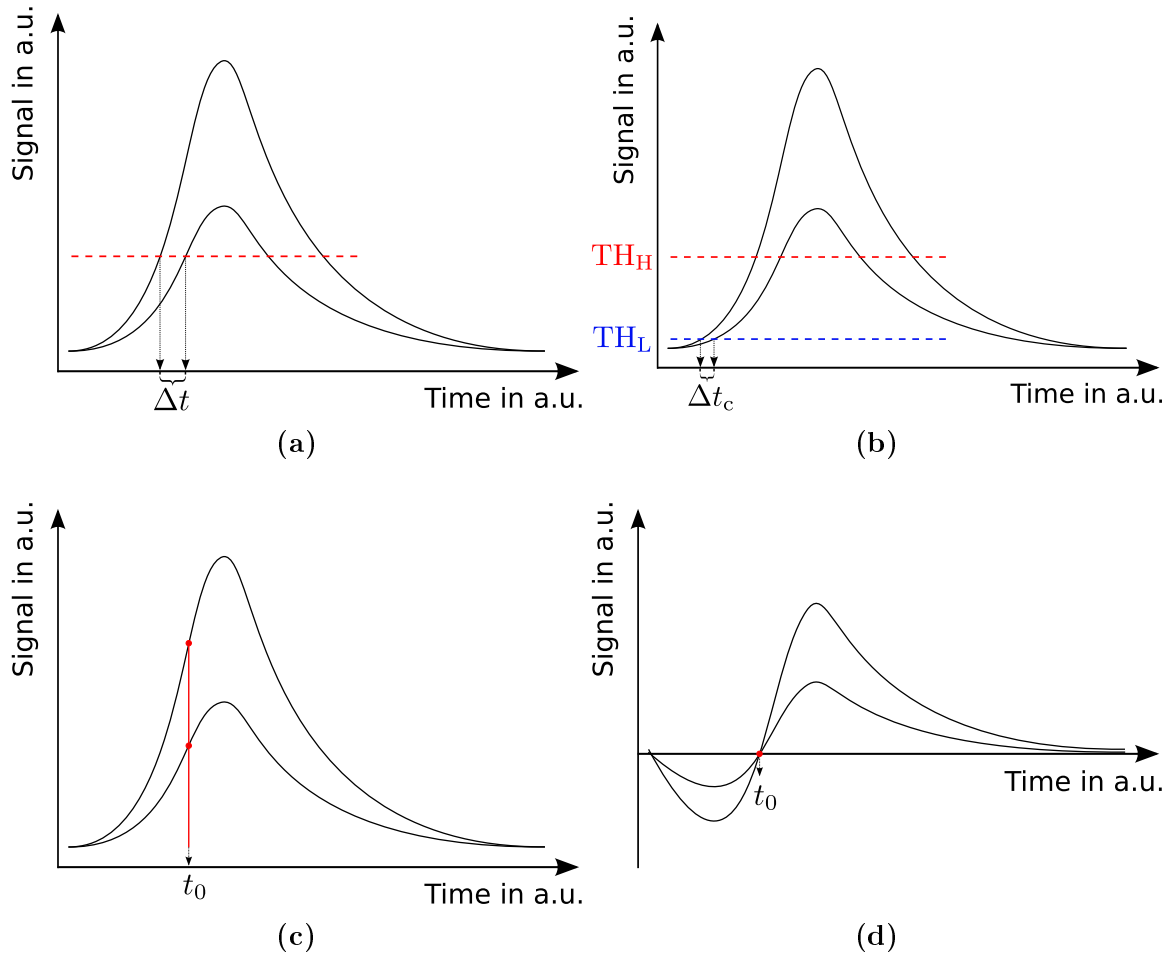
Figure 4.5: (a) Schematic illustration of the time-walk effect. Signals with different amplitudes show different rise times. In spite of the same starting time, the registered time differs by Δt after passing a certain threshold. (b) A possible improvement to $\Delta t_\text{c} < \Delta t$ can be achieved with the *High-Low-Coincidence*, in which TH_H and TH_L correspond to the high and low threshold, respectively. (c) In an ideal case, the time-walk effect disappears, if the time information is extracted with a dynamic threshold (*Constant-Fraction-Discrimination*) and both signals are assigned to the same time t_0. (d) Pulse shapes for both signals after applying the CFD algorithm.

4.3.2 Pile-Up Recovery

Pile-up occurs if two or more signals arrive almost simultaneously in a very short time window. This effect deteriorates the direct determination of the energy and time information with the extraction algorithm described in Sec. 3.1.4. With a nominal hit rate of $500\,\mathrm{kHz}$ at the smallest polar angles, one can expect a pile-up probability of $\sim 13\,\%$ [45]. A pile-up event will be identified in the digitiser module if the ratio of integral and amplitude exceeds a certain threshold. The following describes two methods, which allow the successful recovery of two signals with a time difference not shorter than $50\,\mathrm{ns}$, which is in detail described in [46].
Fig. 4.6 shows two signals with different amplitudes and a time difference of $\sim 200\,\mathrm{ns}$.
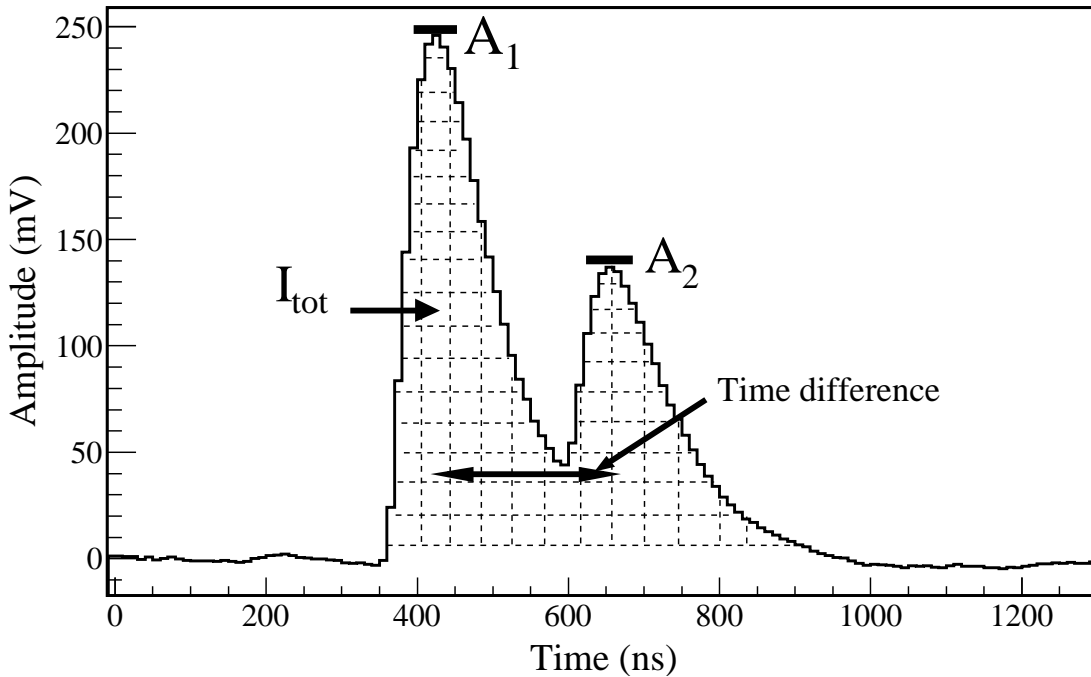
Figure 4.6: Principle of pile-up recovery of energy information [46]. The two digitised signals are generated by LED pulsers with amplitudes of $A_1 \approx 250\,\mathrm{mV}$ and $A_2 \approx 140\,\mathrm{mV}$, respectively.

The integral I of a signal corresponds to the input charge and scales linearly with the amplitude A, according to $I = k \cdot A$. With the knowledge of the constant k, this proportionality can be exploited for the recovery of overlapping signals. If two signals are close to each other, the total integral I_{tot} and the amplitude of the first pulse A_1 in Eq. 4.8 is detected. Thus the relevant energy information of the second pulse A_2

can be calculated via Eq. 4.9.

$$I_{\mathrm{tot}} = k \cdot (A_1 + A_2) \tag{4.8}$$

$$A_2 = \frac{I_{\mathrm{tot}}}{k} - A_1 \tag{4.9}$$

Beside the energies of a pile-up event, the time can be recovered as well. Here, the shaping MWD-shaping-algorithm, presented in Sec. 3.1.4, has to be applied three times with appropriate settings in order to obtain separated pulses (compare Fig. 4.7) [45]. Afterwards the CFT-step can be evaluated on both signals separately and the time information is determinable.
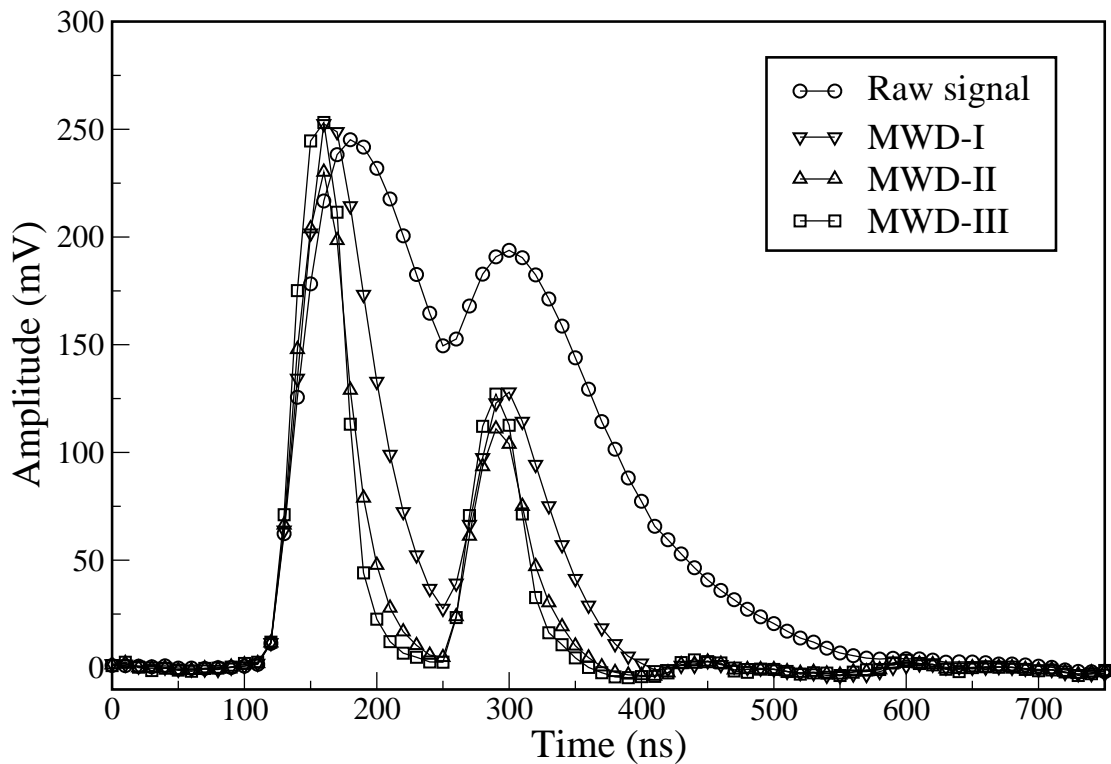
Figure 4.7: Principle of pile-up recovery of time information [46]. The figure shows the single MWD-steps with the two generated signals of Fig. 4.6.

4.3.3 Scintillation Tiles

Due to the extended physics program of PANDA, there is a demand for an additional detector with respect to timing purposes: SciTil[10] [47]. Such a tile itself has roughly a size of the order of $2 \times 2 \times 0.5\,\mathrm{cm}^3$ and is made out of an organic scintillator material with fast rise time and high light output. Studies about the optimum material with an acceptable radiation hardness are presently ongoing. One tile should be in front of each crystal of the barrel EMC. The readout is envisaged with SiPMs[11], which is basically an array of small Avalanche photo diode pixels with excellent timing properties since they are operated in Geiger-Mode delivering extremely short rise-times. An additional SciTil detector would have the following benefits due to the desired time resolution of $100\,\mathrm{ps}$:

- a start detector for TOF measurements of muons and pions (PID)

- improved relative timing for a better correlation between reaction fragments of one event in the barrel and the forward part of the PANDA detector

- ability to identify photons converted via pair production within the DIRC

The final design is not accomplished yet, but in the present status it is foreseen to read out one tile with two SiPMs (compare Fig. 4.8a). This has the advantages of a higher number of collected photons, less light path fluctuations and higher detection efficiency. One quad module (Fig. 4.8b) consists of four SciTils and the signals are forwarded to an ASIC to be developed (Fig. 4.8c).

(a)   (b)   (c)
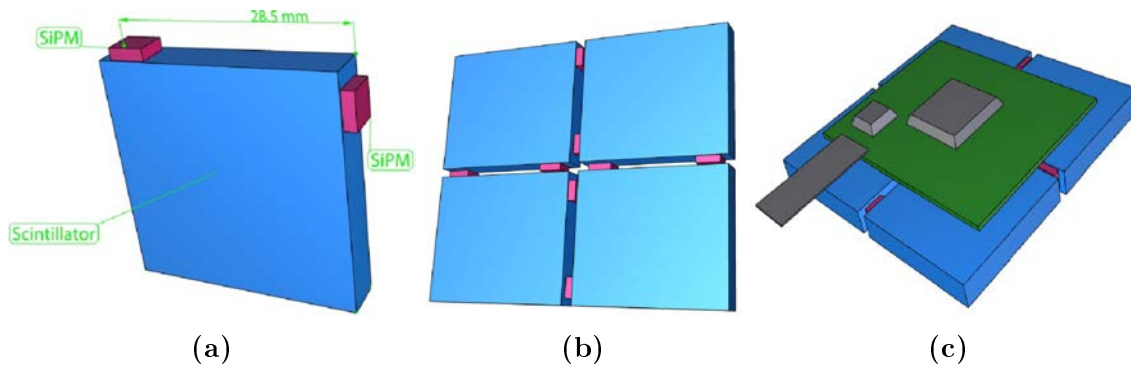
Figure 4.8: (a) Basic layout of a SciTil module read out from two positions. (b) Quad module. (c) The signals of one quad module are further processed by an ASIC.

---

[10]<u>Sc</u>intillating <u>Til</u>e
[11]<u>Si</u>licon <u>Ph</u>oto<u>m</u>ultipliers

4.4 Time Resolution at MAMI 2009 and 2010

The data obtained in the beamtimes at MAMI in 2009 and 2010 are basically treated in the same way. But there are some differences due to the different trigger conditions, which were already listed in Tab. 3.3. In 2009, a coincidence between tagger and central crystal was required, whereas in 2010 a logical OR of all crystals replaced the trigger branch from the prototype. Therefore, the individual time spectra of the corresponding modules have to be interpreted differently. In order to obtain the best possible time resolution, the main focus was set to the runs, where the beam impinged in between two adjacent crystals, corresponding to the black cross in Fig. 3.18. Under these conditions similar signal amplitudes are recorded in the coincident detector due to symmetric energy sharing. Some further results will be presented for comparison and discussion. In most of the cases, only events were accepted where the deposited energy of both crystals were similar within a certain range. In each case, the time reference is plotted and analysed with regard to calibration, time-walk effect and time resolution. All achieved results will be compared and discussed in Sec. 6.2. The energy calibration of the shown data will not be discussed further and was done like explained in Sec. 4.1.

4.4.1 Beamtime MAMI 2009

A logical AND of tagger and central crystal signals triggered the readout chain and all modules were read out simultaneously. The timing of the ECL[12] signals was adjusted in a way that the rising edge of the tagger arrives earlier than the one of the central crystal. Therefore, the central crystal is the time-determining component. The whole readout had a common start and was stopped individually by the crystals themselves. Due to that reason, the time spectrum of the central crystal only consists of a spike (Fig. 4.9a), the position is equal to the generated effective time gate of approximately $405\,\mathrm{ns}$. The time information of the central crystal is contained in the digitised data of the corresponding tagger channels and is shown in Fig. 4.9b. Here an additional smearing of the tagger resolution can be neglected due to the fact that the plastic scintillators of the tagger are read out by PMTs.
To guarantee a similar energy deposition in both detectors, labelled as number 35 and 36 in Fig. 3.18, Eq. 4.10 was set as requirement in the software:

$$E_{35} > E_{36} \cdot 0.8 \text{ and } E_{36} > E_{35} \cdot 0.8. \tag{4.10}$$

To get an information about the resolution of the central crystal, the data, shown in Fig. 4.9c, has to be calibrated relatively by shifting the separate data sets of each

---

[12]<u>E</u>mitter <u>C</u>oupled <u>L</u>ogic
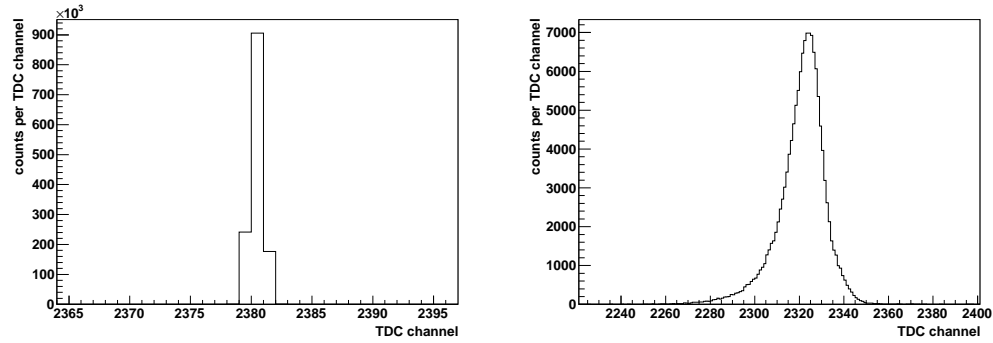
(a) Time spectrum central crystal.

(b) Time spectrum of tagger channel 12.
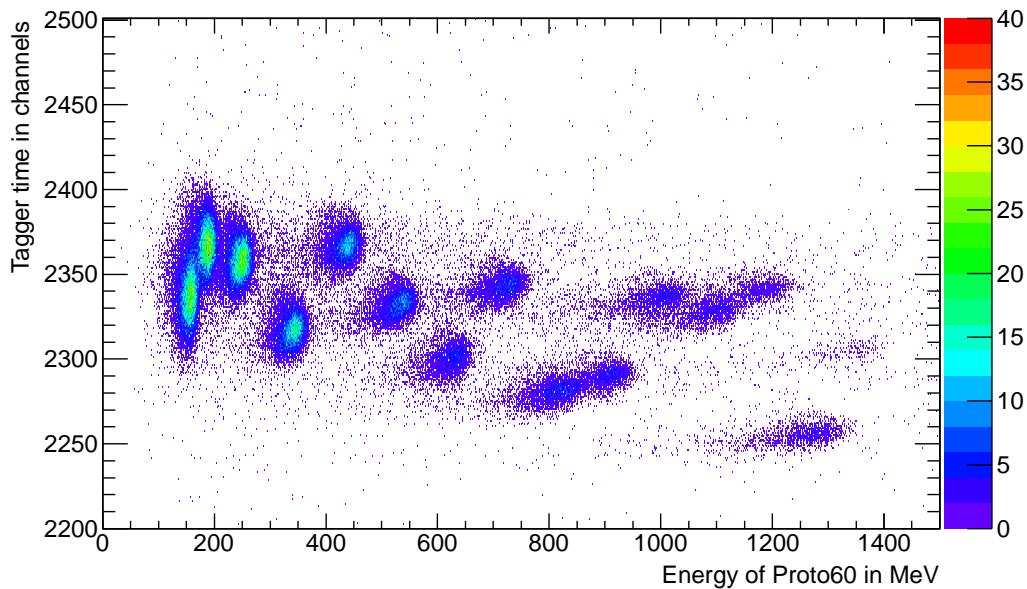
(c) Time spectrum of all tagger channels.

Figure 4.9: Raw time spectra of the central crystal (a) and tagger channel 12 (b), corresponding to an energy of 355.88 MeV, which contains the time resolution of the central crystal. A slight time-walk behaviour is already visible in a tailing to the left hand side. (c) Time spectra of all tagger channels shifted due to delay variations.

tagger channel relatively to each other. The absolute timing signals of the tagger are not compensated for variations of transmission times in the PMTs or cables, respectively. Starting with the tagger channel corresponding to the highest energy, the data of a small energy range was selected, projected to the time axis and fitted with a Gaussian function. The same procedure, with the same energy range, was applied for the next lower tagger channel and the obtained difference of the Gaussian function gives relative shift in time. This procedure was repeated pairwise down to the tagger channel of the lowest energy. This method is exemplary illustrated in Fig. 4.10 for tagger channels 9 and 10, respectively.

(a) Time spectrum tagger channel 9.

(b) Time spectrum tagger channel 10.

(c) Gaussian fit tagger channel 9.

(d) Gaussian fit tagger channel 10.
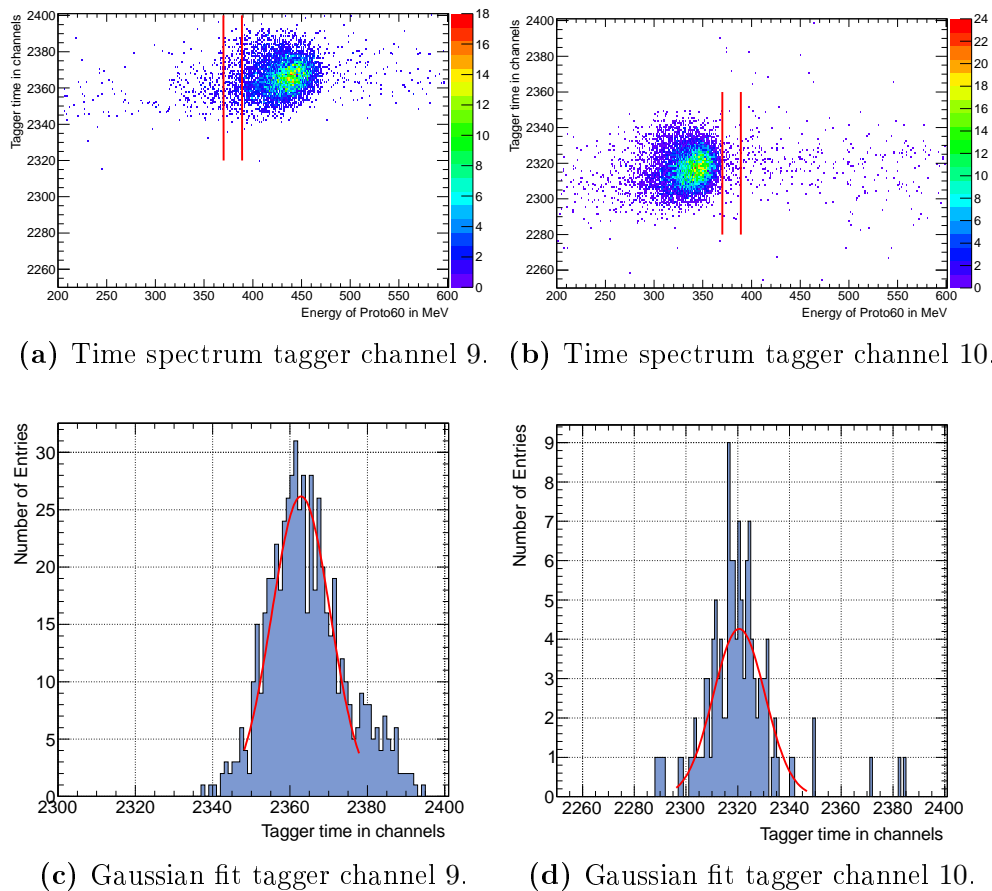
Figure 4.10: Example of the relative time calibration for tagger channels 9 and 10. The selected data within the overlap region of both tagger channels, $370-390\,\text{MeV}$, are projected and fitted with a Gaussian function, in which the difference of the peak position corresponds to the relative shift in time.

The absolute shifts of the tagger channels are not visible in the time spectrum of the difference between the central crystal and its neighbour. Here, the regarded time ref-

erence $t_{36} - t_{35}$ is independent of the jitter caused by the tagger. The time spectrum of crystal 36 contains the intrinsic resolution of both crystals, 35 and 36. Fig. 4.11 shows the time difference $t_{36} - t_{35}$ in terms of channels versus the deposited energy in crystal 35. t_{35} is almost constant due to the mentioned reasons (compare Fig. 4.9a). For absolute calibration, the channels of the TDC have to be converted to ns. This was done in a separate measurement by recording the arrival time of a signal generated with a test pulser with and without a fixed delay of 16 ns (Fig. 4.12). This time difference has to be divided by the corresponding number of channels, which results in a calibration factor of 0.17 ns per TDC channel.
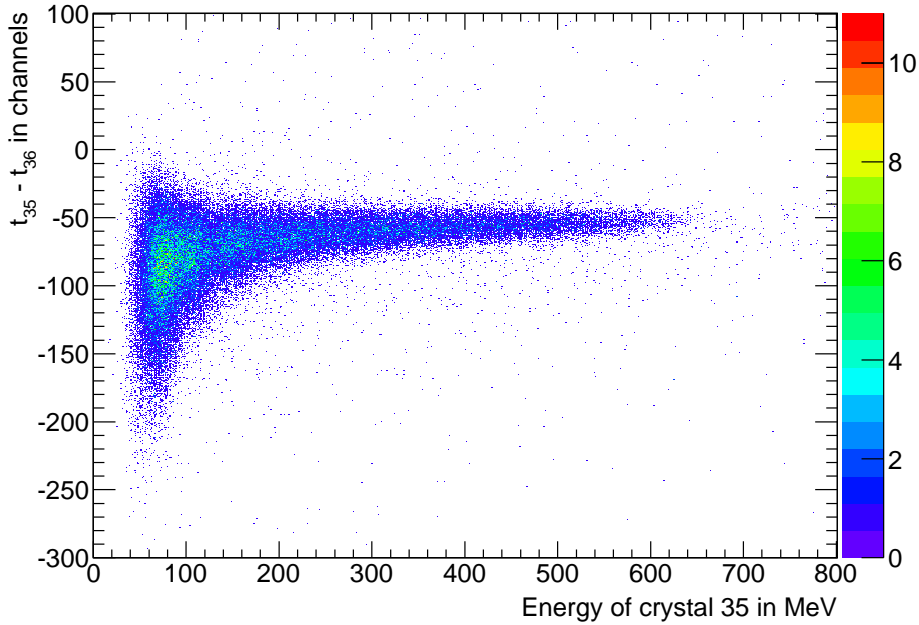
Figure 4.11: Uncalibrated time spectrum of $t_{36} - t_{35}$ in TDC channels.

The calibrated time of the tagger and the difference $t_{36} - t_{35}$ is plotted in 4.13.

4.4.1.1 Time-Walk Correction

Both spectra in Fig. 4.13 show a clear time-walk effect, which becomes dominant for lower energies. For correction purposes, an appropriate energy dependent function has to be selected, which describes the time-walk behaviour. Based on the experiences of
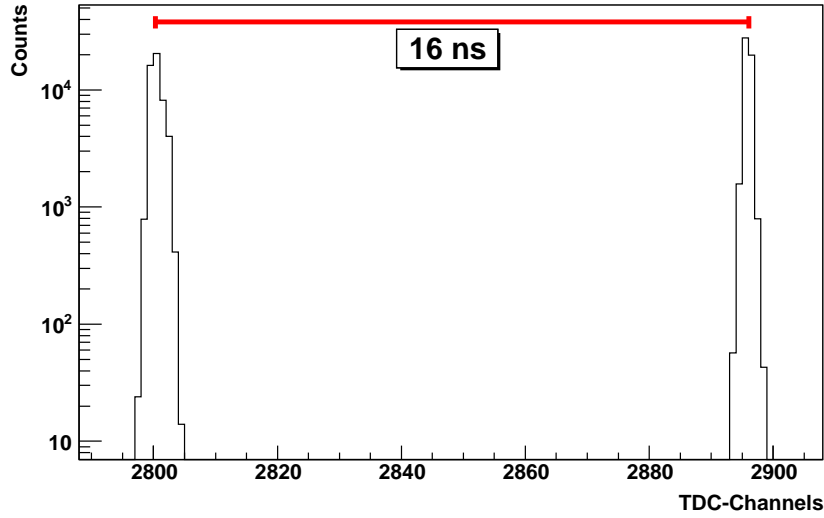
Figure 4.12: Absolute time calibration of the TDC channels.

the TAPS group Gießen [48], Eq. 4.11 was chosen, in which A, B, C and D represent free parameters.

$$t(E) = A \cdot e^{B \cdot \sqrt{E} + C \cdot E} + D \tag{4.11}$$

For the application of $t(E)$, the content of the corresponding spectrum has to be converted into discrete points. This is done by subdividing the histogram in slices with equal width along the energy axis. Each slice is subsequently projected on to the time axis and fitted with a Gaussian function. As a result, the mean values, including standard deviation, are plotted. This procedure was applied to both spectra of 4.10a and 4.10b, and is exemplary shown for the latter one in Fig. 4.14. In order to get proper results, in both cases the spectra were rebinned in groups of five neighbouring bins and only slices with an minimum content of 25 counts were fitted. The fit results can be looked up in Tab. 4.2. The chosen fit function shows a satisfying description of the data points within the fit range. Data points with extremely large error bars suffer from low statistics and should be suppressed by the mentioned requirements to a reasonable level. Above 550 MeV no data points are available due to the low number of counts and the fit is extrapolated to 800 MeV.

In a next step, the time values have to be corrected with the obtained time-walk correction function. Therefore, each data point has to be subtracted from the correction function $t(E)$, in which E represents again the deposited energy in crystal 35. This is displayed for both scenarios in Fig. 4.15 for all energies.
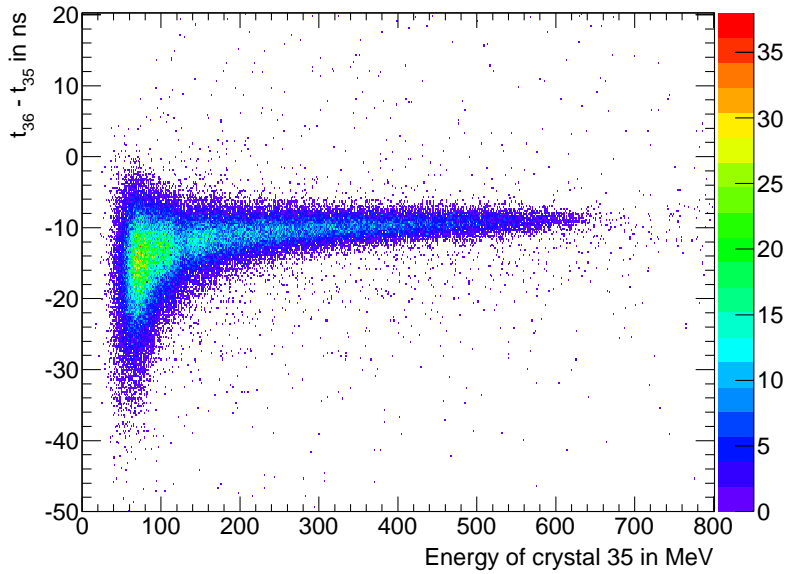
(a) Calibrated time spectrum of $t_{36} - t_{35}$.
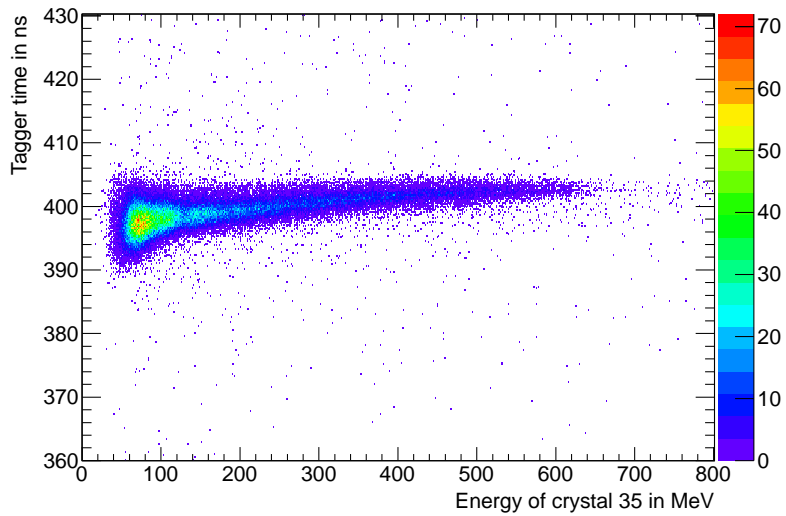
(b) Calibrated time spectrum of all tagger channels, which represents the timing information of crystal 35.

Figure 4.13: Calibrated time spectra Mainz 2009. Both spectra were plotted as a function of the deposited energy of crystal 35 and cover a time range of 70 ns. Already here one can see that the time difference is affected by two time resolutions, namely of crystals 35 and 36. In addition a clear time-walk is visible, the correction of which will be described in Sec. 4.4.1.1

.
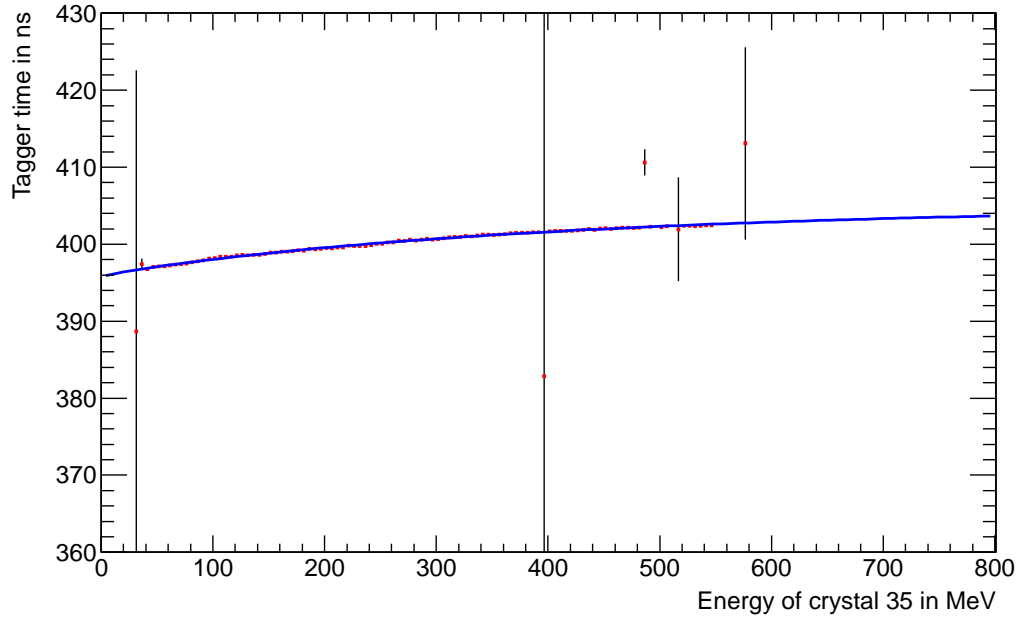
Figure 4.14: Application of time-walk function $t(E)$ for the spectrum in Fig. 4.10b. Each fitted slice in the energy direction has a width of $5\,\mathrm{MeV}$ and a minimum content of 25 events was required. Only a handful of slices deliver improper results with respect to the time-walk correction.

Spectrum	Correction function $t(E)$	χ^2/NDF
$t_{36} - t_{35}$ (Fig. 4.10a)	$t(E) = -42.08\,\mathrm{ns} \cdot e^{-2.41 \cdot 10^{-1} \cdot \sqrt{E/\mathrm{MeV}} - 3.02 \cdot 10^{-3} \cdot E/\mathrm{MeV}} - 8.44\,\mathrm{ns}$	22.42
Tagger time (Fig. 4.10b)	$t(E) = -9.31\,\mathrm{ns} \cdot e^{-6.47 \cdot 10^{-3} \cdot \sqrt{E/\mathrm{MeV}} - 2.16 \cdot 10^{-3} \cdot E/\mathrm{MeV}} + 405.05\,\mathrm{ns}$	25.04

Table 4.2: Fit results time-walk correction.
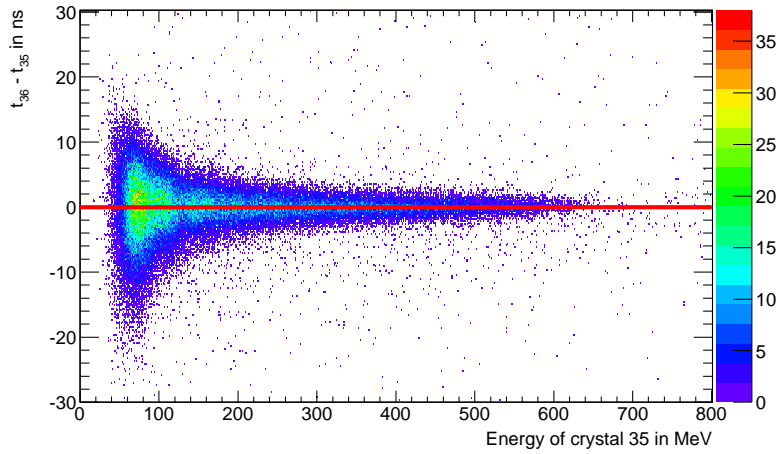
(a)
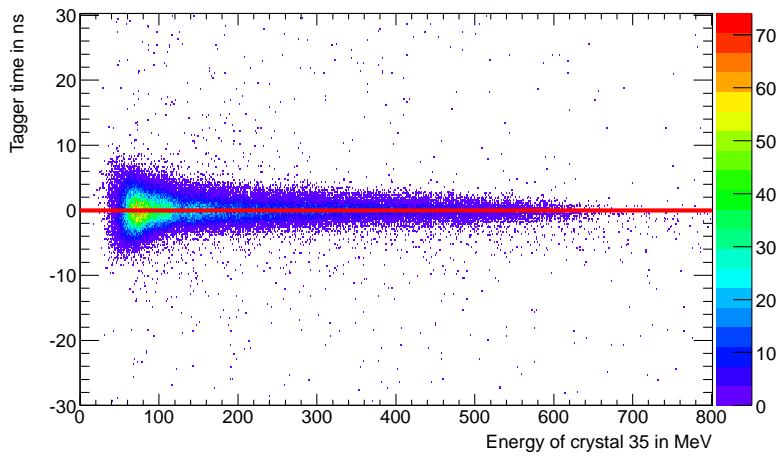
(b)

Figure 4.15: Time spectra after time walk correction for the time difference (a) and the absolute tagger time (b).

4.4.1.2 Time Resolution

The time-walk corrected data serves as basis for determing the final time resolution for the different tagger channels. Therefore, the individual time spectra for the different energies are plotted separately and fitted with a Gaussian function, at which the width determining the final time resolution in terms of ns. This is shown exemplary for the tagger time in Fig. 4.16.
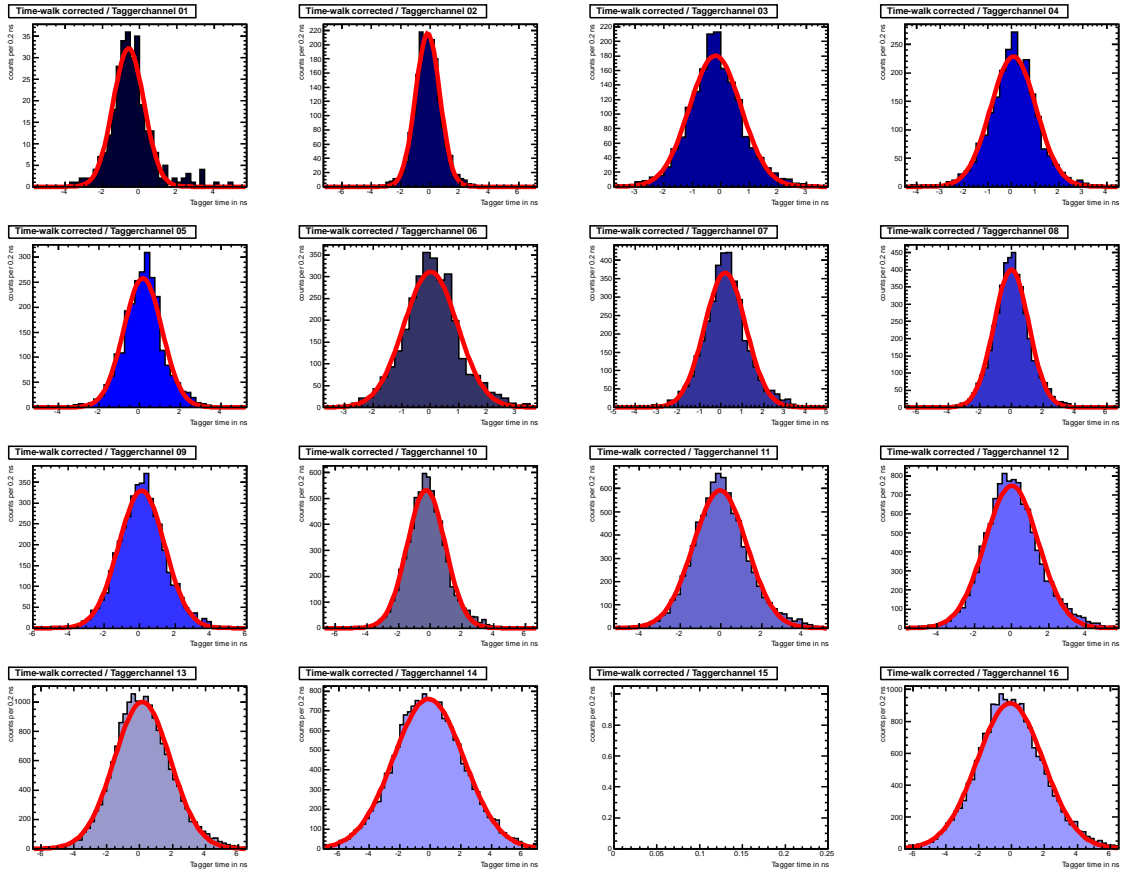
Figure 4.16: Time distributions for the tagger time distinguished by the tagger energy. The fitted Gaussian functions are represented by red coloured lines. Tagger channel was disabled (compare Tab. 3.5.)

The obtained time resolution for both scenarios, time difference and tagger time, is plotted in Fig. 4.17. Furthermore, the data were fitted with Eq. 4.12 from [49].

$$\sigma_t = \sqrt{\left(\frac{N \cdot \sigma_n}{E}\right)^2 + \left(\frac{S}{\sqrt{E}}\right)^2 + C^2} \tag{4.12}$$

The free parameters N, S and C represent the contribution caused by noise, stochastic, and systematic effects, respectively. E is the measured deposited energy and σ_n the noise level, which was determined to $\sim 0.25\,\mathrm{MeV}$.
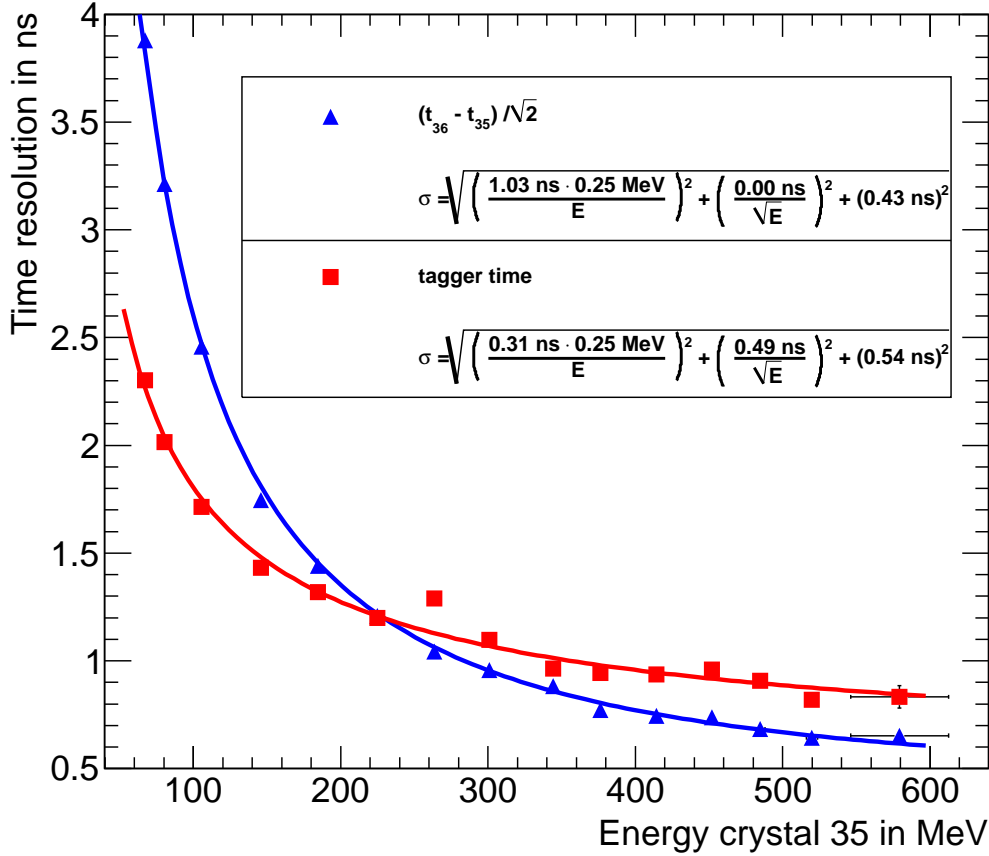
Figure 4.17: Time resolution for the time difference and tagger time as a function of the deposited energy in the central crystal including fits with corresponding colour. The values for the energy axis were extracted by fitting the relevant energy distributions with Eq. 5.1.

In case of the time difference, it was assumed that both crystals contribute equally to the final time resolution. Therefore, to get the resolution for a single module, the overall resolution was divided by $\sqrt{2}$ (compare Eq. 4.13), which is already included in

Fig. 4.17.

$$\sigma^2_{\text{time difference}} = \sigma^2_{36} + \sigma^2_{35}$$
$$\sigma^2_{\text{time difference}} = 2 \cdot \sigma^2 \text{ , for } \sigma_{36} = \sigma_{35} = \sigma$$
$$\Rightarrow \sigma = \frac{\sigma_{\text{time difference}}}{\sqrt{2}} \tag{4.13}$$

The time resolution, deduced by the timing difference of two crystals, is significantly worse at energies below $200\,\text{MeV}$ and becomes slightly better at higher energies. Extracted by the fit, the N-parameter, which symbolises the noise contribution, is almost three times larger than the one obtained by a single unit. Furthermore, the parameter representing the stochastic term of the time difference has a value $1.42 \cdot 10^{-4}\,\text{ns}\sqrt{\text{MeV}}$ and is negligible. This is reasonable, since the applied requirement in Eq. 4.10 demands an almost equal sharing of the deposited energy. In case of the tagger time, which represents for the mentioned reasons the time of crystal 35, a clear statistics-dependence could be extracted. The constant term of the parametrisation dictates the achievable time resolution at higher energies with the described readout.

4.4.2 Beamtime MAMI 2010

In order to cover the low energy region of PANDA down to $50\,\text{MeV}$, the time resolution was as well evaluated for the beamtime at MAMI in 2010. The same data was already analysed in [42], but here the final time resolution was determined without correcting the time-walk and only setting a sharp cut on the energy for the single tagger channels. Only data for photon beams impinging centrally on one crystal are available. Data acquisition was running in a common start mode, in which a logical AND between the tagger channels and all crystals of the PROTO60 served as a trigger for the readout. For both responding modules, the registered time of the rising edge is digitised by TDCs and subsequently stored. The timing was, like in 2009, set in a way that the NIM[13] signals from the tagger arrive earlier than the ones from the crystals. Therefore, the responding crystal is again the time determining component. As a time reference, the difference between central crystal and tagger channel was chosen:

$$t = t_{\text{central crystal}} - t_{\text{responding tagger channel}}. \tag{4.14}$$

A typical time spectrum of the tagger is shown in Fig. 4.18, in which the dotted lines in red correspond to the sharp cut on the relevant events. The application of this cut has to be tuned for each tagger channel. For the determination of the time resolution, the time reference t has to be corrected, due to delay variations of the tagger channels. This was done like explained in Fig. 4.10 and the result is shown in

---

[13]Nuclear Instrumentation Methods
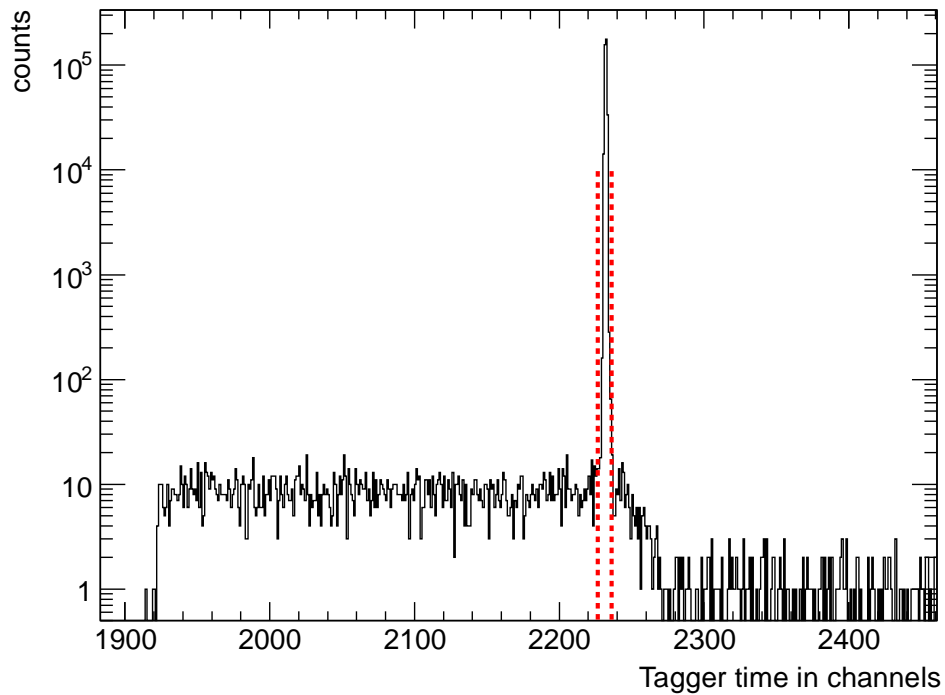
Figure 4.18: Time spectrum of a tagger channel including the cut on the phys-
ical relevant events, marked with red dotted lines. The plateau in the channel
range from ~ 1920 to ~ 2220 corresponds to events, where the signal of the crys-
tal arrives earlier than the one from the tagger. In such an event, which has a
probability on the ppm-level, the latter one is the time determining component.

Fig. 4.19. Furthermore, the relatively shifted time spectra have to be walk-corrected according to Eq. 4.11. The difference between the data in Fig. 4.19 and the obtained correction function for the time-walk is plotted in arbitrary units in Fig. 4.20.
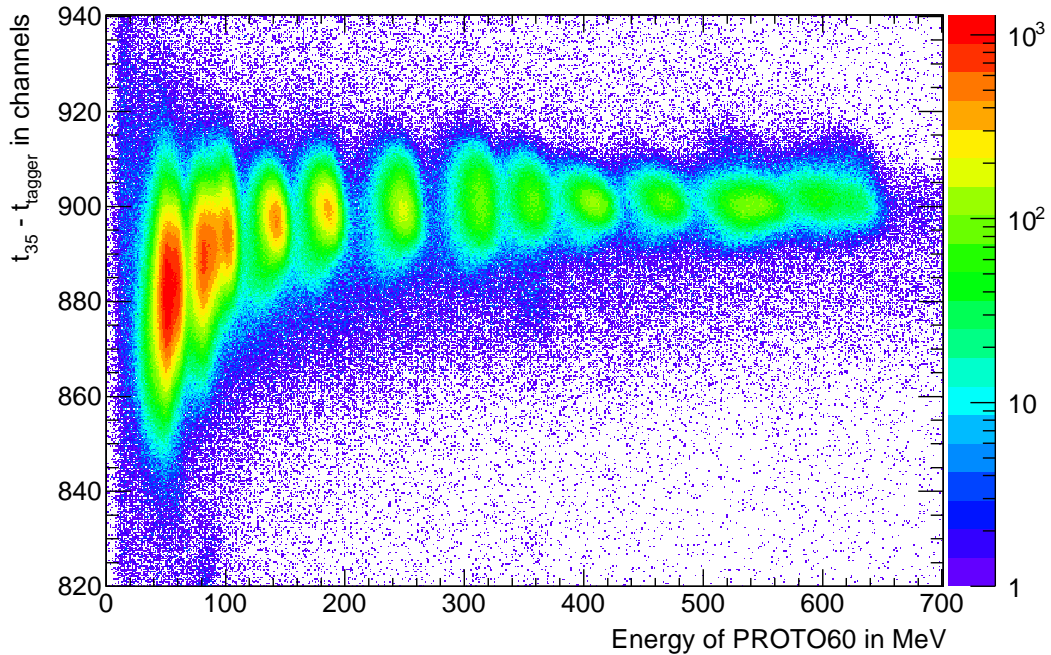
Figure 4.19: Relatively calibrated time spectrum. A clear time-walk is visible. For better visualisation of the data the z-axis is plotted in logarithmic scale. The x-axis shows the deposited energy in the whole PROTO60.

Like in Fig. 4.16 for the beamtime in 2009, the time spectra are plotted separately for each tagger channel and fitted with a Gaussian function in order to determine the final time resolution. The deduced results are shown as function of the deposited energy in Fig. 4.21 and fitted with Eq. 4.12.
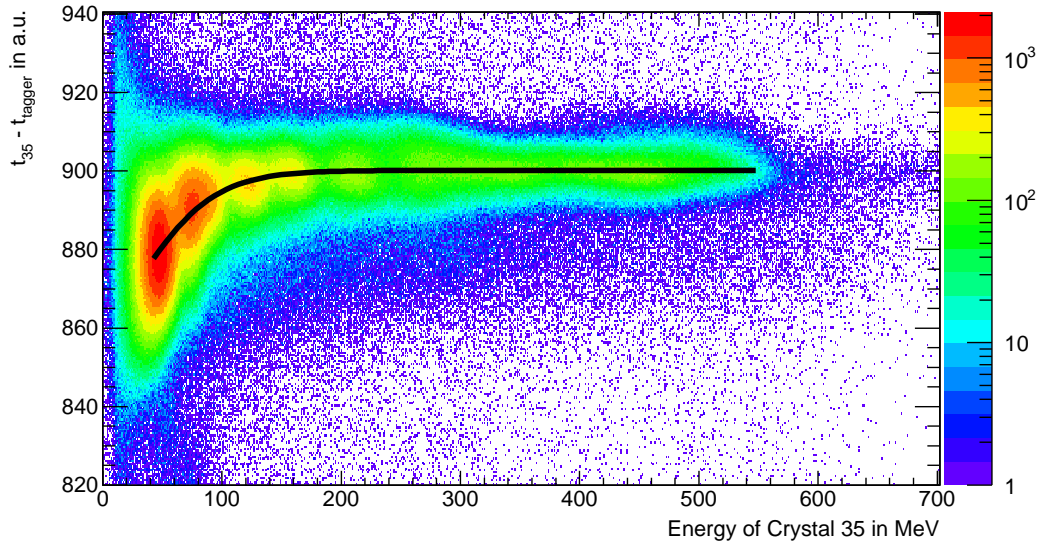
Figure 4.20: Time spectrum as function of the deposited energy in the regarded crystal including time-walk correction function marked in black.
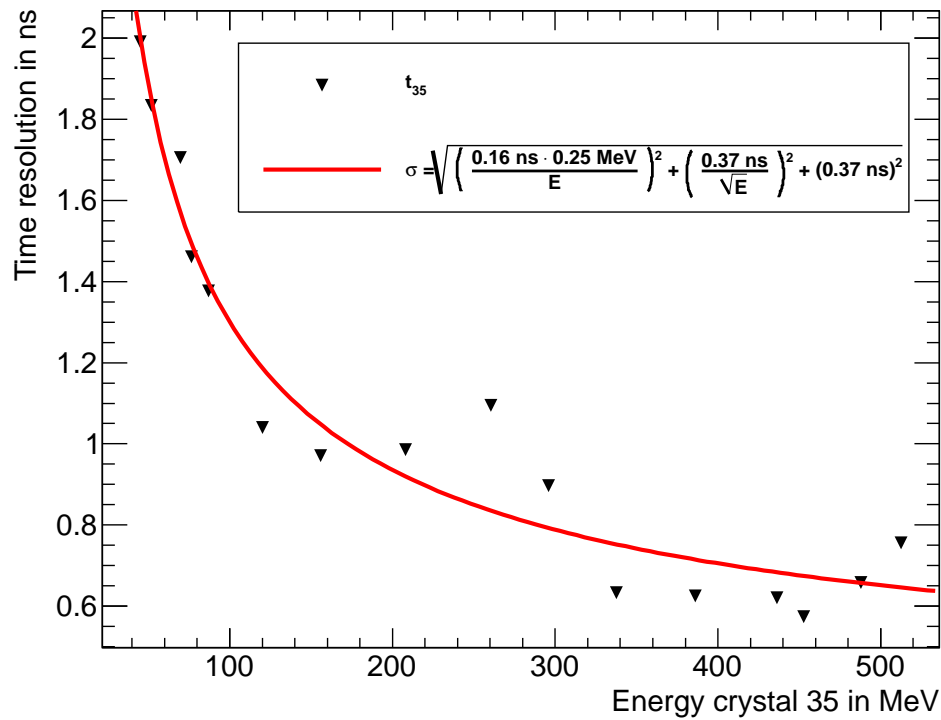
Figure 4.21: Results for the time resolution from the MAMI beamtime in 2010.

4.5 Time Resolution at CERN 2011

In case of the beamtime 2011 at CERN, the time information was extracted like explained in Sec. 3.1.4. Due to the sampling rate of 50 MHz, a trace of the SADC is subdivided into channels with a width of 20 ns. The subsequent application of the CFT-step of the feature extraction allows to obtain time information in the subchannel region. To get a first impression of the data, Fig. 4.22 shows the extracted time information for the central crystal versus the deposited energy of crystal 28 for both runs. The upper histogram of Fig. 4.22 represents the time-energy-correlation for the central crystal of the first run performed at CERN. Therefore, a large fraction of the incoming energy of about ~ 12 GeV is registered by the crystal. In the case of the second run, the main development of the electromagnetic shower occurs either in crystal 28 or in the neighbouring crystal 29. The remaining fraction of the shower deposits energy in the surrounding crystals. This behaviour is also visible in Fig. 5.1. It is recognisable, that the values are distributed within a band with a vertical width of 20 ns, which is connected to the way of extracting the time information. With the CFT-algorithm of the feature extraction, the baseline crossing is always determined within the centres of two neighbouring SADC-samples (compare Fig. 3.3), which have a time difference of 20 ns due the sampling rate of 50 MHz. In addition, a small energy dependence is visible, which can be interpreted as time walk. Especially at small energies the bending of the band structure gets steeper. This effect can be emphasised by plotting the time difference of the neighbouring crystals 28 and 29 versus the deposited energy of crystal 28 (Fig. 4.23). In case of a small energy deposition, the shape of the distribution in Fig. 4.23 is dominated by the time-walk of crystal 28. On the other side, if the majority of the initial energy is deposited within crystal 28, only a small fraction of energy is registered by crystal 29 and its time-walk effect has a significant contribution to the time difference. Moreover, some additional structures become visible at low values on the energy axis next to the actual data. Those are caused by events where both considered crystals only see a small part of the overall energy and the main deposition occurs somewhere else within the prototype matrix.

4.5.1 Position Dependence

The MVD-prototype, which was placed in front of the PROTO60, gave the ability to very accurately select events with a certain point of impact on the PROTO60-matrix. A circle with a radius of 5 mm was chosen as accepted area for the point of impact. The vertical position of the circle was fixed to the centre of the crystal in the corresponding row, whereas the x-coordinate was shifted in steps of 1 mm. The distributions of the time difference of the selected events are shown in Fig. 4.24 for 10 different x-positions
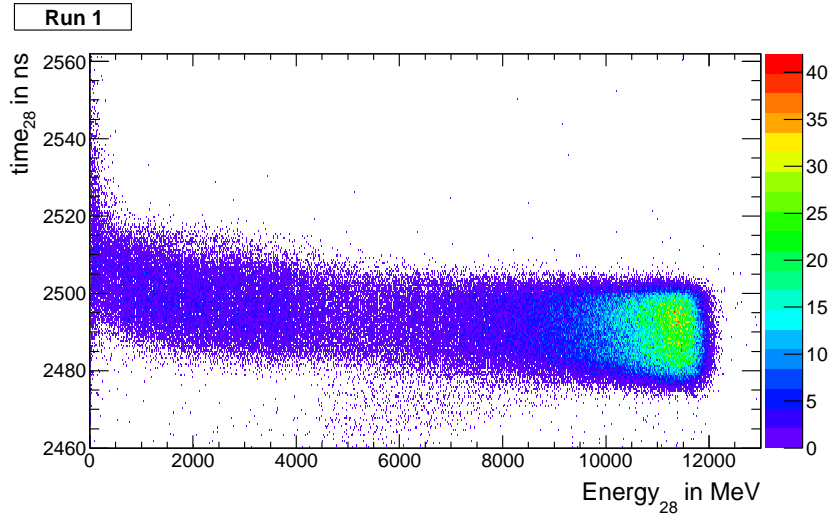
(a)
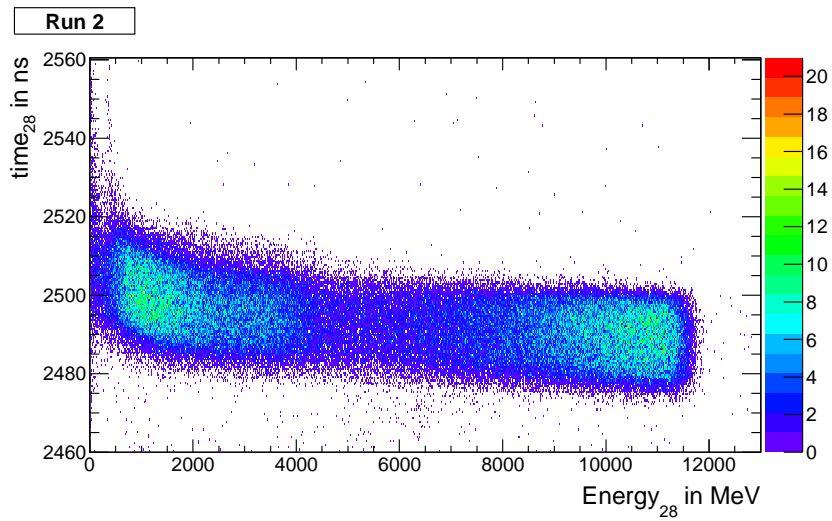
(b)

Figure 4.22: Extracted time spectra of the central crystal as a function of the deposited energy in crystal 28 for run 1 (a) and run 2 (b).
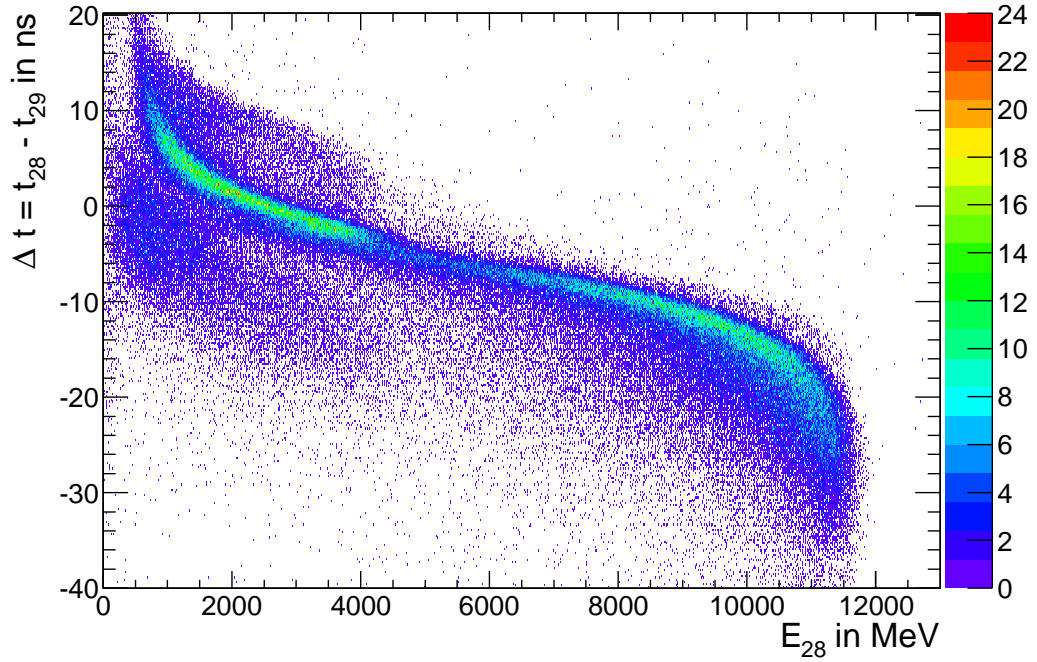
Figure 4.23: Emphasised time-walk for the second run of the CERN beamtime.

of the selected area, which is represented in each histogram by a small sketch with a dashed circle marked in red. Two peaks are visible in the spectra, if the selected area covers two crystals. The right peak in the corresponding histograms originates from events with major energy deposition in crystal 28, whereas the left peak represents the complementary case with a major energy deposition in crystal 29. By shifting the selected area stepwise over the transition region of both crystals, a decrease of the latter one can be observed until its complete disappearance. Furthermore, the time-walk effect becomes visible in the remaining histograms. The more the selected area is centred on the front face, the smaller the overall energy deposition in the neighbouring crystal 29 and therefore, the impact of t_{29} is higher. In addition, the higher the registered energy of crystal 28, the smaller its determined time. Both effects contribute to an enlargement of the time difference $t_{29} - t_{28}$, at which the former effect has a more significant impact. In the energy range from $\sim 2 - 12\,\text{GeV}$ (compare Fig. 4.22), only a small dependence on the energy $\left(\sim -0.9\,\frac{\text{ns}}{\text{GeV}}\right)$ can be observed.
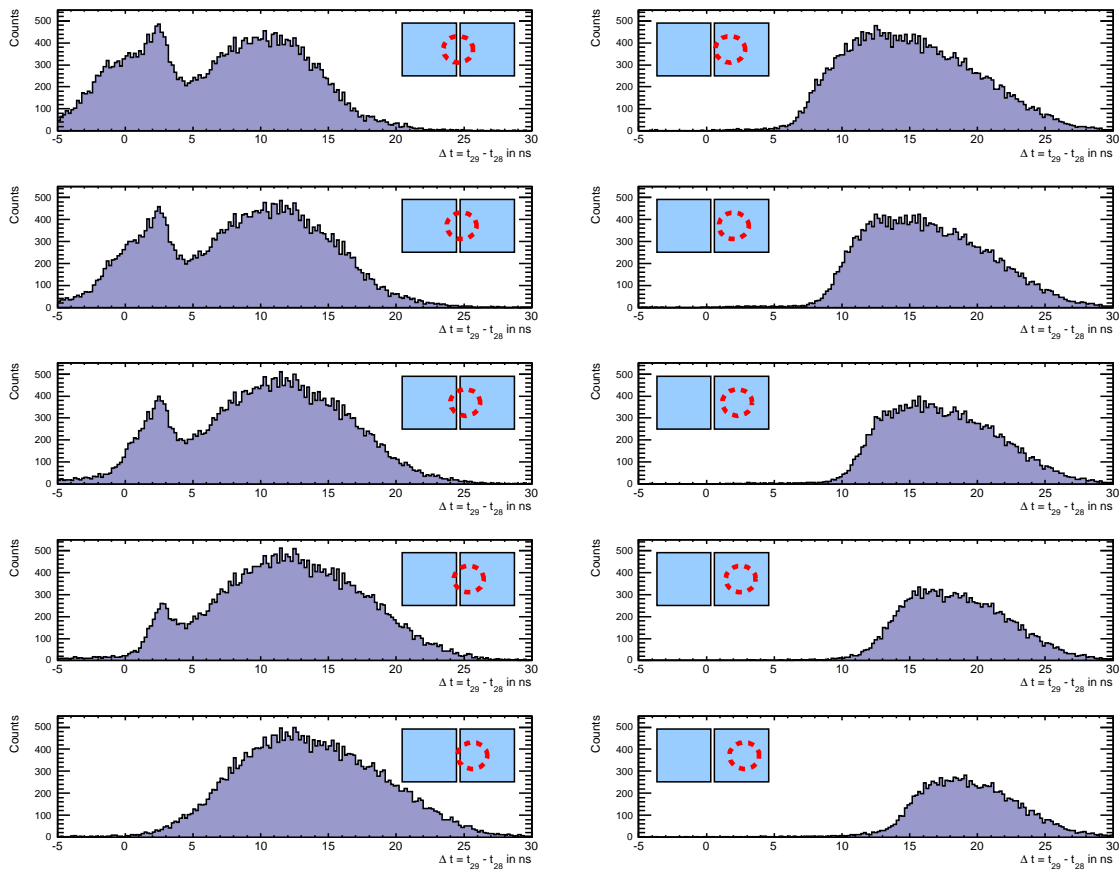
Figure 4.24: Position dependence of the timing.

4.5.2 Time Resolution

In order to overcome the time-walk effect and the dominance of a particular detector in first approximation, a similar requirement like in Eq. 4.10 for the corresponding crystals were set. But here the condition between the neighbouring modules is more strict (Eq. 4.15) and the remaining data is shown in Fig. 4.25. Furthermore, the time resolution is only evaluated for a certain range of the deposited energy in crystal 28 from $5,000\,\mathrm{MeV}$ to $6,000\,\mathrm{MeV}$. Here one can be sure that the main portion of the incoming energy of $\sim 15\,\mathrm{GeV}$ is almost equally shared between the crystals.

$$E_{28} > E_{29} \cdot 0.9 \text{ and } E_{29} > E_{28} \cdot 0.9 \tag{4.15}$$

For a final time resolution, the distribution of the events left over after the mentioned cut is displayed in Fig. 4.26. Due to the fact, that the effect of time-walk can be neglected, a symmetric distribution arises. The width is determined with a Gaussian function and results in $\sigma(\Delta t) = (623.86 \pm 20.97)\,\mathrm{ps}$. It is assumed, that crystals 28 and 29 contribute equally to the obtained resolution, since both were operating with the same gain. Therefore, to extract the resolution of a single module, $\sigma(\Delta t)$ has to be divided by $\sqrt{2}$ (compare Eq. 4.13). Finally the time resolution at a mean deposited energy of $5.5\,\mathrm{GeV}$ for a single crystal can be deduced to

$$\sigma_{28/\mathrm{time}} = \sigma_{29/\mathrm{time}} = \frac{\sigma(\Delta t)}{\sqrt{2}} = (441.14 \pm 14.83)\,\mathrm{ps}. \tag{4.16}$$

136
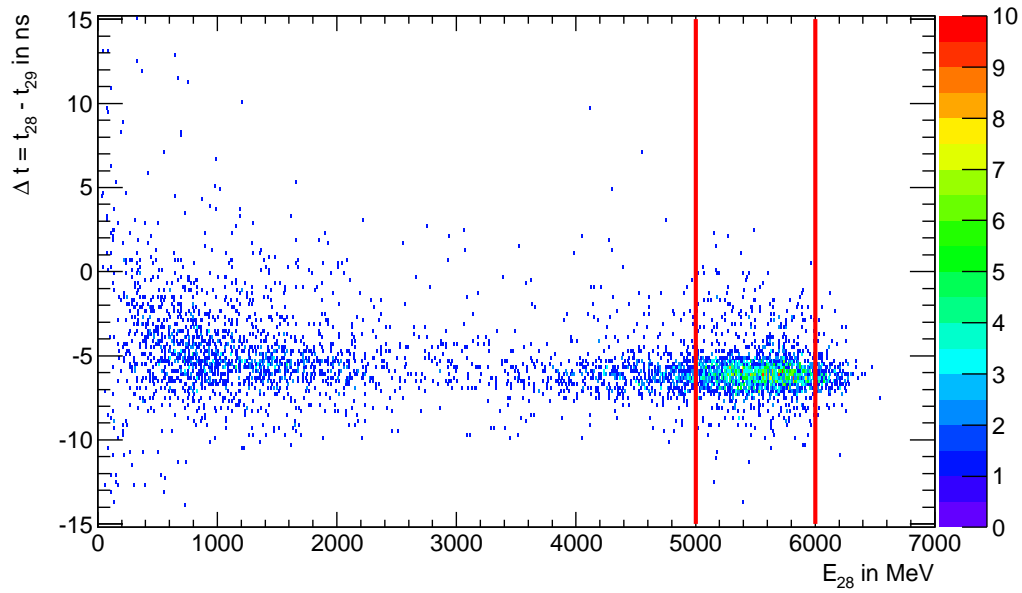
(a)
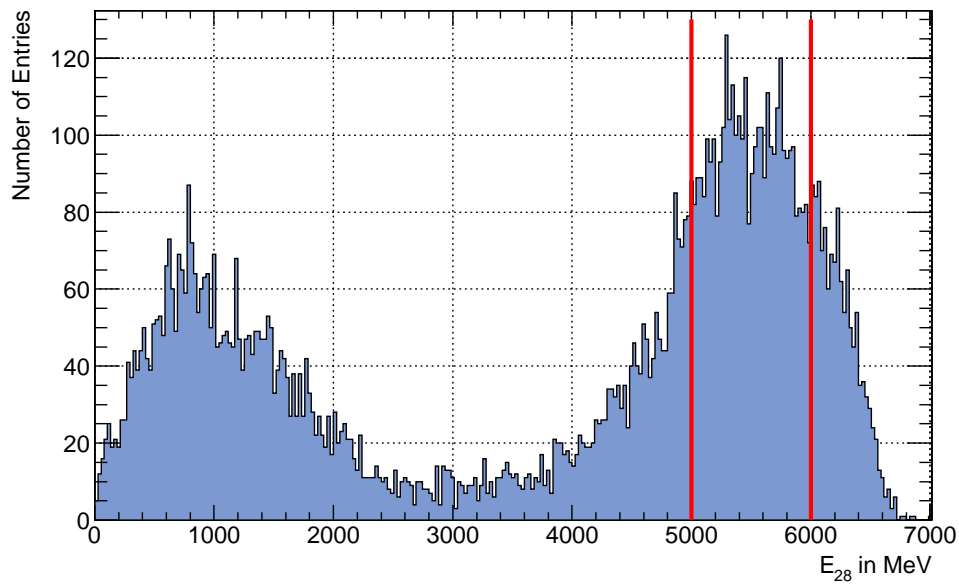
(b)

Figure 4.25: Time difference with energy cut.
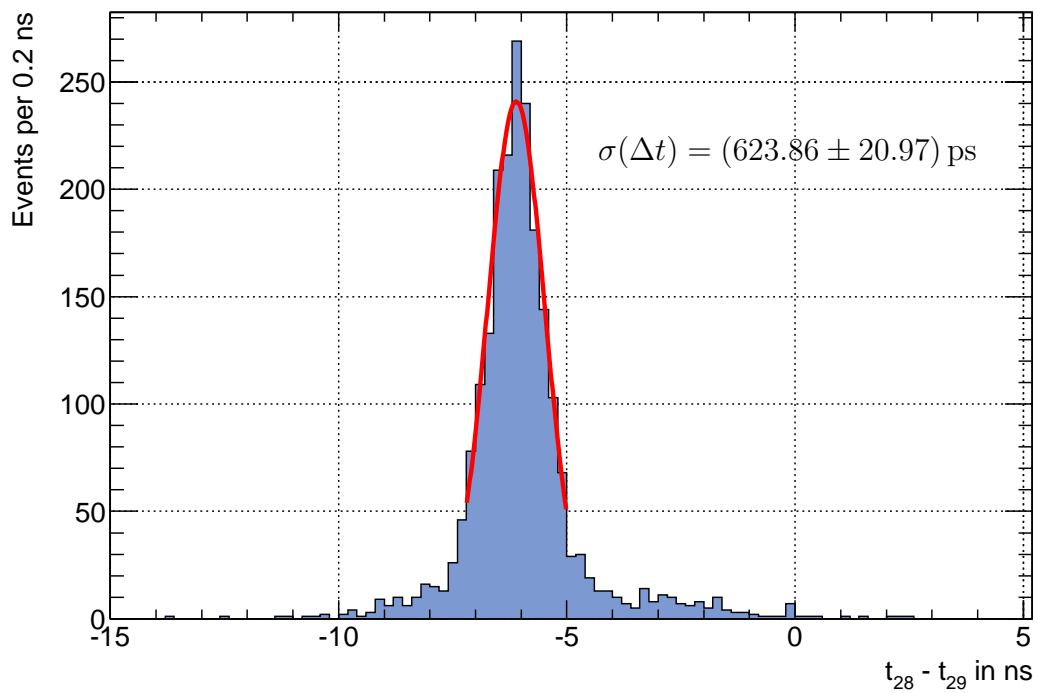
Figure 4.26: Achieved time distribution with the mentioned requirements on the deposited energy of the corresponding crystals.

Chapter 5

Higher Order Energy Correction

Usually the cross section of the individual detector modules of an electromagnetic calorimeter is driven by the Molière radius R_M of the used scintillator material. In case of PANDA and PWO with $R_M = 0.89\,\text{cm}$, crystals with an entrance face of a little bit more than $2 \times 2\,\text{cm}^2$ were produced for all crystal geometries. The major energy of an impinging particle is deposited within the crystal by an initialised electromagnetic shower, if the point of impact occurs in the centre of the front face. Nonetheless a small fraction of the shower leaks laterally out of the crystal and enters either the neighbouring crystal or the energy information is lost in the passive material in between. This effect becomes more crucial the closer the initial particle impinges to the crystal border. The following analysis studies this effect for the PANDA peak energy at $15\,\text{GeV}$ (CERN 2011) for positrons and the discrete energies from 160 to $1,440\,\text{MeV}$ at MAMI (2009) for photons. A possible correction methods for a more homogeneous energy response will be presented with respect to energy dependence and resulting energy resolution. Unfortunately only data sets are available where the prototype was shifted horizontally. An extended experimental programme at the acceleration facility ELSA[1] at Bonn is envisaged to move the prototype along the vertical y-axis. Here the effect of staggered crystal rows can be studied, which is completely ignored in the analyses of this thesis, since the front faces of all crystals in one row are almost parallel to each other. Moreover, one has to state that all corrections performed in this thesis were done along the x-axis, whereas in the final PANDA experiment the applied correction will be a function of the spherical coordinates ϑ and ϕ.

5.1 Position Dependence of the reconstructed Energy

As it was mentioned, a small fraction of the initial energy gets lost due to energy deposition in the so called 'dead material' in between the crystals, which basically

---

[1]Elektronen-Stretcher-Anlage

consists of holding structure and wrapping material (compare Fig. 3.2). To get an impression of the lost energy, Fig. 5.1 shows the reconstructed energy while shooting in between two crystals, namely 28 and 29 (black cross in Fig. 3.19). The shown data were recorded in the beamtime in 2011 at CERN with a 15 GeV positron beam. x_{Si} corresponds to the x-coordinate of the extrapolated point of impact on the PROTO60 based on the tracking information of both silicon detectors. For the extrapolation, the entry face of the PROTO60 is approximated as plane.

Fig. 5.1a and 5.1b show typical distributions of the deposited energy of two single crystals. If the major energy deposition occurs in the neighbour, a significant fraction of the initial energy is leaking to the crystal itself, which becomes visible in a long tail in both cases. By adding up all crystals of the PROTO60 matrix the energy response is almost constant except of a remaining substructure at the gap of both crystals. Here a non-negligible portion of the initial energy gets lost and directly worsens the energy resolution. The same is true for the data collected in the MAMI beamtime of 2009 with an energy range of 160 to 1, 440 MeV.

Another proof of a non-homogeneous detector performance could be extracted with the aid of the tracking detectors. The two silicon-based tracking modules in the CERN beamtime give the ability for an accurate selection of positrons with a certain point of impact on the prototype. Therefore, various data sets were selected, where each of them belong to different circular areas with a fixed diameter of 2 mm. The centre of all circles are on the same vertical position and are shifted in steps of 1 mm. For each data set the distribution of the deposited energy of the prototype was fitted with a Novosibirsk function:

$$f(E) = A \cdot e^{-\frac{\ln[1-\Lambda\tau(E-E_0)]^2}{2\tau^2}+\tau^2}, \tag{5.1}$$
$$\text{with } \Lambda = \frac{\sinh(\tau\sqrt{\ln 4})}{\sigma\tau\sqrt{\ln 4}},$$

in which A, E_0, σ and τ are free parameters. This function takes into account the asymmetric shape of the obtained line shape due to leakage by the tailing parameter τ. The maximum amplitude is represented by A, whereas the energy resolution is given by the ratio of width σ and mean value E_0. The particular obtained resolutions for each circle are shown against the x-coordinate of the circle centre in Fig. 5.2. As expected, the worst energy resolution is obtained for the data at the transition of the crystals and is peaking around 3.3%. In the case of an impinging particle in one of the crystal centres, the resolution saturates at around 1.5%. One has to state that the given absolute values for the energy resolution strongly depend on the chosen diameter of the selected area.

The aim of the introduced correction algorithms in Sec. 5.2 is to correct the energy values close to the gap to a more uniform level and thereby getting a more homogeneous energy response of the detector.
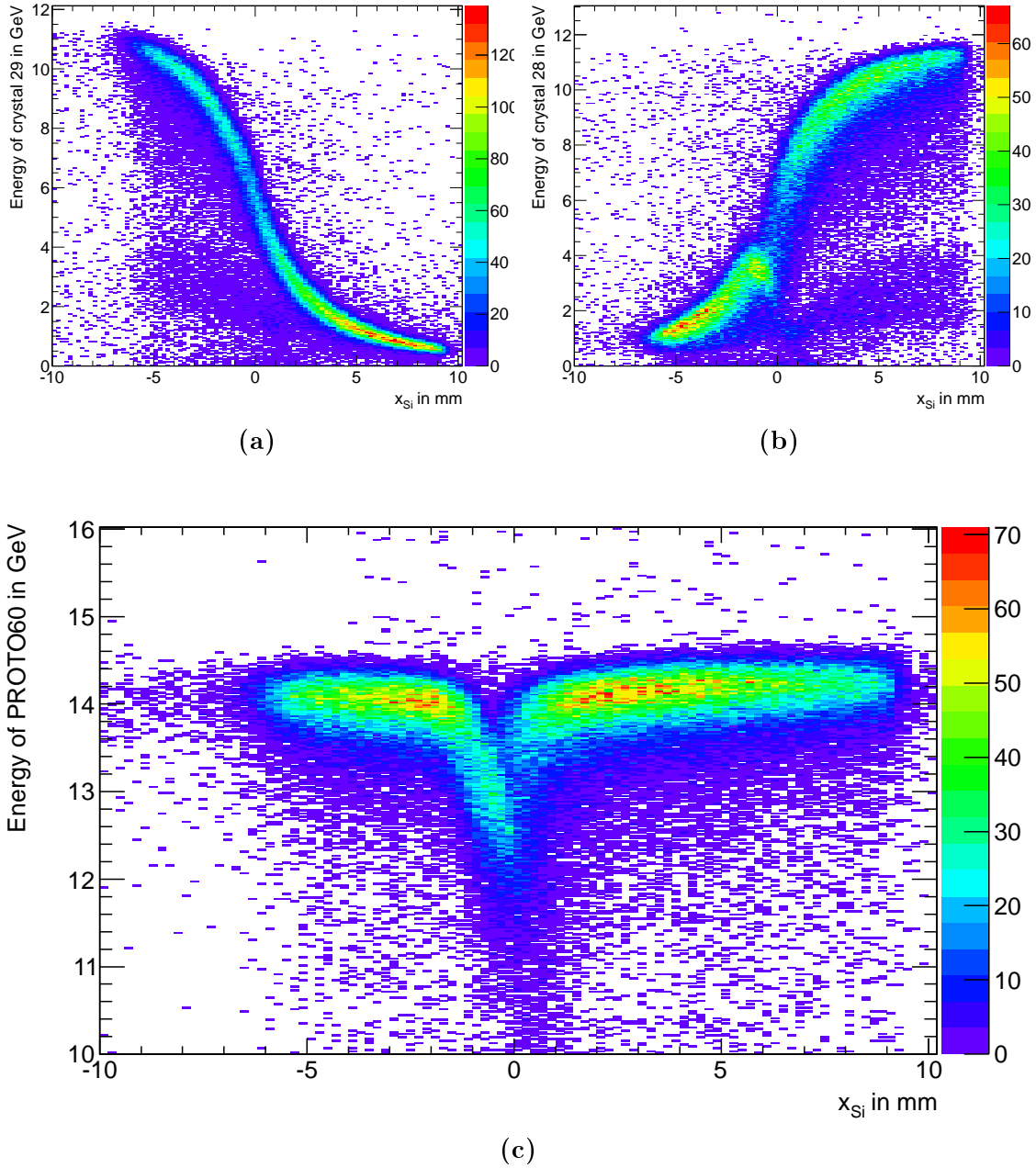
Figure 5.1: Energy spectrum in dependence of x_{Si} for (a) crystal 29, (b) crystal 28, and (c) the PROTO60. The position 0 on the x_{Si}-axis corresponds to the gap of the neighbouring crystal.
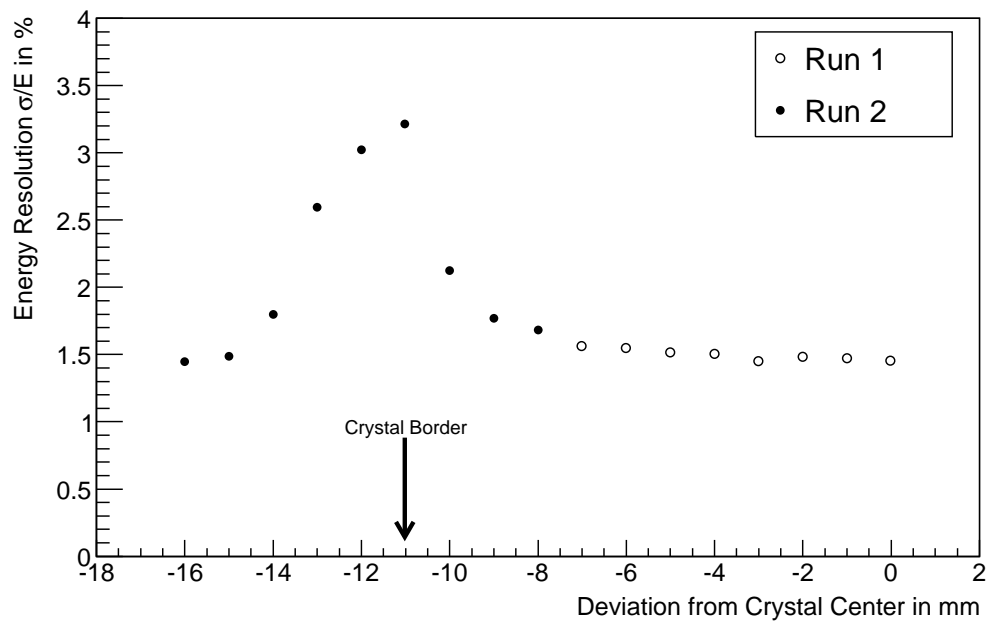
Figure 5.2: Position sensitivity of the energy resolution, in which both runs were included. At the point of transition between the crystals ($\sim -11\,\mathrm{mm}$) a clear worsening of the energy resolution becomes visible.

5.2 Correction Algorithm

Two different methods for the correction of the deposited energy were tested according to their applicability and impact to the energy resolution. The basic idea of both methods is quite similar. The point of impact along the x- or y-direction is expressed in a special parameter. Afterwards, the dependence of the deposited energy on this parameter is approximated with a function, which is afterwards applied for an energy correction.

5.2.1 $\ln\left(\frac{E_2}{E_1}\right)$-Method

The algorithm for correcting the deposited energy, which is called $\ln(E_2/E_1)$-method, was already successfully exploited by the CMS experiment [50] and its application is shown schematically in Fig. 5.3. This method is applicable in both directions in space, by rotating the displayed scheme about $90°$. In this thesis, the method will only be evaluated in x-direction due to the mentioned reasons.
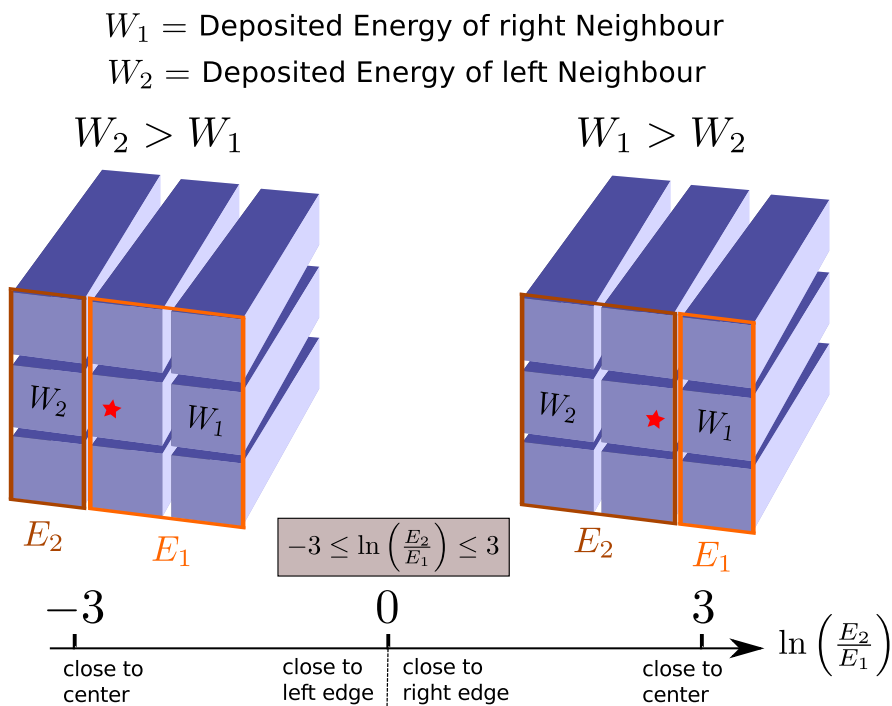
Figure 5.3: $\ln(E_2/E_1)$-method for a 3×3-matrix with view of the beam.

In the following, the $\ln(E_2/E_1)$-method is explained step by step with respect to Fig. 5.3 and the software implementation. For the important steps, the relevant pictures are shown with the obtained data from the CERN beamtime. In order to simplify the application of the $\ln(E_2/E_1)$-method, only events with a maximum energy deposition in crystal 28 were analysed.

The registered energy of the direct neighbours, which are labelled W_1 and W_2 corresponding to the right and the left neighbour, respectively, are compared. This already gives a rough information about the point of impact and is marked in Fig. 5.3 with a red star. According to the distinction of cases for W_1 and W_2, the 3×3 detector matrix is subdivided in two subarrays with summarised energies E_1 and E_2. Afterwards the natural logarithm of the ratio E_2/E_1 gives the final information about the point of impact along the regarded direction at the crystal with maximum energy deposition. The choice of the natural logarithm is connected with the lateral shower spread of the electromagnetic shower. Due to the fact, that the value of $\ln(E_2/E_1)$ is not very intuitive, the axis in the bottom part of Fig. 5.3 shows the corresponding position at the crystal front face. $\ln(E_2/E_1)$ ranging from -3 to 3, whereas $|\ln(E_2/E_1)| \approx 3$ belongs to events with a centrally striking incident particle. In case of $\ln(E_2/E_1) \approx 0$, the energy is almost perfectly shared between the two subarrays and belongs to an impinging particle close to one of the crystal borders. The correlation of the $\ln(E_2/E_1)$-parameter with the impact position along the x-axis is shown for both performed runs in Fig. 5.4. Here, it was distinguished between the reconstructed point of impact by the EMC with a logarithmical point of gravity algorithm (compare Eq. 5.2) and the extrapolated track by the silicon based tracking detectors.

$$x_{\text{reconstructed by EMC}} = \frac{\sum_i w_i \cdot x_i}{\sum_i w_i} \tag{5.2}$$

$$\text{with } w_i = \begin{cases} 0, & W_0 + \ln\left(\frac{E_i}{E_T} \leq 0\right) \\ W_0 + \ln\left(\frac{E_i}{E_T}\right), & \text{else;} \end{cases}$$

$$x_i : \text{ implemented coordinate of crystal } i$$
$$W_0 : \text{ weighting parameter}$$
$$E_T = \sum_i E_i$$

Furthermore, the similarity of the associated histograms in Fig. 5.4 underlines effective operation of reconstruction algorithm of the point of impact (Eq. 5.2), since it delivers an almost perfect linear correlation with values obtained by the tracking units.

In a next step, the obtained distribution of the $\ln(E_2/E_1)$-parameter of the second run (shown in Fig. 5.5a) is subdivided into 50 equal slices ranges from -3 to 3 with a width of 0.12. Here, no explicit cut on the tracking system was set, since the whole algorithm is based only on the information obtained by the EMC. For the events of the i-th slice,

(a)

(b)

(c)

(d)
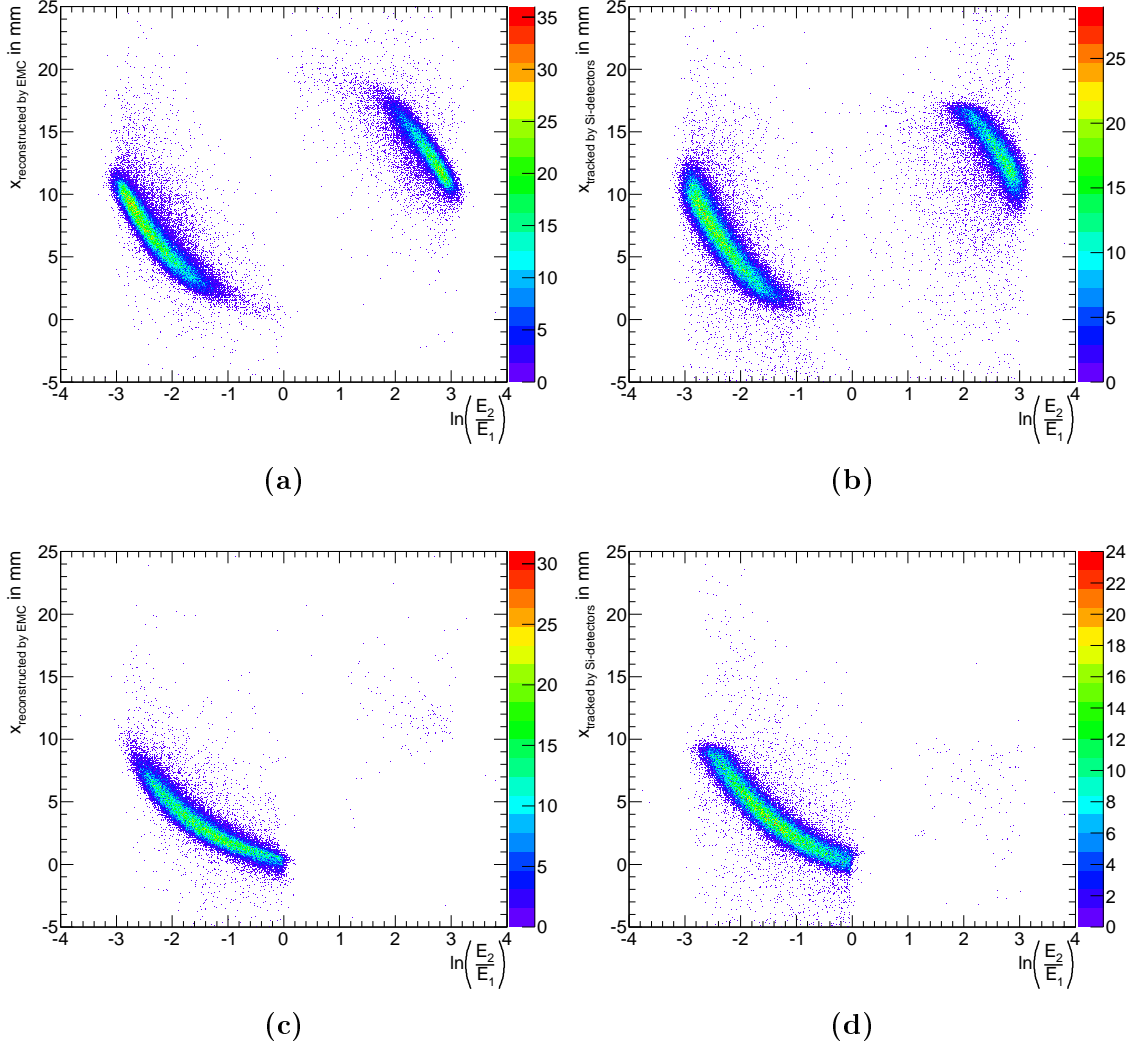
Figure 5.4: Correlation between $\ln(E_2/E_1)$ and the x-coordinate of the point of impact. For a better comparison, only events with an unambiguous reconstructed track of the impinging particle by the tracking devices are shown. Figures (a) and (b) belong to the performed run, where the beam was aimed to the centre of crystal 28 and (c) and (d) to the one in between crystals 28 and 29. Furthermore, the columns correspond to the x coordinates obtained by the pure EMC energy information (according to Eq. 5.2) and the reconstructed track by the tracking detectors. The position 0 corresponds in all cases to the transition of crystal 28 and 29.

which fulfil $0.12 \cdot i - 3 \leq \ln(E_2/E_1) < 0.12 \cdot (i+1) - 3$ with $i \in \{0, 1, 2, \ldots, 49\}$, the deposited energy of the whole 3×3-matrix is plotted and fitted with the Novosibirsk function (Fig. 5.5b). The individual histograms were rebinned and appropriate start parameters for the fit were set to get a reasonable description of the data. To show the application of this correction method, only events for $\ln(E_2/E_1) < -0.1$ were analysed further and corrected, respectively.

In a next step, the mean-parameter of the applied fits in Fig. 5.5b is normalised and plotted in dependence on $\ln(E_2/E_1)$. The trend can be well described with a polynomial of fifth order (Fig. 5.6), which in the following will be called $f(x)$, with $x = \ln(E_2/E_1)$.

Finally, the corrected energy information of the 3×3-matrix can be obtained by dividing the original energy information by $f(x)$:

$$E_{3\times3/\text{new}} = \frac{E_{3\times3/\text{old}}}{f(x)}. \tag{5.3}$$

To see the final achievement of the position correction of the regarded events, Fig. 5.7 shows the corrected 3×3-energy as a function of the tracked x-coordinate and as line shape, which represents the projection on the energy-axis, in comparison to the uncorrected data. Especially close to the crystal border at $x_{\text{Si}} \approx 0\,\text{mm}$, a clear enhancement is visible (Fig. 5.7a), whereas the data at the crystal centre remains almost untouched. This has a direct impact on the tail of the line shape (Fig. 5.7b), which is in case of the corrected one significantly smaller. Already now, it can be seen by eye that the mean value of the distribution becomes larger and the broadness has been reduced.

In order to obtain a quantitative comparison of the result, the lineshapes are fitted with the Novosibirsk function (Eq. 5.1). The energy resolution is, as usual, extracted by dividing the width σ by the mean value E_0. For completeness, the explained procedure was also performed for the first run in the CERN beamtime, where the particle beam was aimed to the centre of crystal 28. For a better comparison, the results are summarised in Tab. 5.1. As expected, the width of the reconstructed line shape is in general broader in the case of run 2. Additionally, the mean value shows a difference of roughly $40\,\text{MeV}$. This can easily be explained with the evaluated 3×3-matrix, which was in all cases the same, namely the crystal 28 and its first surrounding ring. It is obvious that more energy can be deposited, if the initial point of the electromagnetic shower is in a central position of the regarded matrix. This also holds for the fluctuations. The probability for a lateral shower leakage is significantly higher for the run where the beam strikes in between the crystal, and directly results in an increase of the width. Nevertheless, after application of the correction algorithm, the detector shows a significantly more homogeneous behaviour (right column of Tab. 5.1). Furthermore, it can be seen that the correction algorithm only has a minor impact on the final energy resolution. In the case of the second run an absolute improvement of $0.3\,\%$ could be achieved.

146
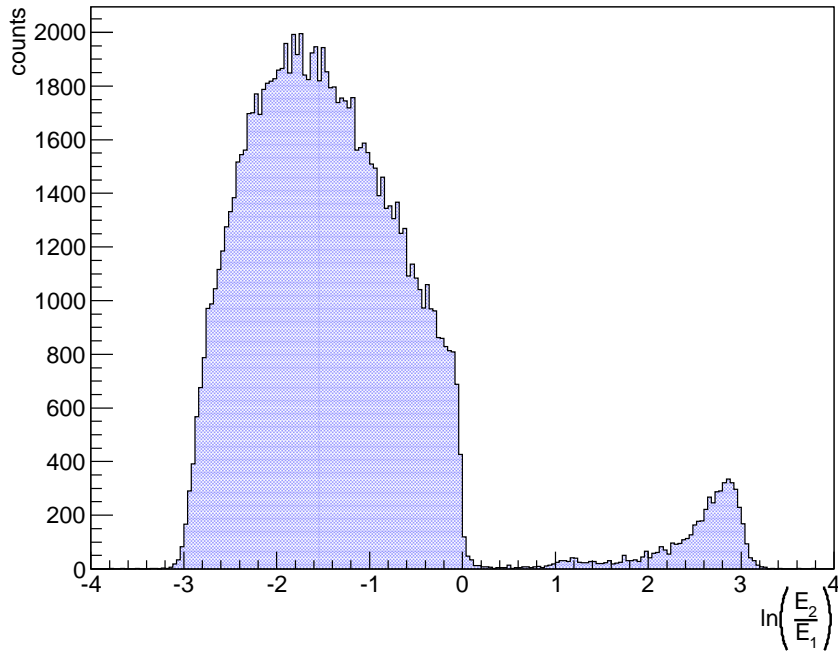
(a)
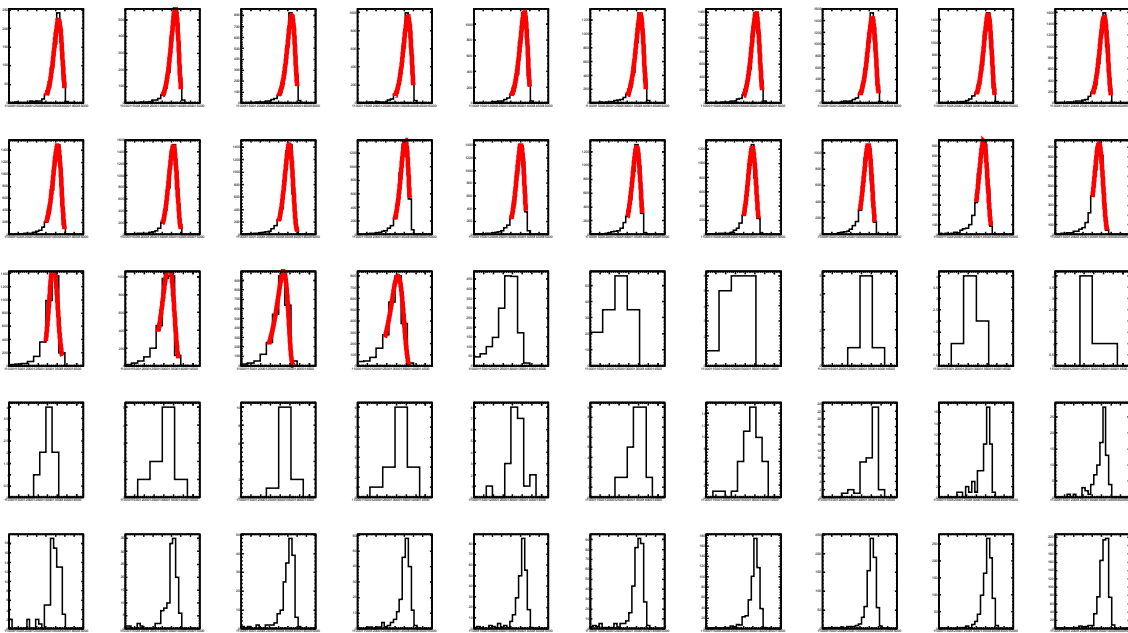
(b)

Figure 5.5: (a) Distribution of $109,400$ events as function of the $\ln(E_2/E_1)$-parameter. For the majority of events, the incident particle impinges on the left half of the crystal. (b) Subsections of the $\ln(E_2/E_1)$-parameters fitted with the Novosibirsk function (Eq. 5.1) marked with red lines.
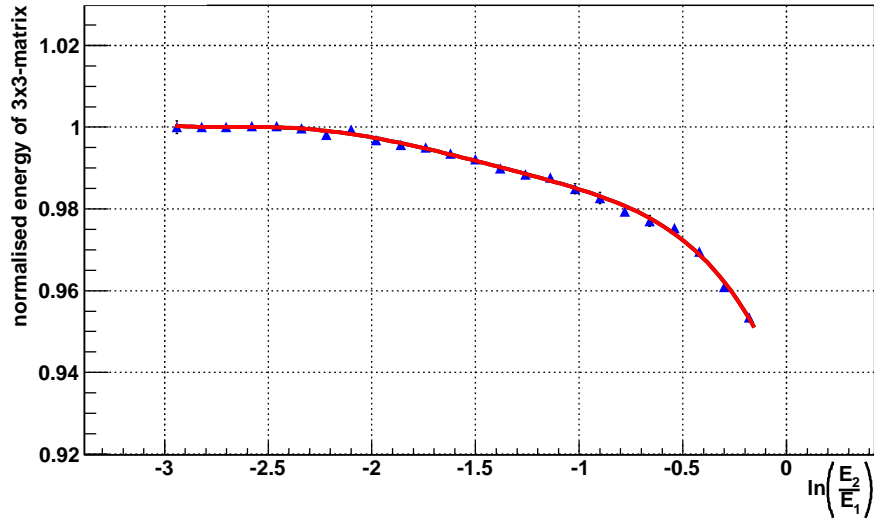
Figure 5.6: Dependence of the $\ln(E_2/E_1)$-parameter of the deposited energy within the 3×3-matrix. The fitted function $f(x)$ is marked in red and shows a good description of the data points.

Run	Parameter	Uncorrected	Corrected
	Width σ/MeV	227.20	221.87
1	Mean value E_0/MeV	13,979.50	13,994.60
	Energy resolution $\frac{\sigma}{E_0}$/%	1.625	1.585
	Width σ/MeV	257.12	230.31
2	Mean value E_0/MeV	13,562.00	13,644.10
	Energy resolution $\frac{\sigma}{E_0}$/%	1.896	1.688

Table 5.1: Achieved results for the 3×3-matrix of the $\ln(E_2/E_1)$-method for both runs at CERN. For the listed results, the correction method was only applied along the horizontal x-direction.
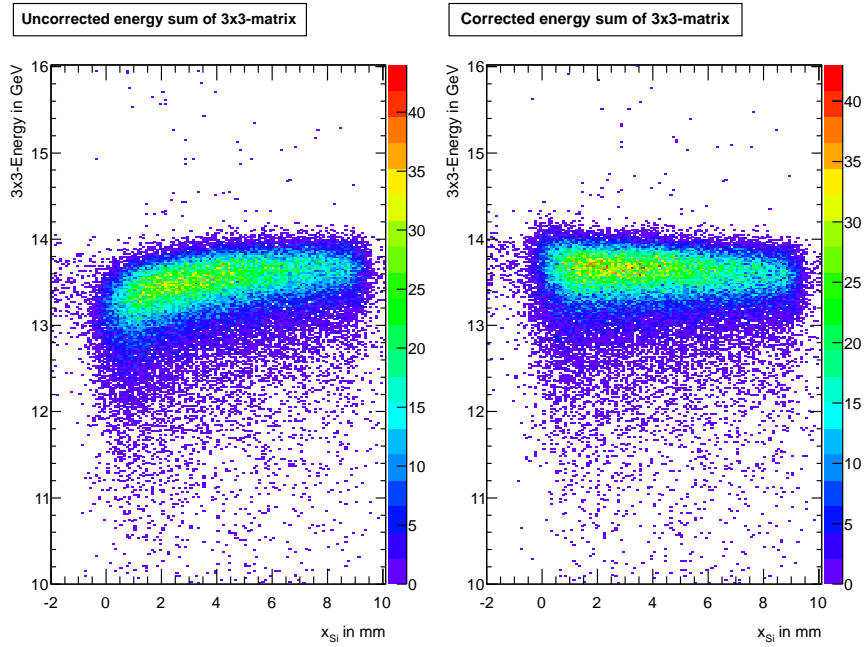
(a)
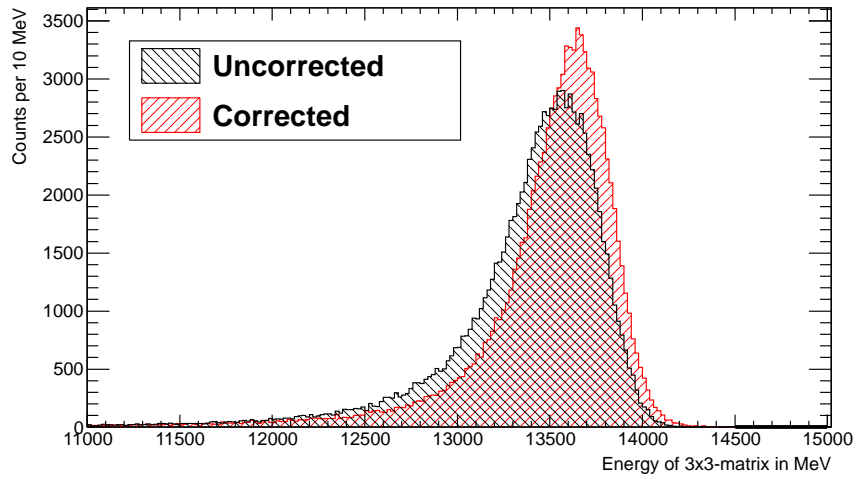
(b)

Figure 5.7: Results position correction for run 2 for events with a maximum energy deposition in crystal 28.

A similar improvement could be achieved along the vertical axis, which is not shown in this thesis. This is connected to the fact that the majority of events impinges close to the crystal centre. As it was mentioned, the next beamtimes with the PROTO60 and other prototypes are envisaged to cover a vertical shift as well, and to study in addition the effect of the staggered crystal alignment.

5.2.1.1 Energy Dependence

The $\ln(E_2/E_1)$-method, described in Sec. 5.2.1, was, for the first time, successfully applied for a PANDA prototype. The next question concerns the energy dependence of this correction algorithm. For the beamtime at MAMI in 2009, a large amount of data is available for different energies from $150 - 1,500\,\mathrm{MeV}$. The data is analysed in the same way as before, but here one has to distinguish between the different energies. The aim of this part of the analysis is to figure out a possible energy dependence of this kind of correction and to see the final impact on the obtained energy resolution. Altogether, four runs were performed in the beamtime 2009 at MAMI. It is expected to get the largest improvements in run 3, where the beam impinged in between two crystals. For completeness and comparison issues, the other runs were analysed as well. Fig. 5.8 shows the energy deposition in the whole PROTO60 for a low and high energetic tagger channel, while the beam was directed between two crystals, labelled here as 35 and 36 (compare Fig. 3.18). Here it is again nicely visible that the deposited energy within the PROTO60 gets significantly smaller for a point of impact close to the crystal borders.

(a) (b)
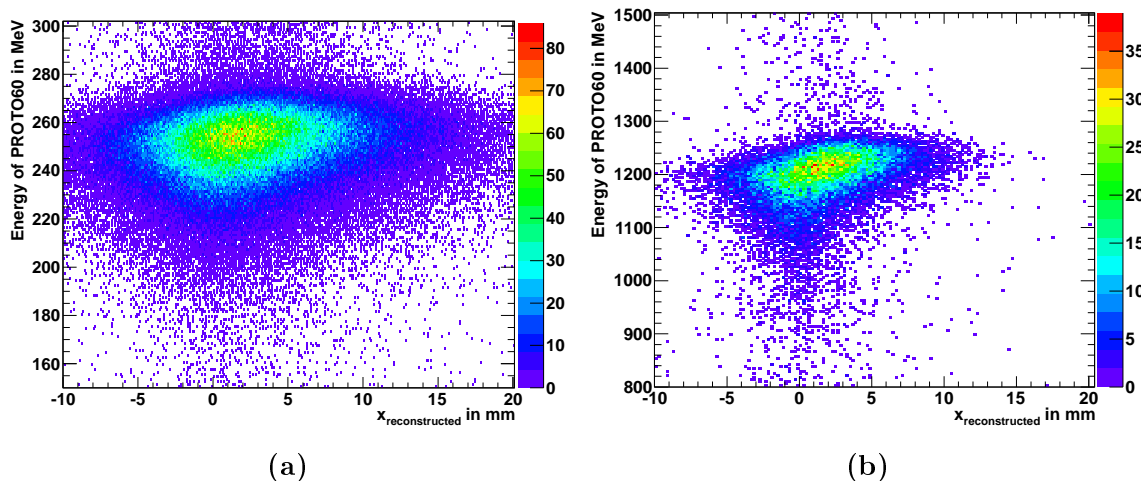
Figure 5.8: Energy spectrum in dependence of $x_{\mathrm{reconstructed}}$ for (a) low energy and (b) high energy. The position 0 on the $x_{\mathrm{reconstructed}}$-axis corresponds to the gap between both crystals. No further cut was required on the pictures.

For correcting the data, the $\ln(E_2/E_1)$-method was applied separately for the different energies. The get the best possible starting point of the analysis concerning statistics, the data of all four runs were summed up. At each incident energy, the $\ln(E_2/E_1)$ parameter was subdivided in to 50 bins with equal width and is shown exemplary for the tagger channel 12 with an incident photon energy of 355.88 MeV in Fig. 5.9. In order to get appropriate fits of the individual subsections, only bins with at least $1,000$ events were considered and analysed. The tagger channel selections the highest energy was completely excluded due to the insufficient amount of events.
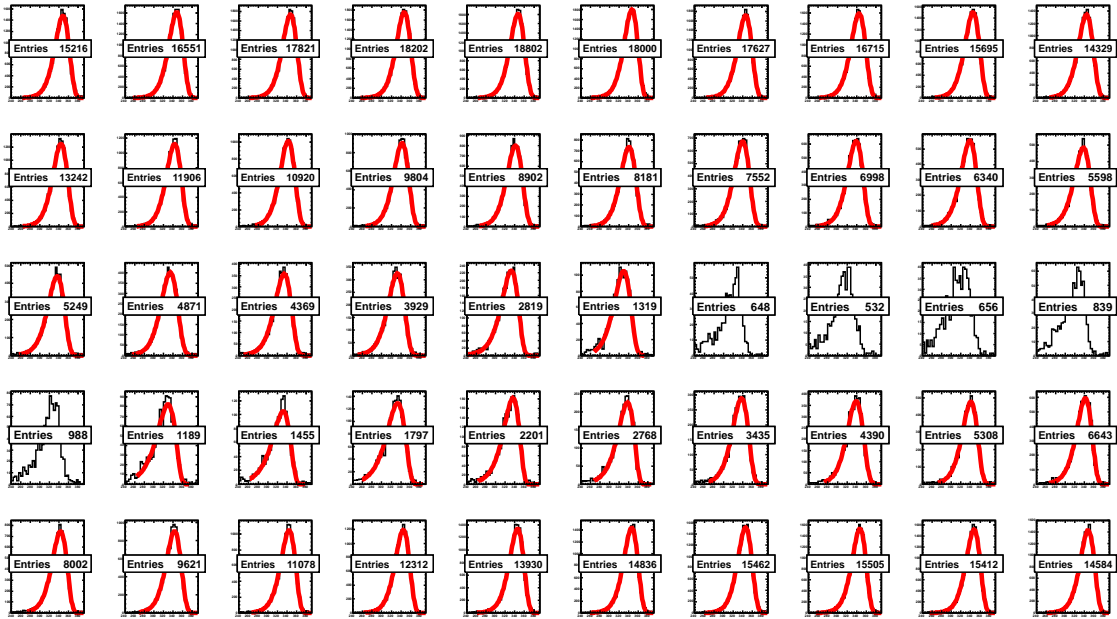
Figure 5.9: Energy distribution in MeV for different $\ln(E_2/E_1)$-parameter (MAMI 2009) for a single tagger channel. The red curves correspond to the applied fit with a Novosibirsk function for histograms with more than $1,000$ events.

In Fig. 5.10a the obtained mean values of the performed fits are plotted as a function of the $\ln(E_2/E_1)$-parameter including the corresponding polynomials. The higher the energy, the smaller the amount of available data. For a better comparison, the obtained correction polynomials are plotted separately and normalised to the $\ln(E_2/E_1)$-value of -3 and 3, respectively.

On the right hand side of Fig. 5.10a less data points are available, especially for the highest energies. Therefore the fit range, or correction range, respectively, is rather limited. The shapes of all correction curves are similar and getting smaller close to the crystal border at $\ln(E_2/E_1) \approx 0$. In a relative view in Fig. 5.10b, only very small deviations in the order of 1% are visible. Here, no correlation with the energy could be registered. By comparing to the obtained correction function at 15 GeV (Fig. 5.6), there is no significant difference. As an additional remark, the shift at $\ln(E_2/E_1) \approx 0$
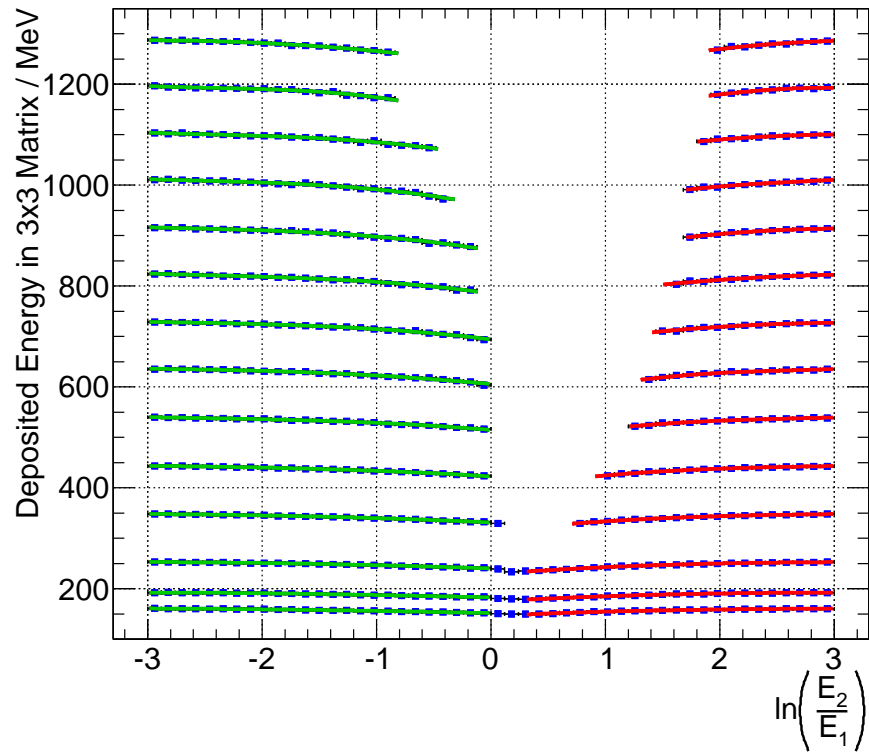
(a)
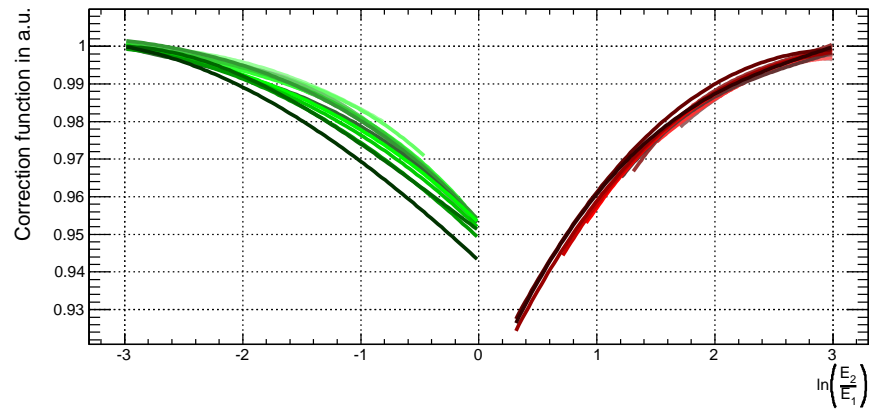
(b)

Figure 5.10: (a) Correction functions of all energies (MAMI 2009). (b) Correction functions for all energies normalised to the energy deposition at $\ln(E_2/E_1) = -3$.

for the both curves from the left and right hand side, respectively, might be caused by a non-perfect alignment of the crystal with respect to the beam axis.

5.2.1.2 Impact on Energy Resolution

In order to see the final achievement concerning the most important observable, the resolution of the uncorrected and corrected energy was determined. Therefore the data was channel-wise corrected using the correction functions as displayed in Fig. 5.10. For the third run (shooting in between crystal 35 and 36), where the major impact of the correction is expected, the lineshapes of the 3×3-matrix are plotted for all energies in Fig. 5.11. The tagger channel with an energy of $1441.06\,\mathrm{MeV}$ was excluded due to insufficient statistics.
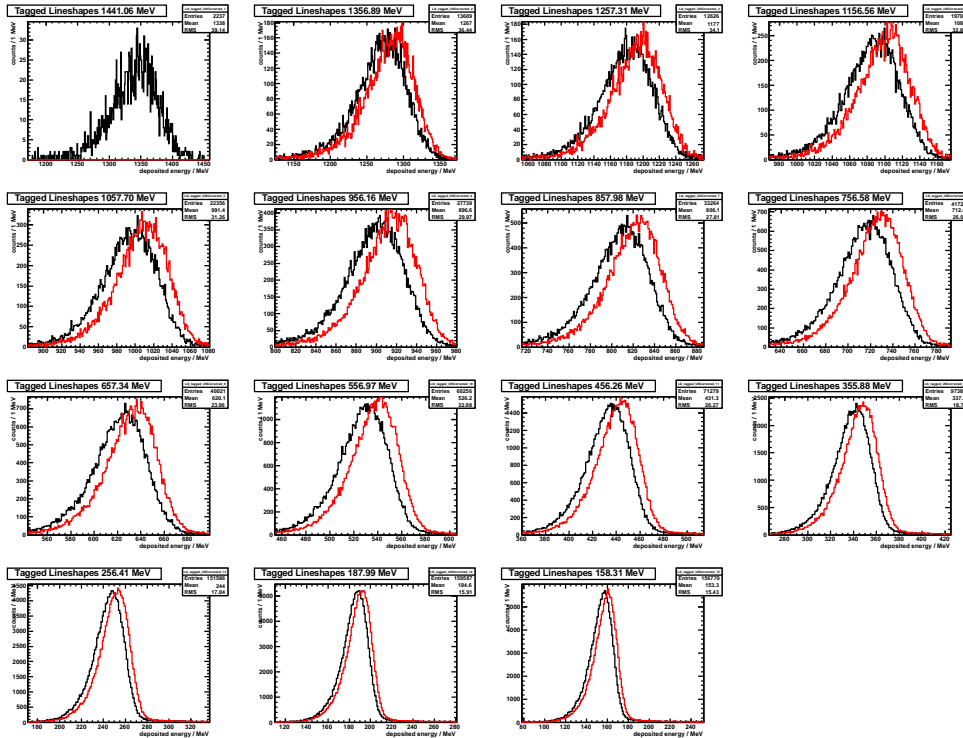
Figure 5.11: Uncorrected (black) and corrected (red) lineshapes of the 3×3-matrix with a threshold of $1\,\mathrm{MeV}$. For the highest energy no correction was possible due to the insufficient statistics.

Afterwards, the lineshapes were fitted with the Novosibirsk function, in which the energy resolution is given by the ratio of width and most probable value. For fitting purposes, appropriate start values for E_0 and σ were set, namely mean value and RMS

of the particular histogram, respectively. This promises a stable and automatic fitting procedure. For the run where the major impact is expected, the lineshapes for the uncorrected and corrected values are shown in Fig. 5.11. The final results for two runs (centrally hitting crystal 35, and in between 35 and 36) of the 2009 beamtime at MAMI are presented as a function of the impinging energy. In addition, the obtained trend of the data points is fitted with the typical three parametric function for describing the energy resolution of an EMC:

$$\frac{\sigma}{E} = \sqrt{\left(\frac{a}{\sqrt{E}}\right)^2 + \left(\frac{b}{E}\right)^2 + c} \tag{5.4}$$

$$\tag{5.5}$$

The free parameter a stands for photon statistics and has a $1/\sqrt{E}$-dependence. b is usually smaller compared to the other parameters and describes the contribution caused by electronics. This term decreases faster with the energy with a $1/E$-dependence. The constant term c includes several systematical effects, like e.g. calibration issues or the inhomogeneous collection of the scintillation light within the crystal. The individual terms are summed up quadratically, since one can, in first order, assume their independence. The result of a fit using Eq. 5.4 gives a rough impression of the discussed effects. For all performed fits of the trend of the energy resolution, the data points were weighted equally. The vertical error bars were determined with the usual error propagation method (compare Eq. 5.6), but are not visible in the chosen y-range in Fig. 5.12 and 5.13. For the x-direction a constant uncertainty of $2\,\mathrm{MeV}$ was assumed.

$$\Delta\left(\frac{\sigma}{E}\right) = \sqrt{\left(\frac{1}{E}\right)^2 \cdot (\Delta\sigma)^2 + \left(\frac{\sigma}{E^2}\right)^2 \cdot (\Delta E)^2} \tag{5.6}$$

The energy resolutions of the first run are shown in Fig. 5.12.
As expected, an overall correction of the deposited energies only has a small impact on the final energy resolution. Furthermore, the displayed fit parameters according to Eq. 5.4 do not differ much for both scenarios. Nevertheless, a slight improvement is visible along the full energy range. The difference $(\sigma/E_{\mathrm{Peak}})_{\mathrm{uncorrected}} - (\sigma/E_{\mathrm{Peak}})_{\mathrm{corrected}}$ is ranging from $0.11\,\%$ to $0.04\,\%$ from the smallest to the highest energy, respectively. However, in the case of shooting in between crystals, the energy correction leads to a significant improvement. In Fig. 5.13 the obtained results are again plotted versus the incident photon energy.

A significant difference between the shown curves becomes visible and is fluctuating around an absolute value of $0.25\,\%$. This improvement is comparable to the result obtained at the CERN beamtime with $0.3\,\%$ at an initial positron energy of $15\,\mathrm{GeV}$.
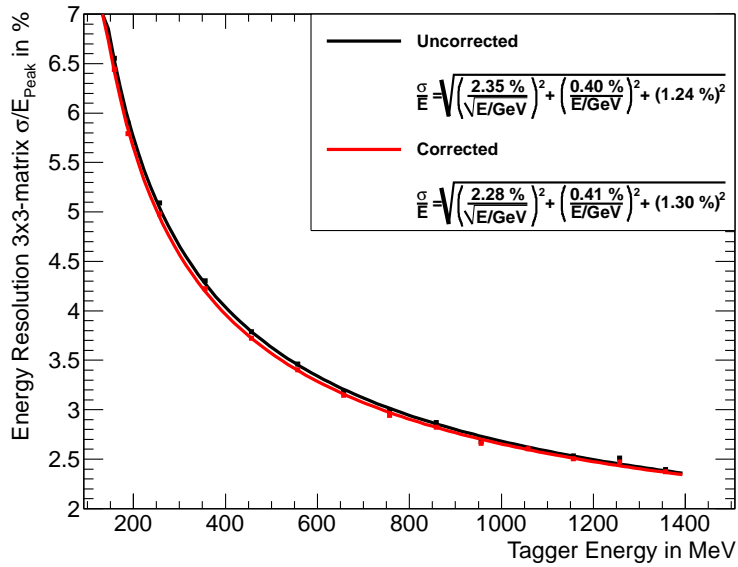
Figure 5.12: Uncorrected (black) and corrected (red) energy resolution for run 1 (MAMI 2009) including the fits according to Eq. 5.4.
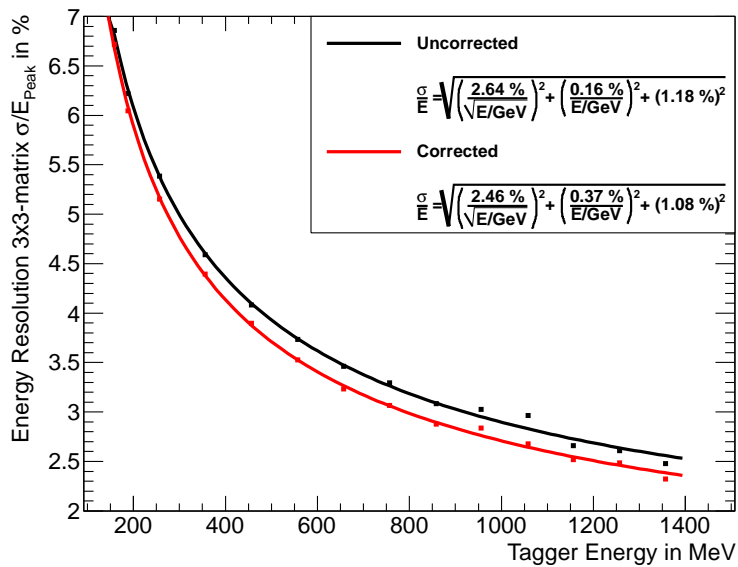
Figure 5.13: Uncorrected (black) and corrected (red) energy resolution for run 3 (MAMI 2009) including the fits according to Eq. 5.4.

Chapter 6

Discussion & Outlook

This chapter is subdivided into three parts to summarise and discuss the presented results in Secs. 2, 4 and 5. The achieved quality of 9, 336 produced PWO[1] crystals from BTCP was already shown in detail in Sec. 2.4. In the first section of the discussion, those results are compared to the obtained quality parameters of the preceding CMS experiment. In addition, an outlook will be provided with respect to the crystals produced by SICCAS and the completion of the PANDA EMC.

In Sec. 6.2 the next main topic concerning time resolution is covered. A comparison to the achieved timing performance of CMS will be given as well. Furthermore, achievable limits with PWO and components, limiting modules for a more accurate time determination, are discussed. An interesting alternative option regarding timing via the detection of Cherenkov light is considered to further improve the time resolution to a higher level.

Sec. 5 shows the successful exploitation of the so called $\ln(E_2/E_1)$-method in various beamtimes for different impinging particles. But there are also other possibilities to correct for the energy loss in the passive material between the crystals, which differ in their applicability.

6.1 Quality Control

Basically, the crystals produced by BTCP show excellent properties, especially in case of the longitudinal transmission (compare Fig. 2.18). Almost all crystals show an optical transmittance at the three relevant wavelengths far above the specified requirements. Only a handful of crystals show an insufficient transmission, mostly at 360 nm. The transmission at 360 nm is important and very selective, since it is significantly correlated with the overall LY of a crystal, which was already proven by previous studies [51]. This relation can at a later stage be exploited as a first order energy calibration of the EMC and is shown exemplary for all crystals of type 1 in

---

[1]Lead tungstate (PbWO$_4$)

Fig. 6.1.
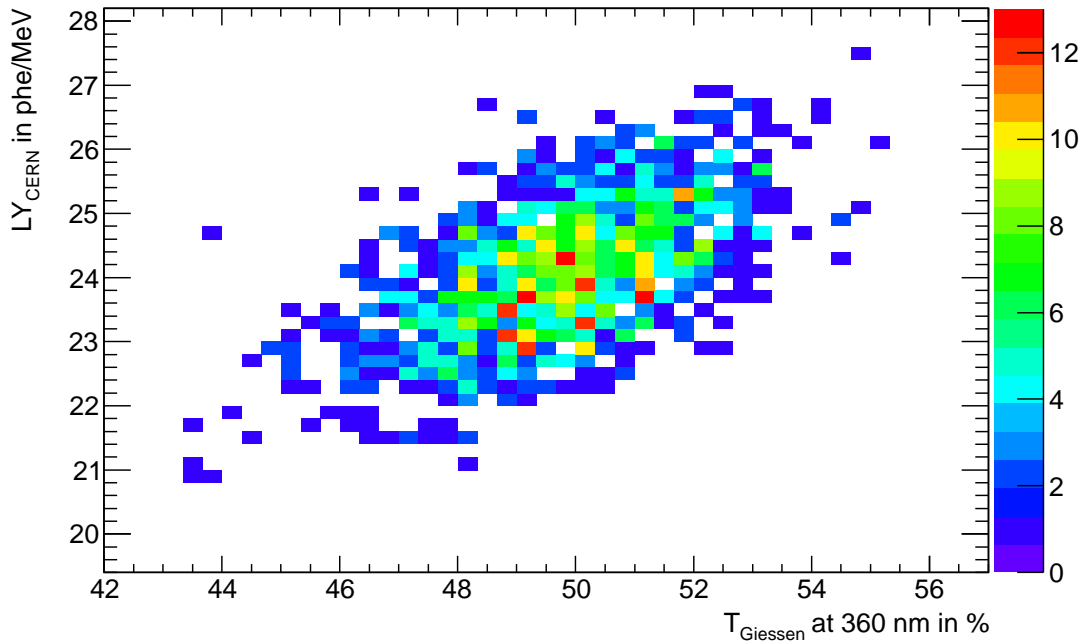
Figure 6.1: Correlation between light yield and transmission at 360 nm for all crystals of type 1 with a correlation coefficient of 0.591.

The parameter $LY(0.1\,\mu s)/LY(1\,\mu s)$, which guarantees a sufficiently fast scintillation kinetics of each crystal, was not selective, since this parameter was considered never a reason for rejection (compare Fig. 2.7). In a similar manner, the geometry of the crystals is not being problematic, in spite of the fact that there are some tails of the displayed distributions (Fig. 2.19) which exceed the rejection limit of $0/-100\,\text{mm}$. Deviations in the order of tens of μm from the desired size can easily be compensated by an appropriate wrapping. Especially the distribution of the length of the crystal shows a significantly large tail towards a shorter length. Here one has furthermore the option to compensate this imbalance with a reduction of the thickness of the optical glue. Overall, there is no urgent necessity to suspend crystals, which slightly fail the requirements with respect to geometry, but shows, on the other hand, satisfying results. For the geometry parameters labelled with AF, CF, AR and CR, some additional substructures are visible at values larger than 0.1 mm, which originate exclusively from crystals of the last lot. These structures are not visible in the test values provided by BTCP. There are different possible explanations, like for instance a systematic change of the 3D-laser device of the ACCOS machine at CERN, probably caused by the long time interval between testing lot 9 and 10. As another explanation, these crystals

might have been cut in a different way, since the mentioned geometrical imperfections only refer to one surface of a crystal. Nevertheless, as mentioned before, there are different possibilities to compensate those geometrical defects.

The next critical requirement concerning quality control is the homogeneity of the transversal transmission, which is quantified by the $\Delta\lambda$-parameter (defined in Eq. 2.4). Here, the relevant distributions can be found in Fig. 2.22, in which the majority of crystals shows a $\Delta\lambda$-parameter well below the limit of 3 nm. From that point of view, one can confirm an excellent longitudinal homogeneity due to the Czochralski method exploited by BTCP. The different shapes of the distributions from BTCP and CERN originate from a different measurement concept of crystal geometries as clarified in Sec. 2.4.6.

The probably most important performance parameter is the light yield which was determined as explained in Secs. 2.3.1 and 2.3.2 via irradiation with low energy photons from a radioactive source. During the analysis of the first delivered lots, which contained primarily crystal types with a large difference in tapering, namely type 1 and EC, a strong correlation with the crystal geometry could be observed and is also visible in Fig. 2.21. This dependency is due to an interplay between absorption and focussing of the generated scintillation light and is known as NUF-effect. It has a significant impact on the final performance of the EMC, especially in case of energy and position resolution. Those aspects, including possible uniformity methods, are in detail evaluated and discussed in [31]. With the knowledge of the NUF-effect, it is astonishing that in Fig. 2.21, the less tapered crystal geometries, like e.g. type 2 and 3 have a higher light yield than type 1, which represents the most tapered version of the used PANDA geometries. But this could be addressed to a by far later date of delivery. The later the date of delivery, the higher the light output of the crystal, since the supplier gathers more experience in the composition of the crystal melt, the purification, and the growing process. The result of an enhanced light yield for crystals, which were delivered at a later stage, is also visible in the case of crystals of type 10. In the corresponding distribution in Fig. 2.21, two structures are present related to crystals part of lot 8 and 10, respectively. In case of the LY, it can be summarised that only the least tapered crystals for both end caps can come close to the rejection limit of 16 phe/MeV. This is documented in Fig. 2.29.

To guarantee the long term stability of the EMC, a sufficient radiation hardness is mandatory. In order to judge if a crystal has a sufficient transmittance and is able to cope with the induced radiation dose, the change of the absorption coefficient Δk for a given integral dose of 30 Gy was determined. This is the most crucial parameter with respect to the rejection limit of $1.1\,\mathrm{m}^{-1}$ leading to an overall rejection rate of approximately 6 %, independent of the crystal geometry. However, the most radiation hard crystals were found among the EC-geometry. This offers the possibility to select those for the inner part of the FEC which will be exposed to the highest expected radiation dose.

A summary of the absolute rejection numbers distinguished by the different relevant

parameters is given in Tab. 6.1.

Property	Rejection limit	Rejection number	Percentage
longitudinal transmission[1]	$T(360\,\mathrm{nm}) \geq 35\,\%$	15	1.61 ‰
	$T(420\,\mathrm{nm}) \geq 60\,\%$	3	0.32 ‰
	$T(620\,\mathrm{nm}) \geq 70\,\%$	2	0.21 ‰
transversal transmission[2]	$\Delta\lambda \leq 3\,\mathrm{nm}$	19	2.04 ‰
light yield[2]	$LY \geq 16\,\mathrm{phe/MeV}$	95	1.02 %
radiation hardness[1]	$\Delta k \leq 1.1\,\mathrm{m}^{-1}$	553	5.92 %
Total rejection number		651	6.97 %

Table 6.1: Rejection summary of the first 10 lots. [1]: measured at Gießen; [2]: measured at CERN. The total rejection number considers possible overlaps among the parameters.

6.1.1 Further Aspects

Test facilities deliver partially uncorrelated results. These differences mainly originate from different treatments of the crystals within the test procedure, which were not completely fixed in the contract with the supplier BTCP. Sources of uncertainty are for instance the time after irradiation for the determination of the Δk-parameter. Here variations can occur due to the presence of a fast recovery component (compare Fig. 2.15). Furthermore, the strong impact of the explained NUF-effect on the chosen way of measuring the LY was not taken into account, which is of course connected to the fact that in case of low energy photons the major scintillation light is generated close to the front face of the crystal. The NUF-effect leads to a deviation between the extreme crystal geometries of $\sim 40\,\%$ in collected light. For quality control, either the set limit on the LY should be adapted to the crystal shape. The experimental setup is in general independent of the measured crystal shape. In the future, the trend probably goes to crystals with a more uniform response including the compromise with the covered solid angle, since the NUF-effect deteriorates the homogeneity of the detector and worsens the energy resolution especially at higher energies. Differences in the distributions could also be observed for the $\Delta\lambda$-parameter for BTCP and CERN, but also here a type-specific variation could be observed (Fig. 2.24).

6.1.2 Comparison to CMS-type PWO crystals

In this subsection, the achieved quality of the PWO crystals analysed in this thesis and the crystals used in the CMS experiment are compared. There are some general differences between the crystals for PANDA and CMS. The calorimeter ECAL of the latter one consists of roughly 5 times more crystals than PANDA, resulting in a finer granularity in angle due to the larger distance to the interaction point. Moreover, the crystals for CMS have a length of $23\,\mathrm{cm}$, which is compensating to the higher energy range and requiring a larger detector volume to contain the shower. An additional requirement is set to a homogeneous response along the long crystal axis, since the centre of gravity of the electromagnetic shower reaches deeper into crystal compared to PANDA energies. The expected photons in the range of $100-200\,\mathrm{GeV}$ deliver sufficient photon statistics. Therefore, the overall energy resolution is dominated by the constant term, which is strongly influenced by a non-linear response. The CMS are homogenised by roughing one of the crystal side faces. As it was already mentioned in Sec. 2.1, the properties of PWO have been improved within an R&D programme. Structural perfection of the crystal matrix has been achieved by an improved control of the stoichiometric composition of the melt and a further development of the doping concentration. Tab. 6.2 summarises the chosen limits and the final quality expressed in the mean values of the most important parameters. Also SICCAS supplied a relative small fraction of the crystals for CMS, but here only crystals for the barrel from BTCP were considered.

Parameter / Unit	CMS		PANDA	
	Limit	Mean value	Limit	Mean value
long. trans. at 360 nm	$\geq 25\,\%$	$38.6\,\%$	$\geq 35\,\%$	$48.8\,\%$
long. trans. at 420 nm	$\geq 55\,\%$	$69.5\,\%$	$\geq 60\,\%$	$71.0\,\%$
long. trans. at 620 nm	$\geq 65\,\%$	$74.7\,\%$	$\geq 70\,\%$	$77.3\,\%$
disp. of transv. trans.	$\leq 3\,\mathrm{nm}$	$0.69\,\mathrm{nm}$	$\leq 3\,\mathrm{nm}$	$0.59\,\mathrm{nm}$
LY	$\geq 8\,\frac{\mathrm{phe}}{\mathrm{MeV}}$	$10.2\,\frac{\mathrm{phe}}{\mathrm{MeV}}$	$\geq 16\,\frac{\mathrm{phe}}{\mathrm{MeV}}$	$20.4\,\frac{\mathrm{phe}}{\mathrm{MeV}}$
radiation hardness	$\leq 1.5\,\mathrm{m}^{-1}$	$1.04\,\mathrm{m}^{-1}$	$\leq 1.1\,\mathrm{m}^{-1}$	$0.81\,\mathrm{m}^{-1}$

Table 6.2: Comparison of quality control of CMS [18, 52] and PANDA.

All parameters of crystals in the PWO-II version for PANDA show significantly improved properties, which is a consequence of the much more stringent requirements. The transparency has been improved especially at $360\,\mathrm{nm}$. This is closely connected to the shifting of the absorption edge to lower wavelengths. At all other wavelengths the improvement is on a minor level but still noticeable. For the dispersion of the transversal transmission a slight improvement could be observed as well and is caused

by the changed sequence of the growing process of the crystals. A significant enhance-ment can be observed in case of the LY, since the obtained mean value has been nearly doubled. But here the overall distribution of the LY is ranging from $\sim 17\,\mathrm{phe/MeV}$ to $\sim 25\,\mathrm{phe/MeV}$ for crystals of the end caps and the most tapered versions (Fig. 2.21), respectively. In case of CMS and its dynamic range of the EMC from $0.15-1,000\,\mathrm{GeV}$, the more crucial parameter is the uniformity of the response along the crystal axis, which was achieved by roughing up one surface of the crystals. A strong correlation between the roughness parameter Ra, which is basically an average of the profile devi-ation (Eq. 6.1), and the homogeneity of the longitudinal dependency of the response could be established [53]:

$$Ra = \frac{1}{l} \int_0^l f(x)dx, \tag{6.1}$$

with $f(x):$ surface profile.

It turned out that $Ra \approx 0.25\,\mu\mathrm{m}$ is an optimum value for the application in the CMS ECAL. The scenario of one roughed surface was also considered for PANDA, but other aspects play a major role, which are in detail discussed in [31]. As a last point, the crystal performance concerning radiation hardness is compared. The set requirement in case of CMS is again less strict, but here one has to distinguish between the different procedures and applied doses and dose rates as well as the operation at different temperatures. In the quality control for CMS the crystals are illuminated until they reach full saturation, and thermal recovery and radiation damage equilibrate. The corresponding dose and dose rate are $\geq 500\,\mathrm{Gy}$ and $\geq 100\,\mathrm{Gy/h}$, respectively. This makes a direct comparison of the given values in Tab. 6.2 more complex. Fig. 6.2 shows the typical dependence of the induced absorption coefficient as a function of the integral dose of a randomly chosen crystal of the mass production [54].

The ratio between change of the absorption coefficient at the saturation level and at $30\,\mathrm{Gy}$ can be estimated to:

$$\frac{\Delta k_{\mathrm{Saturation}}}{\Delta k_{30\,\mathrm{Gy}}} \approx \frac{1.1\,\mathrm{m}^{-1}}{0.9\,\mathrm{m}^{-1}} \approx 1.22. \tag{6.2}$$

Therefore, the mean value of the PANDA crystals has to be scaled, which results in

$$\overline{\Delta k}_{\mathrm{PANDA/30\,Gy}} \cdot 1.22 = 0.81\,\mathrm{m}^{-1} \cdot 1.22 \approx 0.988\,\mathrm{m}^{-1} \lesssim \overline{\Delta k}_{\mathrm{CMS/Saturation}}. \tag{6.3}$$

All in all, it can be stated that nearly all parameters have been successfully improved with respect to the achieved quality for the CMS experiment. Especially the LY values are on average enhanced by a factor two. This fact, in combination with the gain connected to the low operating temperature of $-25\,^\circ\mathrm{C}$, will serve as an excellent base for building up an EMC for the envisaged energy range of PANDA.
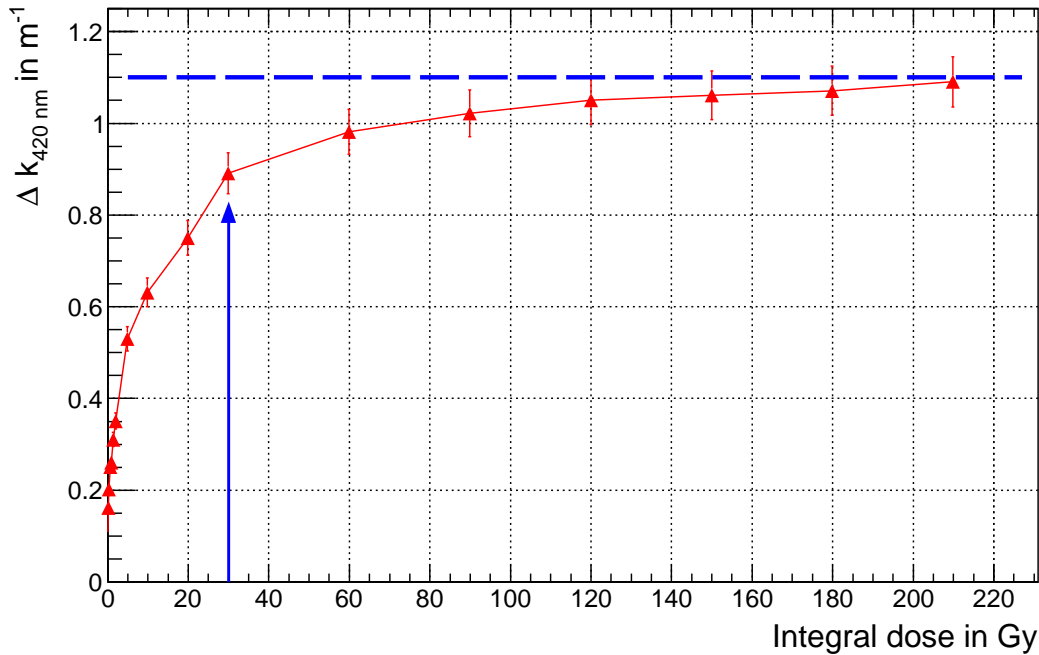
Figure 6.2: Correlation induced change of the absorption coefficient and the integral dose. The dashed blue line corresponds to an estimated saturation level of $1.1 \, \mathrm{m}^{-1}$, whereas the blue arrow marks the value at $30 \, \mathrm{Gy}$ [20].

6.1.3 Outlook with SICCAS crystals

Fig. 2.28 shows the current production status of the PANDA EMC. Due to the fact that BTCP is out of business to deliver additional crystals missing, an alternative supplier has to be found. The most probable and promising candidate is SICCAS, another large crystal producer who is able to handle PWO. Already in the course of the CMS experiment, this company produced a relatively small fraction of $1,825$ crystals. For PANDA, 50 crystals of type 11 geometry were produced by SICCAS and tested by the facilities at CERN and Gießen, according to the most relevant parameters. As it was pointed out in Sec. 2.5.1, the birefringent crystals are produced by the so called Bridgeman method and have therefore a different growing axis, namely the ordinary axis. Here the index of refraction and the absorption coefficient are appreciably higher compared to the extraordinary direction, which implies a reduction of the achievable longitudinal transmission (compare Fig. 2.31). This is directly visible in a shift of the obtained transmission distributions in Fig. 2.32, which is extremely pronounced at $360 \, \mathrm{nm}$. Tab. 6.3 provides a direct comparison of the transmission parameters at the three relevant wavelengths for CMS and PANDA.

The tendency shown in Tab. 6.3 confirms the expectation of a lower longitudinal transmission due to the mentioned reasons. Another interesting conclusion can be

	wavelength	CMS	PANDA
	360 nm	11.3 %	18.2 %
$\overline{T}_{BTCP} - \overline{T}_{SICCAS}$	420 nm	3.7 %	6.0 %
	620 nm	1.4 %	0.1 %

Table 6.3: Comparison of mean values $\overline{T}$ in longitudinal transmission of crystals from BTCP and SICCAS. The data was taken from [52] and from the quality control at Gießen for CMS and PANDA, respectively.

drawn by comparing the homogeneity in transversal transmission for both suppliers. In case of crystals for CMS produced by SICCAS, the mean value of the $\Delta\lambda$-parameter is about 1.71 nm larger compared to the one from BTCP (by [52]). A similar trend is observed in the case of PANDA, but here a quantitative statement is not possible due to the explained sensitivity on geometry (compare Fig. 2.24). Nevertheless, the crystals produced by the Czochralski method (Fig. 2.1a) are definitely much more homogeneous along the long crystal axis, compared to the Bridgeman method (Fig. 2.30).

The situation is contrary for the determined LY. Here the crystals from SICCAS show an excellent performance except the overall homogeneity of the production. The 50 test samples from SICCAS are broadly distributed from ~ 12 phe/MeV to ~ 27 phe/MeV with a mean value of 19.1 phe/MeV, which is high in spite of the type 11-geometry and the less pronounced NUF-effect. A clear negative aspect is the large RMS of 3.6 $\frac{phe}{MeV}$ which might be connected to the instability of the growing process. Concerning the radiation hardness of the SICCAS crystals (Fig. 2.35), no noteworthy deviation to the BTCP crystals could be observed. In the context of the quality parameter of PWO-II with respect to the comparison of both suppliers, similar results were obtained by [51]. After the analysis of the 50 test samples and the gained experiences by CMS, SICCAS crystals are suitable for application in the PANDA EMC. A larger number of crystals as preproduction lot is ordered and should serve as a further reference point for the achievable quality and its spread as well as the production efficiency of the producer.

6.2 Time Resolution

The time resolution of the PROTO60 was determined in Sec. 4 for different readout chains and energy ranges. In the first two beamtimes in 2009 and 2010 at the acceleration facility MAMI at Mainz, the time information was extracted with TDCs, whereas in the CERN beamtime the time stamps were determined offline with the explained feature extraction algorithm (compare Sec. 3.1.4). In all data sets, a clear energy dependent time-walk effect was visible. For a subsequent offline correction, the

particular shape of the time distribution as a function of the deposited energy was described and corrected with Eq. 4.11. The absolute calibration was, in case of TDC based readout, achieved by digitised time spectra of a test pulser with and without delay. Using SADC readout, the time calibration is directly given by the sampling frequency of 50 MHz.

In both MAMI test beamtimes, a time resolution below 1 ns for the processed scenarios above 250 MeV could be achieved. The obtained data for the time resolution was described by a three parametric function (Eq. 4.12). This allows an extrapolation of the time resolution to an energy of 1 GeV, which results in 430 ps for a single module, extracted from two adjacent crystals with similar energy deposition. Conspicuous are the resulting fit parameters in Fig. 4.17. For the regarded time difference, the stochastic term (represented by the $\sqrt{E}^{-1}$-term) disappears, because of the narrow window on the deposited energy. The same behaviour was already confirmed in [49] for similar circumstances. Furthermore, in case of the noise term, the situation is inverted, since here the noise of the crystals contributes.

In the beamtime of 2010, an up to now unexplained structure arises at the medium energies (visible in Fig. 4.21). Currently it is assumed that this anomaly originates from an internal software problem of the tagger readout, which finally results in a mixing of tagger channels. This can in addition be seen in Fig. 4.20 in an unusual broadening in the relevant energy range and could already be observed in [42] and [55]. For the CERN beamtime in 2011, a final time resolution of 441 ps could be determined, again by using the time difference of neighbouring crystals with a shower shared equally corresponding to a mean energy of 5.5 GeV each. The dynamic range for this beamtime was set to cover the expected energy range (compare Tab. 4.1). Therefore, no significant improvement compared to the MAMI beamtimes could be expected due to a similar SNR.

The obtained time resolutions are mainly limited by the LAAPDs due to the reasons mentioned in Sec. 4.3. Measurements with a 3×3 PWO crystal matrix read out by PMTs achieved a single unit time resolution of 130 ps for an incident electron energy of 855 MeV [56].

6.2.1 Obtained Time Resolution of the CMS EMC

The operation mode of the EMC of the CMS experiment is in many aspects similar to the one of the PANDA EMC. Therefore, a direct comparison focussing on timing purposes is advisable. Nevertheless, there are differences concerning the extraction of the time information and will be explained in the following. The pulses are digitised with a sampling frequency of 40 MHz, which implies a channel width of 25 ns of the SADC [49]. Fig. 6.3a shows a typical normalised pulse shape containing 10 pedestal subtracted SADC samples. A possible way for a representation of the pulse shape

independent of the maximum amplitude A_{max} is given in Fig. 6.3b. Here the time information is plotted as a function of the ratio parameter between two consecutive samples and is defined as $R(T) = A(T)/A(T + 25\,\mathrm{ns})$ or $R_i = A_i/A_{i+1}$, which can easily be parametrised by a polynomial. For each sample i, a first order estimation of the time stamp $T_{\mathrm{max}/i}$ can be extracted via $T_{\mathrm{max}/i} = T_i - T(R_i)$. Here T_i corresponds to the time of sample i and $T(R_i)$ to the reconstructed time according to Fig. 6.3b. The particular uncertainty σ_i is derived from

$$\sigma_i = \frac{\partial T(R_i)}{\partial R_i} \Delta R_i, \tag{6.4}$$

in which the error of ΔR_i is determined from noise fluctuation in each sample, estimation of the subtracted pedestal and the truncation of the digitisation. Finally the time stamp T_{max} and its error σ_T of the pulse can be deduced by

$$T_{\mathrm{max}} = \frac{\sum_i \frac{T_{\mathrm{max}/i}}{\sigma_i^2}}{\sum_i \frac{1}{\sigma_i^2}}, \tag{6.5}$$

$$\frac{1}{\sigma_T^2} = \sum_i \frac{1}{\sigma_i^2}. \tag{6.6}$$

Furthermore, for the final EMC detector the crystals have to be synchronised among

(a)   (b)
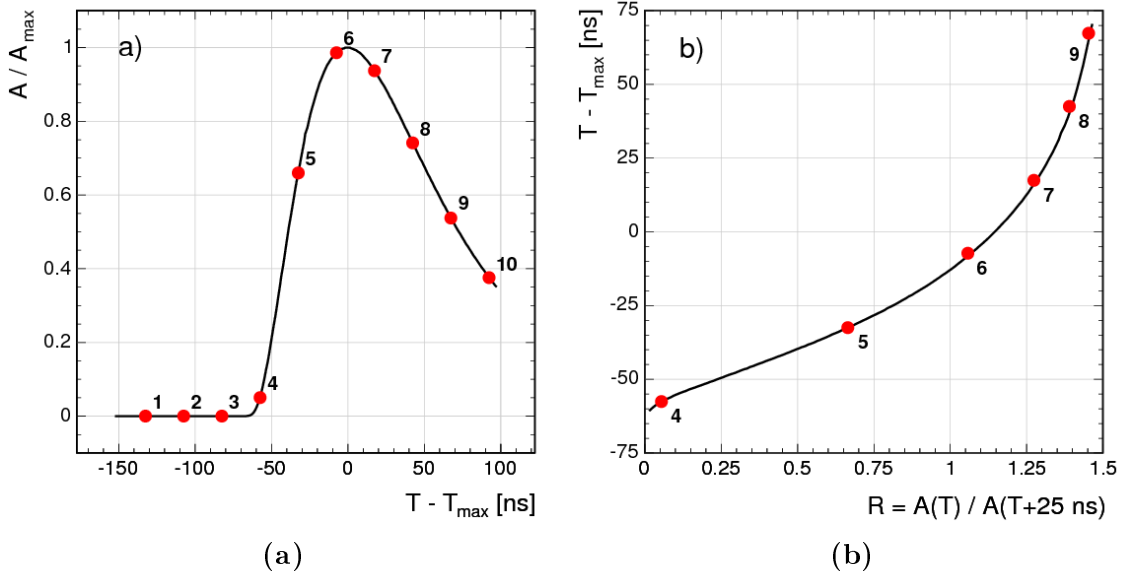
Figure 6.3: (a) Typical pulse comprising 10 discrete data points. (b) Alternative illustration of the pulse shape as a function of the ratio parameter $R(T)$ [49].

each other, due to the different arrival time of particles from the interaction point.

Here, the corresponding solid angle of the particular crystals plays a major role, since the time of flight can vary by a few ns. In case of CMS, this is done by a beam-splash composed of muons [57].

It could be shown that, with a carefully calibrated and synchronised detector, a time resolution below 100 ps ([49]) is possible for large energies corresponding to 20 GeV and 100 GeV in barrel and endcaps, respectively. Here, the time difference between two adjacent crystals with similar energy deposition caused by electrons serves as a time stamp. The constant term of Eq. 4.12 is almost negligible, but as a drawback, the noise term limits the time resolution at smaller energies. At 1 GeV deposited energy, a time resolution of 1.5 ns is expected in the barrel part ($\sigma_{\mathrm{noise}} \sim 140$ MeV).

For unsynchronised data, a time resolution determined with cosmic ray muons at higher energies is limited by the constant term of ~ 380 ps, which is consistent with the applied synchronisation correction and with the results obtained in this thesis.

6.2.2 Outlook on Time Resolution for PANDA

The time resolution deduced in this thesis is not the final one and should be seen as an upper limit regarding timing purposes. As it was explained in the previous sections, the time resolution dramatically depends on the applied gain of the photo sensors. As a next step, with the implementation of the newest version of the ASIC with two separate gain branches, covering the lower and upper part of the energy range, another improvement of the time resolution can be expected. This will be the case in the next generations of EMC prototypes.

Another point is the necessity of a significantly improved time resolution of the EMC at least for charged particles due to the planned SciTil modules in front of the crystals. Latest test results of a SciTil prototype show an achieved time resolution of 210 ps [47]. An additional prototype including both, EMC and SciTil modules, is planned to study and learn more about the interplay of both components. The impact of the SciTil plates in addition to the fused silica bars of the DIRC detector of pair production on the EMC performance is currently under investigation.

As it was mentioned before, with the detection of scintillation light, the time determination is limited to the order of tens of ps. In course of the development in PET[2] technologies in medical science it could be shown that the timing can significantly be improved with the detection of Cherenkov light [58]. In contrast to the generated scintillation light, the Chrerenkov light is produced prompt, but on the other hand there is a comparably low detection yield (for PWO compare 1.3.1.1). Therefore, the QE of the photo sensors has to have a sufficient coverage of the blue to the UV[3]-light and an adequate discrimination ability. Nevertheless, as well in high energy physics

---

[2]Positron Electron Tomography
[3]Ultraviolet

the up to now achieved limits can be overcome via the detection of the Cherenkov component.

6.3 Higher Order Energy Correction

In order to account for the energy loss in the passive material between the crystals or enhanced shower leakage, the obtained energy of for instance a 3×3 cluster has to be corrected. Therefore the given equation for calibration 4.1 has to be extended by an additional position dependent correction factor:

$$E_{\text{cal}}^* = F_{\gamma/e^\pm} \cdot C_{\text{abs}} \cdot \sum_i S_i(t) \cdot c_i \cdot E_{i/\text{uncal}}. \tag{6.7}$$

The additional factor $F_{\gamma/e^\pm}$ is introduced, which is in principle a function of the spherical coordinates ϑ and φ. Moreover, in case of electromagnetic probes one has to distinguish between photons and electrons or positrons, respectively, because of the slightly different way of interaction and the resulting shower profile (compare Tab. 1.6). In this thesis, the factor $F_{\gamma/e^\pm}$ was determined with the so called $\ln(E_2/E_1)$-method (explained in Sec. 5.2.1), in which the value of $\ln(E_2/E_1)$ gives a first order information about the point of impact for a single event. With the knowledge of $F_{\gamma/e^\pm}$ the detected energy is subsequently corrected according to Eq. 5.3. For the analysed beamtimes, this kind of correction function was only determined for a particular transition from one crystal to another in horizontal direction in space, corresponding to the φ-direction. As it was mentioned, a further analysis is planned to apply this correction also to the vertical direction, especially to gain information about the impact of the staggering of the crystals rows.

Tab. 5.1 gives a quantitative summary of the results achieved in the CERN beamtime in both performed runs. Especially in the second run, with an impinging beam in between the crystals, an absolute improvement from $1.896\,\%$ to $1.688\,\%$ could be achieved. Furthermore Fig. 5.7a underlines the necessity of the application of the $\ln(E_2/E_1)$-method to get an uniform detector response. As expected, the more centralised the photons were impinging on the front face of the crystal, the smaller the applied correction and consequently the improvement. In a further analysis for photon energies from $150 - 1,500\,\text{MeV}$ at the MAMI facility at Mainz, an independence of the energy could be evaluated. Also, the achieved lowering of the energy resolution is almost constant over the full energy range and amounts to $0.25\,\%$ for the run shooting in between the crystals. This value is slightly worse but still comparable to the achievements of the CERN beamtime.

6.3.1 Alternatives to the $\ln\left(\frac{E_2}{E_1}\right)$-Method

Sec. 5 documents the successful application of the $\ln(E_2/E_1)$-method for different circumstances. But there are a handful of alternatives, which were partially used in other experiments. One possible option would be the determination of a correction function $F_{\gamma/e^\pm}$ via simulations. But for this strategy one has to fully understand the input and the outcome of such a simulation. Based on the past experiences a perfect agreement between simulation and experiment was up to now not achieved and deviates significantly. Therefore, a correction with a full reliability on a non-perfectly understood simulation is not advisable.

List of Figures

List of Tables

Bibliography

[1] V. Metag, "Group lecture," 2008.

[2] http://www.fair-center.de.

[3] R. Maier, ed., *The high-energy storage ring (HESR)*. 2011. Particle Accelerator Conference.

[4] **PANDA** Collaboration, "Physics Performance Report for PANDA," (2009) , `arXiv:0903.3905v1`.

[5] **PANDA** Collaboration, "Technical Design Report for the: PANDA Straw Tube Tracker," (2012) , `arXiv:205.5441v2 [physics.ins-det]`.

[6] **PANDA** Collaboration, "Technical Design Report for the: PANDA Micro Vertex Detector," (2012) , `arXiv:1207.6581v2 [physics.ins-det]`.

[7] L. Ackermann, "Charakterisierung von Silizium-Streifensensoren für den PANDA Micro-Vertex-Detektor," Diplomarbeit , Technische Universität Dresden, 2009.

[8] **PANDA** Collaboration, "Public technical progress report," 2005.

[9] J. Schwiening, "The Barrel DIRC for the PANDA Experiment at FAIR," 2011. HIC for FAIR Detector Systems Networking Workshop.

[10] http://www-panda.gsi.de/framework/content/detector/det_forward.html.

[11] S. Diehl, "Ansprechverhalten eines Shashlyk-Kalorimeters für hochenergetische Photonen im Energiebereich von 100 MeV bis 770 MeV," Master's thesis, Justus Liebig Universität Gießen, 2012.

[12] H. Löhner, 2012. Talk, PANDA Meeting.

[13] W. Leo, *Techniques for Nuclear and Particle Physics Experiments*. Springer, 1994.

[14] M. Berger *et al.*, "XCOM: Photo Cross Sections Database." http://www.nist.gov/pml/data/xcom/index.cfm.

[15] R. Novotny, "Messmethoden der Kern- und Teilchenphysik.". Lecture.

Bibliography

[16] PDG, *Particle Physics Booklet*, p. 238. 2010.

[17] H. Koch, C. Amsler, E. Aker, and T. Armstrong, "Proposal: the crystal barrel," Tech. Rep. CERN-PSCC-85-56. PSCC-P-90, CERN, Geneva, 1985.

[18] **PANDA** Collaboration, "Technical Design Report for PANDA Electromagnetic Calorimeter (EMC)," (2008) , `arXiv:0810.1216v1 [physics.ins-det]`.

[19] http://webmineral.com/.

[20] D. V. Ivanovich, *Lead tungstate scintilation crystals for the electromagnetic calorimeter of the PANDA experiment.* PhD thesis, Institute for Nuclear Problems, Belrussian State University, Minsk, 2008.

[21] M. Leyhe, "Tests zur Auslese von PWO-Szintillatoren," Master's thesis, Ruhr-Universität Bochum, 2010.

[22] P. Schneider, "Messung der magnetfeldabhängigen Verstärkung von Vakuum-Phototetroden," Bachelor's Thesis (Studienarbeit), Ruhr-Universtität Bochum, 2011.

[23] M. Kavatsyuk, "Trigger-less readout system with pulse pile-up recovery for the panda electromagnetic calorimeter," 2013.

[24] P. Wieczorek, 2012. Talk, PANDA Meeting.

[25] A. Annenkov, "Improved light yield of lead tungstate scintillators," *Nuclear Instruments and Methods in Physics Research Section A: Accelerators, Spectrometers, Detectors and Associated Equipment* **450** no. 1, 71 − 74.

[26] M. Böhm, " Influence of Mo Impurity on the Spectroscopic and Scintillation Properties of PWO Crystals ," *physica status solidi (a)* (1998) .

[27] T. Eißner, "Quality Control of PWO-Crystals for the PANDA Detector," Diplomarbeit , Justus Liebig Universität Gießen, 2009.

[28] E. Auffray, "Performance of ACCOS, an Automatic Crystal quality Control System for the PWO crystals of the CMS calorimeter," *Nuclear Instruments and Methods in Physics Research Section A: Accelerators, Spectrometers, Detectors and Associated Equipment* **456** no. 3, (2001) 325 − 341.

[29] http://www.hund.de/.

[30] S. Baccaro, "Ordinary and extraordinary complex refractive index of the lead tungstate (pbwo4) crystal,".

[31] D. Bremer, *TBA*. PhD thesis, Justus Liebig Universität Gießen, 2013.

[32] http://english.sic.cas.cn/.

[33] http://commons.wikimedia.org/wiki/File:Bridgman-Stockbarger-Verfahren.svg.

[34] M. Kavatsyuk, D. Bremer, V. Dormenev, P. Drexler, T. Eissner, W. Erni, E. Guliyev, T. Hennino, B. Krusche, B. Lewandowski, H. Löhner, M. Moritz, R. Novotny, K. Peters, J. Pouthas, P. Rosier, M. Steinacher, G. Tambave, and A. Wilms, "Performance of the prototype of the electromagnetic calorimeter for PANDA,".

[35] M. Janecek and W. W. Moses, "Optical reflectance measurements for commonly used reflectors," *Nuclear Science, IEEE Transactions on* **55** no. 4, (2008) 2432–2437.

[36] http://www.hamamatsu.com/resources/pdf/ssd/s8664_series_kapd1012e04.pdf.

[37] M. Kavatsyuk, "Private communications.".

[38] J. McGeorge, J. Kellie, J. Annand, J. Ahrens, I. Anthony, A. Clarkson, D. Hamilton, P. Lumsden, E. McNicoll, R. Owens, G. Rosner, and A. Thomas, "Upgrade of the glasgow photon tagging spectrometer for mainz mami-c," *The European Physical Journal A* **37** no. 1, (2008) 129–137. http://dx.doi.org/10.1140/epja/i2007-10606-0.

[39] http://www.kph.uni-mainz.de/mami.php.

[40] http://home.web.cern.ch/.

[41] M. Moritz, *Measurements and improvements of the response of the PANDA-EMC prototype PROTO60 to high energetic particles and photons in accelerator experiments.* PhD thesis, Justus Liebig Universität Gießen, 2013.

[42] W. Lippert, "Konzepte der Kalibration eines Protoyps des EM-Kalorimeters für PANDA," Bachelor's Thesis (Studienarbeit), Universtität Gießen, 2010.

[43] I. Konorov, H. Angerer, A. Mann, and S. Paul, "Soda: Time distribution system for the panda experiment," in *Nuclear Science Symposium Conference Record (NSS/MIC), 2009 IEEE*, pp. 1863–1865. 2009.

[44] P. Lecoq, *Inorganic Scintillators for Detector Systems*, p. 83. Springer, 2006.

[45] G. Tambave, "Pulse pile-up recovery for the front-end electronics of the panda electromagnetic calorimeter," *iopscience* .

[46] G. Tambave, M. Kavatsyuk, E. Guliyev, F. Schreuder, H. Moeini, and H. Löhner, "Pulse pile-up recovery for the front-end electronics of the panda electromagnetic calorimeter," *Journal of Instrumentation* **7** no. 11, (2012) P11001. http://stacks.iop.org/1748-0221/7/i=11/a=P11001.

[47] C. Schwarz, 2013. Talk, XLIV PANDA Meeting.

[48] B. Lemmer, "Measurement of the Excitation Function of Omega Photoproduction on Carbon and Niobium," Diplomarbeit , Justus Liebig Universität Gießen, 2009.

[49] **CMS** Collaboration, "Time Reconstruction and Performance of the CMS Electromagnetic Calorimeter," (2009) , `arXiv:0911.4044v2`.

[50] "Periodic position dependence of the energy measured in the cms electromagnetic calorimeter,". http://inspirehep.net/record/713920/files/NOTE2006_045.pdf.

[51] F. Yang, R. Mao, L. Zhang, and R.-Y. Zhu, "A study on radiation damage in bgo and pwo-ii crystals," *Journal of Physics: Conference Series* **404** no. 1, (2012) 012025. http://stacks.iop.org/1742-6596/404/i=1/a=012025.

[52] E. Auffray, "Overview of the 63,000 pwo barrel crystals for cms ecal production," *Nuclear Science, IEEE Transactions on* (2008) .

[53] J. Descamps and P. Jarry, "Development of a Uniformisation Procedure for the PWO Crystals of the CMS Electromagnetic Calorimeter,". CERN-CMS-NOTE-2001-004.

[54] D. V. Ivanovich, "Private communications.".

[55] D. Bremer, "Reconstruction of Electromagnetic Showers and Determination of the Postion Resolution of a Prototype of the PANDA Electromagnetic Calorimeter," Diplomarbeit , Justus Liebig Universität Gießen, 2010.

[56] R. Novotny, W. Döring, K. Mengel, V. Metag, and C. Pienne, "Response of a pbwo4-scintillator array to electrons in the energy regime below 1 gev," *Nuclear Physics B - Proceedings Supplements* **61** no. 3, (1998) 613 – 618. http://www.sciencedirect.com/science/article/pii/S0920563297006270.

[57] G. Franzoni, "Performance of cms ecal with first lhc data," *Nuclear Instruments and Methods in Physics Research Section A: Accelerators, Spectrometers, Detectors and Associated Equipment* **628** no. 1, (2011) 90 – 94. http://www.sciencedirect.com/science/article/pii/S0168900210014816.

[58] S. E. Brunner. Talk, SCINT 2013, Shanghai.

Acronyms

6N purity level of $\geq 99.9999\%$. 43

ACCOS Automatic Crystal quality Control System. 55, 158

ADC Analogue to Digital Converter. 88

APD Avalanche Photo Diode. 35–38, 108

APFEL ASIC for PANDA Front-end Electronics. 3, 5, 40

APPA Atomic Plasma Physics and Application. 8

ASIC Application Specific Integrated Circuit. 3, 5, 40, 93, 108, 117, 167

BGO $Bi_4Ge_3O_{12}$. 33–35

BTCP Bogoroditsk Techno Chemical Plant. IX, 3, 5, 43, 54, 55, 57, 63, 67–72, 75, 77, 78, 157–161, 163, 164

CBM Compressed, Baryonic Matter. 8

CERN European laboratory for particle physics. VII, IX, 3, 5, 43, 54, 55, 61, 65–68, 70–72, 77, 81, 86, 93, 101, 102, 104, 107, 108, 113, 132, 134, 139, 140, 144, 146, 148, 154, 158–160, 163–165, 168

CFD Constant-Fraction Discriminator. 87, 91, 113, 114

CFT Constant-Fraction Timing. 91, 92, 111, 113, 116, 132

charmonium a bound state of a charm quark and its antiparticle. 10

CMS Compact Muon Solenoid. VIII, IX, 1, 3, 5, 35, 38, 44, 53, 55, 57, 66, 69, 143, 157, 161–165, 167

DAQ Data-Acquisition. 109

DCON Data Concentrator. 109

DIRC Detection of Internally Reflected Cherenkov light. 17–19, 117, 167

Acronyms

ECAL Electromagnetic Calorimeter. 55, 161, 162

ECL Emitter Coupled Logic. 88, 118

ELSA Elektronen-Stretcher-Anlage. 139

EMC Electromagnetic Calorimeter. 1, 3, 5, 8, 9, 12, 19, 23, 34, 37, 46, 81, 88, 105, 109, 110, 117, 144, 145, 154, 157, 159, 162–167

ENC Equivalent Noise Charge. 40

ESR Enhanced Specular Reflector. 83

ESR Experimental Storage Ring. 8

EU European Union. 44

FAIR Facility for Antiproton and Ion Research. 7, 8

FEE Front-End Electronics. 109

FPGA Field Programmable Gate Arrays. 88

FRS Forward Range System. 21

FS Forward Spectrometer. 14, 19–21

FWHM Full Width at Half Maximum. 46, 96

GEANT4 Toolkit for the simulation of the passage of particles through matter / http://geant4.cern.ch/. 106

GEM Gaseous Electron Multipliers. 17, 18

GSI Gesellschaft für Schwerionenforschung GmbH. 7, 8

HDSM Harmonic Double-Sided Microtron. VI, 95–97

HESR High Energy Storage Ring. 8, 9, 20

IOL Input Output Logic. 88

J-FET Junction Field Effect Transistor. 40

LAAPD Large Area Avalanche Photo Diode. 35, 37, 40, 41, 83, 85–87, 90, 93, 99, 112, 165

LEAR Low Energy Antiproton Ring. 12

LED <u>L</u>ight <u>E</u>mitting <u>D</u>iode. 115

LHC <u>L</u>arge <u>H</u>adron <u>C</u>ollider. 33, 34, 101

LINAC <u>Lin</u>ear <u>A</u>ccelerator. 94, 96, 97

LITRANI <u>L</u>ight <u>T</u>ransmission in <u>Ani</u>sotropic media / http://gentitfx.fr/litrani/. 60

LNP-P <u>L</u>ow <u>N</u>oise and Low <u>P</u>ower Charge <u>P</u>reamplifier. VI, 40, 85, 86, 88–91

LY <u>L</u>ight <u>Y</u>ield. 34, 35, 51, 157, 159–162, 164

LYSO $Lu_{2(1-x)}Y_{2x}SiO_5$. 34, 35

MA <u>M</u>oving <u>A</u>verage. 89, 91

MAMI <u>M</u>ainzer <u>M</u>ikrotron. VII–IX, 81, 86, 93–97, 99, 100, 103, 108, 113, 118, 128, 139, 140, 150–152, 154, 164, 165, 168

MDC <u>M</u>ulti-wire <u>D</u>rift <u>C</u>hambers. 20, 21

MDT <u>M</u>ini-<u>D</u>rift <u>T</u>ube. 19

MIP <u>M</u>inimum <u>I</u>onising <u>P</u>article. 16, 25, 106

MUD <u>M</u>uon <u>D</u>etection. 19, 21

MVD <u>M</u>icro <u>V</u>ertex <u>D</u>etector. 12, 16, 17, 19, 102, 132

MWD <u>M</u>oving <u>W</u>indow <u>D</u>econvolution. 89–91, 116

NCE <u>N</u>uclear <u>C</u>ounter <u>E</u>ffect. 38

NESR <u>N</u>ew <u>E</u>xperimental <u>S</u>torage <u>R</u>ing. 8

NIM <u>N</u>uclear <u>I</u>nstrumentation <u>M</u>ethods. 88, 128

NUF <u>N</u>on-<u>U</u>niformity in light collection. 66, 159, 160, 164

NUSTAR <u>N</u>uclear <u>S</u>tructure, <u>A</u>strophysics and <u>R</u>eactions. 8

PANDA Anti-<u>P</u>roton <u>A</u>nnihilation at <u>D</u>armstadt. IX, 1, 3, 5, 8–12, 14, 15, 18–20, 34, 37, 38, 40, 43, 46, 49, 54, 88, 93, 109, 110, 117, 128, 139, 150, 157, 159, 161–165, 167

PCB <u>P</u>rinted <u>C</u>ircuit <u>B</u>oard. 85, 86

PET <u>P</u>ositron <u>E</u>lectron <u>T</u>omography. 167

PID <u>P</u>article <u>I</u>dentification. 19, 21, 25, 117

Acronyms

PMT Photomultiplier Tube. 21, 25, 35, 38, 45, 51, 56, 61, 62, 97, 111–113, 118, 120, 165

PS-ADC Peak Sensing - Analogue to Digital Converter. 87, 88, 93, 108

PWO Lead tungstate (PbWO$_4$). 1, 33, 35, 43, 44, 86, 139, 157, 161, 163–165, 167

QCD Quantum Chromo Dynamics. 10, 11

QDC Charge-to-Digital-Converter, CAMAC, Le Croy 2249W. 62

QE Quantum Effeciency. 36, 85, 167

R&D Research and Developement. 34, 37, 43, 161

RF Radio Frequency. 95

RICH Ring Imaging Cherenkov Counter. 21

RINP Research Institute for Nuclear Problems of Belarussian State University. 57

RMS Root Mean Square. 78, 109, 153, 164

RTM Race Track Microtron. 94–96

SADC Sampling Analogue to Digital Converter. 39, 88, 90, 93, 104, 132, 165

SciTil Scintillating Tile. 117, 167

SEP Single Electron Peak. 51, 62

SICCAS Shanghai Institute of Ceramics, Chinese Academy of Sciences. IX, 1, 3, 5, 63, 75, 78, 157, 161, 163, 164

SiPM Silicon Photomultiplier. 117

SIS Schwer Ionen Synchrotron. 8

SNR Signal-to-Noise Ratio. 111, 112, 165

SODA Synchronisation of Data Acquisition. 3, 5, 109

SPS Super Proton Synchrotron. 93, 101, 102, 108

STT Straw Tube Tracker. 17, 19

TAPS Two Arm Photon Spectrometer. 113, 122

TDC Time-to-Digital-Converter. 56, 57, 87, 88, 98, 121, 122, 128, 164, 165

TOF Time of Flight. 117

TS Target Spectrometer. 14, 17, 19, 21

UNILAC Universal Linear Accelerator. 8

UV Ultraviolet. 167

VPT Vaccum Photo Triode. 35, 38, 40

VPTT Vaccum Photo Tetrode. 35, 38, 39

WLS Wavelength Shifting. 21

Acknowledgements

Erklärung der Urheberschaft

Ich erkläre: Ich habe die vorgelegte Dissertation selbständig und ohne unerlaubte fremde Hilfe und nur mit den Hilfen angefertigt, die ich in der Dissertation angegeben habe.

Alle Textstellen, die wörtlich oder sinngemäß aus veröffentlichten Schriften entnommen sind, und alle Angaben, die auf mündlichen Auskünften beruhen, sind als solche kenntlich gemacht.

Bei den von mir durchgeführten und in der Dissertation erwähnten Untersuchungen habe ich die Grundsätze guter wissenschaftlicher Praxis, wie sie in der "Satzung der Justus-Liebig-Universität Gießen zur Sicherung guter wissenschaftlicher Praxis" niedergelegt sind, eingehalten.

Tobias Eißner
Gießen, im November 2013